

**School of Civil and Mechanical Engineering**

**Passive Control and Numerical Simulation of Vortex-Induced  
Vibration (VIV) of Marine Structures**

**Hamid Matin Nikoo**

**This thesis is presented to the Degree of  
Doctor of Philosophy**

**of**

**Curtin University**

**November 2019**

# DECLARATION

To the best of my knowledge and belief this thesis contains no material previously published by any other person except where due acknowledgement has been made.

This thesis contains no material which has been accepted for the award of any other degree or diploma in any university.



*Hamid Matin Nikoo*

Signature: ..... *11-Nov-19*

Date: 11-Nov-19

# ABSTRACT

When a flow passes a submerged, smooth and slender body such as marine risers, conductors and subsea pipelines, vortex-induced vibration (VIV) may occur due to the interaction between the structure and wake vortex shedding. When the shedding frequency of vortices approaches the natural frequency of the structure, lock-in or synchronisation phenomenon occurs. This phenomenon is associated with large amplitude oscillations of the structure, which in turn may result in the fatigue damage to the structural components or even catastrophic failure to the whole structure. VIV thus has been widely recognised as one of the main causes of structural failures, and it is important to mitigate the adverse action of VIV.

Extensive research works have been carried out in this area and many suppression strategies have been proposed. These strategies can be generally classified into two categories, namely the active and passive methods. Active methods need external energy resources to operate while passive devices require no external power to work. Compared to the active methods, passive methods are thus more applicable in real engineering practices. Several passive suppression devices such as helical strake, controlling rods, surface bumps, splitter plates, fairing and screen shroud have been proposed to suppress VIV of marine slender structures. However, some drawbacks still exist in the current control techniques. For example, helical strake, controlling rods and bumps cause an additional undesired hydrodynamic drag force to the structure. Splitter plates, fairings and shrouds are expensive to manufacture. Moreover, they are susceptible to the marine growth, storm damages and may cause undesired galloping in the structure. Further research efforts are therefore required to introduce new control methods which can provide more feasibility, effectiveness and applicability in real engineering applications.

The primary objective of this thesis is to propose more sophisticated passive suppression methods to mitigate the adverse effect of vortex shedding in marine slender structures. In particular, three different passive strategies are proposed:

(i) By using modified pipe-in-pipe (PIP) system. Conventional PIP systems consist of two concentric pipes, in which the outer pipe protects the product transporting inner pipe against the possible mechanical damages caused by the high external pressure and

dropped objects. Centralizers are normally installed between the inner and outer pipes to make the two pipes concentric. In the present thesis, optimal springs and dashpots are proposed to replace the conventional centralizers and used to connect the inner and outer pipes. By doing so, the two pipes can form a structure-tuned mass damper (TMD) system, which thus has the potential to mitigate the pipeline vibrations induced by various sources. This modified PIP system is proposed to control the VIV of subsea pipelines with suspended spans in the present thesis. Analytical study is carried out in Chapter 2, where the mathematical models of the conventional and modified PIP systems under VIV are presented, solved and validated by the experimental data. A series of sensitivity analysis is then carried out by a MATLAB Simulink code to optimize the connecting system between the inner and outer pipes. Finally, the explicit formulae for optimal spring stiffness and dashpot coefficients are derived. In Chapter 3, three-dimensional (3-D) computational fluid dynamic (CFD) simulations are carried out by developing a two-way coupled Fluid-Structure Interaction (FSI) framework to further investigate the effectiveness of the proposed system for VIV control. Analytical and numerical results show that the revised PIP system can significantly reduce VIV of subsea pipeline.

(ii) By using textured pipe. In the textured pipe, the wall of the pipe is not smooth but with local facets in both cross-sectional and longitudinal directions. Due to its special geometry, textured pipe may have the potential to mitigate VIV by altering the wake vortex street formation. The effectiveness of a single full-diamond textured cylinder for VIV suppression is numerically investigated in Chapter 4. A coupled FSI framework is adopted and 3-D CFD analyses are performed by coupling the ANSYS mechanical and FLUENT solvers together. Numerical results show that the textured cylinder can significantly mitigate the undesired VIV especially when the cylinder is vibrating under a relatively large velocity. Upper excitation regime is eliminated by the textured pipe and the lock-in regime is shorten remarkably.

(iii) By using textured-PIP system. The PIP system proposed in Chapter 2 and 3 is further modified by adopting textured pipe as the outer pipe. By doing so, both the TMD (in Chapters 2 and 3) and shape modification (in Chapter 4) mechanisms can be used to control VIV. The effectiveness of such design is numerically investigated in Chapter 5. The results show that the proposed passive design can further improve the efficiency of the single textured pipe and smooth PIP system in VIV suppression.

Reynolds-Averaged Navier-Stokes (RANS) codes equipped with shear stress transport (*SST*)  $K - \omega$  model is commonly used to simulate VIV. This method is however very difficult to capture the maximum VIV response of the cylinder. The second aim of the present thesis is to improve the accuracy of numerical models for VIV prediction. Two methods are investigated in the present thesis. The low- $R_e$  correction technique is incorporated into RANS *SST*  $K - \omega$  model in Chapter 6, and the 3-D VIV responses of an elastically-mounted cylinder subjected to the subcritical flow fluid regime are numerically investigated. Numerical results show that the adopted method leads to more accurate VIV response estimations compared to the commonly used RANS *SST*  $K - \omega$  method. In Chapter 7, a hybrid turbulence model known as Stress-Blended Eddy Simulation (SBES) is adopted to further improve the accuracy of VIV simulation. Numerical results show that this method can significantly improve the accuracy of VIV simulations compared to the commonly used Direct Numerical Simulation (DNS), RANS and Large Eddy Simulations (LES) methods with much less computational efforts.

## ACKNOWLEDGEMENTS

In the name of God,

I am indebted to many people upon the completion of this research effort:

First and foremost, I would like to express my deep appreciation and respect to my supervisors *Prof. Hong Hao* and *Dr. Kaiming Bi* for their invaluable guidance, insightful comments and encouragement throughout the course of this research. Your wisdom and rigorous attitude in research have given me a profound influence in my academic life.

I gratefully acknowledge the Curtin International Postgraduate Research Scholarship (CIPRS) that financially supports this research work. A big thanks to my friends at the Centre for Infrastructure Monitoring and Protection (CIMP) who all have contributed immensely to my academic life at Curtin University. Special thanks to *Haoran Zuo*, *Ruisheng Ma*, *Tin Do Van* and *Gao Fan* for your help and all the beautiful time we have had over the last four years.

I would like to deeply thank my parents, *Hossein and Zahra*, for their endless love and encouragement in all my pursuits, and my brothers, *Hooman* and *Bahman*, for supporting me spiritually throughout my life.

Words cannot express how grateful I am to my beloved wife, *Shohreh*, for her unconditional love, continued patience and generous support. You taught me how to be an integrated family and how to grow up together. I love you so much *Shohreh*.

Last but not least, I owe a big thanks to my lovely girl, *Rosina*, whose gorgeous smile helped this dissertation a lot!

Hamid Matin Nikoo

November, 2019

## **LIST OF PUBLISHED WORKS AND WORKS PREPARED FOR PUBLICATION**

This thesis contains published work and/or work prepared for publication, which has been co-authored. The bibliographical details of the works are outlined below:

### **Chapter 2:**

Matin Nikoo, H., Bi, K., Hao, H., 2017. Passive vibration control of cylindrical offshore components using pipe-in-pipe (PIP) concept: An analytical study. *Journal of Ocean Engineering*. 142, 39-50.

<https://doi.org/10.1016/j.oceaneng.2017.06.063>

### **Chapter 3:**

Matin Nikoo, H., Bi, K., Hao, H., 2018. Effectiveness of using pipe-in-pipe (PIP) concept to reduce vortex-induced vibrations (VIV): Three-dimensional two-way FSI analysis. *Journal of Ocean Engineering*. 148, 263-276.

<https://doi.org/10.1016/j.oceaneng.2017.11.040>

### **Chapter 4:**

Matin Nikoo, H., Bi, K., Hao, H., 2019. Vortex-induced vibration of a full-diamond textured cylinder at subcritical Reynolds numbers. Under review.

### **Chapter 5:**

Matin Nikoo, H., Bi, K., Hao, H., 2019. Textured pipe-in-pipe system: a compound passive technique for vortex-induced vibration control. Under review.

### **Chapter 6:**

Matin Nikoo, H., Bi, K., Hao, H., 2019. Three-dimensional vortex-induced vibration of a circular cylinder at subcritical Reynolds numbers with low-Re correction. *Journal of Marine Structures* 66, 288-306.

<https://doi.org/10.1016/j.marstruc.2019.05.004>

### **Chapter 7:**

Matin Nikoo, H., Bi, K., Hao, H., 2019. Using stress-blended eddy simulation (SBES) method to simulate vortex-induced vibration (VIV) of an elastically-mounted cylinder. Under review.

## **STATEMENT OF CONTRIBUTION OF OTHERS**

The works presented in this thesis were initiated, designed, executed, interpreted and written by the candidate and the co-authors. Contributions of the co-authors are described below, and the signed contribution form is attached in the Appendix B.

### Chapters 2-7

Thesis supervisors (Hong Hao and Kaiming Bi) defined the overall scope, objectives of the works and suggested research approaches and methodologies. All the numerical simulations and analysis of the results were carried out by the candidate (Hamid Matin Nikoo). The manuscripts were written by Hamid Matin Nikoo with extensively revisions and editions from Kaiming Bi and Hong Hao, both of whom also provided additional intellectual input in the discussions of the results.



# Table of Contents

ABSTRACT.....	i
ACKNOWLEDGEMENTS.....	iv
LIST OF PUBLISHED WORKS AND WORKS PREPARED FOR PUBLICATION.....	v
STATEMENT OF CONTRIBUTION OF OTHERS.....	vi
LIST OF FIGURES.....	xi
LIST OF TABLES.....	xv
<b>Chapter 1 Introduction.....</b>	<b>1</b>
1.1 Background.....	1
1.1.1 VIV suppression techniques.....	1
1.1.2 Numerical study of VIV.....	4
1.2 Research objectives.....	5
1.3 Thesis outline.....	5
1.4 References.....	6
<b>Chapter 2 Passive vibration control of cylindrical offshore components using pipe-in-pipe (PIP) concept: an analytical study.....</b>	<b>11</b>
Abstract.....	11
2.1 Introduction.....	11
2.2 Mathematical Modelling of a Single Cylinder under VIV.....	14
2.2.1 Equation of motion.....	15
2.2.2 Vibration simulation of a single cylinder under VIV.....	16
2.3 Optimized PIP to Control Vibration of Cylindrical Structures Caused by VIV.....	20
2.3.1 Basic governing equations of PIP system and method of solution.....	20
2.3.2 Optimum Design of Non-conventional Tuned Mass Damper (TMD).....	22
2.3.3 Sensitivity Analyses.....	24
2.3.4 Explicit formulae for optimum TMD parameters.....	28
2.4 Effectiveness of Optimized PIP System to Mitigate VIV of Cylindrical Structures.....	29
2.5 Possible Practical Design Options.....	31
2.6 Conclusion.....	32
2.7 References.....	32

**Chapter 3 Effectiveness of using pipe-in-pipe (PIP) concept to reduce vortex-induced vibrations (VIV): three-dimensional two-way FSI analysis ..... 36**

Abstract ..... 36

3.1 Introduction ..... 36

3.2 Method of Solution, Computational Approach and Governing Equations ..... 38

    3.2.1 Two-way Fluid-Structure Interaction (FSI) ..... 39

    3.2.2 Fluid flow model ..... 40

    3.2.3 Structural Dynamics Model ..... 44

3.3 FSI Model of a Single Cylinder ..... 45

    3.3.1 Simulation setup ..... 45

    3.3.2 Mesh dependency study ..... 46

    3.3.3 Model validation ..... 47

3.4 Modified PIP System ..... 50

3.5 Results and discussion ..... 53

3.6 Conclusion ..... 61

3.7 References ..... 61

**Chapter 4 Vortex-induced vibration of a full-diamond textured cylinder at subcritical Reynolds numbers ..... 65**

Abstract ..... 65

4.1 Introduction ..... 65

4.2 Textured pipe ..... 68

4.3 Methodology ..... 69

    4.3.1 Fluid-structure interaction (FSI) set-up ..... 69

    4.3.2 Fluid part ..... 70

    4.3.3 Mechanical part ..... 75

    4.3.4 General numerical set-up ..... 77

4.4 Two-way FSI model verification ..... 78

    4.4.1 Mesh independency test ..... 78

    4.4.2 Validation ..... 79

4.5 Results and discussion ..... 81

    4.5.1 Oscillations and hydrodynamic forces ..... 81

    4.5.2 Response frequencies ..... 88

4.5.3	Wake vortex modes .....	90
4.6	Conclusion .....	93
4.7	References .....	93
<b>Chapter 5 Textured pipe-in-pipe system: a compound passive technique for vortex-induced vibration control .....</b>		<b>98</b>
	Abstract .....	98
5.1	Introduction .....	98
5.2	Methodology .....	101
5.2.1	Fluid part .....	102
5.2.2	Structural part .....	105
5.2.3	FSI setup .....	108
5.3	Verification study .....	109
5.3.1	Mesh independency test .....	109
5.3.2	Validation of the FSI model .....	110
5.4	Results and discussion .....	112
5.4.1	Cylinder oscillations .....	112
5.4.2	Wake vortex modes .....	116
5.4.3	Synchronization or lock-in phenomenon .....	116
5.4.4	Drag force .....	118
5.5	Conclusion .....	120
5.6	References .....	120
<b>Chapter 6 Three-dimensional vortex-induced vibration of a circular cylinder at subcritical Reynolds numbers with Low-<i>Re</i> correction .....</b>		<b>124</b>
	Abstract .....	124
6.1	Introduction .....	124
6.2	Method of Solution, Computational Approach and Governing Equations .....	128
6.2.1	Two-way FSI .....	128
6.2.2	Computational fluid model .....	130
6.2.3	Structural dynamics model and the associated hydrodynamics loads .....	134
6.3	Mesh dependency study .....	134
6.4	Results and discussion .....	136

6.4.1	Oscillation amplitudes and hydrodynamic forces .....	137
6.4.2	Response frequencies .....	146
6.4.3	Wake vortex streets .....	148
6.5	Conclusion .....	153
6.6	References .....	153
<b>Chapter 7 Using stress-blended eddy simulation (SBES) method to simulate vortex-induced vibration of an elastically-mounted cylinder .....</b>		<b>157</b>
	Abstract .....	157
7.1	Introduction .....	157
7.2	FSI numerical framework .....	162
7.2.1	Fluid module .....	163
7.2.2	Mechanical module .....	166
7.2.3	General numerical settings .....	168
7.3	Mesh grid sensitivity study .....	168
7.4	Results and discussion .....	169
7.4.1	Vibration responses .....	170
7.4.2	Phase angles .....	172
7.4.3	Response frequencies .....	174
7.4.4	Wake topology .....	175
7.5	Conclusion .....	179
7.6	References .....	179
<b>Chapter 8 Conclusions and recommendations .....</b>		<b>184</b>
8.1	Thesis contributions and concluding remarks .....	184
8.1.1	Novel techniques for VIV suppression .....	184
8.1.2	Numerical models for VIV prediction .....	185
8.2	Recommendations for future research works .....	185
<b>Bibliography Disclaimer .....</b>		<b>187</b>
<b>Appendices .....</b>		<b>188</b>

# LIST OF FIGURES

<b>Figure 2-1:</b> Experimental setup of a single cylinder under VIV: (a) Hydraulic towing tank; (b) Force measurement device; (c) and (d) Schematic diagrams of the pendulum rig (Rahman, 2015). .....	17
<b>Figure 2-2:</b> Root Mean Square of the observed fluid coefficient $CF$ from the experimental tests (Rahman, 2015). .....	19
<b>Figure 2-3:</b> Schematic of the dynamic Simulink model for a single cylindrical structure under VIV. 19	
<b>Figure 2-4:</b> Comparisons of the normalized amplitudes obtained from the experimental data and the analytical solutions for different aspect ratios (a) $LD = 13$ (b) $LD = 10$ (c) $LD = 7.5$ and (d) $LD = 5$ . .....	20
<b>Figure 2-5:</b> Structural and analytical models of the modified PIP system (a) structural model and (b) analytical model. ....	21
<b>Figure 2-6:</b> Mean square displacement response index ( $N$ ) of a main system with different TMD masses. (a) $\mu = 0.05$ ; (b) $\mu = 0.1$ ; (c) $\mu = 0.4$ ; (d) $\mu = 0.9$ . ( $\zeta_o = 0.031$ ).....	26
<b>Figure 2-7:</b> Intensity contour of $N$ of a main system with different TMD masses. (a) $\mu = 0.05$ ; (b) $\mu = 0.1$ ; (c) $\mu = 0.4$ ; (d) $\mu = 0.9$ . ( $\zeta_o = 0.031$ ). .....	27
<b>Figure 2-8:</b> Influence of damping ratio on the optimum index. ....	27
<b>Figure 2-9:</b> Optimum tuning parameters obtained from numerical searching scheme: (a) optimum TMD damping ratio ( $\zeta_{iopt}$ ) and (b) optimum tuning frequency ratio ( $f_{opt}$ ). ....	28
<b>Figure 2-10:</b> Variation of optimum tuning parameters as a function of mass ratio ( $\mu$ ) for various damping ratios of main system ( $\zeta_o$ ). ....	28
<b>Figure 2-11:</b> Different pipe models under VIV: (a) A single pipe as presented in section 2.2 (b) a PIP system connected by a very rigid spring and (c) a modified PIP system with the optimized parameters. ....	30
<b>Figure 2-12:</b> The dynamic Simulink model for a modified PIP system under VIV. ....	30
<b>Figure 2-13:</b> Comparisons of normalized transverse vibration amplitudes of a single pipe system with the optimized PIP system. (a) $LD = 13$ ; (b) $LD = 10$ ; (c) $LD = 7.5$ ; (d) $LD = 5$ . ....	31
<b>Figure 3-1:</b> (a)&(b) 3-D Computational domain and corresponding mesh grids, (c) mesh around the cylinder and (d) mesh in the $xy$ -plane and the corresponding boundary conditions. ....	43
<b>Figure 3-2:</b> Mesh grids for the solid part (a single cylinder) of FSI simulation. ....	45
<b>Figure 3-3:</b> Time histories of normalized amplitude responses ( $A^*$ ) with different meshes ( $U^* = 4.2$ ). ....	46
<b>Figure 3-4:</b> Power spectral density (PSD) of the normalized amplitude responses ( $A^*$ ) with different meshes ( $U^* = 4.2$ ). ....	47
<b>Figure 3-5:</b> FSI model validation (a) normalized amplitude and (b) normalized frequency. ....	48
<b>Figure 3-6:</b> Time histories of normalized amplitude response( $A^*$ ), lift coefficient ( $CL$ ) and associated spanwise velocity contours at different VIV branches: (a) initial branch (b) upper branch and (c) lower branch. ....	50
<b>Figure 3-7:</b> Different pipe models: (a) a single cylinder (b) a PIP system connected by rigid spring ( $ki = \infty$ ) and dashpot (c) a modified PIP system with the optimized parameters .....	52
<b>Figure 3-8:</b> Finite element model of the PIP system in the 3-D FSI simulation. ....	53
<b>Figure 3-9:</b> Normalized time histories of the oscillating displacement for the conventional and optimized PIP systems: (a) $U^* = 3.7$ , (b) $U^* = 4.2$ , (c) $U^* = 4.9$ and (d) $U^* = 6.8$ . ....	54
<b>Figure 3-10:</b> PSDs of the normalized oscillating displacement for the conventional and optimized PIP systems: (a) $U^* = 3.7$ , (b) $U^* = 4.2$ , (c) $U^* = 4.9$ and (d) $U^* = 6.8$ . ....	55

<b>Figure 3-11:</b> Normalized relative displacements between the outer and inner pipes when the PIP system is vibrating at (a) $U^* = 3.7$ , (b) $U^* = 4.2$ , (c) $U^* = 4.9$ and (d) $U^* = 6.8$ .	56
<b>Figure 3-12:</b> The influence of optimized PIP system on the lift and drag coefficients: (a) and (b) $U^* = 3.7$ and (c) and (d) $U^* = 4.2$ .	58
<b>Figure 3-13:</b> Phase relations between the outer pipe oscillation and driving lift force in the optimized PIP for (a) $U^* = 3.7$ , (b) $U^* = 4.2$ , (c) $U^* = 4.9$ and (d) $U^* = 6.8$ .	58
<b>Figure 3-14:</b> $Q$ Iso-surfaces of the vortices street around the conventional and optimized PIP for $U^* = 4.2$ .	59
<b>Figure 3-15:</b> Contour of velocity around the conventional and optimized PIP at the middle surface ( $z = 2.5D$ ) of computational domain for $U^* = 4.2$ .	60
<b>Figure 4-1:</b> Geometry details of a full-diamond (octagonal) textured pipe (adopted partly from Yang et al. (2016)).	68
<b>Figure 4-2:</b> (a) 3-D computational fluid domain adopted in the Fluent solver and mechanical details of the elastically-mounted (b) smooth cylinder and (c) textured pipe modelled in the Mechanical solver.	70
<b>Figure 4-3:</b> (a) An overview of the mesh grids and the utilized boundary conditions, (b) $xy$ -plane of the domain and the associated block number.	73
<b>Figure 4-4:</b> Details of different mesh grids adopted for the different sub-domains in (a) textured cylinder and (b) smooth cylinder.	74
<b>Figure 4-5:</b> FLUID30 element with different shape functions used for modelling the fluid medium.	74
<b>Figure 4-6:</b> Comparisons between the present FSI model and the previous experimental studies on the smooth cylinders: (a) normalized maximum amplitude response ( $A^*$ ) and (b) dominant peaks in the spectrum of the cylinder oscillation.	79
<b>Figure 4-7:</b> Normalized time histories of the cylinder oscillations under four typical normalized velocities: (a) $U^* = 2$ , (b) $U^* = 5$ , (c) $U^* = 8$ and (d) $U^* = 10$ .	82
<b>Figure 4-8:</b> Comparisons of the normalized maximum amplitude responses ( $A^*$ ) between the smooth and textured cylinders.	82
<b>Figure 4-9:</b> Comparisons of the phase angle ( $\phi$ ) between the smooth and textured cylinders.	84
<b>Figure 4-10:</b> Normalized hydrodynamic force coefficient time histories of the smooth and textured cylinders under three typical normalized velocities: (a) $U^* = 2$ , (b) $U^* = 5$ and (c) $U^* = 8$ .	85
<b>Figure 4-11:</b> Comparisons of the maximum normalized force coefficients between the smooth and textured cylinders under different normalized velocities $U^*$ .	86
<b>Figure 4-12:</b> Comparisons of the mean streamlines between the smooth and textured cylinders under different normalized velocities: (a) $U^* = 2$ (b) $U^* = 4$ , (c) $U^* = 6$ and (d) $U^* = 10$ .	86
<b>Figure 4-13:</b> Comparisons of the $Q$ Iso-surfaces of the vortex streets between the (a) smooth cylinder and (b) textured cylinder vibrating under $U^* = 4$ .	87
<b>Figure 4-14:</b> Comparisons of the $Q$ Iso-surfaces of the vortex streets between the (a) smooth cylinder and (b) textured cylinder vibrating under $U^* = 8$ .	87
<b>Figure 4-15:</b> Normalized PSDs of the cylinder vibrations: (a) smooth cylinder and (b) textured cylinder.	89
<b>Figure 4-16:</b> Dominant peaks in the spectrum of the normalized cylinder oscillations: (a) smooth cylinder and (b) textured cylinder.	89
<b>Figure 4-17:</b> Dominant peaks in the spectrum of the normalized transverse force frequency: (a) smooth cylinder and (b) textured cylinder.	89
<b>Figure 4-18:</b> Contours of wake vortex streets along the smooth and textured cylinders at three cross sections ( $ZD = 0, 4$ and $8$ ) under different normalized velocities: (a) $U^* = 2$ (b) $U^* = 4$ and (c) $U^* = 8$ .	91

<b>Figure 4-19:</b> The instantaneous vortex wake modes obtained for the smooth and textured cylinders at different normalized velocities: (a) $U^* = 2$ (b) $U^* = 4$ (c) $U^* = 8$ and (d) $U^* = 10$ .	92
<b>Figure 5-1:</b> Schematic views of different pipe systems: (a) smooth pipe (b) textured pipe and (c) textured-PIP.	99
<b>Figure 5-2:</b> Computational fluid domain adopted in the Fluent solver for different pipe types (a) 3-D view and boundary conditions (b) $xy$ -plan view and the corresponding mesh grids and (c) the mesh grids in the main circular subdomain.	105
<b>Figure 5-3:</b> Different pipe systems in the ANSYS Mechanical solver: (a) a smooth cylinder, (b) a textured pipe and (c) a textured-PIP system.	106
<b>Figure 5-4:</b> Normalized maximum amplitude response ( $A^*$ ) obtained from the experimental and numerical studies.	111
<b>Figure 5-5:</b> Dominant peaks in the spectra of the cylinder oscillations obtained from the experimental and numerical studies.	111
<b>Figure 5-6:</b> Typical wake vortex modes in different branches (a) initial branch ( $U^* = 3$ ) (b) upper branch ( $U^* = 5$ ) and (c) lower branch ( $U^* = 9$ ).	112
<b>Figure 5-7:</b> Normalized time histories of the cylinder oscillations under typical reduced velocities: (a) $U^* = 2$ , (b) $U^* = 4$ , (c) $U^* = 6$ , (d) $U^* = 8$ , (e) $U^* = 10$ and (f) $U^* = 12$ .	115
<b>Figure 5-8:</b> Normalized maximum amplitude responses ( $A^*$ ) between different pipes.	115
<b>Figure 5-9:</b> Comparisons of the phase angle ( $\phi$ ) between the deferent pipes/systems.	116
<b>Figure 5-10:</b> Contours of wake vortex streets along different cylinders at three cross sections ( $ZD = 0, 4$ and $8$ ) under different normalized velocities: (a) $U^* = 2$ (b) $U^* = 4$ and (c) $U^* = 8$ .	118
<b>Figure 5-11:</b> Lock-in or synchronization regimes obtained from different cylinders: (a) smooth cylinder (Matin Nikoo et al., 2019a) (b) textured pipe (Matin Nikoo et al., 2019b) and (c) textured-PIP system.	119
<b>Figure 5-12:</b> Comparisons of the drag forces obtained from different pipe systems.	120
<b>Figure 6-1:</b> (a) 3-D fluid domain adopted in the FLUENT solver and (b) suspended solid cylinder modelled in the ANSYS Mechanical solver.	129
<b>Figure 6-2:</b> Two-way FSI procedure.	130
<b>Figure 6-3:</b> (a) 3-D multi-block computational domains and the corresponding mesh grids, (b) mesh in the $xy$ -plane, the corresponding boundary conditions and the associated block number.	133
<b>Figure 6-4:</b> Time histories of the normalized oscillation ( $A_y$ ), the force coefficients ( $CL, CD$ ) and the corresponding normalized PSDs with different normalized velocities (a) $U^* = 2$ , (b) $U^* = 4$ , (c) $U^* = 6$ , (d) $U^* = 8$ and (e) $U^* = 10$ .	139
<b>Figure 6-5:</b> Comparison of the normalized maximum amplitude response ( $A^*$ ) between the present model and the previous experimental studies.	140
<b>Figure 6-6:</b> Phase plane portraits of $CL(t)$ versus $A_y(t)$ obtained from the testing results (Khalak and Williamson, 1999) and the present model for the (a) initial (b) upper and (c) lower excitation regimes.	141
<b>Figure 6-7:</b> PDF of the phase angle ( $\phi$ ) between the lift force and cylinder crossflow displacement in different branches: (a&b) initial branch $U^* = 2&3$ ; (c&d) upper branch $U^* = 4&5$ ; and (e&f) lower branch $U^* = 9&10$ .	142
<b>Figure 6-8:</b> Comparison of the phase angle ( $\phi$ ) between the present model and previous experimental studies.	142
<b>Figure 6-9:</b> Comparison of the normalized maximum amplitude response ( $A^*$ ) between the present model and other numerical investigations adopting $SSTK - \omega$ method.	145
<b>Figure 6-10:</b> Comparisons of the maximum normalized force coefficients between the current model and previous experimental and numerical results: (a) maximum lift coefficient $CL_{max}$ and (b) maximum drag coefficient $CD_{max}$ .	145

<b>Figure 6-11:</b> Normalized PSDs of cylinder oscillations under different normalized velocities. ....	147
<b>Figure 6-12:</b> Dominant peaks in the spectrum of oscillation obtained in the present study (Matin Nikoo et al., 2019) and from previous experimental data. ....	147
<b>Figure 6-13:</b> Normalized PSDs when $U^* = 12$ . ....	147
<b>Figure 6-14:</b> Comparisons between the wake vortex streets obtained in the present study (Matin Nikoo et al., 2019) and previous experimental study (Govardhan and Williamson, 2000), (a) $U^* = 3$ (initial branch), (b) $U^* = 5$ (upper branch) and (c) $U^* = 9$ (lower branch). ....	148
<b>Figure 6-15:</b> Contours of the pressure along the cylinder surface for (a) $U^* = 2$ (b) $U^* = 3$ (c) $U^* = 4$ (d) $U^* = 5$ , (e) $U^* = 9$ and (f) $U^* = 10$ . ....	150
<b>Figure 6-16:</b> Contours of vortex streets along the cylinder at three cross sections ( $ZD = 0, 4$ and $8$ ) at (a) initial (b) upper and (c) lower branches. ....	151
<b>Figure 6-17:</b> Q Iso-surfaces of the vortex streets around the cylinder at different normalized velocities (a) $U^* = 3$ (b) $U^* = 5$ (c) $U^* = 7$ (d) $U^* = 9$ . ....	152
<b>Figure 7-1:</b> Obtained normalized maximum responses in the VIV numerical simulations by using different turbulence models: (a) RANS (b) DNS (c) LES and (d) DES. ....	161
<b>Figure 7-2:</b> (a) An overview of the mesh grids and the corresponding boundary conditions, (b) $xy$ -plane view of the domain. ....	163
<b>Figure 7-3:</b> Elastically-mounted cylinder suspended by four linear springs modelled in the ANSYS Mechanical module. ....	166
<b>Figure 7-4:</b> Schematic view of the fluid domain discretized with different grid densities. ....	169
<b>Figure 7-5:</b> Comparisons of the normalized maximum amplitudes between the experimental data and the most accurate numerical results obtained based on different turbulence models. ....	171
<b>Figure 7-6:</b> Comparisons of the PDFs of the phase angles ( $\phi$ ) obtained by the SBES and RANS models: (a) $U^* = 3$ , (b) $U^* = 5$ , (c) $U^* = 6$ and (d) $U^* = 10$ . ....	173
<b>Figure 7-7:</b> Comparisons of the dominant phase angles between the experimental and numerical simulations with SBES and RANS models. ....	174
<b>Figure 7-8:</b> Dominant peaks in the spectrum of the cylinder oscillations obtained from the test results and numerical simulations with SBES and RANS models. ....	175
<b>Figure 7-9:</b> Comparisons of the wake vortex streets along the cylinder at three cross sections ( $ZD = 0, 4$ and $8$ ) of the cylinder under different normalized velocities: (a) $U^* = 3$ (b) $U^* = 5$ and (c) $U^* = 9$ . ....	177
<b>Figure 7-10:</b> 2-D comparisons of the wake vortex streets at the middle cross section ( $zD = 4$ ) of the cylinder under different normalized velocities: (a) $U^* = 3$ (b) $U^* = 5$ and (c) $U^* = 9$ . ....	177
<b>Figure 7-11:</b> Typical (a) 2S and (b) 2P modes obtained in the water tunnel tests carried out by Klamo (2007) under subcritical Reynolds numbers. ....	178
<b>Figure 7-12:</b> Spanwise flow view of instantaneous wake structures obtained from SBES and RANS turbulence models under different normalized velocities: (a) $U^* = 3$ (b) $U^* = 5$ and (c) $U^* = 9$ . ....	178
<b>Figure 7-13:</b> Typical spanwise flow visualization in the water tunnel tests carried out by Klamo (2007). ....	178



# LIST OF TABLES

<b>Table 1-1:</b> Drawbacks of some passive devices for VIV control (Blevins, 2000, Raghavan et al., 2008, Holland et al., 2017).....	3
<b>Table 2-1:</b> Experimental matrix performed in Rahman (2015).....	18
<b>Table 2-2:</b> The range of examined current velocity and corresponding vortex shedding frequency (Rahman, 2015).....	18
<b>Table 2-3:</b> Obtained optimal parameters for a TMD system with different mass ratios based on the numerical searching technique.....	25
<b>Table 2-4:</b> Peak normalized amplitudes of the single pipe model and the optimized PIP system under VIV and the corresponding suppression ratio. ....	31
<b>Table 3-1:</b> Non-dimensional parameters associated with the vibrations of a cylinder and PIP system induced by vortex shedding.....	39
<b>Table 3-2:</b> Mesh convergence testing results. ....	46
<b>Table 3-3:</b> Adopted previous studies for model validation.....	47
<b>Table 3-4:</b> RMS displacements of the traditional and optimized PIP systems and the corresponding reduction ratios.....	56
<b>Table 4-1:</b> Mesh convergence test results. ....	78
<b>Table 5-1:</b> Mesh convergence tests. ....	110
<b>Table 6-1:</b> Properties of the cylinder and surrounding fluid.....	135
<b>Table 6-2:</b> Mesh convergence testing results. ....	135
<b>Table 6-3:</b> Number of elements generated in each BCK in different case scenarios.....	136
<b>Table 6-4:</b> Adopted previous studies and governing parameters.....	137
<b>Table 7-1:</b> Summary of VIV experiments. ....	160
<b>Table 7-2:</b> Summary of numerical VIV simulations. ....	160
<b>Table 7-3:</b> Mesh convergence test results.....	169

# Chapter 1 Introduction

---

## 1.1 Background

Many shallow-water hydrocarbon reservoirs are being exhausted and the exploration of new energy resources is moving into deep and ultra-deep waters. The oil and gas industry is therefore heavily involved in construction of offshore floating structures which conventionally comprise many vertical and horizontal cylindrical components such as marine risers, mooring lines, conductors and pipelines. Throughout their service lives, these structures are exposed to a destructive phenomenon known as the vortex-induced vibration (VIV), which not only affects the efficiency of production but also may cause fatigue damages to the structure. In extreme cases, when the frequency of vortex shedding approaches the natural frequency of the structure/structural component, responses with remarkably large amplitude are expected, which may even result in the catastrophic failure to the whole structure. It is therefore imperative to better understand the mechanism of this effect and propose efficient while economic approaches to suppress the adverse vibrations. In the present thesis, three novel passive vibration control techniques are proposed to more effectively control VIV, and two attempts are made to improve the accuracy and efficiency of current numerical techniques. Previous studies in the corresponding fields are reviewed in this chapter.

### 1.1.1 VIV suppression techniques

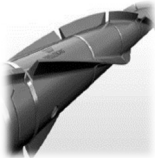
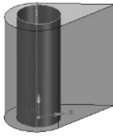


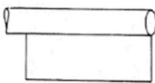


Significant efforts have been made to attenuate the destructive effect of VIV and different methods with different suppression mechanisms have been proposed. These methods can be generally classified into two categories based on whether energy input is required, namely the active and passive suppression methods. Active control strategies require external energy resources to operate. The energy can be supplied by different resources such as electrical systems ([Artana et al., 2003](#), [Thomas et al., 2008](#), [Jiang et al., 2019](#)), air-bubble injections ([Abbassian and Moros, 1996](#)), magnetic fields ([Mutschke et al., 1998](#), [Zhang et al., 2014](#)), feedback techniques ([Baz and Ro, 1991](#), [Carini et al., 2015](#)), thermal effects ([Lecordier et al., 1991](#), [Chatterjee, 2014](#)), secondary flows ([Seal and Smith, 1999](#), [Muralidharan et al., 2013](#), [Yao and Jaiman, 2017](#)), slot bleeds ([Fu and Rockwell, 2005](#)) and synthetic jets ([Tensi et al., 2002](#), [Ma](#)

[and Feng, 2019](#)). In general, active methods can effectively reduce the vibrations, they are however not easy to be employed in real practices especially in marine environment. For example, electrical methods are appropriate for aerodynamic applications such as aircrafts while its application in the ocean is dubious ([Thomas et al., 2008](#), [Rashidi et al., 2016](#)), air-bubble injection is uneconomical for marine riser systems with large deflections in deep waters ([Abbassian and Moros, 1996](#)), magnetic and feedback controls are very expensive to be employed ([Rashidi et al., 2016](#)), and too much heating is required for thermal techniques to become active ([Chatterjee, 2014](#)). Passive approaches, which need no external power to operate, are in general more practical and economical compared to the active methods especially for offshore and marine structures ([Rashidi et al., 2016](#)).

The literature on the passive control of VIV is very rich and several techniques have been proposed by different researchers. Among these methods, the helical strake and fairing might be the most widely used ones, and extensive studies have been made on the helical strake ([Zhou et al., 2011](#), [Sui et al., 2016](#), [Holland et al., 2017](#), [Senga and Larsen, 2017](#)) and fairing ([Allen, 2003](#), [Masters et al., 2008](#), [Assi et al., 2014](#), [Yu et al., 2015](#), [Wang et al., 2015](#)) respectively. Previous studies revealed that helical strake can reduce VIV response over a broad range of Reynolds numbers, but its efficiency decreases as the flow velocity increases. Fairing has much lower drag force in comparison with the helical strake, and can significantly suppress the VIV with the drag and lift forces reduced by up to 31% and 99% respectively. [Kiu et al. \(2011\)](#), [Park et al. \(2012\)](#), [Bernitsas and Raghavan \(2014\)](#) and [Gao et al. \(2015\)](#) studied the effect of surface roughness on the VIV reduction, and they showed that the amplitude of vibration and drag force can be reduced by increasing the intensity of roughness on the body. In addition, the lock-in regime can be significantly reduced if it is distributed properly on the cylinder. The results of a 2-D numerical study also revealed that surface roughness causes a delay in boundary layer separation ([Seman et al., 2015](#)). [Zhang et al. \(2016, 2017, 2018\)](#) and [Assi and Bearman \(2018\)](#) studied the influence of shape modification/wavy cylinders to the wake vortices and the associated forces on the cylinder. It was concluded that the vibration of the wavy cylinder can be mitigated compared to the smooth cylinder when the damping of the structure is high, and the drag force can be reduced by 12.5% by a wavy cylinder. Tripping wires were proposed by [Quadrante and Nishi \(2014\)](#) with a range of angular positions from 15° to 165° to

suppress the vibration of a circular cylinder. The results showed that VIV can be either intensified or suppressed depending on the position of tripping wires. The effectiveness of using perforated shrouds to control VIV was investigated by [Azmi et al. \(2012\)](#), and 50% reduction was obtained. [Gozmen and Akilli \(2015\)](#) and [Sanli and Akilli \(2018\)](#) applied permeable cylinder to control the flow over the body, and it was concluded that the unsteady wake flow structure disappears with the increase of porosity. [Zhou et al. \(2015, 2016\)](#) experimentally showed that dimpled surface can significantly reduce the VIV of cylindrical components. The effectiveness of using controlling rods to control VIV was studied by [Wu et al. \(2012\)](#) and [Song et al. \(2017\)](#). The results showed that transverse vibration amplitude of the main cylinder depends highly on the attack angles and VIV suppression can be achieved only for attack angles higher than 45°. [Assi et al. \(2009, 2014\)](#) and [Law and Jaiman \(2017\)](#) studied the effectiveness of splitter plates for VIV reduction, and showed that the maximum drag reduction can be achieved up to about 38% with the parallel plates, and the splitter plate may experience galloping at high reduced velocities. The results obtained by [Yoon et al. \(2014\)](#) showed that tin flat plates can reduce the VIV up to 17%.

**Table 1-1:** Drawbacks of some passive devices for VIV control ([Blevins, 2000](#), [Raghavan et al., 2008](#), [Holland et al., 2017](#)).

Control technique		Disadvantages
Helical strake	 www.oedigital.com	<ul style="list-style-type: none"> <li>- impose additional drag coefficient;</li> <li>- may adversely affect the stress and then cause an increase in deflection and buckling</li> <li>- efficiency decrease by increasing the turbulence intensity</li> </ul>
Fairing		<ul style="list-style-type: none"> <li>- expensive to manufacture;</li> <li>- difficult to handle and time consuming for installation</li> <li>- susceptible to storm damage</li> <li>- subjected to change of geometry as a result of marine growth</li> </ul>
Perforated shroud		<ul style="list-style-type: none"> <li>- is comparatively expensive</li> <li>- will lost its efficiency in the course of time because of growing marine growth</li> </ul>
Axial rods/slats		<ul style="list-style-type: none"> <li>- appropriate primarily in air</li> </ul>
Splitter plate		<ul style="list-style-type: none"> <li>- is only appropriate where the flow direction does not vary significantly.</li> <li>- rotatable flat is also expensive and difficult to implement</li> </ul>
Spoiler/ribbon plates		<ul style="list-style-type: none"> <li>- may cause significant drag forces on the structure</li> <li>- difficulty to maintenance</li> </ul>
Bumps		<ul style="list-style-type: none"> <li>- low efficiency in comparison with its cost</li> <li>- difficult to construct</li> </ul>

All the above mentioned approaches can control VIV for a certain extent. However, some drawbacks are still associated with these passive methods as summarized in Table 1-1. In particular, helical strakes and bumps may impose an additional undesired drag force to the structure. Splitter plates, fairings and shrouds are expensive to manufacture and the control effectiveness depends on the orientation and flow conditions ([Huang, 2011](#), [Dhanak and Xiros, 2016](#)). They are also susceptible to the marine growth, extreme storm damages and may even cause galloping in the structure ([Huang, 2011](#)). Further research attempts are therefore necessary to develop more feasible yet effective techniques for VIV control.

### **1.1.2 Numerical study of VIV**

Besides experimental studies (e.g. [Khalak and Williamson \(1996, 1997, 1999\)](#), [Gabbai and Benaroya \(2005\)](#), [Williamson and Govardhan \(2008\)](#), [Mackowski and Williamson \(2013\)](#)), extensive researches attempts have also been made to study the VIV phenomenon by using numerical tools. The chaotic flow behind a cylinder causes challenges for computational modelling because it involves extremely complex features such as small scale shear layer vortices, transition and large scale vortex shedding behind the structure. Three numerical turbulence models have been primarily adopted by different researchers for VIV simulation. These methods include the Direct Numerical Simulation (DNS) (e.g. [Gsell et al. \(2019\)](#), [Lucor and Triantafyllou \(2008\)](#), [Navrose and Mittal \(2013\)](#), [Zhao et al. \(2014\)](#), [Lucor et al. \(2005\)](#), [Zhao and Cheng \(2014\)](#)), the Large Eddy Simulation (LES) (e.g. [Zhang et al. \(2017\)](#), [Al-Jamal and Dalton \(2004\)](#)), and the Reynolds-Averaged Navier-Stokes Simulation (RANS) (e.g. [Li et al. \(2014\)](#), [Zhao et al. \(2014\)](#), [Khan et al. \(2018\)](#), [Pan et al. \(2007\)](#), [Guilmineau and Queutey \(2004\)](#)). In DNS technique, Navier-Stokes equations with entire range of spatial and temporal properties of the turbulence are directly solved without any approximation. Large scale turbulence motions of the flow which contain most of the kinetic energy, momentum and scalar transport are solved explicitly in the LES method, whereas the effect of the small scales is modelled using a sub-grid model. Flow quantities are not directly solved but averaged in the RANS approach. DNS and LES methods are therefore very time consuming, which makes them computationally too expensive even for a problem with very simple geometry ([Chaouat, 2017](#), [Tu et al., 2018](#)). RANS method, on the other hand, is the least computationally intensive method, which makes it most commonly used in the VIV simulation. However, this

method is inherently poor in simulating the flows with massive separation and show significant weaknesses in the separated regions where the unsteady scales play an important role ([Yeon et al., 2016](#), [Yadav et al., 2019](#), [Kornev et al., 2019](#)). This model thus is very difficult to accurately capture the VIV responses especially the maximum VIV amplitude. It is therefore imperative to develop more reliable models for VIV simulation with improved accuracy and affordable computational cost.

## **1.2 Research objectives**

This research work has two main objectives: (i) to propose effective and economic strategies to suppress VIV, and (ii) to improve the accuracy and efficiency of numerical methods for VIV simulation. The specific objectives of the thesis are listed below:

- To analytically investigate the efficiency of using pipe-in-pipe (PIP) concept to suppress VIV.
- To perform three-dimensional (3-D) computational fluid dynamics (CFD) analyses to examine the effectiveness of three novel passive control techniques, namely the PIP system, textured pipe and textured-PIP system, for VIV suppression.
- To improve the accuracy of the most widely used RNAS turbulence model for VIV simulation.
- To investigate an advanced hybrid turbulence model in order to reach a balance between the accuracy and computational cost.

## **1.3 Thesis outline**

This thesis consists of eight chapters, presented as a series of technical papers (Chapters 2-7) combining together. The contents of each chapter following the current introductory chapter are described as follows:

In Chapter 2, analytical models of the conventional and modified PIP systems under VIV are developed. The dynamic equilibrium equations are solved and validated by the experimental data. The explicit formulae for predicting the optimal spring stiffness and dashpot coefficients are derived. The effectiveness of using modified PIP system is demonstrated by comparing the results with the conventional PIP system.

To further demonstrate the effectiveness of using modified PIP system for VIV control, 3-D CFD simulations are carried out in Chapter 3 by developing a two-way coupled fluid-structure interaction (FSI) framework, namely by coupling ANSYS mechanical and FLUENT solvers together. The model is validated by the benchmark experimental data, and the control mechanism and effectiveness are examined.

In Chapter 4, the effectiveness of using single full-diamond textured cylinder for VIV suppression is numerically investigated by adopting the same methodology and setups used in Chapter 3. The control mechanism and effectiveness are examined by comparing the results with those obtained from the counterpart smooth cylinder.

As a combination of the techniques presented in Chapters 2 and 3 (on the modified PIP) and Chapter 4 (on the textured pipe), a textured-PIP system is proposed to mitigate VIV in Chapter 5. The effectiveness of such design is investigated by performing 3-D CFD simulations again.

In Chapter 6, the low- $R_e$  correction technique is incorporated into the RANS model equipped with  $SST K - \omega$  to improve the accuracy of this most widely used model for VIV simulation. The numerical results in terms of the oscillation amplitude, hydrodynamic forces, response frequencies and wake vortices are discussed and compared with the traditional RANS method in detail.

Chapter 7 adopts a hybrid turbulence method known as the Stress-Blended Eddy Simulation (SBES) model to further improve the accuracy and efficiency for VIV simulation. For comparison, the results are compared with the method presented in Chapter 6, i.e., the RANS model with low- $Re$  correction.

Chapter 8 summarizes the concluding remarks of this research, and recommendations for the future studies are also suggested.

It should be noted that this thesis is compiled by combing the technical papers prepared by the candidate during his PhD study. Therefore, Chapters 2-7 can be read independently. To make each technical paper/chapter complete, some parts may overlap across different chapters. However, to follow the requirements of thesis by publications specified by Curtin University, these parts are kept in the present thesis.

## 1.4 References

Abbassian, F., Moros, T. (1996). The use of air-bubble spoilers to suppress vortex-induced vibrations of risers. *SPE Production and Facilities*, 11 (01), 35-40.

- Al-Jamal, H., Dalton, C. (2004). Vortex induced vibrations using Large Eddy Simulation at a moderate Reynolds number. *Journal of Fluids and Structures*, 19 (1), 73-92.
- Allen, D. (2003). Performance characteristics of short fairings. Offshore Technology Conference.
- Artana, G., Sosa, R., Moreau, E., Touchard, G. (2003). Control of the near-wake flow around a circular cylinder with electrohydrodynamic actuators. *Experiments in Fluids*, 35 (6), 580-588.
- Assi, G.R.S., Bearman, P.W. (2018). Vortex-induced vibration of a wavy elliptic cylinder. *Journal of Fluids and Structures*, 80, 1-21.
- Assi, G.R.S., Bearman, P.W., Kitney, N. (2009). Low drag solutions for suppressing vortex-induced vibration of circular cylinders. *Journal of Fluids and Structures*, 25 (4), 666-675.
- Assi, G.R.S., Bearman, P.W., Tognarelli, M.A. (2014). On the stability of a free-to-rotate short-tail fairing and a splitter plate as suppressors of vortex-induced vibration. *Ocean Engineering*, 92, 234-244.
- Azmi, A.M., Zhou, T., Cheng, L., Wang, H., Chua, L.P. (2012). On the effectiveness and mechanism of vortex-induced vibration suppression using a screen cylinder. The 22nd International Offshore and Polar Engineering Conference, Rhodes, Greece.
- Baz, A., Ro, J. (1991). Active control of flow-induced vibrations of a flexible cylinder using direct velocity feedback. *Journal of Sound and Vibration*, 146 (1), 33-45.
- Bernitsas, M.M., Raghavan, K. (2014). Reduction of vortex induced forces and motion through surface roughness control. *Google Patents*.
- Blevins, R.D. (2000). Flow-induced vibration. *Krieger*.
- Carini, M., Pralits, J.O., Luchini, P. (2015). Feedback control of vortex shedding using a full-order optimal compensator. *Journal of Fluids and Structures*, 53, 15-25.
- Chaouat, B. (2017). The State of the Art of Hybrid RANS/LES Modeling for the Simulation of Turbulent Flows. *Flow, Turbulence and Combustion*, 99 (2), 279-327.
- Chatterjee, D. (2014). Dual role of thermal buoyancy in controlling boundary layer separation around bluff obstacles. *International Communications in Heat and Mass Transfer*, 56, 152-158.
- Dhanak, M.R., Xiros, N.I. (2016). Springer handbook of ocean engineering. *Springer*, United States.
- Fu, H., Rockwell, D. (2005). Shallow flow past a cylinder: control of the near wake. *Journal of Fluid Mechanics*, 539, 1-24.
- Gabbai, R., Benaroya, H. (2005). An overview of modeling and experiments of vortex-induced vibration of circular cylinders. *Journal of Sound and Vibration*, 282 (3), 575-616.
- Gao, Y., Fu, S., Wang, J., Song, L., Chen, Y. (2015). Experimental study of the effects of surface roughness on the vortex-induced vibration response of a flexible cylinder. *Ocean Engineering*, 103, 40-54.
- Gozmen, B., Akilli, H. (2015). Effects of Permeable Cylinders on Wake Region. *Research On Engineering Structures and Materials*, 1 (2), 109-120.
- Gsell, S., Bourguet, R., Braza, M. (2019). One versus two-degree-of-freedom vortex-induced vibrations of a circular cylinder at  $Re=3900$ . *Journal of Fluids and Structures*, 85, 165-180.
- Guilmineau, E., Queutey, P. (2004). Numerical simulation of vortex-induced vibration of a circular cylinder with low mass-damping in a turbulent flow. *Journal of Fluids and Structures*, 19 (4), 449-466.



- Holland, V., Tezdogan, T., Oguz, E. (2017). Full-scale CFD investigations of helical strakes as a means of reducing the vortex induced forces on a semi-submersible. *Ocean Engineering*, 137, 338-351.
- Huang, S. (2011). VIV suppression of a two-degree-of-freedom circular cylinder and drag reduction of a fixed circular cylinder by the use of helical grooves. *Journal of Fluids and Structures*, 27 (7), 1124-1133.
- Jiang, D., Zhang, H., Fan, B., Zhao, Z., Gui, M., Chen, Z. (2019). Vortex structures and drag reduction in turbulent channel flow with the effect of space-dependent electromagnetic force. *Ocean Engineering*, 176, 74-83.
- Khalak, A., Williamson, C.H.K. (1996). Dynamics of a hydroelastic cylinder with very low mass and damping. *Journal of Fluids and Structures*, 10 (5), 455-472.
- Khalak, A., Williamson, C.H.K. (1997). Fluid forces and dynamics of a hydroelastic structure with very low mass and damping. *Journal of Fluids and Structures*, 11 (8), 973-982.
- Khalak, A., Williamson, C.H.K. (1999). Motions, forces and mode transitions in vortex-induced vibrations at low mass-damping. *Journal of Fluids and Structures*, 13 (7-8), 813-851.
- Khan, N.B., Ibrahim, Z., Khan, M.I., Hayat, T., Javed, M.F. (2018). VIV study of an elastically mounted cylinder having low mass-damping ratio using RANS model. *International Journal of Heat and Mass Transfer*, 121, 309-314.
- Kiu, K.Y., Stappenbelt, B., Thiagarajan, K.P. (2011). Effects of uniform surface roughness on vortex-induced vibration of towed vertical cylinders. *Journal of Sound and Vibration*, 330 (20), 4753-4763.
- Kornev, N., Shevchuk, I., Abbas, N., Anschau, P., Samarbakhsh, S. (2019). Potential and limitations of scale resolved simulations for ship hydrodynamics applications. *Ship Technology Research*, 1-14.
- Law, Y.Z., Jaiman, R.K. (2017). Wake stabilization mechanism of low-drag suppression devices for vortex-induced vibration. *Journal of Fluids and Structures*, 70, 428-449.
- Lecordier, J.C., Hamma, L., Paranthoen, P. (1991). The control of vortex shedding behind heated circular cylinders at low Reynolds numbers. *Experiments in Fluids*, 10 (4), 224-229.
- Li, W., Li, J., Liu, S. (2014). Numerical simulation of vortex-induced vibration of a circular cylinder at low mass and damping with different turbulent models. OCEANS 2014 - TAIPEI, 1-7.
- Lucor, D., Foo, J., Karniadakis, G.E. (2005). Vortex mode selection of a rigid cylinder subject to VIV at low mass-damping. *Journal of Fluids and Structures*, 20 (4), 483-503.
- Lucor, D., Triantafyllou, M.S. (2008). Parametric study of a two degree-of-freedom cylinder subject to vortex-induced vibrations. *Journal of Fluids and Structures*, 24 (8), 1284-1293.
- Ma, L.Q., Feng, L.H. (2019). Vortex formation and evolution for flow over a circular cylinder excited by symmetric synthetic jets. *Experimental Thermal and Fluid Science*, 104, 89-104.
- Mackowski, A., Williamson, C. (2013). An experimental investigation of vortex-induced vibration with nonlinear restoring forces. *Physics of Fluids*, 25 (8), 087101.
- Masters, R.H., Masters, R.W., Sykes, M., Leverette, S.J., Schaudt, K.J. (2008). Twin fin fairing. *Google Patents*.
- Muralidharan, K., Muddada, S., Patnaik, B.S.V. (2013). Numerical simulation of vortex induced vibrations and its control by suction and blowing. *Applied Mathematical Modelling*, 37 (1), 284-307.
- Mutschke, G., Shatrov, V., Gerbeth, G. (1998). Cylinder wake control by magnetic fields in liquid metal flows. *Experimental Thermal and Fluid Science*, 16 (1-2), 92-99.

- Navrose, Mittal, S. (2013). Free vibrations of a cylinder: 3-D computations at  $Re=1000$ . *Journal of Fluids and Structures*, 41, 109-118.
- Pan, Z.Y., Cui, W.C., Miao, Q.M. (2007). Numerical simulation of vortex-induced vibration of a circular cylinder at low mass-damping using RANS code. *Journal of Fluids and Structures*, 23 (1), 23-37.
- Park, H., Bernitsas, M.M., Ajith Kumar, R. (2012). Selective roughness in the boundary layer to suppress flow-induced motions of circular cylinder at  $30,000 < Re < 120,000$ . *Journal of Offshore Mechanics and Arctic Engineering*, 134 (4), 041801-041801.
- Quadrante, L.A.R., Nishi, Y. (2014). Amplification/suppression of flow-induced motions of an elastically mounted circular cylinder by attaching tripping wires. *Journal of Fluids and Structures*, 48, 93-102.
- Raghavan, A.K., Chan-Hyun, S., Bangalore, H.L.G. (2008). Passive control of vortex-induced vibrations: an Overview. *Recent Patents on Mechanical Engineering*, 1 (1), 1-11.
- Rashidi, S., Hayatdavoodi, M., Esfahani, J.A. (2016). Vortex shedding suppression and wake control: A review. *Ocean Engineering*, 126, 57-80.
- Sanli, B.G., Akilli, H. (2018). Effects of Permeable Cylinder on the Flow Structure in Deep Water. *Fluid Dynamics*, 53 (5), 711-721.
- Seal, C., Smith, C. (1999). The control of turbulent end-wall boundary layers using surface suction. *Experiments in Fluids*, 27 (6), 484-496.
- Seman, M.A., Ismail, F., Ismail, N., Ismail, M., Yusoff, H. (2015). Effect of Counter-Rotating Cylinder with Surface Roughness on Stagnation and Separation Point-A Computational Approach. *Indian Journal of Science and Technology*, 8 (30), 1-6.
- Senga, H., Larsen, C.M. (2017). Forced motion experiments using cylinders with helical strakes. *Journal of Fluids and Structures*, 68, 279-294.
- Song, Z., Duan, M., Gu, J. (2017). Numerical investigation on the suppression of VIV for a circular cylinder by three small control rods. *Applied Ocean Research*, 64, 169-183.
- Sui, J., Wang, J., Liang, S., Tian, Q. (2016). VIV suppression for a large mass-damping cylinder attached with helical strakes. *Journal of Fluids and Structures*, 62, 125-146.
- Tensi, J., Boué, I., Paillé, F., Dury, G. (2002). Modification of the wake behind a circular cylinder by using synthetic jets. *Journal of Visualization*, 5 (1), 37-44.
- Thomas, F.O., Kozlov, A., Corke, T.C. (2008). Plasma actuators for cylinder flow control and noise reduction. *AIAA Journal*, 46 (8), 1921-1931.
- Tu, J., Yeoh, G.H., Liu, C. (2018). Computational fluid dynamics: a practical approach. *Butterworth-Heinemann*.
- Wang, J., Zheng, H., Tian, Z. (2015). Numerical simulation with a TVD-FVM method for circular cylinder wake control by a fairing. *Journal of Fluids and Structures*, 57, 15-31.
- Williamson, C.H.K., Govardhan, R.N. (2008). A brief review of recent results in vortex-induced vibrations. *Journal of Wind Engineering and Industrial Aerodynamics*, 96 (6-7), 713-735.
- Wu, H., Sun, D.P., Lu, L., Teng, B., Tang, G.Q., Song, J.N. (2012). Experimental investigation on the suppression of vortex-induced vibration of long flexible riser by multiple control rods. *Journal of Fluids and Structures*, 30, 115-132.

- Yadav, R., Verma, I., Orsino, S., Sharkey, P., Nakod, P., Li, S. (2019). Bluff-body stabilized flame simulations using SBES in combination with the flamelet generated manifold combustion model, AIAA Scitech 2019 Forum. *American Institute of Aeronautics and Astronautics*.
- Yao, W., Jaiman, R. (2017). Feedback control of unstable flow and vortex-induced vibration using the eigensystem realization algorithm. *Journal of Fluid Mechanics*, 827, 394-414.
- Yeon, S.M., Yang, J., Stern, F. (2016). Large-eddy simulation of the flow past a circular cylinder at sub-to super-critical Reynolds numbers. *Applied Ocean Research*, 59, 663-675.
- Yoon, J., Kim, J., Choi, H. (2014). Control of laminar vortex shedding behind a circular cylinder using tabs. *Journal of Mechanical Science and Technology*, 28 (5), 1721-1725.
- Yu, Y., Xie, F., Yan, H., Constantinides, Y., Oakley, O., Karniadakis, G.E. (2015). Suppression of vortex-induced vibrations by fairings: A numerical study. *Journal of Fluids and Structures*, 54, 679-700.
- Zhang, H., Fan, B.c., Chen, Z.h., Li, H.z. (2014). Numerical study of the suppression mechanism of vortex-induced vibration by symmetric Lorentz forces. *Journal of Fluids and Structures*, 48, 62-80.
- Zhang, K., Katsuchi, H., Zhou, D., Yamada, H., Bao, Y., Han, Z., Zhu, H. (2018). Numerical study of flow past a transversely oscillating wavy cylinder at  $Re=5000$ . *Ocean Engineering*, 169, 539-550.
- Zhang, K., Katsuchi, H., Zhou, D., Yamada, H., Han, Z. (2016). Numerical study on the effect of shape modification to the flow around circular cylinders. *Journal of Wind Engineering and Industrial Aerodynamics*, 152, 23-40.
- Zhang, K., Katsuchi, H., Zhou, D., Yamada, H., Zhang, T., Han, Z. (2017). Numerical simulation of vortex induced vibrations of a flexibly mounted wavy cylinder at subcritical Reynolds number. *Ocean Engineering*, 133, 170-181.
- Zhao, M., Cheng, L. (2014). Vortex-induced vibration of a circular cylinder of finite length. *Physics of Fluids*, 26 (1), 015111.
- Zhao, M., Cheng, L., An, H., Lu, L. (2014). Three-dimensional numerical simulation of vortex-induced vibration of an elastically mounted rigid circular cylinder in steady current. *Journal of Fluids and Structures*, 50, 292-311.
- Zhou, B., Li, Y., Wang, X., Guo, W., Tan, S.K. (2016). Experimental study of dynamic drag and lift characteristics of dimpled cylinders. *Marine Technology Society Journal*, 50 (1), 56-61.
- Zhou, B., Wang, X., Guo, W., Gho, W.M., Tan, S.K. (2015). Control of flow past a dimpled circular cylinder. *Experimental Thermal and Fluid Science*, 69, 19-26.
- Zhou, T., Razali, S.M., Hao, Z., Cheng, L. (2011). On the study of vortex-induced vibration of a cylinder with helical strakes. *Journal of Fluids and Structures*, 27 (7), 903-917.

# Chapter 2 Passive vibration control of cylindrical offshore components using pipe-in-pipe (PIP) concept: an analytical study

Journal of Ocean Engineering. Vol. 142, Pages 39-50, [10.1016/j.oceaneng.2017.06.063](https://doi.org/10.1016/j.oceaneng.2017.06.063).

---

## ABSTRACT

This paper aims to propose a design of using the revised PIP system to control vortex-induced vibrations (VIV) of cylindrical structural components. Analytical studies are carried out to examine the effectiveness of the proposed method. To this end, the fluid-induced vibration of a single pipe is investigated and the equation of motion of the system is solved and validated by the experimental data. This single pipe system is then extended to the proposed PIP system and its dynamic behaviour under the excitation of vortex shedding is simplified as a Two-Degree-of-Freedom (2DoF) system. The optimal damping ratio and tuning frequency of the revised PIP system are obtained through a series of numerical searching technique and sensitivity analyses. Explicit formulae are also derived for practical ease of use. The governing equation of the system under VIV is solved in the time domain using the MATLAB/Simulink program. The responses of the single pipe system and the proposed PIP system due to vortex shedding are calculated and compared. Analytical results demonstrate that the proposed PIP system can significantly suppress the VIV of offshore cylindrical components. It could be then a cost-effective passive solution to suppress vibration of marine cylindrical components.

## 2.1 Introduction

The exploration of energy resources has been moving into deep (above ~500m) and ultra-deep (above ~1500m) waters ([Saint-Marcoux, 2014](#), [Song et al., 2016](#)). Various marine structural components such as subsea pipelines, marine risers and conductors are heavily used in the oil and gas industries to explore and transport these resources. During their service lives, these structures may expose to different vibrations induced by different sources such as earthquake excitation and/or vortex shedding. Vortex-induced vibration (VIV) is of special interest both in the industry and academic societies since many structural failures observed in offshore structures are associated with VIV. Considerable research work has been conducted to attenuate such

destructive vibrations ([Williamson and Govardhan, 2004](#), [Raghavan et al., 2008](#), [Choi et al., 2008](#), [Rashidi et al., 2016](#)). These approaches can be generally divided into two broad categories: passive control and active control ([Gad-el-Hak, 2000](#)). Compared to the active control, passive control requires no external power to operate, it is, therefore, relatively less expensive and easier to install. Helical strakes and fairings have been most extensively used in engineering practices due to their effectiveness ([Khorasanchi and Huang, 2014](#), [Zeinoddini et al., 2015](#)). For example, wind tunnel tests conducted by [Zhou et al. \(2011\)](#) showed that the intensity of vortices shed from the straked cylinder are weakened considerably and the vibration amplitude of the cylinder can be suppressed up to 98%. Experimental tests conducted by [Gao et al. \(2016\)](#) showed that fully-covered flexible riser with a helical strake can control the VIV in both uniform and linearly sheared currents up to 96% and 99%, respectively. However, the coverage of 75% and 50% yield the effective performance in uniform and linearly sheared currents. [Allen \(2003\)](#) experimentally investigated the suppression performance of fairing for offshore risers. It was shown that fairing has much lower drag coefficient in comparison with helical strake and can significantly suppress the VIV. Besides helical strake and fairing, many alternative methods have also been proposed by different researchers to control VIV. [Azmi et al. \(2012\)](#) studied the effectiveness and mechanism of screen shroud to mitigate VIV amplitude and showed that this technique is able to suppress VIV by around 50%. The effect of porous media on the reduction of lift coefficient of cylinders undergoing VIV was numerically investigated by [Zhao and Cheng \(2010\)](#). The results revealed that the reduction of lift coefficient depends on the thickness of the porous layer and Darcy number. [Zhu and Yao \(2015\)](#) carried out a series of numerical analyses to study the effectiveness of using control rods to suppress VIV and their results showed that nine rods can control VIV with a reasonable cost from an economic perspective. [Kiu et al. \(2011\)](#) studied the effect of surface roughness on the VIV response in subcritical flow regimes. The results showed that by increasing the surface roughness, the maximum drag force, amplitude of response and width of lock-in region will decrease. [Park et al. \(2012\)](#) proposed a Passive Turbulence Control (PTC) device to control VIV, and their results indicated that the proposed system can suppress the maximum amplitude of VIV up to 63%. [Bernitsas and Raghavan \(2014\)](#) patented a Surface Roughness Control (SRC) device to suppress VIV in high Reynold numbers regime; their experimental results showed that by attaching roughness strips, if distributed properly, noticeable reduction can be

achieved. The effect of surface roughness on the VIV response of a flexible cylinder with large aspect ratio was experimentally studied by [Gao et al. \(2015\)](#). It was concluded that the level of surface roughness plays an important role in VIV response; a rough cylinder has a larger vortex shedding frequency with a narrower lock-in region and lower displacement response. A series of experimental tests conducted by [Owen et al. \(2001\)](#) showed that attaching hemi-spherical bumps (caps) with a constant longitudinal spacing and an angular separation of 45° can reduce drag force and VIV response up to 25%. They also reported a drag and VIV reduction for a wavy circular cylinder with a sinuous axis up to 47%. [Assi et al. \(2009\)](#) studied the effectiveness of a series of free to rotate splitter plates including single splitter plate, double splitters plates and parallel plates. The results showed that a maximum drag reduction of up to 38% can be achieved with parallel plates.

Although a few of afore-mentioned devices have been used in engineering practices, certain drawbacks of these devices may considerably affect their performances especially when they are intended to be applied in the deep and ultra-deep waters. For example, some devices (e.g. helical strake) may impose an additional drag force to the structure; some others (e.g. shrouds and axial slats ([Kumar et al., 2008](#))) are expensive to manufacture, not easy to install, susceptible to marine growth and prone to storm damage, etc. It is, therefore, important to develop more efficient, cost effective and practical passive control devices to control VIV.

A conventional PIP system comprises an internal insulated pipe (product pipe) which carries product flow and an outer pipe (sleeve pipe) which provides mechanical protection against the high external hydrostatic pressure and other mechanical damages ([Bai and Bai, 2005](#)). Thermal insulation layers are normally wrapped around the inner pipe to keep the temperature of the product. Centralizers which are used to centralize the inner pipe to prevent possible damage to the thermal insulation layer during installation, are normally installed along the pipe with an interval varying from 2 to 12 meters ([Bai and Bai, 2012](#)). Extensive research works have been carried out on the conventional PIP system, and these works mainly focused on the structural instabilities such as the buckling of the system (e.g. [Kyriakides \(2002\)](#), [Zheng et al. \(2014\)](#), [Wang et al. \(2015\)](#), [Alrsai and Karampour \(2016\)](#)). More recently, [Bi and Hao \(2016\)](#) slightly revised the conventional system and proposed a novel PIP system by replacing the hard centralizers with soft springs and dashpots. This revised PIP system

was simplified as a structure-TMD system with the outer pipe acting as the main structure and the inner pipe performing as the TMD. This system was then proposed to mitigate seismic induced vibrations of subsea pipelines and numerical analyses were carried out to examine the effectiveness of the proposed method. Numerical results showed that this revised system can significantly suppress seismic induced vibrations of both the inner and outer pipes ([Bi and Hao, 2016](#)). It does not vary too much from the traditional design, and will not be too expensive to manufacture. The system may have then great potential applications in the offshore and marine structures.

This paper proposes a passive design based on the revised PIP system to control the offshore cylindrical components under VIV, and is organized as follows: Section 2.2 presents the mathematical model of a single cylinder under vortex shedding. The equation of motion of this single pipe system is solved and validated by the experimental data. This single pipe system is then extended to the modified PIP system in Section 2.3 where the equation of motion of the modified PIP system under VIV is derived. A simple MATLAB Simulink code is developed to solve the governing equation. To obtain the optimized connecting system, a series of sensitivity analysis is carried out to derive the explicit formulae for optimal spring stiffness and dashpot coefficients. The responses of the conventional and modified PIP systems subjected to vortex shedding are calculated in Section 2.4 and the effectiveness of the proposed design is discussed in that section.

## **2.2 Mathematical Modelling of a Single Cylinder under VIV**

Extensive efforts have been made to study the oscillating behaviour of circular cylinders under VIV. Comprehensive review of these methods can be found in [Williamson and Govardhan \(2008\)](#) and [Sarpkaya \(2004\)](#). There are mainly three approaches to investigate the VIV phenomenon including numerical simulations, semi-empirical models and experimental tests. In the numerical simulations, the equation of fluid motion, known as the Navier-Stokes equation, is directly solved. This method is quite expensive in terms of the computational time. Consequently, several alternative methods have been proposed to more efficiently investigate this problem such as phenomenological models or wake oscillator models, Single-Degree-of-Freedom (SDOF) and force-decomposition models ([Gabbai and Benaroya, 2005](#)). The main difference between the alternative approaches and the direct numerical simulation is that the time-dependent behaviour of the fluid at the rear of the structure

is modelled rather than being directly computed. For example, in the wake oscillator models, the displacement of the mounted body and wake oscillations are coupled through a pair of non-dimensional differential equations, i.e., the equation of the cylinder's motion and van der Pol oscillator ([Facchinetti et al., 2004](#), [Farshidianfar and Zanganeh, 2010](#)). SDOF model, on the other hand, employs a single ordinary differential equation to describe the in-plane crossflow oscillation of the body. In the force-decomposition models, the fluid force is split into an excitation and a reaction part that can define all the motion-dependent force components ([Gabbai and Benaroya, 2005](#)). The force-decomposition approach, which relies on experimental measurements of certain components of fluid forces, is in essence an SDOF method. This method can describe and simulate experimental tests and thus is of great interest to study the nature of VIV, especially when strong computational and practical limitations arise respectively for numerical and experimental studies. Moreover, it is believed that SDOF models are reasonably accurate for the purpose of evaluating the maximum VIV responses; therefore, they are sufficient for most wind and ocean engineering applications ([Goswami et al., 1993](#)). In this the present study, the force-decomposition method is therefore employed to study VIV.

### 2.2.1 Equation of motion

The equation of crossflow vibration ( $y$ ) of an elastically-mounted rigid cylinder with diameter  $D$  under VIV oscillations can be written as ([Gabbai and Benaroya, 2005](#)):

$$m\ddot{y} + 2m\omega_n\zeta_s\dot{y} + m\omega_n^2y = F_{fluid}(t) = F_L - F_R \quad (2-1)$$

where  $m$  is the mass of the oscillating system,  $\omega_n$  is the natural frequency of the structure and  $\zeta_s$  is the structural damping ratio. The dot over the symbols denotes differentiation with respect to time. The time-dependent term  $F_{fluid}(t)$  can be further divided into two components: the excitation or lift force ( $F_L$ ) and the fluid reaction ( $F_R$ ). The above equation can be re-written in a non-dimensional form as follows:

$$\ddot{y} + 2\omega_n\zeta_s\dot{y} + \omega_n^2y = \beta\omega_s^2C_{fluid}(t) \quad (2-2)$$

where  $C_{fluid}(t)$  is the time-varying fluid coefficient on the oscillating structure defined by  $C_{fluid}(t) = C_L - C_R$ . Where,  $C_L$  and  $C_R$  are the vortex lift and reaction coefficients, respectively,  $\omega_s$  is Strouhal frequency which is defined as below:



$$\omega_s = 2\pi f_s = 2\pi S_t U/D \quad (2-3)$$

where  $S_t$  is the Strouhal number and  $U$  is the free-stream velocity of the flow;  $\beta$  is a mass parameter or inverse Skop-Griffin parameter:

$$\beta = \rho D^2 / 8\pi^2 S_t^2 m \quad (2-4)$$

in which  $\rho$  is the fluid density. When the cylinder is vibrating within the lock-in region, in which the wake formation and fluctuating motion have a frequency near to the structural vibration frequency, the fluctuating transverse and total fluid force coefficient is nearly sinusoidal. So the total fluid coefficient can be expressed as:

$$C_{fluid}(t) = C_F \sin(\omega t + \varphi) \quad (2-5)$$

where  $\varphi$  is the phase difference between the fluid force and displacement of the cylinder. After substituting Equation (2-5) into Equation (2-2), the equation of cylinder motion becomes:

$$\ddot{y} + 2\omega_n \zeta_s \dot{y} + \omega_n^2 y = \beta \omega_s^2 C_F \sin(\omega t + \varphi) \quad (2-6)$$

Equation (2-6) can accurately simulate a cylinder under VIV when the empirical values  $C_F$  are obtained from the experimental results.

### 2.2.2 Vibration simulation of a single cylinder under VIV

In this section, the SDOF model is used to simulate an experimental test carried out by [Rahman \(2015\)](#) aiming at developing a validated analytical model for further analysis, i.e., the analysis of the proposed PIP system. Figure 2-1 shows the schematic view of the experimental setup.

A towing tank with the length, width and depth of 50m, 1.25m and 1.10m, respectively was used in the tests. The testing cylinder was towed by the towing cable in the still water. The cylinder was mounted to a four-armed pendulum system, and two linear springs were used to restrain the cylinder in the transverse direction. A set of tension load cells were used to measure the hydrodynamic forces acting on the rig. It should be noted that the experiment focused on the crossflow vibration of the cylinder and the motion in the in-line direction was ignored. Moreover, the experiment was conducted in the subcritical flow region with Reynolds numbers ranging from  $7.4 \times 10^3$  to  $2 \times 10^5$ , corresponding to the range of reduced velocity  $U_r$  ( $U_r = U/f_n D$ ;  $\omega_n = 2\pi f_n$ ) from 2 to 14 ([Rahman and Thiagarajan, 2013](#), [Rahman, 2015](#)). Detailed information

regarding the experimental setup can be found in [Rahman \(2015\)](#). To consider the effect of aspect ratio (the proportion of cylinder length to the diameter), four cases (with  $L/D=13, 10, 7.5$  and  $5$ ) are examined in the present study using the parameters listed in Table 2-1 and Table 2-2, and the fluid coefficients  $C_F$  obtained from the tests as shown in Figure 2-2.

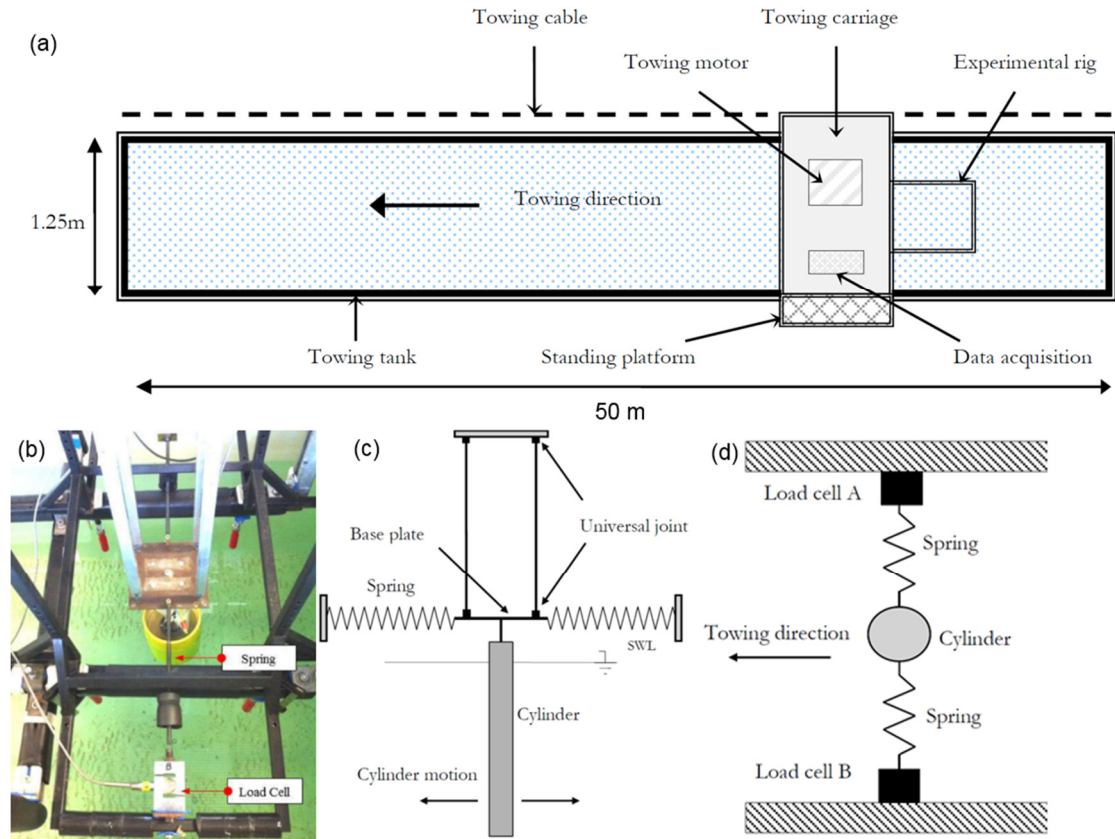


**Figure 2-1:** Experimental setup of a single cylinder under VIV: (a) Hydraulic towing tank; (b) Force measurement device; (c) and (d) Schematic diagrams of the pendulum rig ([Rahman, 2015](#)).

As can be seen from Table 2-1, the Strouhal numbers obtained in the tests are between 0.098 and 0.146 and they depend on the aspect ratio. On the other hand, it is widely known that a Strouhal number for a circular cylinder is around 0.2. Two reasons result in the different and relatively small Strouhal numbers in the tests: (i) when the aspect ratio is small, the three-dimensional (3-D) wake effect can trigger the wake turbulent region around the cylinder ([Rahman et al., 2016](#)) and (ii) different aspect ratios can cause changes to the correlation length of vortex shedding ([Norberg, 1994](#)). The obtained results are consistent with the work done by [Gouda \(1975\)](#), in which it was indicated that a steady value of Strouhal number of 0.2 can be governed when the cylinder aspect ratio is larger than nearly 50. Moreover, using end plate can also cause

a significant influence on the Strouhal frequency as extensively discussed by [Szepessy and Bearman \(1992\)](#).

**Table 2-1:** Experimental matrix performed in [Rahman \(2015\)](#).

	$L$ (m)	$D$ (m)	$L/D$	$k$ (N/m)	$m$ (kg)	$m_{osc, in\ water}$ (kg)	$f_n$ (Hz)	$\zeta$	$S_t$
Exp. 1	0.78	0.06	13	245	5.73	3.53	0.99	0.031	0.146
Exp. 2	0.60	0.06	10	245	4.41	2.71	1.12	0.031	0.130
Exp. 3	0.60	0.08	7.5	245	7.84	4.82	0.865	0.036	0.111
Exp. 4	0.40	0.08	5	245	5.22	3.21	1.035	0.032	0.098

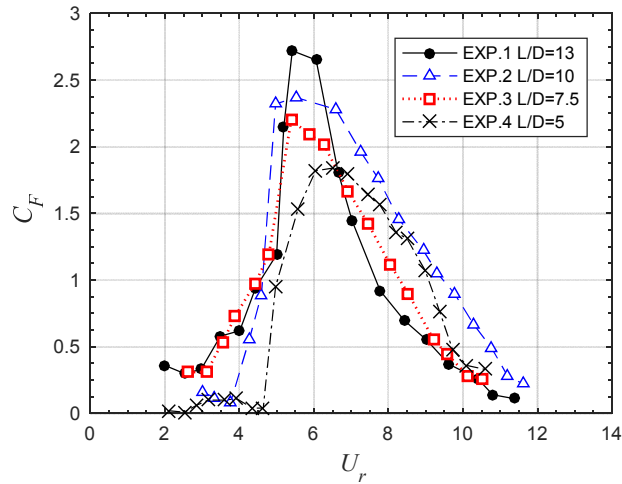
**Table 2-2:** The range of examined current velocity and corresponding vortex shedding frequency ([Rahman, 2015](#)).

	$L/D$	$U$ (m/s)	$f_s$ (Hz) = $S_t U/D$	$f_s/f_n$
Exp. 1	13	[0.12 0.98]	[0.29 2.38]	[0.29 2.41]
Exp. 2	10	[0.14 1.10]	[0.30 2.38]	[0.27 2.13]
Exp. 3	7.5	[0.14 1.10]	[0.19 1.51]	[0.22 1.75]
Exp. 4	5	[0.17 1.37]	[0.21 1.68]	[0.20 1.62]

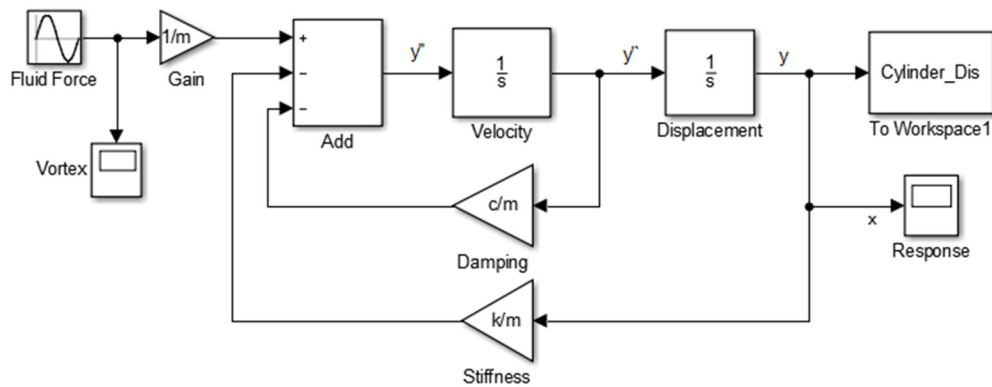
A time-domain Simulink model (Figure 2-3) is developed in MATLAB to solve Equation (2-6). On the left side of the Simulink model, the external fluid force including two feedback loops is entered to the system. The first one refers to the cylinder velocity and it is multiplied by the damping, and the second loop stands for the cylinder displacement, which is multiplied by the stiffness of the spring. The symbol  $\frac{1}{s}$  is an integrator block, which outputs the value of the integral of its input signal with respect to time. All the parameters including the mass, damping and stiffness coefficients are the same as those in the experimental test ([Rahman, 2015](#)).

Figure 2-4 compares the normalized amplitudes of the cylinder oscillations ( $A_y/D$ ) obtained from the experiments and the analytical results over a range of reduced velocities. It can be seen that there is a good agreement between the experimental and semi-empirical results, which demonstrate the accuracy of the dynamic Simulink model as shown in Figure 2-3. The comparisons also indicate that the accuracy of the SDOF model is slightly decreased for lower aspect ratios (especially in Figure 2-4(d)). This is because when the aspect ratio is small, the vortex formation frequency and the corresponding lift force change, which lead to the instability of the wake structure and further arise the 3-D effects ([Rahman et al., 2016](#)). The SDOF model, which in essence a simplified single ordinary differential equation to describe the crossflow VIV response, will be therefore difficult to accurately capture all the features of fluid behaviour. It is also worth mentioning that nonlinear effects associated with VIV and added mass variation in the lock-in region ([Gabbai and Benaroya, 2005](#)) are inherently considered by varying the fluid coefficient ( $C_F$ )

obtained from experimental test ([Rahman and Thiagarajan, 2013](#), [Rahman, 2015](#)) (see Figure 2-2).



**Figure 2-2:** Root Mean Square of the observed fluid coefficient  $C_F$  from the experimental tests ([Rahman, 2015](#)).



**Figure 2-3:** Schematic of the dynamic Simulink model for a single cylindrical structure under VIV.

Figure 2-4 also shows that within a certain reduced velocity range (normally known as the lock-in or synchronization region), the oscillating amplitudes of the cylinder are significant, which means there is a broad range, but not just one particular frequency, that can cause significant vibrations to the cylinder. The suppression of VIV is therefore important for the cylindrical offshore structures. The lock-in regions are different for different aspect ratios, but generally speaking for the investigated aspect ratios, lock-in phenomenon take place when the reduced velocity is between 5 and 9.

It should be noted that some assumptions are made in the derivation of Equation (2-6) ([Gabbai and Benaroya, 2005](#)). They are: 1) the cylinder is rigid and the flow around the body is fully correlated and two-dimensional; and 2) the dynamic behaviour of the flow field around the oscillating body and the effect of geometry are not considered. This model, therefore, might not be a comprehensive model. However, it is fairly

accurate for the preliminary study to examine the effectiveness of the proposed system especially considering the good matches between the analytical and experimental results as shown in Figure 2-4. This semi-empirical model will be extended to study the behaviour of modified PIP system under VIV in the following sections.

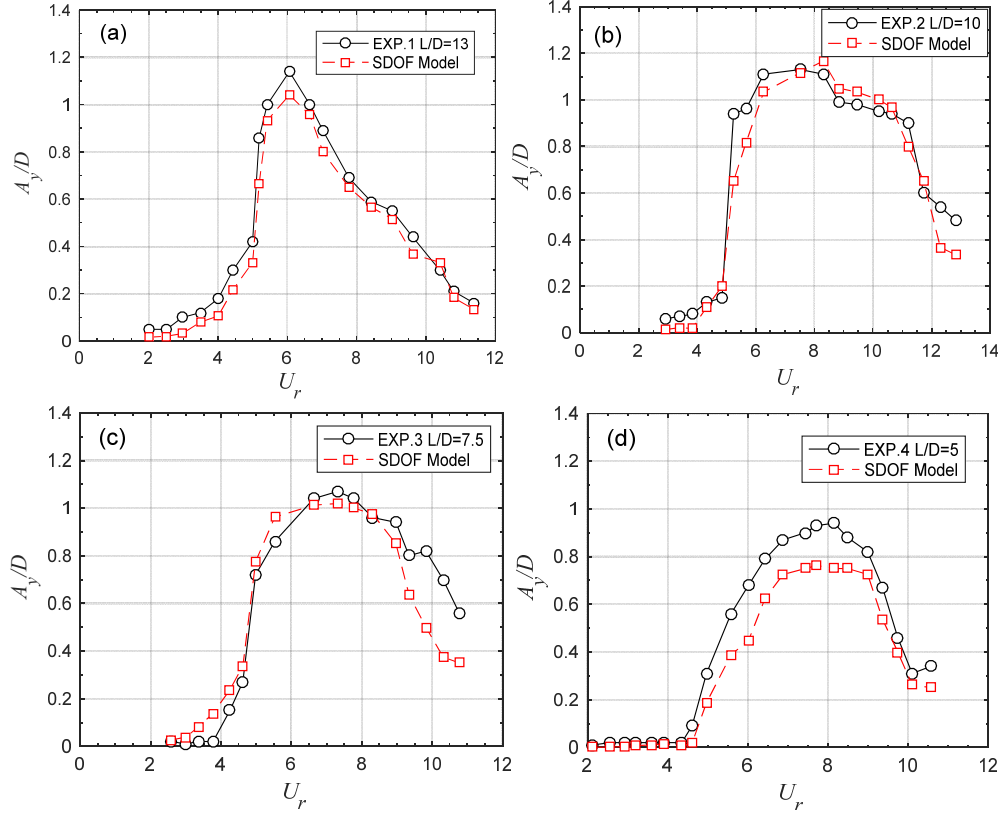


**Figure 2-4:** Comparisons of the normalized amplitudes obtained from the experimental data and the analytical solutions for different aspect ratios (a)  $L/D = 13$  (b)  $L/D = 10$  (c)  $L/D = 7.5$  and (d)  $L/D = 5$ .

### 2.3 Optimized PIP to Control Vibration of Cylindrical Structures Caused by VIV

In this section, the simplified governing equation of the modified PIP system subjected to VIV is firstly presented and then the optimal values of the spring stiffness and damping coefficient are investigated.

#### 2.3.1 Basic governing equations of PIP system and method of solution

Figure 2-5 shows the structural and simplified analytical models of the modified PIP system. As shown in Figure 2-5(a), the coaxial inner and outer pipes are connected by the springs and dashpots. This system can be simplified as a two-degree-of-freedom (Two-DOF) system consisting of a primary oscillator (the outer pipe) and an auxiliary TMD (the inner pipe) as shown in Figure 2-5(b). It should be noted that for a conventional structure-TMD system, the mass ratio between the TMD and the main

structure is normally in an order of 1% to 5% percent. For this modified PIP system, the mass ratio, however, can be much larger and in certain cases the mass of the inner pipe can be almost the same as the outer pipe. This system is normally regarded as a non-conventional TMD system (Bi and Hao, 2016).

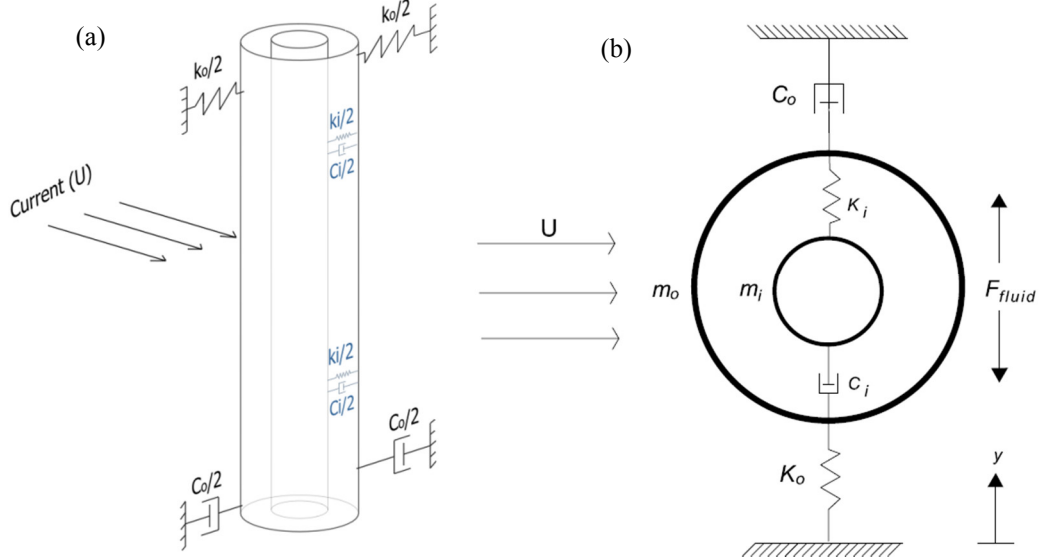


**Figure 2-5:** Structural and analytical models of the modified PIP system (a) structural model and (b) analytical model.

As shown in Figure 2-5(b), the primary oscillator is characterized by a mass  $m_o$ , a linear stiffness  $k_o$  and a constant viscous damping coefficient  $c_o$ . The natural frequency and viscous damping ratio of the primary structure are therefore  $\omega_o = \sqrt{k_o/m_o}$  and  $\zeta_o = c_o/2\sqrt{k_o m_o}$ . Similar to the main system, the corresponding parameters for the TMD system are  $m_i$ ,  $k_i$ ,  $c_i$ , with  $\omega_i = \sqrt{k_i/m_i}$  and  $\zeta_i = c_i/2\sqrt{k_i m_i}$ .

When this system is subjected to the vortex shedding excited crossflow vibration, the equation of motion can be expressed as:

$$\begin{bmatrix} m_o & 0 \\ 0 & m_i \end{bmatrix} \begin{Bmatrix} \ddot{y}_o \\ \ddot{y}_i \end{Bmatrix} + \begin{bmatrix} c_o + c_i & -c_i \\ -c_i & c_i \end{bmatrix} \begin{Bmatrix} \dot{y}_o \\ \dot{y}_i \end{Bmatrix} + \begin{bmatrix} k_o + k_i & -k_i \\ -k_i & k_i \end{bmatrix} \begin{Bmatrix} y_o \\ y_i \end{Bmatrix} = \begin{Bmatrix} F_{fluid}(t) \\ 0 \end{Bmatrix} \quad (2-7)$$

where  $y_o$  and  $y_i$  are the in-plane transverse displacements of the outer and inner pipes, respectively.

To facilitate the optimization of the spring stiffness and damping coefficient, it is convenient to define the mass ratio  $\mu$  and tuning frequency ratio  $f$  as follows:

$$\mu = m_i/m_o \quad (2-8)$$

$$f = \omega_i/\omega_o = \sqrt{1/\mu (k_i/k_o)} \quad (2-9)$$

### 2.3.2 Optimum Design of Non-conventional Tuned Mass Damper (TMD)

TMD systems have been widely used to attenuate the undesirable vibrations of engineering structures due to their simplicity ([Gutierrez Soto and Adeli, 2013](#), [Dinh and Basu, 2015](#)). To make the system effective, the key factor is to obtain the optimal values of the spring stiffness and damping coefficient. Various methods have been proposed to estimate the optimal TMD parameters (e.g. harmony search ([Bekdaş and Nigdeli, 2011](#)) and equivalent linearization ([Anh and Nguyen, 2013](#))). It should be noted that most of these methods consider the conventional TMD system, i.e., the system with small mass ratio. Very limited studies reported the optimization of TMD system with large mass ratio. For example, [Hoang et al. \(2008\)](#) presented explicit formulas to optimize the TMD parameters with large mass ratio when the main system is subjected to earthquake loading, i.e., base excitation. For the modified PIP system, vortex shedding induced force is applied on the external pipe, i.e., on the main structural mass. The optimization formulas for this case are different from those presented in [Hoang et al. \(2008\)](#). To the best knowledge of the authors, no open literature presents straightforward explicit formulas for tuning parameters of the non-conventional TMD system (with high mass ratio) when the external force is applied on the main structure. The optimization of the modified PIP system is introduced in this section.

It is well known that the vibrations of cylindrical offshore components induced by vortex shedding include characteristics as follows. The current flow and vortex shedding frequency vary in space and time ([Veritas, 2000](#), [ISO, 2015](#)). The vibration of cylindrical structures in steady current can be divided into different categories: (i) the forced vibration by Karman vortex shedding, which excites the structure at a dominant frequency; (ii) the vibration in the synchronization or lock-in region, which occurs not only near a dominant frequency but also over a broad range of input frequencies (current velocities); (iii) turbulence-induced vibration in which the structures are excited by a broad-band frequency out of the lock-in region and (iv) excitation induced by tip-vortices in the high flow velocity regime ([Nakamura et al., 2013](#)). Due to these reasons, there is a wide range of current velocities/vortex shedding frequencies, within which the oscillations should be suppressed as discussed in

Section 2.2. The external force applied to the main system can be assumed as a stationary Gaussian random process with a constant power spectral density (PSD).

In the present study, the vibration amplitude of the external pipe is taken as the parameter to be suppressed (as demonstrated by [Bi and Hao \(2016\)](#)), the vibration of the inner pipe can be mitigated as well due to the large mass ratio of the system). For a TMD system subjected to a excitation with a constant PSD  $S_0$ , the mean square displacement of the external pipe (the objective function) can be expressed by [Bakre and Jangid \(2007\)](#):

$$\sigma_{y_o}^2 = \int_{-\infty}^{\infty} S_0 |H_{y_o}(\omega)|^2 d\omega \quad (2-10)$$

in which  $H_{y_o}(\omega)$  is the frequency response function, and it has the following form:

$$H_{y_o}(\omega) = 1/\Delta m_o (-\omega^2 + 2i\zeta_i\omega_i\omega + \omega_i^2) \quad (2-11)$$

where

$$\Delta = \omega^4 - 2i[\omega_o\zeta_o + (1 + \mu)\zeta_i\omega_i]\omega^3 - [\omega_o^2 + (1 + \mu)\omega_i^2 + 4\omega_i\omega_o\zeta_i\zeta_o]\omega^2 + 2i\omega_i\omega_o[\omega_i\zeta_o + \omega_o\zeta_i]\omega + \omega_o^2\omega_i^2 \quad (2-12)$$

Substituting Equation (2-11) into Equation (2-10), the objective function ( $\sigma_{y_o}^2$  or  $N$ ) becomes ([Bakre and Jangid, 2007](#)):

$$N = \frac{1}{4}(I/L) \quad (2-13)$$

where

$$I = \zeta_i[1 - f^2(2 + \mu) + f^4(1 + \mu)^2] + \mu f^3\zeta_o + 4f^2\zeta_i^3(1 + \mu) + 4f\zeta_i^2\zeta_o[1 + f^2(1 + \mu)] + 4f^2\zeta_i\zeta_o^2 \quad (2-14)$$

$$L = [\mu f\zeta_i^2 + \zeta_i\zeta_o\{1 - 2f^2 + f^4(1 + \mu)^2 + 4f^2\zeta_i^2(1 + \mu) + 4f\zeta_i\zeta_o[1 + f^2(1 + \mu)] + 4f^2\zeta_o^2\} + \mu f^3\zeta_o^2] \quad (2-15)$$

For an undamped primary structure, it is possible to obtain closed-form expressions for the optimum TMD parameters by solving the optimization condition equations:

$$\partial N/\partial f = 0, \partial N/\partial \zeta_i = 0 \quad (2-16)$$

However, for a damped primary system, Equation (2-16) cannot be solved for the closed-form expressions and normally a numerical searching technique is adopted to obtain the optimal parameters ([Bakre and Jangid, 2007](#), [Salvi and Rizzi, 2015](#)). For a given mass ratio ( $\mu$ ) and damping ratio of the main system ( $\zeta_o$ ), the numerical



searching algorithm seeks the optimal frequency ratio ( $f^{opt}$ ) and damping ratio of the TMD system ( $\zeta_i^{opt}$ ) in such a way that the objective function  $N$ , attains a minimum value.

Table 2-3 tabulates the obtained optimal parameters for the TMD system and the corresponding response quantities for five different main system damping ratios ( $\zeta_o = 0.02, 0.04, 0.06, 0.08, 0.1$ ). The superscript *opt* indicates the optimal TMD tuning parameters. It should be noted that the numerical searching technique itself is not new and many researchers have adopted this method to obtain the optimal TMD parameters. However, most of previous studies emphasized mainly on the small mass ratio as mentioned above. For example, [Bakre and Jangid \(2007\)](#) presented the optimal values when the mass ratio is up to 0.1. For ease of use in practical applications, in the present study, the optimal parameters for the high mass ratio up to 0.9 are underlined and tabulated in Table 2-3.

### 2.3.3 Sensitivity Analyses

The optimal values estimated in Table 2-3 are based on a given mass ratio ( $\mu$ ) and the damping ratio ( $\zeta_o$ ) of the main structure. In real engineering practices, some uncertainties inevitably exist. For example, marine growth surrounding the outer pipe can change the mass ratio of the system and can also influence the damping ratio of the main structure. The robustness of the system is therefore important. To demonstrate the robustness of the system, four different mass ratios ( $\mu = 0.05, 0.1, 0.4, 0.9$ ) are considered. In each case, the damping ratio ( $\zeta_o$ ) of the main oscillator is kept the same; specifically  $\zeta_o = 0.031$ , the same value as in Exp. 1 in Table 2-1. Figure 2-6 and Figure 2-7 show the variation and contour of the response optimization index ( $N$ ) against different TMD parameters. The results demonstrate that mass ratio significantly influences the robustness of the system. When the mass ratio is small (e.g. in Figure 2-6(a) and (b)), the smallest optimization index can be obtained only within a very narrow range. This is why it is generally reported that the control effectiveness of the conventional-TMD system is sensitive to the mass ratio (e.g. [Hoang et al. \(2008\)](#), [Reggio and Angelis \(2015\)](#)). When the mass ratio becomes larger (e.g. in Figure 2-6(c) and (d)), the results become rather flat around the minimum value  $N^{opt}$ , which means the system will be effective even if the parameters shift away from the optimal values. For the PIP system, the mass ratio can reach more than 80% (e.g. [Bi and Hao \(2016\)](#)), this property will significantly facilitate the design of the connecting device (which is

represented by a spring and dashpot in the analytical model) within the annulus of the PIP system.

**Table 2-3:** Obtained optimal parameters for a TMD system with different mass ratios based on the numerical searching technique.

$\mu$	$\zeta_o = 0.02$			$\zeta_o = 0.04$			$\zeta_o = 0.06$			$\zeta_o = 0.08$			$\zeta_o = 0.1$		
	$\zeta_i^{opt}$	$f^{opt}$	$N^{opt}$	$\zeta_i^{opt}$	$f^{opt}$	$N^{opt}$	$\zeta_i^{opt}$	$f^{opt}$	$N^{opt}$	$\zeta_i^{opt}$	$f^{opt}$	$N^{opt}$	$\zeta_i^{opt}$	$f^{opt}$	$N^{opt}$
0.10	0.153	0.929	2.6243	0.153	0.926	2.2507	0.153	0.924	1.9634	0.153	0.921	1.7366	0.152	0.919	1.5536
0.15	0.184	0.899	2.1992	0.184	0.896	1.9327	0.184	0.893	1.7193	0.184	0.890	1.5451	0.184	0.887	1.4007
0.20	0.209	0.871	1.9319	0.209	0.868	1.7242	0.209	0.865	1.5536	0.209	0.862	1.4112	0.209	0.859	1.2910
0.25	0.230	0.845	1.7431	0.230	0.842	1.5729	0.230	0.839	1.4304	0.230	0.836	1.3096	0.230	0.833	1.2062
0.30	0.248	0.822	1.6004	0.248	0.818	1.4562	0.248	0.815	1.3337	0.248	0.812	1.2287	0.248	0.809	1.1377
0.35	0.264	0.800	1.4874	0.264	0.796	1.3623	0.264	0.793	1.2550	0.264	0.790	1.1619	0.264	0.787	1.0807
0.40	0.278	0.779	1.3951	0.278	0.776	1.2847	0.278	0.773	1.1890	0.278	0.769	1.1055	0.278	0.766	1.0320
0.45	0.291	0.760	1.3177	0.291	0.757	1.2190	0.291	0.754	1.1328	0.291	0.750	1.0569	0.291	0.747	0.9898
0.50	0.303	0.742	1.2517	0.303	0.739	1.1624	0.303	0.736	1.0839	0.303	0.732	1.0145	0.303	0.729	0.9527
0.55	0.314	0.725	1.1945	0.313	0.722	1.1130	0.313	0.719	1.0410	0.313	0.716	0.9769	0.313	0.713	0.9196
0.60	0.324	0.709	1.1442	0.323	0.706	1.0694	0.323	0.703	1.0028	0.323	0.700	0.9434	0.323	0.697	0.8900
0.65	0.332	0.695	1.0997	0.333	0.691	1.0305	0.333	0.688	0.9686	0.333	0.685	0.9132	0.332	0.683	0.8632
0.70	0.341	0.680	1.0598	0.341	0.677	0.9954	0.341	0.674	0.9377	0.341	0.671	0.8858	0.341	0.669	0.8387
0.72	0.344	0.675	1.0450	0.344	0.672	0.9824	0.344	0.669	0.9262	0.344	0.666	0.8755	0.344	0.663	0.8296
0.74	0.347	0.67	1.0308	0.347	0.667	0.9698	0.347	0.664	0.9150	0.347	0.661	0.8656	0.347	0.658	0.8207
0.76	0.351	0.664	1.0171	0.35	0.662	0.9578	0.35	0.659	0.9043	0.35	0.656	0.8560	0.35	0.653	0.8121
0.78	0.354	0.659	1.0040	0.354	0.656	0.9461	0.353	0.654	0.8939	0.353	0.651	0.8467	0.353	0.648	0.8038
0.80	0.357	0.654	0.9913	0.356	0.652	0.9349	0.356	0.649	0.8839	0.356	0.646	0.8377	0.356	0.643	0.7957
0.82	0.359	0.65	0.9791	0.359	0.647	0.9240	0.359	0.644	0.8742	0.359	0.641	0.8291	0.359	0.638	0.7879
0.84	0.362	0.645	0.9673	0.362	0.642	0.9135	0.362	0.639	0.8648	0.362	0.636	0.8206	0.362	0.634	0.7803
0.86	0.365	0.64	0.9559	0.365	0.637	0.9034	0.365	0.634	0.8558	0.364	0.632	0.8125	0.364	0.629	0.7730
0.88	0.367	0.636	0.9449	0.367	0.633	0.8935	0.367	0.63	0.8470	0.367	0.627	0.8046	0.367	0.625	0.7659
0.90	0.37	0.631	0.9342	0.37	0.628	0.8840	0.37	0.625	0.8384	0.37	0.623	0.7969	0.37	0.620	0.7589

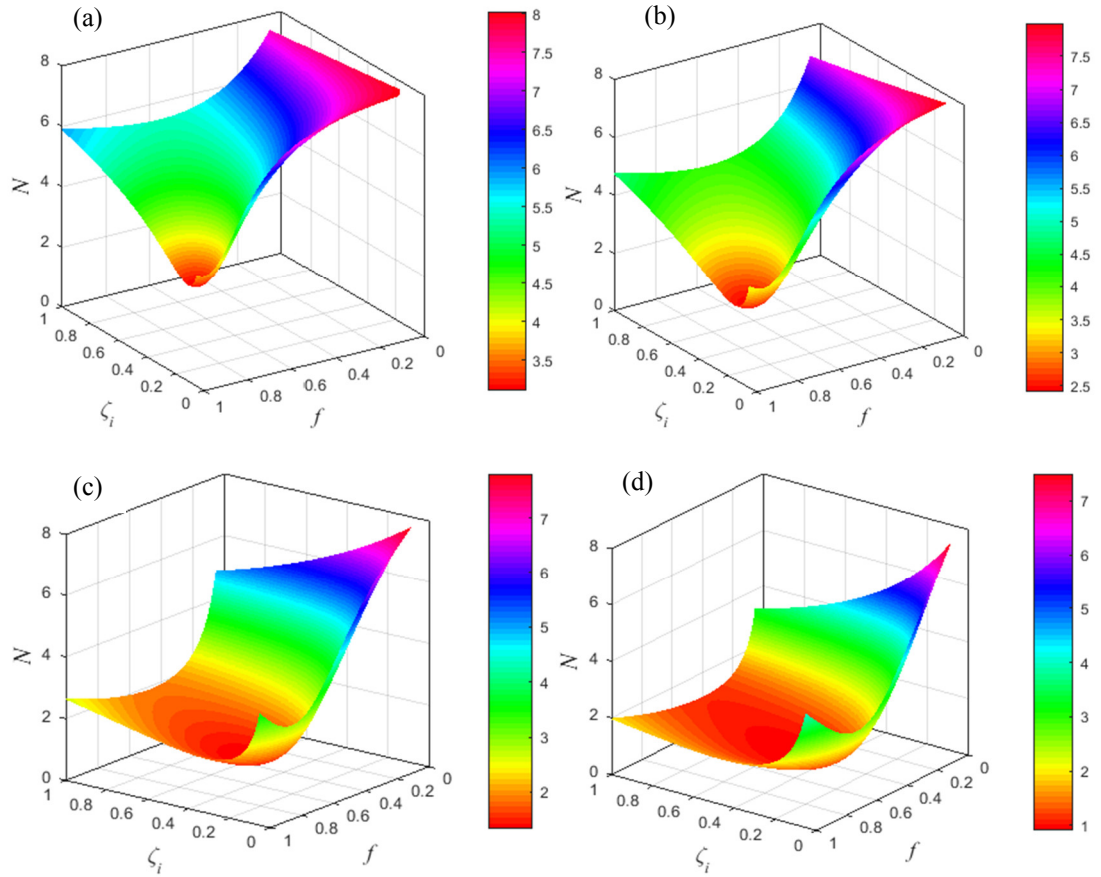


**Figure 2-6:** Mean square displacement response index ( $N$ ) of a main system with different TMD masses. (a)  $\mu = 0.05$ ; (b)  $\mu = 0.1$ ; (c)  $\mu = 0.4$ ; (d)  $\mu = 0.9$ . ( $\zeta_o = 0.031$ ).

In Figure 2-6 and Figure 2-7 a damping ratio of  $\zeta_o = 0.031$  is assumed. The optimum index ( $N^{opt}$ ) with different damping ratio is shown in Figure 2-8. As shown, increasing the damping of the main oscillator leads to better performance of the structure-TMD system (lower values of  $N^{opt}$ ) and when the mass ratio is large, the influence of damping ratio becomes less evident. These results again demonstrate the robustness of the non-conventional TMD system to suppress undesired vibrations.

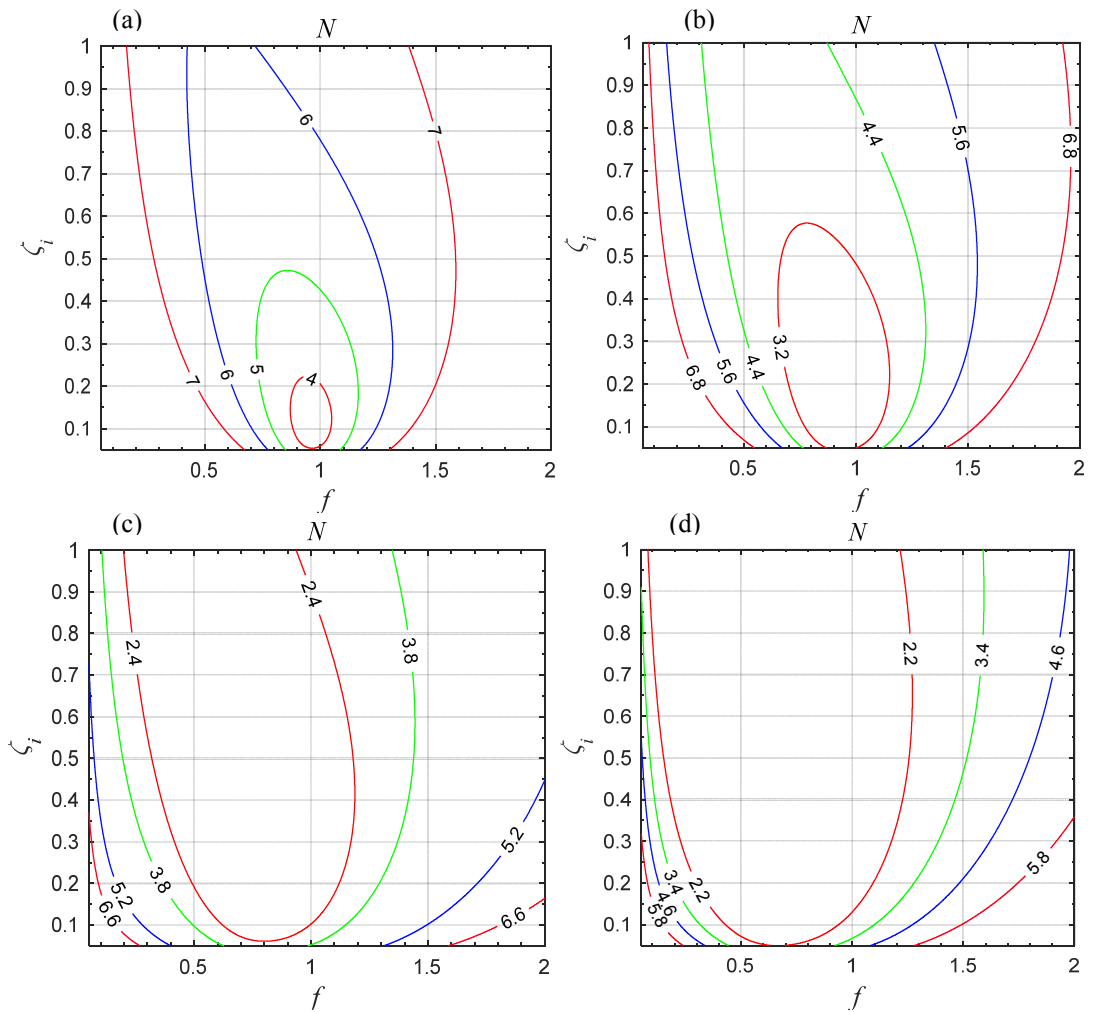


**Figure 2-7:** Intensity contour of  $N$  of a main system with different TMD masses. (a)  $\mu = 0.05$ ; (b)  $\mu = 0.1$ ; (c)  $\mu = 0.4$ ; (d)  $\mu = 0.9$ . ( $\zeta_o = 0.031$ ).

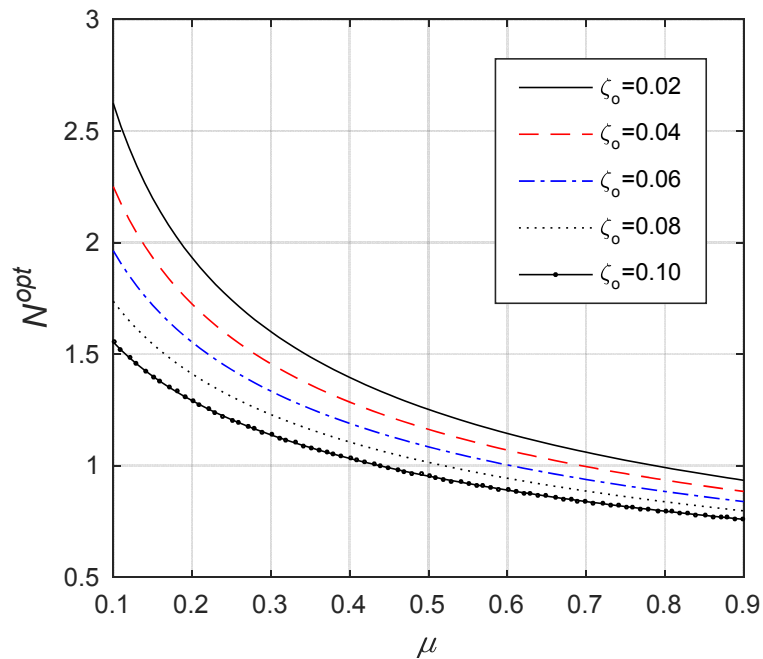


**Figure 2-8:** Influence of damping ratio on the optimum index.

### 2.3.4 Explicit formulae for optimum TMD parameters

In this section, for easy use in engineering applications, explicit mathematical expressions for optimal tuning parameters for a non-conventional structure-TMD system under an external force are estimated by a curve fitting scheme. The tuning results obtained from the numerical searching technique are shown in Figure 2-9 and Figure 2-10. It can be seen that  $\zeta_o$  slightly influence  $f^{opt}$  while it almost has no effect on  $\zeta_i^{opt}$ . Equations (2-17) and (2-18) are obtained by using the surface curve fitting in MATLAB.

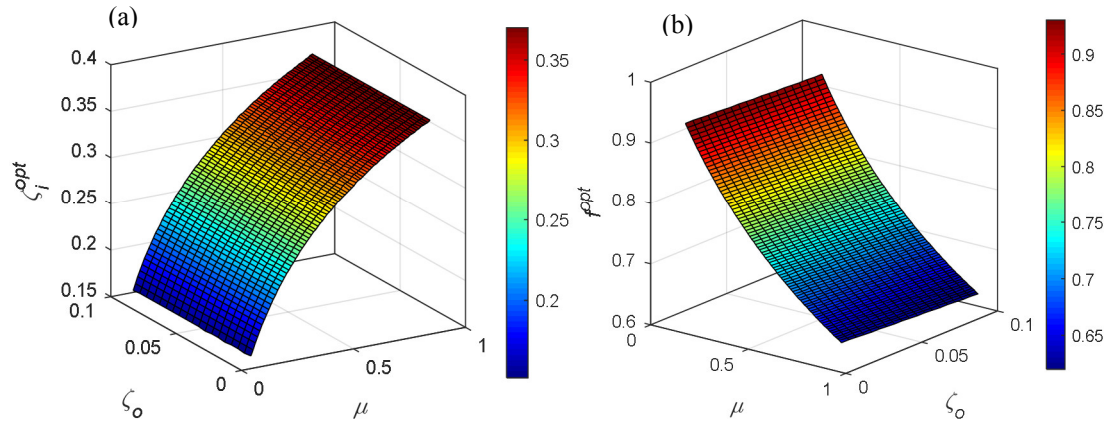


**Figure 2-9:** Optimum tuning parameters obtained from numerical searching scheme: (a) optimum TMD damping ratio ( $\zeta_i^{opt}$ ) and (b) optimum tuning frequency ratio ( $f^{opt}$ ).

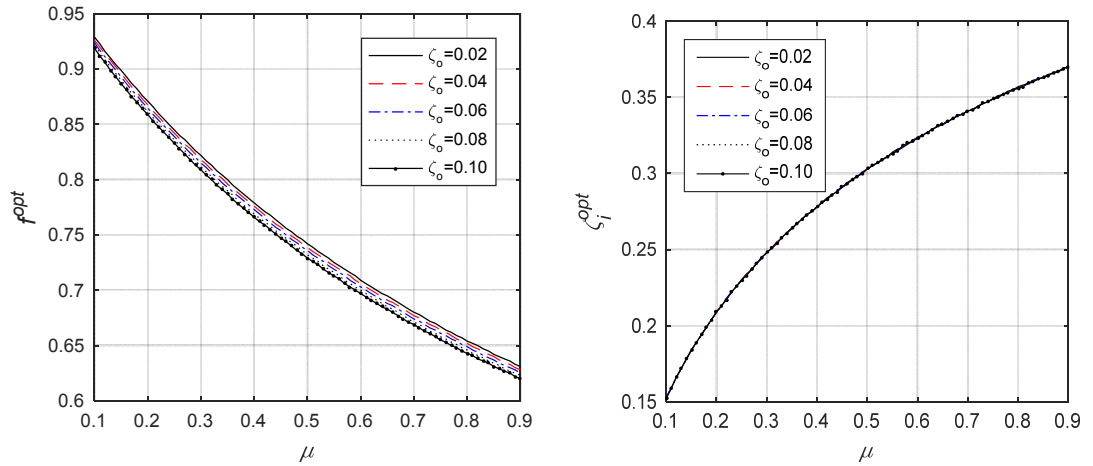


**Figure 2-10:** Variation of optimum tuning parameters as a function of mass ratio ( $\mu$ ) for various damping ratios of main system ( $\zeta_o$ ).

$$f^{opt} = 1.01 - 0.48\sqrt{\mu} - 0.06\sqrt{\zeta_o} \quad (2-17)$$

$$\zeta_i^{opt} = 0.10 \ln(\mu) + 0.37 \quad (2-18)$$

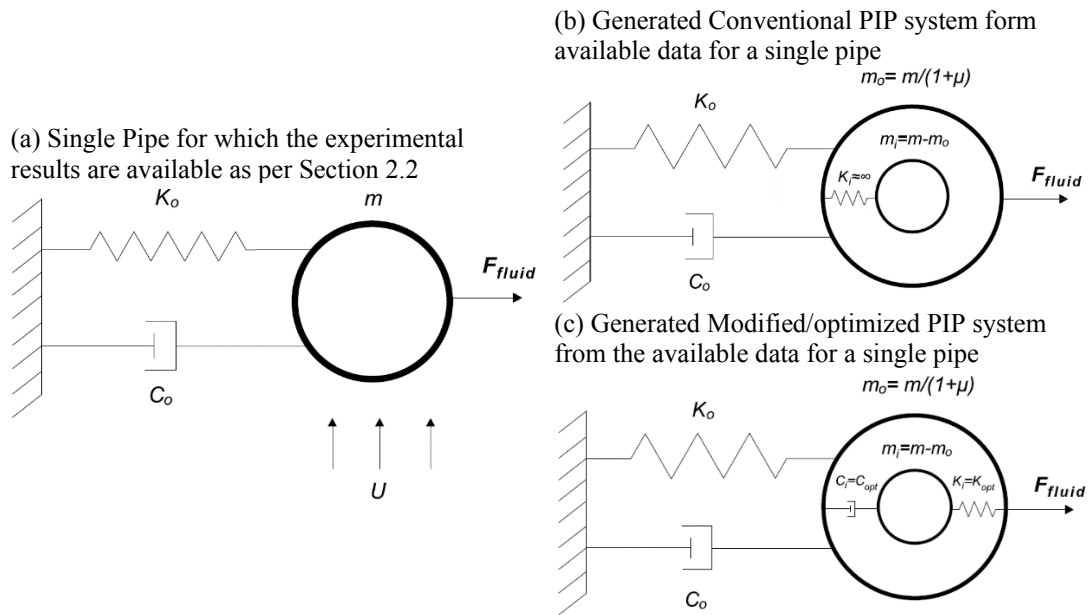
$R$ -square, which reflects the reliability of the curve fitting ( $R = 1$  means accurate estimation of the values), reach 0.999 and 0.995, respectively in the present study.

## 2.4 Effectiveness of Optimized PIP System to Mitigate VIV of Cylindrical Structures

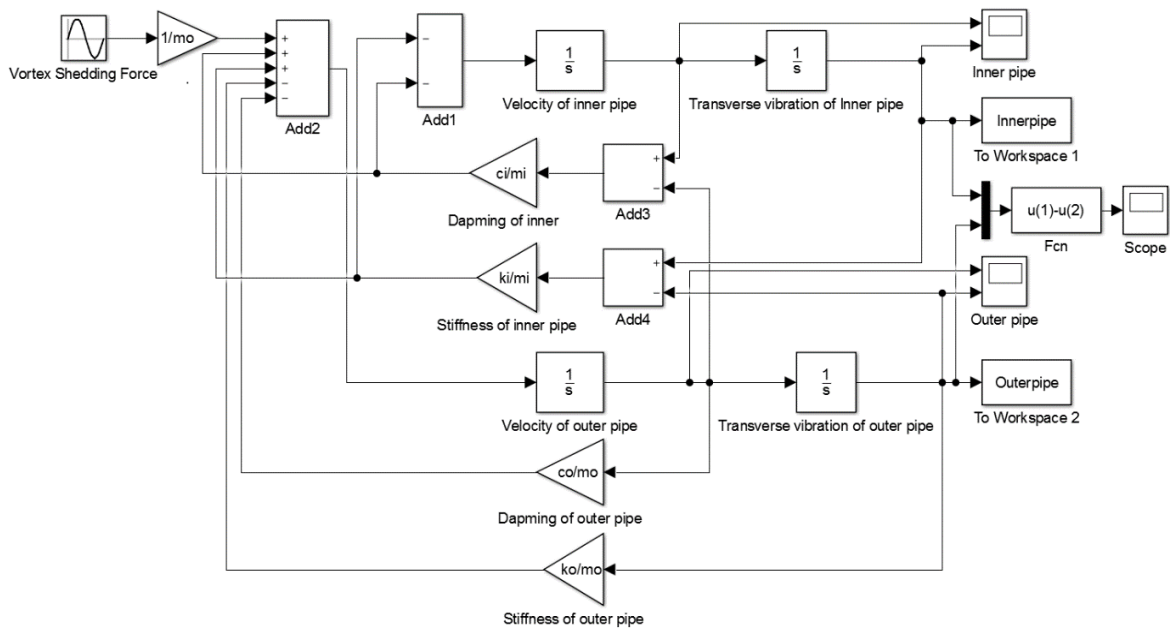
This section investigates the effectiveness of using modified PIP system to mitigate VIV. The cylindrical structure tested in [Rahman \(2015\)](#) is adopted again. However, the single pipe in the test is divided into two pipes in order to form a PIP system. For these two systems, the total mass of the pipe(s) is kept the same. For example, if the mass of the single pipe is  $m$ , the masses of the outer and inner pipes can be determined by the mass ratio as  $m_o = m/(1 + \mu)$  and  $m_i = m - m_o$ . As discussed before, the mass ratio of a PIP system can be quite large and without losing generality, a mass ratio of  $\mu = 0.8$  and  $\zeta_o = 0.031$  are assumed in the present study to demonstrate the effectiveness of the proposed design. It should be noted that by dividing a single pipe into two, the thicknesses of each pipe becomes smaller, which may cause certain problems in real applications. For example, the thinner external pipe may not be enough to withstand the external hydrostatic pressure when it is submerged. However, the purpose of this paper is to investigate the effectiveness of the proposed concept, therefore, such problems are not considered in the present study.

Figure 2-11(a) shows the single pipe tested in [Rahman \(2015\)](#). Figure 2-11(b) and (c) show the modified PIP systems. A very stiff spring ( $k_i \simeq \infty$ ) is used to connect the inner and outer pipes in Figure 2-11(b). These two pipes will therefore vibrate together when they are subjected to VIV and this system actually becomes the same as that of Figure 2-11(a). In Figure 2-11(c), the optimal spring and dashpot are used to connect the inner and outer pipes. Relative displacement is allowed between the inner and outer pipes and this system can be simplified as a structure-TMD system as mentioned above. In the present study, the optimal tuning frequency and damping ratio can be estimated as  $f^{opt} = 0.65$  and  $\zeta_i^{opt} = 0.35$  according to Equations (2-17) and (2-18).

The equation of motion of the proposed PIP system (a two-DoF system) has been derived in Section 2.3 and can be represented by Equation (2-7). To solve this equation, a time-domain Simulink model is developed in MATLAB again and shown in Figure 2-12. To validate this model, the vibration of the system shown in Figure 2-11(b) is calculated and compared with those obtained in Figure 2-4 (the red curves). Exactly same results are obtained. The accuracy of this Simulink model is therefore validated and it is applied to calculate the PIP response shown Figure 2-11(c). It should be noted that the same CF values as shown in Figure 2-2 are used for different pipe systems.



**Figure 2-11:** Different pipe models under VIV: (a) A single pipe as presented in section 2.2 (b) a PIP system connected by a very rigid spring and (c) a modified PIP system with the optimized parameters.



**Figure 2-12:** The dynamic Simulink model for a modified PIP system under VIV.

Figure 2-13 compares the normalized crossflow fluctuations of the single pipe and the optimized PIP systems. The dark curves are the results obtained from the single pipe model and the red curves are from the optimized PIP system. Figure 2-13 clearly shows that with the optimized PIP system, the vibration induced by vortex shedding can be significantly suppressed within all the considered reduced velocities. In other words, this system is not sensitive to the frequency of excitation. This is because the mass ratio of this PIP system is quite large, and it is not sensitive to the external vibration

sources as discussed in Section 2.3.3. It should be mentioned that for PIP system, similar to single pipe, reduced velocity is defined as  $U_r = U/f_n D$ .

Table 2-4 tabulates the maximum amplitudes for different systems and the corresponding reduction ratios. It can be seen that the maximum reduction ratio can reach 87% when the aspect ratio is 13. Aspect ratio seems only slightly influence the control efficiency. For the investigated cases the reduction ratios are more or less the same with an average value about 84%.

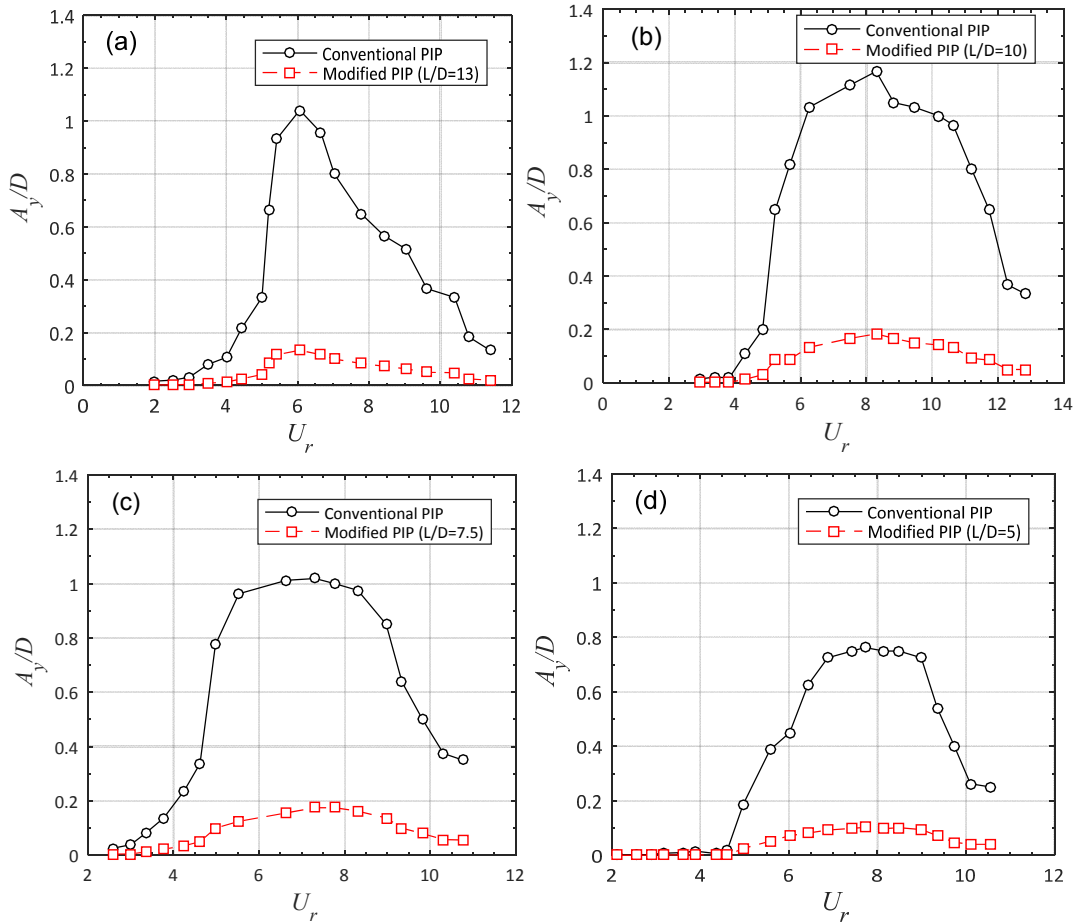


**Figure 2-13:** Comparisons of normalized transverse vibration amplitudes of a single pipe system with the optimized PIP system. (a)  $L/D = 13$ ; (b)  $L/D = 10$ ; (c)  $L/D = 7.5$ ; (d)  $L/D = 5$ .

**Table 2-4:** Peak normalized amplitudes of the single pipe model and the optimized PIP system under VIV and the corresponding suppression ratio.

Aspect ratio ( $L/D$ )	Single pipe	Optimized PIP	Suppression ratio
13	1.04	0.13	87%
10	1.17	0.18	84%
7.5	1.02	0.17	82%
5	0.76	0.10	86%

## 2.5 Possible Practical Design Options

In this paper, analytical studies are carried out to examine the effectiveness of using PIP system to mitigate VIV. The connecting device is crucial for the design and it is



simplified as a spring and dashpot in the present study. In engineering practical, polyurethane foam (PUF) or rotational friction hinge device with spring (RFHDS) as suggested by [Bi and Hao \(2016\)](#) might be the options to provide the required stiffness and damping of the connecting device. Further experimental studies will be carried out in the next step to find the most appropriate option.

## 2.6 Conclusion

This paper proposes using modified PIP system to mitigate vortex induced vibrations of cylindrical offshore components such as risers and deep sea pipelines. The effectiveness of the proposed method is investigated through analytical solutions by simplifying the system as a structure-TMD system. The equation of motion of the PIP system is derived and implemented into the MATLAB/Simulink code and validated by the experimental data. The optimal parameters for the connecting spring and dashpot are calculated and explicit formulae for these parameters are derived. Analytical results show that VIV can be significantly suppressed by the proposed PIP system and this system is not sensitive to the external excitation frequency contents and variations of the mass ratio. This system is believed having great application potentials to control VIV of offshore cylindrical components.

## 2.7 References

- Allen, D. (2003). Performance characteristics of short fairings. Offshore Technology Conference, Houston, Texas, USA, 1-9.
- Alrsai, M., Karampour, H. (2016). Propagation Buckling of Pipe-in-Pipe Systems, an Experimental Study. The 20th ISOPE Pacific/Asia Offshore Mechanics Symposium, Gold Coast, Australia, 408-413.
- Anh, N.D., Nguyen, N.X. (2013). Design of TMD for damped linear structures using the dual criterion of equivalent linearization method. *International Journal of Mechanical Sciences*, 77, 164-170.
- Assi, G.R.S., Bearman, P.W., Kitney, N. (2009). Low drag solutions for suppressing vortex-induced vibration of circular cylinders. *Journal of Fluids and Structures*, 25 (4), 666-675.
- Azmi, A.M., Zhou, T., Cheng, L., Wang, H., Chua, L.P. (2012). On the effectiveness and mechanism of vortex-induced vibration suppression using a screen cylinder. The 22nd International Offshore and Polar Engineering Conference, Rhodes, Greece, 586-594.
- Bai, Y., Bai, Q. (2005). Subsea pipelines and risers. *Elsevier*.
- Bai, Y., Bai, Q. (2012). Subsea engineering handbook. *Gulf Professional Publishing*, USA.
- Bakre, S., Jangid, R. (2007). Optimum parameters of tuned mass damper for damped main system. *Structural Control and Health Monitoring*, 14 (3), 448-470.
- Bekdaş, G., Nigdeli, S.M. (2011). Estimating optimum parameters of tuned mass dampers using harmony search. *Engineering Structures*, 33 (9), 2716-2723.

- Bernitsas, M.M., Raghavan, K. (2014). Reduction of vortex induced forces and motion through surface roughness control. *Google Patents*.
- Bi, K., Hao, H. (2016). Using pipe-in-pipe systems for subsea pipeline vibration control. *Engineering Structures*, 109, 75-84.
- Choi, H., Jeon, W.P., Kim, J. (2008). Control of flow over a bluff body, Annual review of fluid mechanics. *Annual Reviews*, Palo Alto, 113-139.
- Dinh, V.N., Basu, B. (2015). Passive control of floating offshore wind turbine nacelle and spar vibrations by multiple tuned mass dampers. *Structural Control and Health Monitoring*, 22 (1), 152-176.
- Facchinetti, M.L., De Langre, E., Biolley, F. (2004). Coupling of structure and wake oscillators in vortex-induced vibrations. *Journal of Fluids and Structures*, 19 (2), 123-140.
- Farshidianfar, A., Zanganeh, H. (2010). A modified wake oscillator model for vortex-induced vibration of circular cylinders for a wide range of mass-damping ratio. *Journal of Fluids and Structures*, 26 (3), 430-441.
- Gabbai, R., Benaroya, H. (2005). An overview of modeling and experiments of vortex-induced vibration of circular cylinders. *Journal of Sound and Vibration*, 282 (3), 575-616.
- Gad-el-Hak, M. (2000). Flow control: passive, active and reactive flow management. *Cambridge Univ. Press*, UK.
- Gao, Y., Fu, S., Wang, J., Song, L., Chen, Y. (2015). Experimental study of the effects of surface roughness on the vortex-induced vibration response of a flexible cylinder. *Ocean Engineering*, 103, 40-54.
- Gao, Y., Yang, J., Xiong, Y., Wang, M., Peng, G. (2016). Experimental investigation of the effects of the coverage of helical strakes on the vortex-induced vibration response of a flexible riser. *Applied Ocean Research*, 59, 53-64.
- Goswami, I., Scanlan, R.H., Jones, N.P. (1993). Vortex-induced vibration of circular cylinders. II: new model. *Journal of Engineering Mechanics*, 119 (11), 2288-2302.
- Gouda, B. (1975). Some measurements of the phenomena of vortex shedding and induced vibrations of circular cylinder. *Technische Universitat Berlin Report DLR-FB*, 75-01.
- Gutierrez Soto, M., Adeli, H. (2013). Tuned mass dampers. *Archives of Computational Methods in Engineering*, 20 (4), 419-431.
- Hoang, N., Fujino, Y., Warnitchai, P. (2008). Optimal tuned mass damper for seismic applications and practical design formulas. *Engineering Structures*, 30 (3), 707-715.
- ISO. (2015). 19901-1: 2015, Petroleum and natural gas industries-specific requirements for offshore structures-Part 1: Metocean design and operating conditions. *British Standards Institute*.
- Khorasanchi, M., Huang, S. (2014). Instability analysis of deepwater riser with fairings. *Ocean Engineering*, 79, 26-34.
- Kiu, K.Y., Stappenbelt, B., Thiagarajan, K.P. (2011). Effects of uniform surface roughness on vortex-induced vibration of towed vertical cylinders. *Journal of Sound and Vibration*, 330 (20), 4753-4763.
- Kumar, R.A., Sohn, C.-H., Gowda, B.H. (2008). Passive control of vortex-induced vibrations: an overview. *Recent Patents on Mechanical Engineering*, 1 (1), 1-11.
- Kyriakides, S. (2002). Buckle propagation in pipe-in-pipe systems.: Part I. Experiments. *International Journal of Solids and Structures*, 39 (2), 351-366.

- Nakamura, T., Kaneko, S., Inada, F., Kato, M., Ishihara, K., Nishihara, T., Mureithi, N.W., Langthjem, M.A. (2013). Flow-induced vibrations: classifications and lessons from practical experiences. *Butterworth-Heinemann*.
- Norberg, C. (1994). An experimental investigation of the flow around a circular cylinder: influence of aspect ratio. *Journal of Fluid Mechanics*, 258, 287-316.
- Owen, J.C., Bearman, P.W., Szewczyk, A.A. (2001). Passive control of VIV with drag reduction. *Journal of Fluids and Structures*, 15 (3), 597-605.
- Park, H., Bernitsas, M.M., Ajith Kumar, R. (2012). Selective roughness in the boundary layer to suppress flow-induced motions of circular cylinder at  $30,000 < \text{Re} < 120,000$ . *Journal of Offshore Mechanics and Arctic Engineering*, 134 (4), 041801-041801.
- Raghavan, A.K., Chan-Hyun, S., Bangalore, H.L.G. (2008). Passive control of vortex-induced vibrations: an overview. *Recent Patents on Mechanical Engineering*, 1 (1), 1-11.
- Rahman, M.A. (2015). Vortex-induced vibration of circular cylindrical structure with different aspect ratios. *University of Western Australia*, Department of Mechanical Engineering, PhD Thesis.
- Rahman, M.A., Thiagarajan, K. (2013). Vortex-induced vibration of cylindrical structure with different aspect ratio. The 23th International Offshore and Polar Engineering Conference, Anchorage, Alaska, USA, 395-401.
- Rahman, M.A.A., Leggoe, J., Thiagarajan, K., Mohd, M.H., Paik, J.K. (2016). Numerical simulations of vortex-induced vibrations on vertical cylindrical structure with different aspect ratios. *Ships and Offshore Structures*, 11 (4), 405-423.
- Rashidi, S., Hayatdavoodi, M., Esfahani, J.A. (2016). Vortex shedding suppression and wake control: A review. *Ocean Engineering*, 126, 57-80.
- Reggio, A., Angelis, M.D. (2015). Optimal energy-based seismic design of non-conventional Tuned Mass Damper (TMD) implemented via inter-story isolation. *Earthquake Engineering & Structural Dynamics*, 44 (10), 1623-1642.
- Saint-Marcoux, J.-F. (2014). Recent trends and future of ultra deepwater oil fields. The 24th International Ocean and Polar Engineering Conference, Busan, Korea, 1-8.
- Salvi, J., Rizzi, E. (2015). Optimum tuning of Tuned Mass Dampers for frame structures under earthquake excitation. *Structural Control and Health Monitoring*, 22 (4), 707-725.
- Sarpkaya, T. (2004). A critical review of the intrinsic nature of vortex-induced vibrations. *Journal of Fluids and Structures*, 19 (4), 389-447.
- Song, L., Fu, S., Cao, J., Ma, L., Wu, J. (2016). An investigation into the hydrodynamics of a flexible riser undergoing vortex-induced vibration. *Journal of Fluids and Structures*, 63, 325-350.
- Szepessy, S., Bearman, P. (1992). Aspect ratio and end plate effects on vortex shedding from a circular cylinder. *Journal of Fluid Mechanics*, 234, 191-217.
- Veritas, N. (2000). Environmental conditions and environmental loads. *Det Norske Veritas*.
- Wang, Z., Chen, Z., Liu, H. (2015). Numerical study on upheaval buckling of pipe-in-pipe systems with full contact imperfections. *Engineering Structures*, 99, 264-271.
- Williamson, C.H.K., Govardhan, R.N. (2004). Vortex-induced vibrations. *Annu. Rev. Fluid Mech.*, 36, 413-455.
- Williamson, C.H.K., Govardhan, R.N. (2008). A brief review of recent results in vortex-induced vibrations. *Journal of Wind Engineering and Industrial Aerodynamics*, 96 (6-7), 713-735.

Zeinoddini, M., Farhangmehr, A., Seif, M.S., Zandi, A.P. (2015). Cross-flow vortex induced vibrations of inclined helically straked circular cylinders: An experimental study. *Journal of Fluids and Structures*, 59, 178-201.

Zhao, M., Cheng, L. (2010). Finite element analysis of flow control using porous media. *Ocean Engineering*, 37 (14-15), 1357-1366.

Zheng, J., Palmer, A., Brunning, P., Gan, C.T. (2014). Indentation and external pressure on subsea single wall pipe and pipe-in-pipe. *Ocean Engineering*, 83, 125-132.

Zhou, T., Razali, S.F.M., Hao, Z., Cheng, L. (2011). On the study of vortex-induced vibration of a cylinder with helical strakes. *Journal of Fluids and Structures*, 27 (7), 903-917.

Zhu, H., Yao, J. (2015). Numerical evaluation of passive control of VIV by small control rods. *Applied Ocean Research*, 51, 93-116.

# Chapter 3 Effectiveness of using pipe-in-pipe (PIP) concept to reduce vortex-induced vibrations (VIV): three-dimensional two-way FSI analysis

Journal of Ocean Engineering. Vol. 148, Pages 263-276, [10.1016/j.oceaneng.2017.11.040](https://doi.org/10.1016/j.oceaneng.2017.11.040).

---

## ABSTRACT

Pipe-in-pipe (PIP) systems have been increasingly used in offshore applications because of their favourable thermal insulation capacity. Very recently, the conventional PIP system was slightly revised by using carefully designed springs and dashpots to connect the inner and outer pipes. This revised PIP system can be considered as a structure-Tuned Mass Damper (TMD) system. It therefore has the potential to mitigate the offshore structural vibrations induced by various sources such as earthquake excitation and/or vortex shedding. This paper carries out three-dimensional (3-D) numerical simulations to investigate the effectiveness of the proposed method. The crossflow oscillation of the conventional and optimized PIP systems are numerically investigated by developing a two-way coupled Fluid-Structure Interaction (FSI) framework for computational fluid dynamics (CFD) analysis. The developed FSI model is validated with the available experimental and numerical benchmark data on a single cylinder. This validated model is then extended to the PIP system to study its efficiency for Vortex-Induced Vibration (VIV) suppression. Numerical results show that the optimized PIP system can noticeably reduce VIV.

## 3.1 Introduction

When a circular cylinder is placed in a fluid flow, vortex shedding may result in vibrations to the cylinder, and this is known as the vortex-induced vibration (VIV). VIV has been widely recognized as the cause of the damage of many engineering structures such as subsea pipelines, marine risers, anchoring lines, spar buoys and bridge cables. Extensive research works have been conducted to address VIV due to its significance ([Bearman, 2011](#), [Oruç, 2017](#)).

To mitigate the adverse effects of VIV, several vibration control techniques have been proposed. These techniques can be broadly divided into two subgroups: the passive

and active control methods. Active control requires external power to operate, which imposes challenges in real engineering practices especially in the offshore environment, where providing complex actuators as well as excessive power would be problematic and costly. Passive control devices, on the other hand, require no external power, are relatively less expensive and easier to install. Hence, for marine structures, various passive control techniques have been widely introduced to suppress VIV ([Rashidi et al., 2016](#)). These devices include for example the helical strake ([Holland et al., 2017](#), [Senga and Larsen, 2017](#)), fairing ([Assi et al., 2014](#), [Yu et al., 2015](#)), dart-like overlay ([Zhu et al., 2016](#)), splitter plates and C-shaped foil ([Soumya and Prakash, 2017](#), [Law and Jaiman, 2017](#)), controlling rods ([Song et al., 2017](#)), attached plate ([Ozkan et al., 2017](#)), screen shroud ([Cicolin and Assi, 2017](#)) and Surface Roughness Control (SRC) techniques ([Bernitsas and Raghavan, 2014](#)). However, it should be noted that although some of these devices have been applied in engineering practices, certain drawbacks exist which may considerably affect their performances especially when they are located in the deep and ultra-deep waters. For example, helical strake and splitter plates usually impose an additional hydrodynamic drag force to the structure; shrouds and axial slats are expensive to manufacture, not easy to install, susceptible to marine growth and prone to storm damage. It is therefore important to develop more efficient, cost effective and practical passive control devices to effectively control VIV of offshore cylindrical structures ([Oruç, 2017](#)).

Pipe-in-pipe (PIP) systems are becoming more and more widely used especially in the deep and ultra-deep waters ([Karampour et al., 2017](#)). A conventional PIP system is comprised of an internal insulated pipe (the product pipe) and an outer pipe (the sleeve pipe). The inner pipe is used to carry the product flow and the outer pipe provides mechanical protection against the high external hydrostatic pressure. Centralizers, normally made of hard polymeric rings, are clamped on the inner pipe with certain spacing to ensure the concentric positions of the two pipes ([Bai and Bai, 2012](#)). Instead of using the hard polymeric centralizers, [Bi and Hao \(2016b\)](#) proposed a modified system by using specially designed connecting devices between the inner and outer pipes. The modified PIP system then forms a structure-Tuned Mass Damper (TMD) system with the outer pipe acting as the primary structure and the inner pipe performing as the TMD. It therefore has the potential to mitigate the pipeline vibrations induced by various sources. [Bi and Hao \(2016b\)](#) carried out numerical simulations to investigate the effectiveness of using this concept to mitigate seismic induced

vibrations of subsea pipeline with free spans. Numerical results show that both the vibrations of the inner and outer pipes can be significantly reduced by using this method. Very recently, [Matin Nikoo et al. \(2017\)](#) used this design concept for VIV control and analytical studies were carried out to examine the effectiveness of the proposed method by simplifying the system as a two-degree-of-freedom (2-DOF) system. Analytical results demonstrate that the modified PIP system can significantly suppress the VIV of offshore cylindrical structures.

This paper is an extension of the recent work carried out by the authors ([Matin Nikoo et al., 2017](#)). In this paper, a two-way coupled Fluid-Structure Interaction (FSI) framework is developed and detailed three dimensional (3-D) numerical simulations are carried out to further investigate the effectiveness of the proposed system for VIV control. Compared to the analytical study, the fluid-pipe interaction can be more realistically simulated and the 3-D vortices around the cylinder can be readily captured. The paper is organized as follows: The two-way Fluid-Structure Interaction (FSI) method and the governing equations of the fluid and structure are presented in Section 3.2; in Section 3.3, VIV response of a single pipe is modelled and validated by a series of experimental and numerical benchmark data in the literature; the validated model is then extended to the optimized PIP system in Section 3.4 and the effectiveness of the proposed method to control flow-induced oscillations is investigated in Section 3.5; and finally some conclusions are drawn in Section 3.6.

### **3.2 Method of Solution, Computational Approach and Governing Equations**

A set of non-dimensional parameters will be used in the analysis of a single cylinder and PIP system subjected to VIV. For readers' easy reference, these parameters are defined in Table 3-1, in which the mass ratio  $m^*$  is defined as the ratio of the cylinder mass ( $m$ ) to the displaced mass of the fluid with kinematic viscosity of  $\nu$ ;  $\rho$  denotes the density of the fluid,  $D$  the cylinder diameter, and  $L$  the spanwise cylinder length;  $U$  stands for the fluid flow velocity,  $f$  and  $f_n$  are the oscillation and natural frequency of the cylinder in the air respectively,  $f_s$  is the Strouhal frequency and  $y_{max}$  is the maximum transverse displacement of the cylinder;  $m_i, m_o$  and  $\omega_i, \omega_o$  are the mass and vibrating frequencies of the inner and outer pipes, respectively.

**Table 3-1:** Non-dimensional parameters associated with the vibrations of a cylinder and PIP system induced by vortex shedding.

Mass ratio	$m^*$	$\frac{m}{\pi\rho D^2 L/4}$
Normalized (reduced) velocity	$U^*$	$\frac{U}{f_n D}$
Transversal response amplitude	$A^*$	$\frac{y_{max}}{D}$
Frequency ratio	$f^*$	$\frac{f}{f_n}$
Reynolds number	$R_e$	$\frac{UD}{\nu}$
Aspect ratio	-	$\frac{L}{D}$
Strouhal number	$S_t$	$\frac{f_s D}{U}$
TMD-Mass ratio	$\mu$	$\frac{m_i}{m_o}$
TMD-Frequency ratio	$f_{tmd}$	$\frac{\omega_i}{\omega_o}$
Normalized time	$t^*$	$\frac{tU}{D}$

### 3.2.1 Two-way Fluid-Structure Interaction (FSI)

VIV phenomenon is a multi-physics problem where the responses of the structure and flow field are both time-dependent and they interact with each other, i.e., it is, in essence, a fluid-structure interaction (FSI) problem. In this study, a coupled fluid-structure model is developed through a two-way algorithm by coupling the ANSYS Mechanical and FLUENT finite volume solvers together ([ANSYS®, 2016](#)). In this algorithm, in each time step, the fluid equations (Section 3.2.2.2) are solved and the hydrodynamic loads are transferred to the mechanical model and applied as the input loads on the cylinder. Within the same time step, the structural dynamics equation (Section 3.2.3) is then solved and the calculated cylinder motion is transferred back to the fluid, which subsequently affects the mesh grids of the fluid. To calculate the displacements of the fluid mesh, the smoothing dynamic grid motion is used based on the diffusion equation ([Zhao and Cheng, 2011](#)):

$$\nabla \cdot (\gamma \nabla \vec{u}) = 0 \quad (3-1)$$

where  $\nabla$  is the differential operator,  $\vec{u}$  denotes the mesh displacement velocity, and  $\gamma$  is the diffusion coefficient, which describes how the boundary motion diffuses into the interior of the deforming mesh. With a constant  $\gamma$ , boundary motion diffuses uniformly throughout the grids domain, while with a non-uniform coefficient, nodes with high



diffusivity tend to move together. In the present study, a non-uniform diffusion coefficient is adopted as a function of the normalized cell volume size  $V$  as follows:

$$\gamma = \frac{1}{V^\alpha} \quad (3-2)$$

in which  $\alpha$  is the diffusion parameter. A value between the range of 0 and 2 has been shown to be practical ([Han et al., 2015](#)), and it is set as 1.5 in the present study. With this value, the grids in the immediate vicinity of the cylinder wall moves rigidly with the cylinder, i.e., the uniformity of the near wall mesh resolution is preserved and the outermost grids are kept fixed. Mesh deformation takes place in the region in between. This area is given sufficient space so that fair mesh quality can be ensured even in the case with large VIV amplitude.

### 3.2.2 Fluid flow model

#### 3.2.2.1 Turbulent and sub-grid scale (SGS) models

Various numerical approaches such as the direct numerical simulation (DNS), large-eddy simulation (LES) and Reynolds-Averaged Navier-Stokes (RANS) methods have been proposed to simulate the fluid field for the VIV problem ([Al-Jamal and Dalton, 2004](#)). In the DNS technique, Navier-Stokes equations with entire range of spatial and temporal properties of the turbulence are directly solved without any approximation from the smallest energy dissipative scales to the largest kinetic energy carrying scales. DNS solution requires extremely fine, fully 3-D meshes and therefore enormous amount of computational time. To save computing resources, turbulent fluctuations of flow quantities are not solved in the RANS approach. This approach is therefore incapable of accurately predicting the boundary layer transition to turbulence. LES method has received extensive attention recently ([Yang, 2015](#)). The rationale behind the LES technique is a separation between the large and small scales turbulence motions. In this method, large scale turbulence motions of the flow containing most of the kinetic energy, momentum and scalar transport are solved explicitly, whereas the effect of the small scales is modelled using a sub-grid scale (SGS) model. Thus, LES has the potential of being more accurate than RANS simulations ([Catalano et al., 2003](#)) but less time consuming than the DNS approach. In this study, LES method is used to model the turbulent flow around the cylinder.

To get a full solution for LES method, various SGS models such as the conventional algebraic Smagorinsky and dynamic Smagorinsky-Lilly models have been proposed

(Sagaut, 2006). Previous studies (e.g. Breuer (1998, 2000), Kim et al. (2015)) revealed that the dynamic Smagorinsky-Lilly model yields better solution. The dynamic Smagorinsky-Lilly model is therefore used to model the sub scale turbulent flow in the present study.

### 3.2.2.2 Governing equations

Some previous studies (e.g. Zhao et al. (2014)) indicated that the 2-D Navier-Stokes equations are not able to accurately predict the VIV in the turbulent/chaotic flow regime. To more realistically simulate the VIV responses, a detailed 3-D model is adopted in the present study and the 3-D turbulent fluid flow around the cylinder is modelled by solving the incompressible Navier-Stokes equations in conjunction with the LES technique and dynamic Smagorinsky-Lilly SGS model.

Applying the filtering process to the incompressible Navier-Stokes using the space-dependent volume filter function ( $G(x, \bar{\Delta})$ ) gives the continuity and filtered momentum equations (Sagaut, 2006):

$$\frac{\partial \bar{u}_i}{\partial x_i} = 0, \quad (3-3)$$

$$\frac{\partial \bar{u}_i}{\partial t} + \frac{\partial \overline{u_i u_j}}{\partial x_j} = -\frac{1}{\rho} \frac{\partial \bar{p}}{\partial x_i} + \frac{\partial}{\partial x_j} \left[ \nu \left( \frac{\partial \bar{u}_i}{\partial x_j} + \frac{\partial \bar{u}_j}{\partial x_i} \right) \right] \quad (3-4)$$

where  $\bar{\Delta}$  denotes the grid filter width and it is often taken as the cube root of the grid cell volume, i.e.,  $\bar{\Delta} = \sqrt[3]{\Delta_i \Delta_j \Delta_k}$ . The scale that is larger than  $\bar{\Delta}$  is retained in the flow and will be solved directly, whereas the effects of scale smaller than  $\bar{\Delta}$  will be modelled by SGS.  $\bar{u}_i$  and  $\bar{u}_j$  ( $i, j \in [1, 2, 3]$ ) denote the filtered velocity components in the streamwise ( $x$ ), crossflow ( $y$ ) and spanwise ( $z$ ) directions, respectively.  $\bar{p}$  is the filtered pressure and  $\nu$  is the kinematic viscosity of the fluid. The term  $\overline{u_i u_j}$  can be written as follows:

$$\overline{u_i u_j} = \tau_{ij} + \bar{u}_i \bar{u}_j \quad (3-5)$$

where  $\tau_{ij}$  represents the non-resolvable SGS stress, which needs to be approximated to represent the effect of the unresolved SGS motion on the resolved grid scale motion. Therefore, Equation 3.4 becomes:

$$\frac{\partial \bar{u}_i}{\partial t} + \frac{\partial \overline{u_i u_j}}{\partial x_j} = -\frac{1}{\rho} \frac{\partial \bar{p}}{\partial x_i} + \frac{\partial}{\partial x_j} \left[ \nu \left( \frac{\partial \bar{u}_i}{\partial x_j} + \frac{\partial \bar{u}_j}{\partial x_i} \right) \right] - \frac{\partial \tau_{ij}}{\partial x_j} \quad (3-6)$$

by adopting a turbulent eddy viscosity ( $\nu_t$ ) and Boussinesq's approximations, SGS stress can be related to the resolved large-scale strain rate tensor  $\bar{S}_{ij}$ :

$$\tau_{ij} - \frac{1}{3}\delta_{ij}\tau_{kk} = -2\nu_t\bar{S}_{ij}, \quad \bar{S}_{ij} = \frac{1}{2}\left(\frac{\partial\bar{u}_i}{\partial\bar{x}_j} + \frac{\partial\bar{u}_j}{\partial\bar{x}_i}\right) \quad (3-7)$$

in which  $\delta_{ij}$  denotes the Kronecker delta,  $\delta_{ij} = 1$  if  $i = j$  and  $\delta_{ij} = 0$  when  $i \neq j$ . It is to ensure that normal stresses are taken as isotropic. Unlike the RANS modelling, where the eddy viscosity represents all turbulent scales, the SGS viscosity  $\nu_t$  only represents the small scales. In the conventional Smagorinsky model, the SGS viscosity can be expressed as ([Sagaut, 2006](#)):

$$\nu_t = (C_s\bar{\Delta})^2|\bar{S}| \quad (3-8)$$

where  $|\bar{S}|$  denotes the norm of the strain rate tensor and  $C_s$  is the Smagorinsky constant, which normally varies between 0.065 and 0.2. However, it should be noted that the Smagorinsky coefficient is not a universal constant and this may affect the accuracy of the results ([Sagaut, 2006](#)). Moreover, this model requires a damping function next to the solid wall boundary conditions because fluid viscosity dominates the turbulence as the wall is approached ([Atluri et al., 2009](#)). In order to overcome these drawbacks, dynamic Smagorinsky-Lilly method was introduced. In this method this coefficient is no longer a constant value, but is a dynamic, local and time-dependent variable determined based on the energy content of the smallest resolved scale. More detailed information regarding the calculation of the dynamic Smagorinsky constant  $C_s$  can be found in [Sagaut \(2006\)](#).

### 3.2.2.3 Computational fluid domain and boundary conditions

Figure 3-1(a) shows an elastically mounted rigid circular cylinder in a steady flow. Fluid domain dimension plays a critical role in the accuracy of VIV response calculation, especially for the case of a moving cylinder. To solve the governing equations presented in Section 3.2.2.2, a multi-block rectangular domain, as illustrated in Figure 3-1(b), (c) and (d), is adopted in the present study.

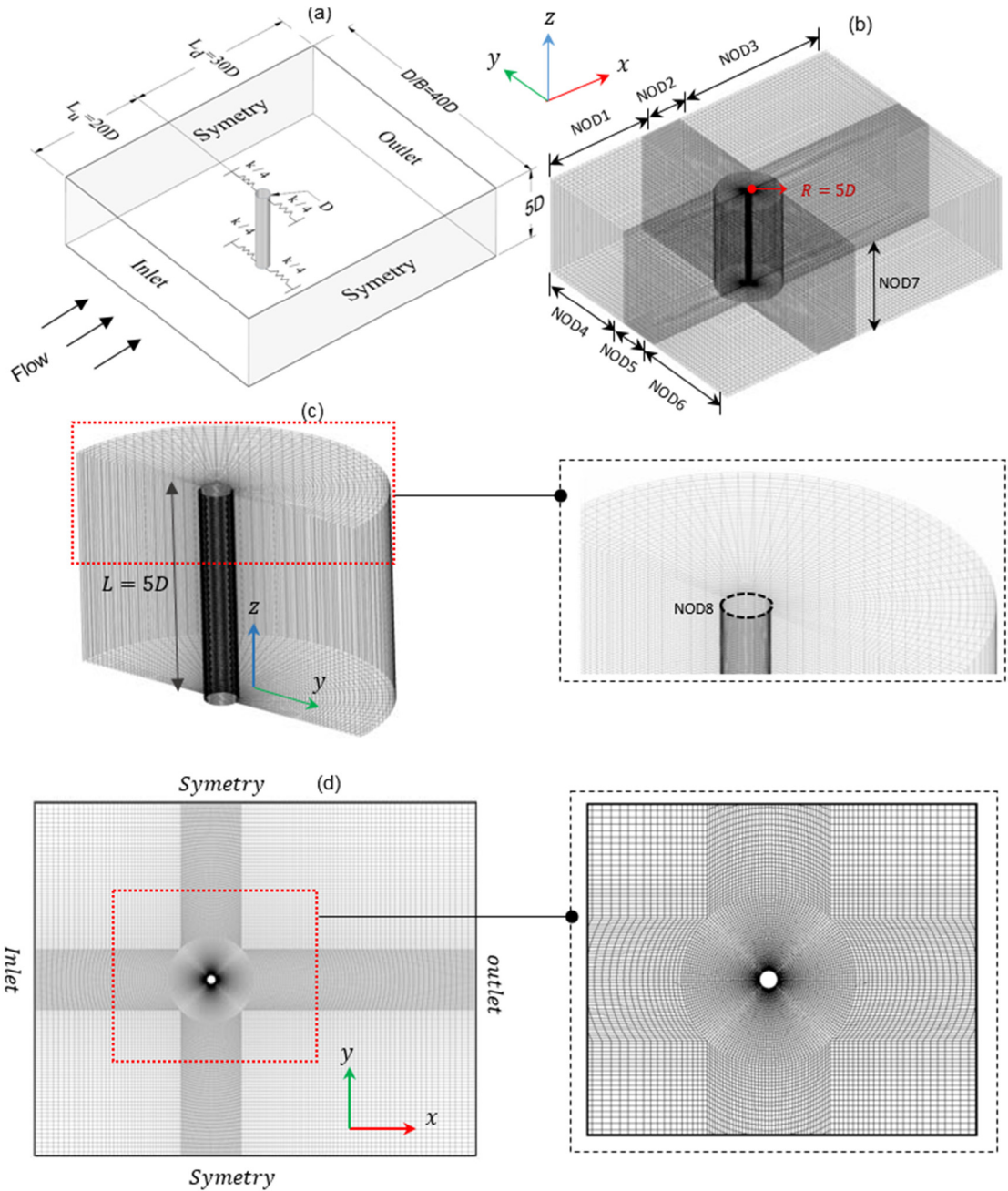


**Figure 3-1:** (a)&(b) 3-D Computational domain and corresponding mesh grids, (c) mesh around the cylinder and (d) mesh in the  $xy$ -plane and the corresponding boundary conditions.

A blockage factor  $B = 2.5\%$ , defined as the ratio of the cylinder diameter ( $D$ ) to the crossflow dimension of domain is considered ([Prasanth and Mittal, 2008](#)). A value of  $L/D = 5$  is adopted for the spanwise length of the fluid domain ([Zhao et al., 2014](#), [Yeon et al., 2016](#), [Law and Jaiman, 2017](#)).

As shown in Figure 3-1(b), a fine mesh is adopted for an annular sub-domain close to the cylinder, while larger meshes are generated when they are far away from the cylinder. The circular domain surrounding the cylinder (Figure 3-1(c)) is discretized with uniformly spaced grids in the azimuthal coordinate and exponentially stretched

in the radial direction. The remaining rectangular blocks are meshed with hexahedral elements. As shown in Figure 3-1(d), a steady uniform flow with a freestream velocity of  $u = u_\infty$  is specified at the inflow boundary in the positive  $x$ -direction. Transverse and spanwise velocity components are set as zero at the inlet boundary ( $v = w = 0$ ). For the top, bottom and two lateral boundaries of the domain, symmetry (free-slip) plane conditions are applied, i.e., the velocity component perpendicular to the boundary is zero. The zero-gradient condition for velocity is applied at the outlet boundary where the reference pressure is assigned to zero. On the test cylinder smooth surface, non-slip wall condition is specified, i.e., the fluid velocity on this surface is the same with the cylinder's displacement speed.

### 3.2.3 Structural Dynamics Model

In the developed FSI model, the cylinder is suspended by the body-ground type springs at the two spanwise boundary surfaces. Remote displacement constraints are assigned for these two boundaries, which allows cylinder to vibrate only in the crossflow direction ( $y$ ). It should be noted that this simplification ignores the flow-induced in-line oscillations of the cylinder. This is a reasonable simplification since as indicated by many researchers (e.g. [Bearman \(1984\)](#)) the in-line oscillations are not excited noticeably when the Reynolds number  $R_e$  is smaller than 1200. In the present study, a  $R_e=1000$  is adopted in the numerical simulation as will be discussed in Section 3.3.1. This simplification is actually widely adopted by many other researchers (e.g. [Zhao et al. \(2014\)](#), [Zhang et al. \(2017a\)](#)). Outer surface of the cylinder is set to be a FSI interface, on which required model quantities can transfer during the transient analysis. Figure 3-2 shows the generated computational mesh grids for the single pipe. To achieve a fully-mapped data transfer between two components, the solid part (cylinder) is discretized by the same mesh grids on the fluid-solid interface. To encourage the maximum amplitude oscillations, the structural damping coefficient is assumed as zero ([Zhao et al., 2014](#), [Zhang et al., 2017a](#)).

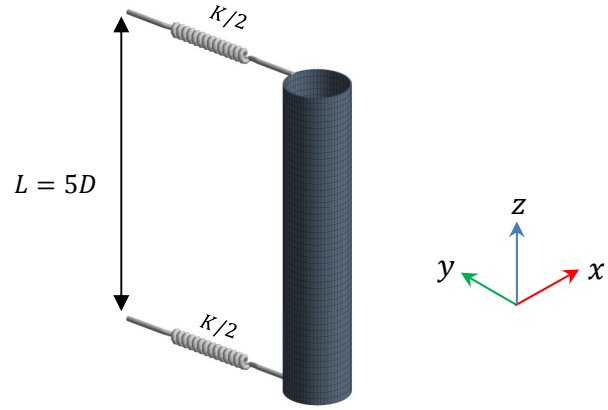


**Figure 3-2:** Mesh grids for the solid part (a single cylinder) of FSI simulation.

The crossflow equation of motion of an elastically mounted rigid cylinder subjected to VIV can be expressed as follows:

$$[M]\{\ddot{y}\} + [C]\{\dot{y}\} + [K]\{y\} = F_L(t) \quad (3-9)$$

where  $[M]$ ,  $[C]$  and  $[K]$  are the mass, damping and stiffness matrix respectively.  $\{y\}$  is the crossflow displacement vector and the over dot denotes differentiation with respect to time  $t$ .  $F_L(t)$  represents the total lift force vector in the crossflow direction of the cylinder and can be calculated by integrating the pressure and wall shear forces over the whole cylinder surface.

### 3.3 FSI Model of a Single Cylinder

To verify of the developed FSI model, results from previous experiments and 3-D numerical models for a single cylinder are adopted as benchmarks in the present study. The numerical results calculated based on the developed FSI model are compared with these benchmark results.

#### 3.3.1 Simulation setup

In the present study, the mass ratio ( $m^*$  in Table 3-1) is assumed as 2 as adopted in many previous studies ([Zhao and Cheng, 2014](#), [Gsell et al., 2016](#)). A moderate Reynolds number  $Re = 1000$  is selected in the numerical simulation. This value is chosen because: (i) it allows numerical simulations to be conducted at affordable computational time without compromising the accuracy of the results while the three-dimensionality of the turbulent fluid flow can develop sufficiently ([Lei et al., 2001](#)) and (ii) this value is in the range of subcritical Reynolds numbers ( $300 < Re < 1.5 \times 10^5$ ) where the wake flow is in the turbulent regime, in which nearly all real-life offshore and marine structures lie ([Sumer, 2006](#)). Semi-Implicit Method for Pressure-Linked Equations (SIMPLE) is used to derive the pressure-velocity coupling on mesh

grids and the equation for pressure correction (Tu et al., 2018). A second-order central-differencing interpolation scheme is used for the convection term. This scheme provides improved accuracy for LES. The time step of all simulations is 0.02s. 8 coupling steps with 30 FLUENT sub-iterations for each coupling step are used to achieve the accurate convergence of the results.

### 3.3.2 Mesh dependency study

In order to ensure that the numerical results are independent of the adopted mesh size, mesh convergence tests are carried out. Four different meshes as tabulated in Table 3-2 are investigated. In this table, the number of division (NOD) stands for the number of nodes seeding on each edge of the domain (see Figure 3-1(b)). Figure 3-3 and Figure 3-4 show the comparisons of the normalized amplitude time history and associated spectra VIV responses of the cylinder under the reduced velocity of  $U^* = 4.2$  with different mesh sizes. The calculated Strouhal number ( $S_t$ ), root mean square lift coefficient ( $C_L^{rms}$ ) and normalized amplitude ( $A^*$ ) are also tabulated in Table 3-2. It can be seen that coarse-1 and coarse-2 meshes lead to obvious differences in the results while the medium mesh size can result in similar results compared to the dense mesh, which means the results obtained from the medium mesh size are converged. The medium mesh size is therefore adopted in the numerical simulations in the present study.

**Table 3-2:** Mesh convergence testing results.

	NOD1	NOD2	NOD3	NOD4	NOD5	NOD6	NOD7	NOD8	N <sub>element</sub>	$S_t$	$C_L^{rms}$	$A^*$
Coarse-1	25	30	35	25	30	25	25	40	250,500	0.2	0.76	0.63
Coarse-2	30	35	40	30	35	30	30	50	413,700	0.2	0.80	0.73
Medium	40	45	50	40	45	40	40	60	925,200	0.2	0.94	0.80
Dense	45	50	55	45	50	45	45	60	1,291,500	0.2	0.98	0.81

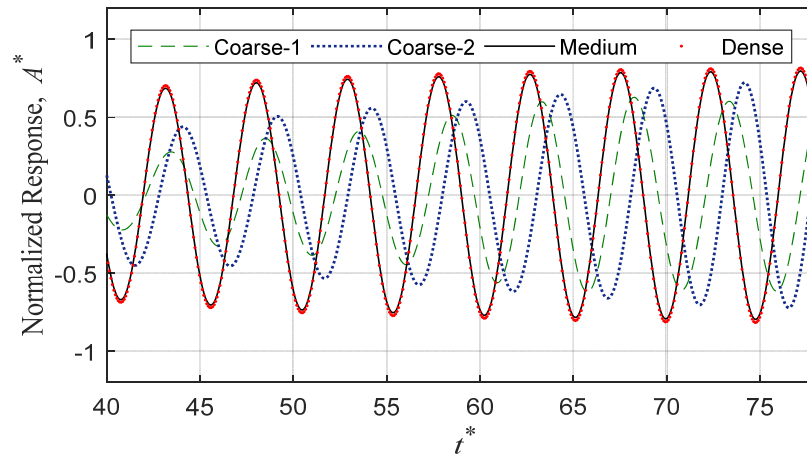


**Figure 3-3:** Time histories of normalized amplitude responses ( $A^*$ ) with different meshes ( $U^* = 4.2$ ).

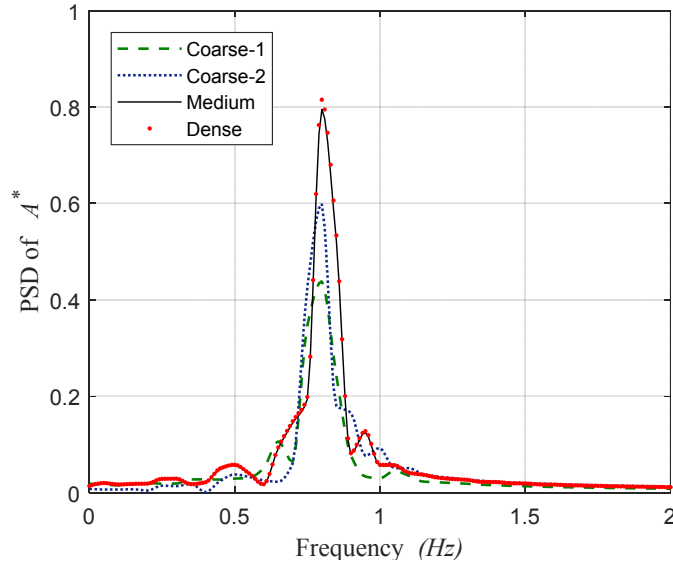


**Figure 3-4:** Power spectral density (PSD) of the normalized amplitude responses ( $A^*$ ) with different meshes ( $U^* = 4.2$ ).

### 3.3.3 Model validation

To validate the developed numerical model, the obtained results are compared with previous experimental and 3-D numerical benchmark measurements/results as mentioned above. Table 3-3 summarizes the adopted previous studies and the corresponding parameters.

**Table 3-3:** Adopted previous studies for model validation.

	Method of Study	$Re$	$m^*$	$A^*$
<a href="#">Khalak and Williamson (1997)</a>	Experimental	2000-12000	2.4	0.97
<a href="#">Assi et al. (2006)</a>	Experimental	3000-13000	$\sim 2$	0.90
<a href="#">Kiu et al. (2011)</a>	Experimental	Subcritical regime ( $1.7 - 8.3 \times 10^4$ )	2.36	0.96
<a href="#">Lucor et al. (2005)</a>	DNS	1000	2	0.78
<a href="#">Zhao et al. (2014)</a>	DNS	1000	2	0.72

It is commonly known that three typical amplitude response branches are associated with the VIV responses of an elastically mounted cylinder with low mass ratio ([Williamson and Govardhan, 2004](#)). For the low normalized velocities, there exists an “initial” branch where two single vortices shed per cycle (2S vortex shedding mode) and the mean forces and cylinder response are in phase. For the intermediate and large normalized velocities there is an “upper” and a “lower” branch associated with two pairs of vortices shed per cycle (2P vortex shedding mode). Figure 3-5 shows the normalized amplitude and frequency responses at different reduced velocities obtained in the present study and from the literature. For fair comparison, some efforts are made to convert the reduced velocities based on the natural frequency in the water to those based on the structural natural frequency in the air as adopted by [Zhao et al. \(2014\)](#).



As shown in Figure 3-5(a), the maximum normalized amplitude ( $A_{max}^*$ ) in the upper branch ( $U^*$  around 4 to 6) obtained from the current numerical model (0.79) is slightly lower than the experimental data (see  $A^*$  in Table 3-3). This is mainly because of the differences in the mass ratios and Reynolds numbers and, less significantly, the difference in the end conditions of the experimental tests ([Khalak and Williamson, 1999](#), [Al-Jamal and Dalton, 2004](#)). [Lucor et al. \(2005\)](#) and [Zhao et al. \(2014\)](#) carried out 3-D numerical simulations with the same mass ratio and Reynolds number as adopted in the present study. Figure 3-5(a) and Table 3-3 show that their results (0.78 and 0.72 respectively) are in good agreements with that obtained in the present study. For the results in the lower branch ( $\sim U^* > 7$ ), the normalized amplitude responses obtained from the experimental studies and numerical simulations show some fluctuations, which indicates that vortex induced motions of the bluff body is a highly nonlinear resonant response and different experimental set-ups and numerical assumptions can lead to slightly different results. Figure 3-5(b) shows the normalized frequency responses ( $f^*$ ) with respect to different reduced velocities. As shown the results obtained from the present study match well with other studies.

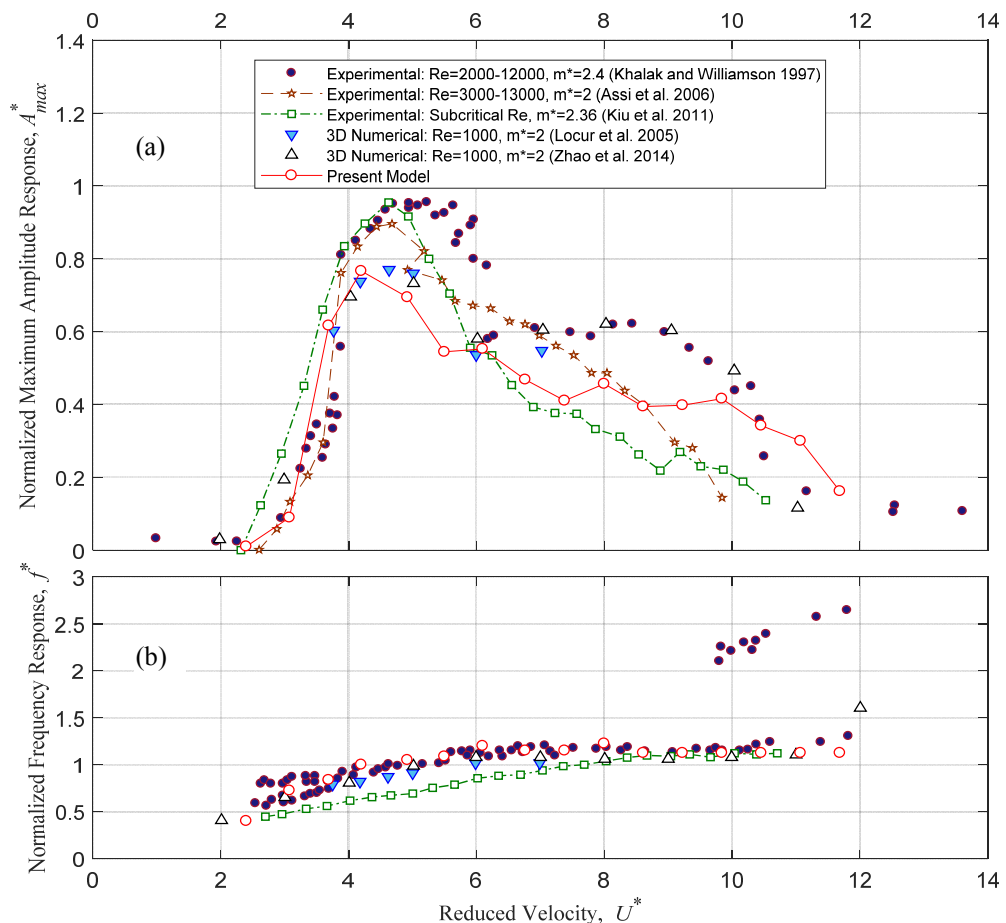


**Figure 3-5:** FSI model validation (a) normalized amplitude and (b) normalized frequency.

To further check the accuracy of the FSI model, the phase relation between the normalized response ( $A^*$ ) and the lift coefficient ( $C_L$ ) are studied. As shown in Figure 3-6(a), at the initial branch with normalized velocity  $U^* = 3.1$ , 2S wake mode with two dominant single vortices shed alternately per cycle, and the cylinder vibration is in-phase with the lift coefficient. Figure 3-6(b) shows that when the reduced velocity reaches  $U^* = 4.9$  (in the upper branch), the phase relation between vibration and lift coefficient remains the same, while the wake mode switches to 2P vortex pattern consisting of two pairs of vortices shed from two sides of the cylinder per cycle. As the reduced velocity continues to increase, the VIV responses of the body transits into the lower branch. At this branch (Figure 3-6(c)), the wake mode remains 2P, a phase lag between the crossflow displacement and lift coefficient is, however, obtained. These VIV response characteristics captured in the present study are in consistent with previous experimental measurements ([Khalak and Williamson, 1997](#), [1999](#)), which again reflects the accuracy of the FSI model. Figure 3-6 also shows that the wake vortex shedding along the spanwise of the cylinder are different. This variation cannot be captured by the commonly used 2-D models, which implies the importance of 3-D numerical modelling for the bluff-body fluid dynamics.

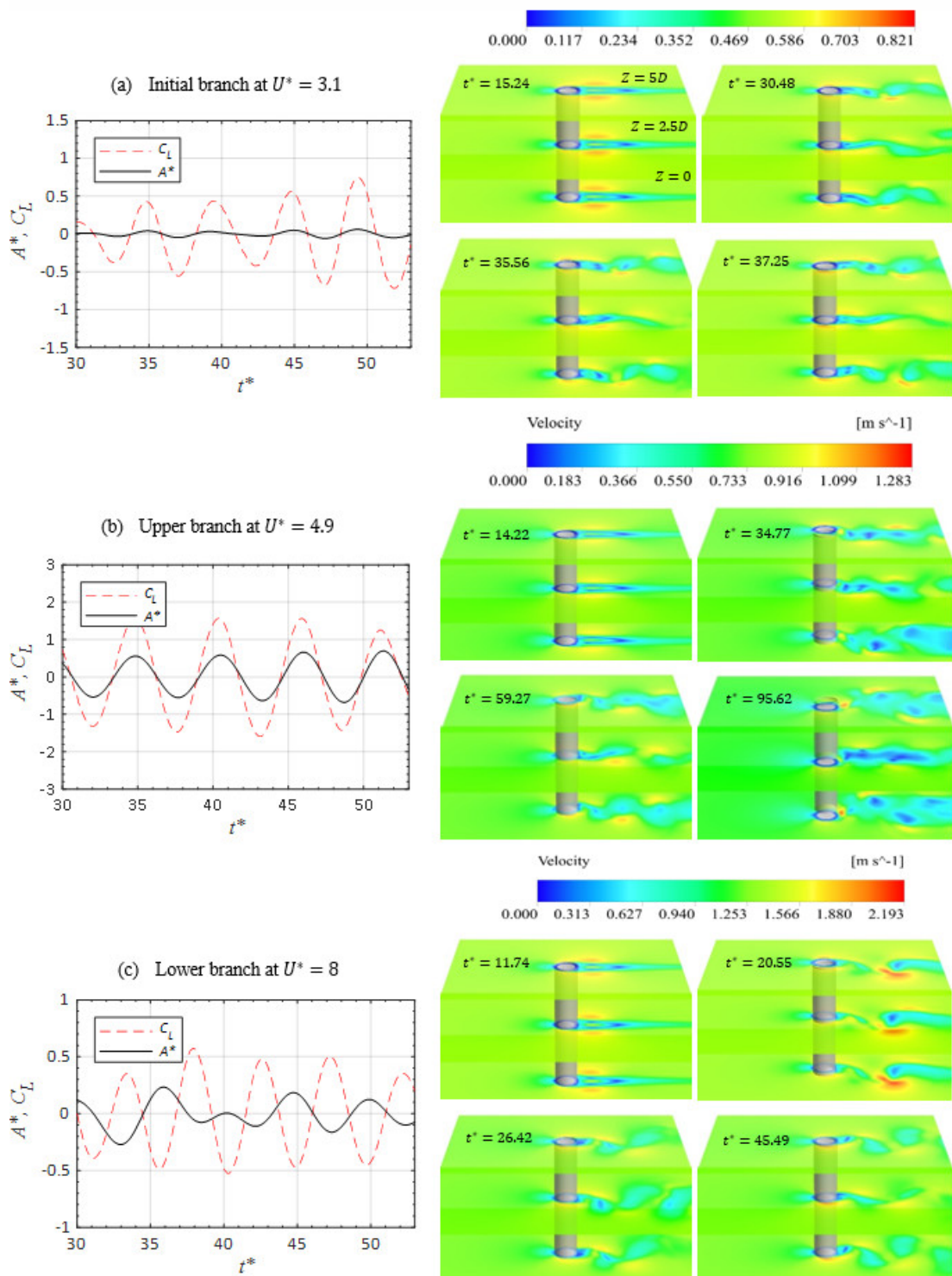


**Figure 3-6:** Time histories of normalized amplitude response ( $A^*$ ), lift coefficient ( $C_L$ ) and associated spanwise velocity contours at different VIV branches: (a) initial branch (b) upper branch and (c) lower branch.

### 3.4 Modified PIP System

The authors proposed the concept of using modified PIP system to control VIV of offshore cylindrical components and analytical studies were carried out to examine the effectiveness of the proposed method (Matin Nikoo et al., 2017). In the modified PIP

system, the hard polymeric centralizers are replaced by various possible connections such as the polyurethane foam (PUF), viscoelastic material or rotational friction hinge device with spring (RFHDS) ([Bi and Hao, 2016b, 2016a](#)). By carefully selecting the parameters of these connection devices (optimization), the system can then be simplified as a structure-TMD system and has the potential for VIV suppression. It should be noted that the mass ratio between the inner and outer pipes in the revised PIP system is normally much larger (e.g. it reached 85.3% in [Bi and Hao \(2016b\)](#)) than that in the conventional TMD system (generally 1% to a few percent), the modified PIP system can be regarded as a non-conventional TMD system. For a non-conventional TMD system, its effectiveness for vibration control becomes less sensitive to the optimized parameters, i.e., the system is still effective for VIV suppression though the parameters of the connecting devices (stiffness and damping) vary obviously from the optimized values. This property makes the selection of connecting devices easy.

In the analytical study ([Matin Nikoo et al., 2017](#)), the fluid-induced vibration of a single pipe (Figure 3-7(a)) was firstly investigated and the equation of motion of the system was solved and validated by the experimental data. The single pipe system was then extended to the revised PIP system by keeping the total masses of the PIP system and single pipe the same. The dynamic behavior of the PIP system under the excitation of vortex shedding was then simplified as a two-degree-of-freedom (2DOF) system. Two connections were considered by [Matin Nikoo et al. \(2017\)](#), the first connection was that the inner and outer pipes are rigidly connected (Figure 3-7(b)), i.e., a rigid spring with an infinite stiffness is adopted to connect the inner and outer pipes. With this connection, the two pipes can vibrate together. This connection can approximately simulate the behaviour of the conventional PIP system since in the conventional PIP system, only a very small gap (normally 5mm) is reserved between the centralizer and the external pipe and the two pipes can almost vibrate together ([Bi and Hao, 2016b](#)). In the second scenario, the optimized connecting devices were used and they were represented by the optimized springs and dashpots (Figure 3-7(c)).

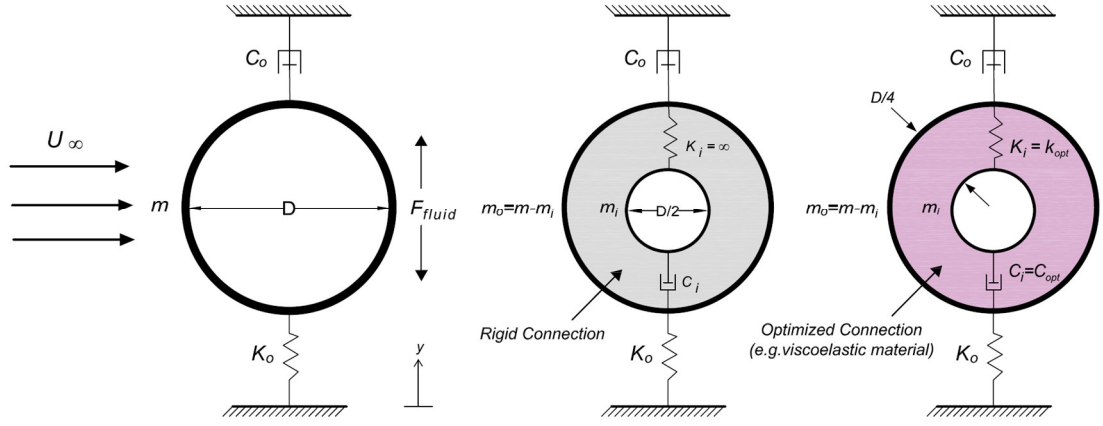


**Figure 3-7:** Different pipe models: (a) a single cylinder (b) a PIP system connected by rigid spring ( $k_i = \infty$ ) and dashpot (c) a modified PIP system with the optimized parameters

[Matin Nikoo et al. \(2017\)](#) derived the formulas for the optimized parameters:

$$f_{tmd}^{opt} = 1.10 - 0.48\sqrt{\mu} - 0.06\sqrt{\zeta_o} \quad (3-10)$$

$$\zeta_i^{opt} = 0.10 \ln(\mu) + 0.37 \quad (3-11)$$

in which  $f_{tmd}^{opt}$  is the optimal frequency ratio,  $\zeta_i^{opt}$  is the optimized damping ratio,  $\mu = m_i/m_o$  is the mass ratio between the inner pipe and outer pipe, and  $\zeta_o$  is the damping ratio of the main system (the external pipe), which is assumed as zero in the present study as mentioned above. The optimal stiffness ( $K_{opt}$ ) and damping coefficient ( $C_{opt}$ ) in Figure 3-7(c) therefore can be calculated as:

$$K_{opt} = f_{tmd}^{opt2} \mu K_o \quad (3-12)$$

$$C_{opt} = 2\zeta_i^{opt} \sqrt{K_{opt}m_i} \quad (3-13)$$

In the present study, the same concept as adopted by [Matin Nikoo et al. \(2017\)](#) is used again, i.e., the single pipe is split into two pipes to make the total masses of the two systems the same, and the diameter of the inner pipe is assumed as half of the outer pipe based on a real project in the North sea ([Logstor, 1997](#)) as shown in Figure 3-7. Figure 3-8 shows the numerical model of the PIP system. The outer pipe is modelled exactly the same as that of the single pipe as discussed in Section 3.2.3. The inner pipe is meshed with the same numbers of elements in the circumferential and spanwise directions as the outer pipe. Combin14 elements are used to model the springs and dashpots that connect the inner and outer pipes. This element is a uniaxial tension-compression element with up to three degrees of freedom at each node, and the spring and damping capability of the element can realistically simulate the proposed

connection between the inner and outer pipes. No mass, bending or torsion is considered for these spring-damper elements and only the crossflow direction ( $y$ ) is set to free. The corresponding parameters ( $K_{opt}$  and  $C_{opt}$ ) are calculated based on Equations (3-12) and (3-13). It should be noted that the inner pipe and outer pipe may contact with each when the relative displacement between the inner and outer pipes is larger than the annulus size. To consider the possible contact in the numerical simulation, a pair-based contact approach is used between the outer surface of the inner pipe and the inner surface of the outer pipe. In this method, 3-D contact elements (CONTA174) are associated with the 3-D target segment elements (TARGE170). Contact occurs when the contact elements penetrate the associated target surface.

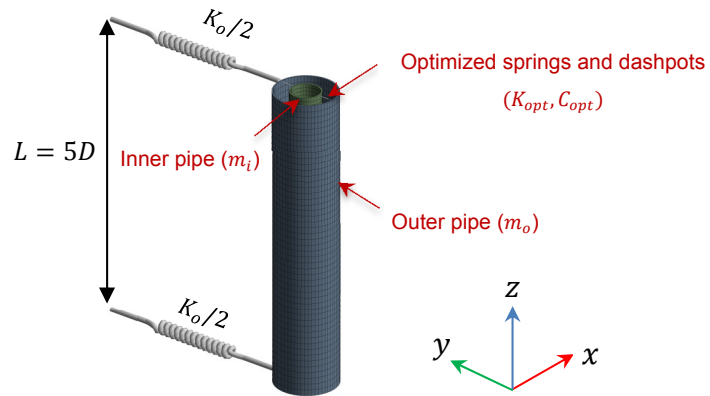


**Figure 3-8:** Finite element model of the PIP system in the 3-D FSI simulation.

### 3.5 Results and discussion

It is widely recognized that the oscillating amplitudes of a cylinder under VIV are significant within a certain reduced velocity range, this range is normally defined as the upper branch and/or the synchronization region. As shown in Figure 3-5(a), this reduced velocity range is about from 4 to 7 in this study. In the present study, numerical simulations are only carried out near the upper branch, and in particular four reduced velocities with  $U^* = 3.7, 4.2, 4.9$  and  $6.8$ , are considered. The responses of the revised PIP system under VIV are calculated. For comparison, the corresponding results for the single pipe are also calculated. It should be noted that with the conventional PIP design, the inner and outer pipes almost vibrate together ([Bi and Hao, 2016b](#)), which means the responses of the single pipe is almost the same as the conventional PIP system. In the numerical simulation, only the transverse motion is considered. The mass ratio between the inner pipe and outer pipe is assumed as 0.5. Figure 3-9 and Figure 3-10 compare the normalized oscillation displacements and the associated power spectral densities (PSDs) of the conventional (Figure 3-7(b) and

optimized PIP systems (Figure 3-7(c)). The dark curves are the results obtained from the conventional PIP model and the red curves are from the modified PIP system. The results show that the proposed concept is quite effective for the VIV suppression. The normalized displacements and corresponding PSDs obtained from the optimized PIP are evidently smaller than those obtained from the conventional PIP system. Two main reasons result in this effect: (i) the vortex formation at the wake of the primary cylinder is disorganized through the alteration of the rigid-body motion of the outer pipe and (ii) partial amount of input energy is transferred from the main structure (the outer pipe) to the tuned absorber (the inner pipe) and further dissipated by the inner pipe (the TMD effect). Figure 3-9 also shows that the system seems not quite effective at the beginning, this is because at the initial stage of the transient analysis the oscillating responses of the whole system are not fully developed, the relative displacement between the inner and outer pipes is therefore small and the function of the TMD cannot be fully developed.

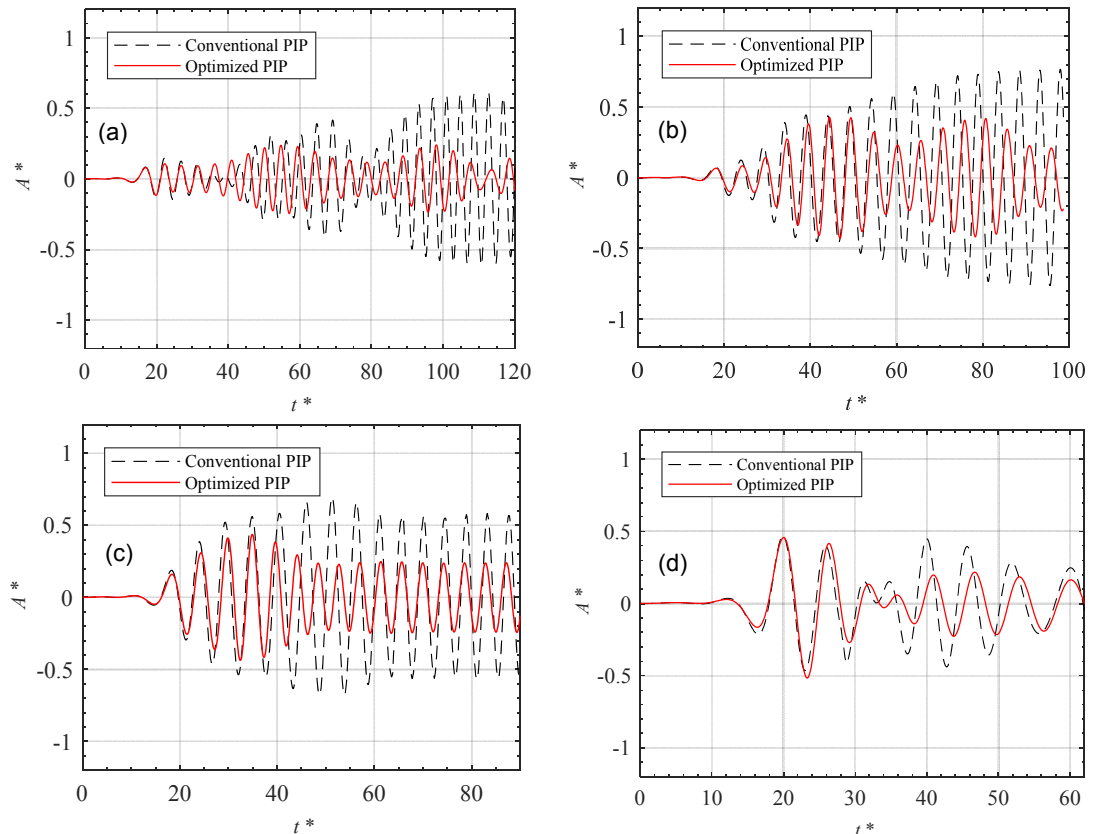


**Figure 3-9:** Normalized time histories of the oscillating displacement for the conventional and optimized PIP systems: (a)  $U^* = 3.7$ , (b)  $U^* = 4.2$ , (c)  $U^* = 4.9$  and (d)  $U^* = 6.8$ .

To more clearly show the effectiveness of the proposed system, Table 3-4 summarizes the root-mean-square (RMS) displacements of the traditional and optimized PIP systems during the whole calculation time. The corresponding reduction ratios are also

shown in the table. It can be seen that the reduction is obvious when  $U^* = 3.7, 4.2$  and  $4.9$  with the maximum reduction ratio reaching 56% at  $U^* = 3.7$ . When  $U^* = 6.8$ , the effectiveness is decreased as compared to the first three reduced velocities. As shown in Table 3-4, the reduction ratio of the displacement response at this reduced velocity ( $U^* = 6.8$ ) is 21%. This is because as shown in Figure 3-9, the vibration of the system is the smallest when  $U^* = 6.8$ , and the TMD function is less developed compared to the first three cases, which in turn results in the smallest reduction ratio. However, it should be noted that these results are obtained during the whole calculation time, if the reduction ratio is considered from the more evident development of the TMD function ( $t^* > \sim 30$  in the case of  $U^* = 6.8$ ), the reduction ratio reaches 41% for this case. On the other hand, the results also indicate that it does not necessarily mean the largest reduction ratio can be achieved when the vibration is the most violent. As shown in the table, the largest amplitude occurs when  $U^* = 4.2(0.37)$ , while the reduction ratio is the smallest (47%) in these three cases. This is mainly due to the fact that VIV responses of offshore cylindrical components (with low mass ratio) depend highly on the frequency of vortex shedding, the oscillating frequency of the cylinder and the added mass. All these vary in a rather non-linear fashion.

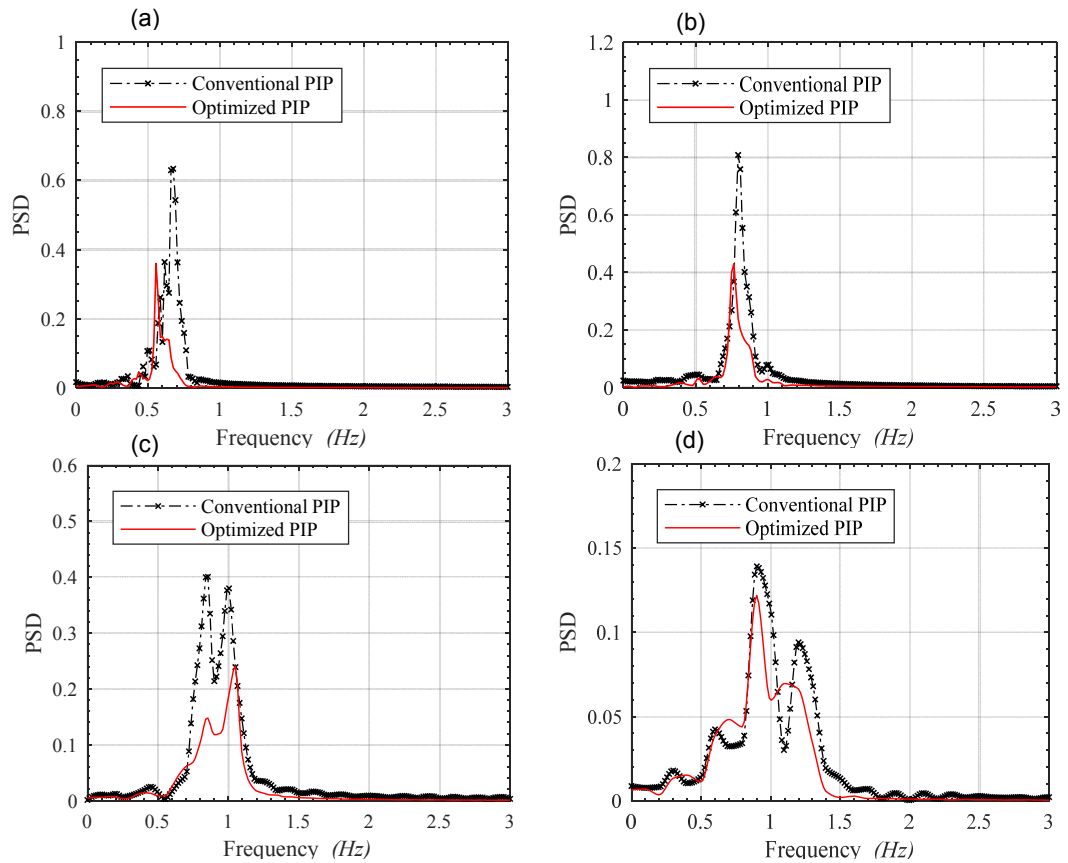


**Figure 3-10:** PSDs of the normalized oscillating displacement for the conventional and optimized PIP systems: (a)  $U^* = 3.7$ , (b)  $U^* = 4.2$ , (c)  $U^* = 4.9$  and (d)  $U^* = 6.8$ .



**Table 3-4:** RMS displacements of the traditional and optimized PIP systems and the corresponding reduction ratios.

$U^*$	Conventional PIP	Optimized PIP	Reduction ratio
	$A_{rms}^*$	$A_{rms}^*$	$A_{rms}^*$
3.7	0.266	0.116	56%
4.2	0.373	0.198	47%
4.9	0.359	0.185	48%
6.8	0.211	0.167	21%

As mentioned in Section 3.4, the inner and outer pipes may contact with each other if the vibration of the system is too violent. To address this issue, the normalized relative displacements between the outer and inner pipes ( $A_{relative}^*$ ) are calculated and shown in Figure 3-11. For comparison, the normalized annulus size (0.25) is also plotted in this figure by the red dash lines. The figure clearly shows that the inner pipe can oscillate freely in the outer pipe and no contact occurs in the present study. It should be noted that when contacts occurs, the control effectiveness can be slightly decreased ([Bi and Hao, 2016b](#)) due to the fact that the TMD function cannot be fully developed. To examine the influence of contact on the control effectiveness is an interesting topic but it is out of the scope of the present study.

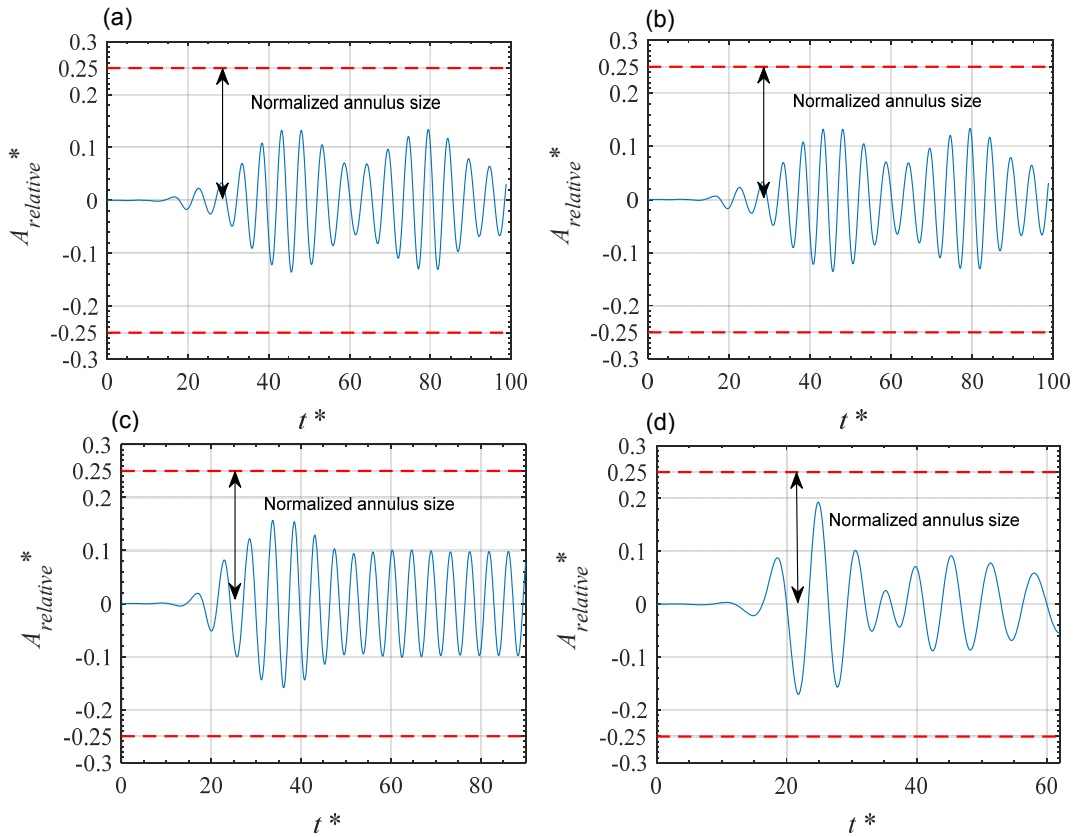


**Figure 3-11:** Normalized relative displacements between the outer and inner pipes when the PIP system is vibrating at (a)  $U^* = 3.7$ , (b)  $U^* = 4.2$ , (c)  $U^* = 4.9$  and (d)  $U^* = 6.8$ .

In the design of controlling devices for VIV suppression, it is desirable to reduce the amplitude of structural vibrations by having low lift and drag coefficients ([Dhanak and Xiros, 2016](#)). Figure 3-12 plots the lift and drag coefficients of the conventional and modified PIP systems at the reduced velocities of  $U^* = 3.7$  and 4.2. It can be seen that the optimized PIP system can obviously diminish the lift and drag coefficients at the wall of the structures. These results again clearly demonstrate the effectiveness of the proposed method for VIV suppression. Figure 3-12(b) and (d) also show that the drag coefficients of  $C_D < 1$  can be obtained in the numerical simulations, this is because of the beating phenomenon as reported by some other researchers (e.g. [Mittal \(2013\)](#), [Kim et al. \(2014\)](#)).

As discussed in Section 3.3.3, the phase relationships between the lift force and vibration amplitude are different in the three branches (initial, upper and lower branches) for a single cylinder. For the PIP system, no such investigation has been reported. Figure 3-13 shows the phase difference between the lift force coefficient and outer pipe displacement. It can be seen from Figure 3-13(a) that, similar to the single pipe, no phase difference is obtained between the displacement and lift force when  $U^* = 3.7$  (the initial state of upper branch). When  $U^* = 4.9$ , the phase relations between the single pipe and PIP system, however, becomes different. As shown in Figure 3-6(b) no obvious phase difference can be obtained in the single pipe case. However, in the PIP system, obvious phase differences are developed as shown in Figure 3-13(c). The results indicate that the PIP system can alter the phase relationships between the lift force and vibration amplitude compared to the single pipe system especially in higher reduced velocity range. This then further alters the structural responses.

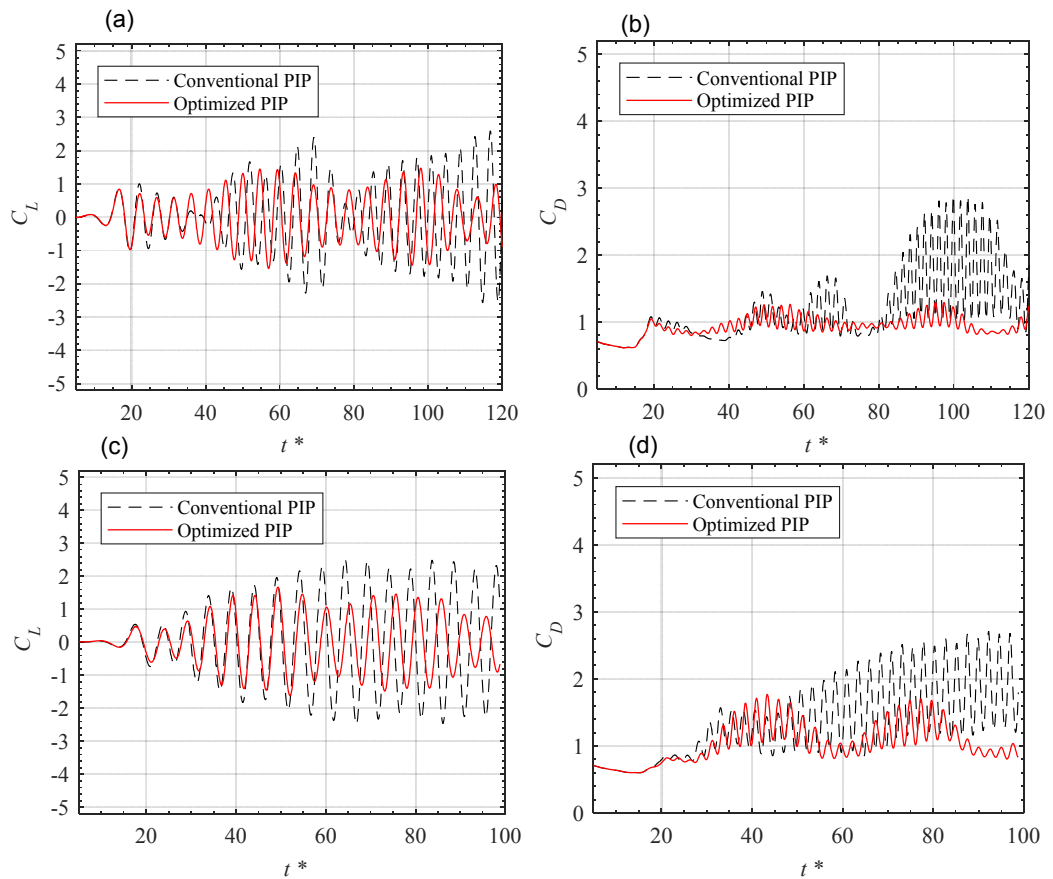


**Figure 3-12:** The influence of optimized PIP system on the lift and drag coefficients: (a) and (b)  $U^* = 3.7$  and (c) and (d)  $U^* = 4.2$ .

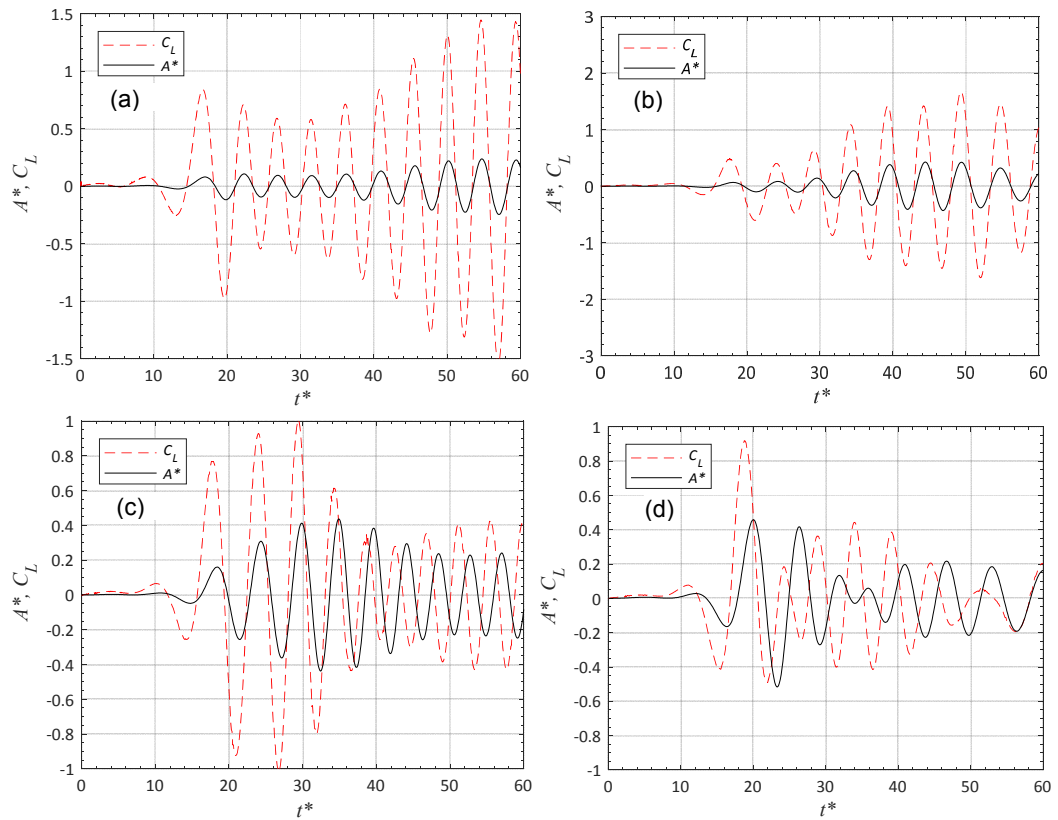


**Figure 3-13:** Phase relations between the outer pipe oscillation and driving lift force in the optimized PIP for (a)  $U^* = 3.7$ , (b)  $U^* = 4.2$ , (c)  $U^* = 4.9$  and (d)  $U^* = 6.8$ .

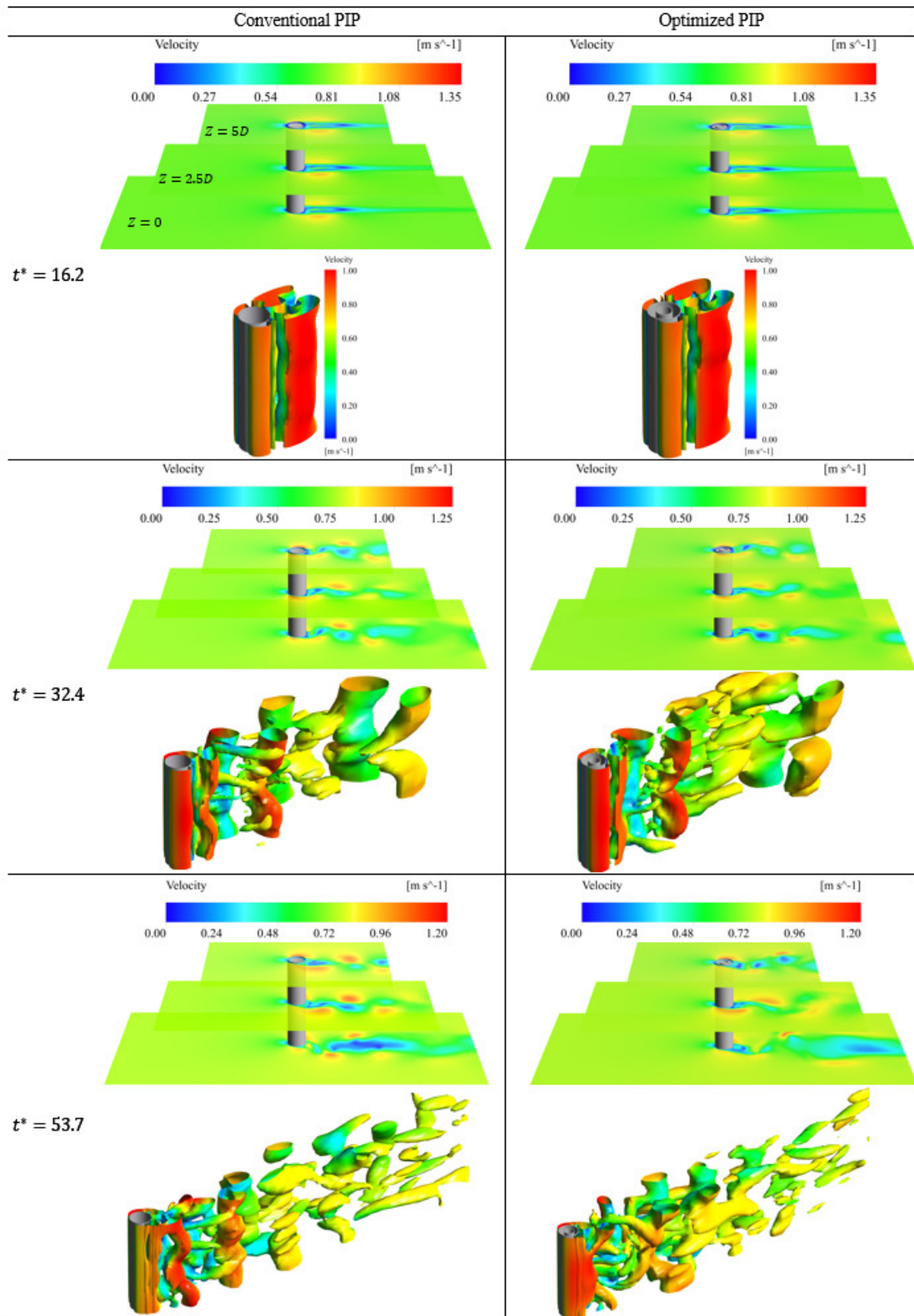


**Figure 3-14:**  $Q$  Iso-surfaces of the vortices street around the conventional and optimized PIP for  $U^* = 4.2$ .

The 3-D vortices around the cylinder can be captured by using the 3-D numerical model developed in the present study. Figure 3-14 shows the 3-D wake turbulence structures around the external pipe when  $U^* = 4.2$ , and the  $Q$  iso-surfaces obtained

based on the  $Q$ -criterion ([Hunt et al., 1988](#)) are plotted. This criterion is suitable for the identification of vortex in the incompressible fluid ([Zhang et al., 2017b](#)). It can be seen that the wake flow is totally three-dimensional for both systems and the application of the PIP can alter the wake vortices street compared to the single pipe. At the initial stage (e.g. for  $t^* = 16.2$ ), there is no significant difference between the wake topology of the conventional and optimized PIP systems. When time increases (e.g. for  $t^* = 32.4$  and  $53.7$ ), the wake patterns of the two systems, however, vary significantly. This is because the TMD effect is not developed at the initial stage, while it is activated when time goes by as discussed above, which further changes the pipe responses and the vortices street. To further identify how PIP system alters the mechanism of vortex shedding formation and the vibration of the cylinder, the 2-D wake topology formation and the transverse vibration of the conventional and optimized PIP systems at the middle surface ( $z = 2.5D$ ) are plotted in Figure 3-15. It can be seen that the PIP system can prevent the development of vortex shedding and cause a reduction in the width of the wake vortices street compared to the conventional PIP system, which has a direct influence on the drag force as indicated by [Law and Jaiman \(2017\)](#), and further suppresses the undesired vibrations of the cylinder.

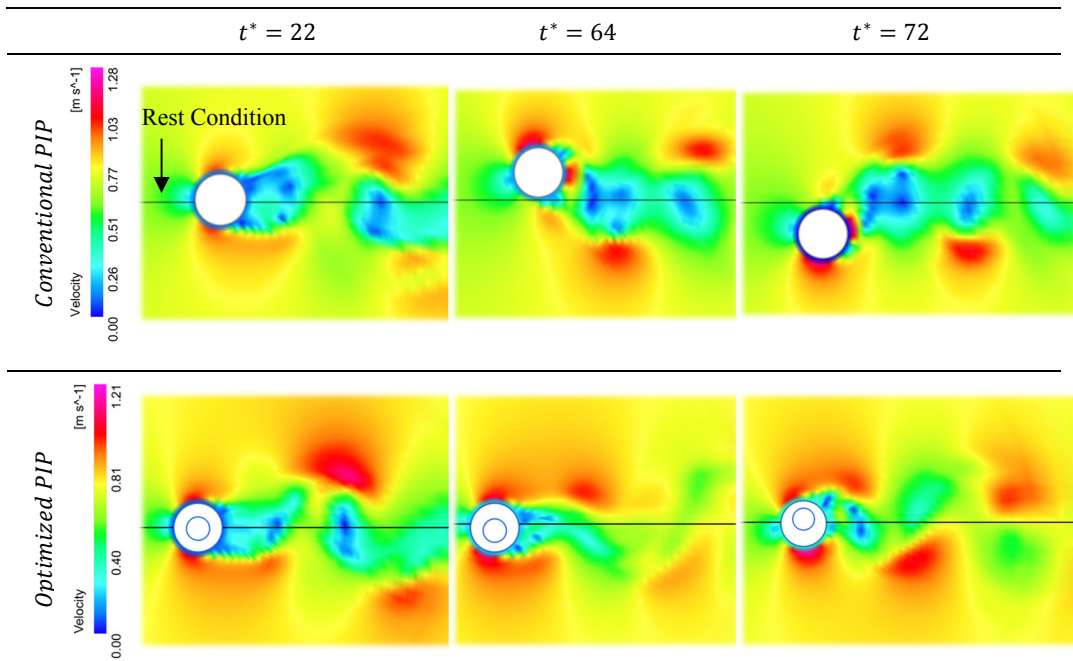


**Figure 3-15:** Contour of velocity around the conventional and optimized PIP at the middle surface ( $z = 2.5D$ ) of computational domain for  $U^* = 4.2$ .

### 3.6 Conclusion

This paper carries out 3-D numerical simulations on the effectiveness of using PIP system for VIV suppression of offshore cylindrical components. A coupled CFD-FSI framework is developed by coupling the ANSYS Mechanical and FLUENT finite volume solvers. The numerical model is firstly validated by the previous experimental and numerical results on a single cylinder. The validated model is then extended to the PIP system. Numerical results reveal that VIV can be significantly suppressed by using the optimized PIP system. The reduction is most evident in the upper reduced velocity range where the vibration of the system is most violent. The effectiveness is slightly decreased in the lower branch range. Moreover, comparing to the conventional PIP system, the optimized PIP system can obviously change the wake vortices formation and alter the phase lag between the lift force and vibration amplitude.

### 3.7 References

- Al-Jamal, H., Dalton, C. (2004). Vortex induced vibrations using large eddy simulation at a moderate Reynolds number. *Journal of Fluids and Structures*, 19 (1), 73-92.
- ANSYS®. (2016). Academic research, release 17.2, Theory guide.
- Assi, G.R.S., Bearman, P.W., Tognarelli, M.A. (2014). On the stability of a free-to-rotate short-tail fairing and a splitter plate as suppressors of vortex-induced vibration. *Ocean Engineering*, 92, 234-244.
- Assi, G.R.S., Meneghini, J.R., Aranha, J.A.P., Bearman, P.W., Casaprima, E. (2006). Experimental investigation of flow-induced vibration interference between two circular cylinders. *Journal of Fluids and Structures*, 22 (6), 819-827.
- Atluri, S., Rao, V., Dalton, C. (2009). A numerical investigation of the near-wake structure in the variable frequency forced oscillation of a circular cylinder. *Journal of Fluids and Structures*, 25 (2), 229-244.
- Bai, Y., Bai, Q. (2012). Subsea engineering handbook. *Gulf Professional Publishing*, USA.
- Bearman, P. (2011). Circular cylinder wakes and vortex-induced vibrations. *Journal of Fluids and Structures*, 27 (5), 648-658.
- Bearman, P.W. (1984). Vortex shedding from oscillating bluff bodies. *Annual review of fluid mechanics*, 16 (1), 195-222.
- Bernitsas, M.M., Raghavan, K. (2014). Reduction of vortex induced forces and motion through surface roughness control. *The University of Michigan, Ann Arbor, MI, USA*.
- Bi, K., Hao, H. (2016a). Numerical simulation on the effectiveness of using viscoelastic materials to mitigate seismic induced vibrations of above-ground pipelines. *Engineering Structures*, 123, 1-14.
- Bi, K., Hao, H. (2016b). Using pipe-in-pipe systems for subsea pipeline vibration control. *Engineering Structures*, 109, 75-84.
- Breuer, M. (1998). Numerical and modeling influences on large eddy simulations for the flow past a circular cylinder. *International Journal of Heat and Fluid Flow*, 19 (5), 512-521.

- Breuer, M. (2000). A challenging test case for large eddy simulation: high Reynolds number circular cylinder flow. *International Journal of Heat and Fluid Flow*, 21 (5), 648-654.
- Catalano, P., Wang, M., Iaccarino, G., Moin, P. (2003). Numerical simulation of the flow around a circular cylinder at high Reynolds numbers. *International Journal of Heat and Fluid Flow*, 24 (4), 463-469.
- Cicolin, M.M., Assi, G.R.S. (2017). Experiments with flexible shrouds to reduce the vortex-induced vibration of a cylinder with low mass and damping. *Applied Ocean Research*, 65, 290-301.
- Dhanak, M.R., Xiros, N.I. (2016). Springer handbook of ocean engineering. *Springer*, United States.
- Gsell, S., Bourguet, R., Braza, M. (2016). Two-degree-of-freedom vortex-induced vibrations of a circular cylinder at  $Re=3900$ . *Journal of Fluids and Structures*, 67, 156-172.
- Han, X., Lin, W., Tang, Y., Zhao, C., Sammut, K. (2015). Effects of natural frequency ratio on vortex-induced vibration of a cylindrical structure. *Computers & Fluids*, 110 (Supplement C), 62-76.
- Holland, V., Tezdogan, T., Oguz, E. (2017). Full-scale CFD investigations of helical strakes as a means of reducing the vortex induced forces on a semi-submersible. *Ocean Engineering*, 137, 338-351.
- Hunt, J.C., Wray, A.A., Moin, P. (1988). Eddies, streams, and convergence zones in turbulent flows, Center for Turbulence Research Report, 198-208.
- Karampour, H., Alrsai, M., Albermani, F., Guan, H., Jeng, D.-S. (2017). Propagation Buckling in Subsea Pipe-in-Pipe Systems. *Journal of Engineering Mechanics*, 143 (9), 04017113.
- Khalak, A., Williamson, C.H.K. (1997). Fluid forces and dynamics of a hydroelastic structure with very low mass and damping. *Journal of Fluids and Structures*, 11 (8), 973-982.
- Khalak, A., Williamson, C.H.K. (1999). Motions, forces and mode transitions in vortex-induced vibrations at low mass-damping. *Journal of Fluids and Structures*, 13 (7-8), 813-851.
- Kim, S., Wilson, P.A., Chen, Z.-M. (2014). Numerical simulation of force and wake mode of an oscillating cylinder. *Journal of Fluids and Structures*, 44, 216-225.
- Kim, S., Wilson, P.A., Chen, Z.-M. (2015). Effect of turbulence modelling on 3-D LES of transitional flow behind a circular cylinder. *Ocean Engineering*, 100, 19-25.
- Kiu, K., Stappenbelt, B., Thiagarajan, K. (2011). Effects of uniform surface roughness on vortex-induced vibration of towed vertical cylinders. *Journal of Sound and Vibration*, 330 (20), 4753-4763.
- Law, Y.Z., Jaiman, R.K. (2017). Wake stabilization mechanism of low-drag suppression devices for vortex-induced vibration. *Journal of Fluids and Structures*, 70, 428-449.
- Lei, C., Cheng, L., Kavanagh, K. (2001). Spanwise length effects on three-dimensional modelling of flow over a circular cylinder. *Computer methods in applied mechanics and engineering*, 190 (22), 2909-2923.
- Logstor. (1997). Shell mallard, HT/HP pipeline project, The North Sea. *Logstor oil & gas*.
- Lucor, D., Foo, J., Karniadakis, G. (2005). Vortex mode selection of a rigid cylinder subject to VIV at low mass-damping. *Journal of Fluids and Structures*, 20 (4), 483-503.
- Matin Nikoo, H., Bi, K., Hao, H. (2017). Passive vibration control of cylindrical offshore components using pipe-in-pipe (PIP) concept: An analytical study. *Ocean Engineering*, 142, 39-50.
- Mittal, S. (2013). Free vibrations of a cylinder: 3-D computations at  $Re=1000$ . *Journal of Fluids and Structures*, 41, 109-118.

- Oruç, V. (2017). Strategies for the applications of flow control downstream of a bluff body. *Flow Measurement and Instrumentation*, 53 (Part B), 204-2014.
- Ozkan, G.M., Firat, E., Akilli, H. (2017). Passive flow control in the near wake of a circular cylinder using attached permeable and inclined short plates. *Ocean Engineering*, 134, 35-49.
- Prasanth, T., Mittal, S. (2008). Vortex-induced vibrations of a circular cylinder at low Reynolds numbers. *Journal of Fluid Mechanics*, 594, 463-491.
- Rashidi, S., Hayatdavoodi, M., Esfahani, J.A. (2016). Vortex shedding suppression and wake control: A review. *Ocean Engineering*, 126, 57-80.
- Sagaut, P. (2006). Large eddy simulation for incompressible flows: an introduction. *Springer Science & Business Media*.
- Senga, H., Larsen, C.M. (2017). Forced motion experiments using cylinders with helical strakes. *Journal of Fluids and Structures*, 68, 279-294.
- Song, Z., Duan, M., Gu, J. (2017). Numerical investigation on the suppression of VIV for a circular cylinder by three small control rods. *Applied Ocean Research*, 64, 169-183.
- Soumya, S., Prakash, K.A. (2017). Effect of splitter plate on passive control and drag reduction for fluid flow past an elliptic cylinder. *Ocean Engineering*, 141, 351-374.
- Sumer, B.M. (2006). Hydrodynamics around cylindrical structures. *World scientific*, Singapore.
- Tu, J., Yeoh, G.H., Liu, C. (2018). Computational fluid dynamics: a practical approach. *Butterworth-Heinemann*.
- Williamson, C.H.K., Govardhan, R.N. (2004). Vortex-induced vibrations. *Annu. Rev. Fluid Mech.*, 36, 413-455.
- Yang, Z. (2015). Large-eddy simulation: Past, present and the future. *Chinese Journal of Aeronautics*, 28 (1), 11-24.
- Yeon, S.M., Yang, J., Stern, F. (2016). Large-eddy simulation of the flow past a circular cylinder at sub-to super-critical Reynolds numbers. *Applied Ocean Research*, 59, 663-675.
- Yu, Y., Xie, F., Yan, H., Constantinides, Y., Oakley, O., Karniadakis, G.E. (2015). Suppression of vortex-induced vibrations by fairings: A numerical study. *Journal of Fluids and Structures*, 54, 679-700.
- Zhang, K., Katsuchi, H., Zhou, D., Yamada, H., Zhang, T., Han, Z. (2017a). Numerical simulation of vortex induced vibrations of a flexibly mounted wavy cylinder at subcritical Reynolds number. *Ocean Engineering*, 133, 170-181.
- Zhang, Y., Liu, K., Xian, H., Du, X. (2017b). A review of methods for vortex identification in hydroturbines. *Renewable and Sustainable Energy Reviews*, 81 (1), 1269-1285.
- Zhao, M., Cheng, L. (2011). Numerical simulation of two-degree-of-freedom vortex-induced vibration of a circular cylinder close to a plane boundary. *Journal of Fluids and Structures*, 27 (7), 1097-1110.
- Zhao, M., Cheng, L. (2014). Vortex-induced vibration of a circular cylinder of finite length. *Physics of Fluids*, 26 (1), 015111.
- Zhao, M., Cheng, L., An, H., Lu, L. (2014). Three-dimensional numerical simulation of vortex-induced vibration of an elastically mounted rigid circular cylinder in steady current. *Journal of Fluids and Structures*, 50, 292-311.



Zhu, H., Zhao, H., Yao, J., Tang, Y. (2016). Numerical study on vortex-induced vibration responses of a circular cylinder attached by a free-to-rotate dartlike overlay. *Ocean Engineering*, 112, 195-210.

# Chapter 4 Vortex-induced vibration of a full-diamond textured cylinder at subcritical Reynolds numbers

Under review

---

## ABSTRACT

Textured pipe has been proposed to improve the propagation buckling capacity of subsea pipelines recently. Due to its special geometry, textured pipe may have the potential to mitigate the vortex induced vibration (VIV) by altering the wake vortex street formation. In the present study, the effectiveness of using a full-diamond textured pipe for VIV suppression is numerically investigated in a coupled fluid-structure interaction (FSI) framework. Three-dimensional (3-D) Computational Fluid Dynamics (CFD) analyses are performed by using the Reynolds-Averaged Navier-Stokes (RANS) turbulence model equipped with shear stress transport (*SST*)  $K - \omega$  model at the subcritical Reynolds numbers ( $R_e$ ) with  $R_e \in [2000, 12000]$ . The results are compared in detail with an equivalent conventional smooth cylinder subjected to the same flow conditions. Numerical results show that the textured cylinder can significantly mitigate the undesired VIV and the associated hydrodynamic forces. It eliminates the upper excitation regime in the conventional smooth cylinder and the width of the synchronization regime is also remarkably reduced.

## 4.1 Introduction

Slender cylindrical components operating in the marine environment are susceptible to a variety of structural stability problems such as the lateral, upheaval and propagation buckling ([Karampour et al., 2017](#)). Among them, propagation buckling might be the most critical problem for the pipelines operating in the deep and ultra-deep waters where a local buckle can quickly propagate along the pipe due to the high external hydrostatic pressure, which in turn may result in severe damages to the pipeline ([Karampour and Albermani, 2016](#)). Recently, [Khalilpasha and Albermani \(2013\)](#) proposed a novel origami or textured cylinder (refer to Figure 4-1) to arrest this mechanical instability problem, and it was found that this cylinder could offer a substantial increase in the propagation buckling capacity without increasing its wall thickness as compared to the equivalent smooth pipe. With the same design concept,

[Yang et al. \(2016\)](#) showed that an octagonal origami tube can considerably increase the energy absorption capacity and simultaneously reduce the sharp initial peak force in the pipe under the uniaxial loading. More recently, they further showed that introducing ellipsoidal dimples to the circular tube could remarkably improve the crushing response of the pipe ([Yang et al., 2017](#)). This type of structure may also find wide applications in the solar panels, robots and space satellites ([Callens and Zadpoor, 2018](#)).

On the other hand, when flow past a bluff body, it is often accompanied with an undesired vibration known as vortex induced vibration (VIV). VIV is a common phenomenon for slender structures such as subsea pipelines, marine risers and anchoring lines. When the frequency of vortex shedding is close to the body natural frequency, synchronization or lock-in phenomenon may occur and responses with remarkably large amplitude are expected, which in turn may result in the fatigue damage to the structural components or even catastrophic failure to the whole structure. It is therefore by all means necessary to suppress the adverse effect of VIV. Several control techniques have been proposed by different researchers, and these methods can be generally divided into two broad types: (i) the active control methods such as the windward-suction-leeward-blowing (WSLB) ([Dong et al., 2008](#), [Wang et al., 2016](#)) and the synthetic jets ([Glezer and Amitay, 2002](#), [Wang et al., 2017](#)), and (ii) the passive control methods such as the helical strake ([Zdravkovich, 1981](#), [Bearman and Branković, 2004](#), [Holland et al., 2017](#), [Senga and Larsen, 2017](#)), fairing ([Grant and Patterson, 1977](#), [Assi et al., 2014](#), [Yu et al., 2015](#)), dart-like overlay ([Zhu et al., 2016](#)), splitter plates and C-shaped foil ([Roshko, 1961](#), [Apelt et al., 1973](#), [Soumya and Prakash, 2017](#), [Law and Jaiman, 2017](#)), controlling rods ([Strykowski and Sreenivasan, 1990](#), [Song et al., 2017](#)), screen shroud ([Cicolin and Assi, 2017](#)) and pipe-in-pipe (PIP) method ([Matin Nikoo et al., 2017, 2018a](#)). Comprehensive reviews of the different VIV control mechanisms can be found in [Choi et al. \(2008\)](#) and [Rashidi et al. \(2016\)](#), interested readers can refer to these papers for more information.

Besides the above mentioned techniques, shape or surface modification has also been recognized as an effective method for VIV attenuation. The rationale behind this approach is manipulating the flow behind the cylinder. In terms of the phenomenological mechanism, shape modification technique can be roughly classified into three categories. In the first group (which is also known as the boundary layer

control), surface/shape modification is applied to the cross-section of the body. In this technique, the separation point, defined as where the shear stress reduces to zero in the boundary layer, is retreated by making a large momentum against the adverse pressure gradient ([Zhang et al., 2016](#)). Flow control methods like surface roughness ([Achenbach, 1971](#), [Gao et al., 2018b](#)), grooves ([Ko et al., 1987](#), [Cheng et al., 2017](#)), dimpled ([Bearman and Harvey, 1993](#), [Zhou et al., 2015](#)) and polygonal shapes ([Zhang et al., 2016](#)) fall into this category. In the second group, contrary to the first category, surface/shape modification is implemented in the axial direction of the body. The main advantage of this approach lies in the three-dimensionality of the flow separation control mechanism, which is more stable than the two-dimensional condition. This type of shape modification includes the spanwise sinusoidal perturbation method ([El-Gammal et al., 2007](#)), hemispherical bumps ([Owen et al., 2001](#)), wavy cylinder ([Zhang et al., 2017](#)), twisted cylinder ([Jung and Yoon, 2014](#)) and fined cylinder ([McClure and Yarusevych, 2016](#)). In the third category, as a combination of the previous two types, surface/shape modifications are adopted in both the cross-sectional and spanwise directions. The most widely used practice, i.e., the helical strake belongs to this group. Previous studies such as that conducted by [Sui et al. \(2016\)](#) have shown that helical strakes can effectively suppress the crossflow vibration up to 85% compared to the conventional smooth cylinder. However, it may cause an undesired larger drag force than a plain cylinder ([Holland et al., 2017](#)).

For the textured pipe, as the wall is not smooth but with local facets in both the cross-sectional and longitudinal directions, it may have the potential for VIV suppression as specified in the third group of surface modification approach. However, to the best knowledge of the authors, no such study has been reported in the literature yet. As a first attempt, this paper aims to investigate the oscillation behaviour of an octagonal textured cylinder subjected to VIV. A two-way coupled Fluid-Structure Interaction (FSI) model is developed and detailed three dimensional (3-D) numerical simulations are carried out. The numerical results are compared with an equivalent conventional smooth cylinder. This paper is organized as follows: Section 4.2 briefly introduces the textured pipe; the general methodologies used to model the fluid flow and corresponding body vibrations are presented in Section 4.3; in Section 4.4, the adopted numerical framework is validated by a series of experimental benchmark data in the

literature; the effectiveness of using textured cylinder for VIV suppression is then investigated in Section 4.5; and finally some conclusions are drawn in Section 4.6.

## 4.2 Textured pipe

The textured pipe is cylindrical in the global sense with local facets rather than a smooth wall along its longitudinal direction. With different parameters, different facet shapes can be obtained for the textured pipe. In the present study, a full-diamond pattern known as the Yoshimura origami shape (Yang et al., 2016) is adopted. Figure 4-1 illustrates the geometric shape of the textured cylinder. As shown, the cylinder consists of a series of periodically arrayed diamond lobes, in which the solid and dashed lines represent the mountains and valleys in the folded full-diamond module respectively. The relationship between different geometry parameters can be described as follows (Yang et al., 2016):

$$\cos \theta = \frac{b}{l} \tan \frac{\pi}{2N} \quad (4-1)$$

$$\varphi = \pi - 4\alpha = \pi - \frac{2\pi}{N} \quad (4-2)$$

$$\tan \alpha = \frac{l}{b} \cos \theta \quad (4-3)$$

where  $\theta$  is the angle between folded lobes along the circumference and the horizontal plane as shown in Figure 4-1.  $N$  is the number of folded lobes, and it is selected as  $N = 8$  in the present study,  $\alpha$  is the horizontal projection of the angle between the horizontal crease and the other two creases (in the same lobe),  $\varphi$  is the interior angle of the cross-sectional polygon,  $l$  and  $b$  are the width and the distance between the vertexes of the two neighboring diamond lobes, respectively.  $l = b$  is adopted in this study to form a full-diamond textured pipe.

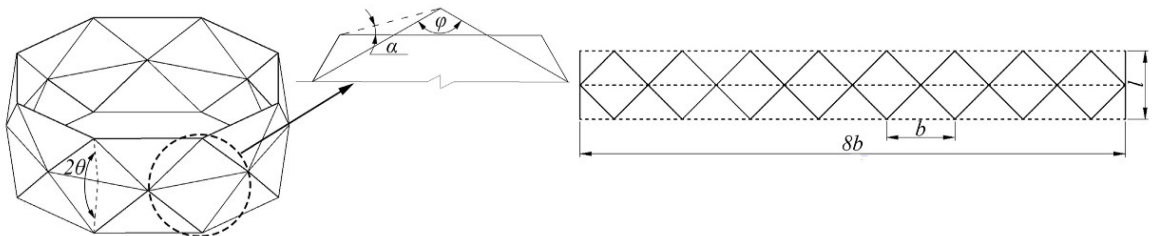


**Figure 4-1:** Geometry details of a full-diamond (octagonal) textured pipe (adopted partly from Yang et al. (2016)).

For comparison, a conventional smooth cylinder is also investigated in the present study. Except for the different cross sections, the smooth cylinder has the same

diameter and mass with the textured pipe. The 3-D schematic views of the smooth and textured cylinders can be found in Figure 4-2.

It should be noted that both the outer and inner surfaces of the full-diamond textured pipe investigated in this study are textured. As will be discussed in section 4.5.1, the VIV suppression mechanism of the textured pipe is due to the disorganizing the correlation of vortex shedding around the outer surface of the cylinder. The inner surface can therefore be either smooth or textured without loss of functionality.

### **4.3 Methodology**

#### **4.3.1 Fluid-structure interaction (FSI) set-up**

It is well recognized that flow-induced vibration phenomenon needs to be investigated through a coupled FSI framework. In this study, a two-way FSI algorithm is developed by coupling the ANSYS Mechanical finite element (FE) solver for the solid part (i.e., the cylinder) together with the FLUENT finite volume (FV) solver for the fluid part (i.e., the water) ([ANSYS®, 2016](#)). ANSYS Multi-field framework is then used to solve the FSI problem ([Wang and Xiao, 2016](#), [Matin Nikoo et al., 2018a](#)). In this framework, at each time step, the fluid motion equations (section 4.3.2.1) are first solved in the FLUENT FV solver and the estimated hydrodynamic loads are transferred to the mechanical part as inputs on the cylinder. Within the same time step, the structural dynamics equation (section 4.3.3) is then solved in the ANSYS Mechanical FE solver, which in turn causes deformation in the mesh grids of the fluid part (section 4.3.2.3). This procedure continues up to reach an almost steady state response of the system.

Figure 4-2 shows the overall view of the numerical setup adopted in this study. A 3-D fluid domain (Figure 4-2(a)) is utilized in the FLUENT part to simulate the fluid flow over a smooth cylinder (Figure 4-2(b)), and an equivalent textured cylinder (Figure 4-2(c)), which are both suspended by four linear springs in the Mechanical part. The outer surfaces of the both cylinders, as shown in Figure 4-3(a), are set to be the FSI interface, on which the hydrodynamic forces estimated by the FLUENT solver, and the associated body oscillations calculated by the Mechanical solver are sequentially transferred throughout the FSI transient analysis. More details regarding different parts (i.e., the fluid part and the mechanical part) are presented in the following subsections.

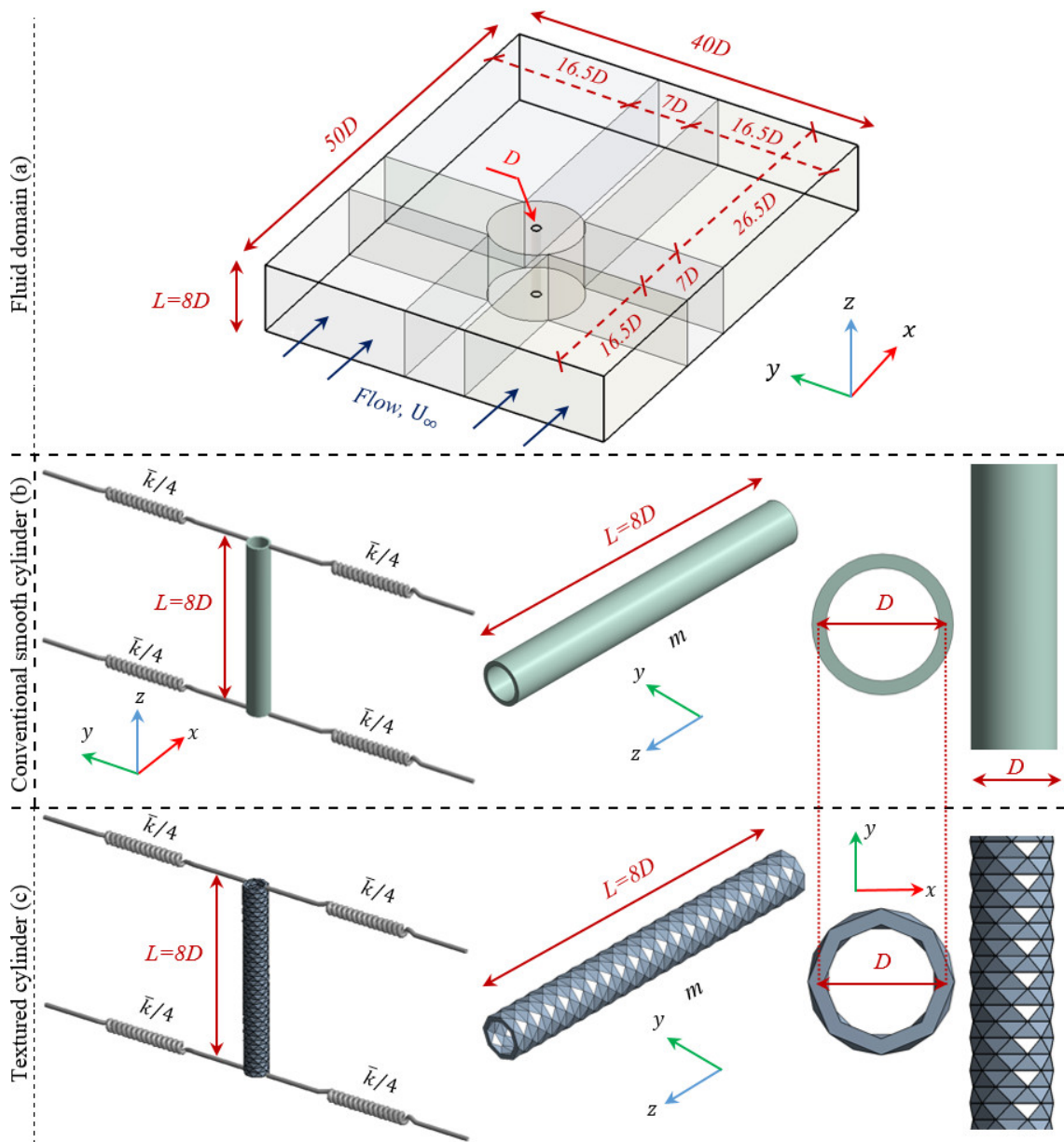


**Figure 4-2:** (a) 3-D computational fluid domain adopted in the Fluent solver and mechanical details of the elastically-mounted (b) smooth cylinder and (c) textured pipe modelled in the Mechanical solver.

### 4.3.2 Fluid part

#### 4.3.2.1 Fluid flow and turbulence model

Reynolds Averaged Navier-Stokes (RANS)-based codes have been widely used to simulate VIV responses of bluff bodies and the associated wake vortices modes (e.g. [Gao et al. \(2018b\)](#), [Wang et al. \(2018\)](#)). Compared with the other approaches, RANS models can provide a reasonable balance between the computational effort and the accuracy of results ([Argyropoulos and Markatos, 2015](#)). Therefore, the RANS codes are used to simulate the incompressible turbulent flow passing the objective cylinders in the present study.

In this method, the mean continuity and momentum equations can be written as follows (Cebeci, 2004):

$$\frac{\partial \bar{u}_j}{\partial x_j} = 0 \quad (4-4)$$

$$\rho \frac{\partial \bar{u}_i}{\partial t} + \rho \frac{\partial}{\partial x_j} (\bar{u}_i \bar{u}_j) = -\frac{\partial \bar{p}}{\partial x_i} + \frac{\partial}{\partial x_j} (\bar{\tau}_{ij} - \rho \overline{u_i'' u_j''}) \quad (4-5)$$

where  $\rho$  is the fluid density,  $t$  is time,  $x_i$  and  $x_j$  are the components of the position vectors of the fluid unit ( $i, j \in [1,2,3]$ ),  $\bar{u}$ ,  $\bar{p}$  represent the time averages of the velocity and pressure respectively.  $\overline{u_i'' u_j''}$  is the Reynolds-stress tensor which represents the small-scale fluctuation of fluid velocity related to the turbulence.  $\bar{\tau}_{ij}$  is the viscous stress tensor which can be expressed as below:

$$\bar{\tau}_{ij} = \mu \left( \frac{\partial \bar{u}_i}{\partial x_j} + \frac{\partial \bar{u}_j}{\partial x_i} \right) \quad (4-6)$$

where  $\mu$  is the fluid dynamic viscosity.

The two-equation eddy viscosity shear stress transport (*SST*)  $K - \omega$  model introduced by Menter (1994) is used for modelling the turbulence. This model estimates the eddy viscosity by providing two additional transport equations for the turbulent kinetic energy  $K$  and its dissipation rate  $\omega$ . Basically, two principal advantages are offered by *SST*  $K - \omega$  when it is implemented to simulate the VIV: (i) it can accurately predict the flow separation under the strong adverse pressure gradients and (ii) can be adopted as a low- $R_e$  turbulence model without any extra damping wall function. The authors' very recent study (Matin Nikoo et al., 2018b) showed that the inclusion of low- $R_e$  correction can significantly improve the accuracy of the VIV responses obtained by the RANS *SST*  $K - \omega$  method, which is also incorporated in the current numerical simulations through a correction coefficient ( $\alpha^*$ ) to damp the eddy viscosity parameter ( $\mu_t = \alpha^* \rho K / \omega$ ) (Wilcox, 2006).

#### 4.3.2.2 Computational domain and mesh generation

As shown in Figure 4-2(a), a 3-D rectangular computational fluid domain consisting of 9 volumetric blocks is developed in order to capture the VIV responses and the wake vortices. Figure 4-3 outlines the computational blocks, generated mesh grids and the corresponding boundary conditions used for both the smooth and textured cylinders. In both cases, the center of the elastically-mounted cylinders are located at



$20D$  and  $30D$  from the inlet and outlet boundaries respectively, in which  $D$  is the cylinders' mean diameter. The crossflow width of the domain is set to be  $40D$  in such a way that the cylinders are placed in the center of the domain, i.e.,  $20D$  from the lateral free-slip boundaries. The spanwise length of the domain is chosen as  $8D$ . This computational domain is selected because previous studies ([Prasanth and Mittal, 2008](#), [Zhao et al., 2014](#), [Law and Jaiman, 2017](#), [Matin Nikoo et al., 2018a](#)) showed that it can reliably take into account the three-dimensionality and blockage effects on the VIV responses of bluff bodies. A steady uniform flow with a freestream velocity of  $u = U_\infty$  is specified at the velocity-inlet boundary ( $x = -20D$ ), whereas transverse and spanwise velocity components are set as zero ( $v = w = 0$ ). For the top, bottom and two lateral boundaries, i.e.,  $z = \pm 4D$  and  $y = \pm 20D$ , symmetry (free-slip) plane conditions are applied. The zero-gradient condition for velocity is applied at the outlet boundary ( $x = 30D$ ), where the reference pressure is assigned to be zero. On the cylinders' outer surface, non-slip wall condition is specified, i.e., the fluid velocity on this surface is the same as the cylinder's displacement speed estimated in the mechanical part. FLUID30 elements ([ANSYS®, 2016](#)) with different shape functions are used to model the fluid medium. Each element node has four degrees of freedom, namely the translations in the nodal  $x$ ,  $y$ ,  $z$  directions, and the pressure. The elements also have the capability to include damping within the fluid part.

There must be an optimum balance between the number of generated mesh grids and the computational time required to solve the governing equations as presented in Section 4.3.2.1. For this purpose, for both the smooth and textured pipes, in each quadrilateral sub-domains, i.e., blocks 1 to 8 as shown in Figure 4-3(b), finer meshes are generated for areas close to the main annular sub-domain surrounding the cylinder, i.e., block 9, while coarser meshes are generated when they are far away from this block. It should be noted that in the case of textured cylinder, the existence of sharp edges on the small facets causes inherent challenges to generate sound yet optimum computational grids in the immediate vicinity of the body. To overcome this challenge, block 9 is discretized by different grid functions when smooth cylinder and textured pipe are considered as shown in Figure 4-3(b). The mesh details are shown in Figure 4-4, and Figure 4-5 shows the FLUID30 element with different shape functions adopted for each sub-domains in this study. As shown, mesh grids with 8-Node hexahedral shape function are used for all the sub-domains (i.e., blocks 1 to 9) in the

smooth cylinder, whereas it is adopted only for the quadrilateral sub-domains (i.e., blocks 1 to 8) in the textured pipe. In order to account for the viscous effect on the non-slip wall boundary as well as resolve the rapid variation of flow variables that occur within the boundary layer region, for block 9 in the textured pipe, very small mesh grids with 6-Nodes wedge shape function are generated for the regions very close to the sharp edges of the textured cylinder. Elements with 4-Node tetrahedral shape function are utilized for the zone located in the middle parts of block 9. Finally, to make a smooth transition from 4-Node to the 8-Node hexahedral elements, 5-Node pyramid elements are adopted for the outermost layer of block 9.

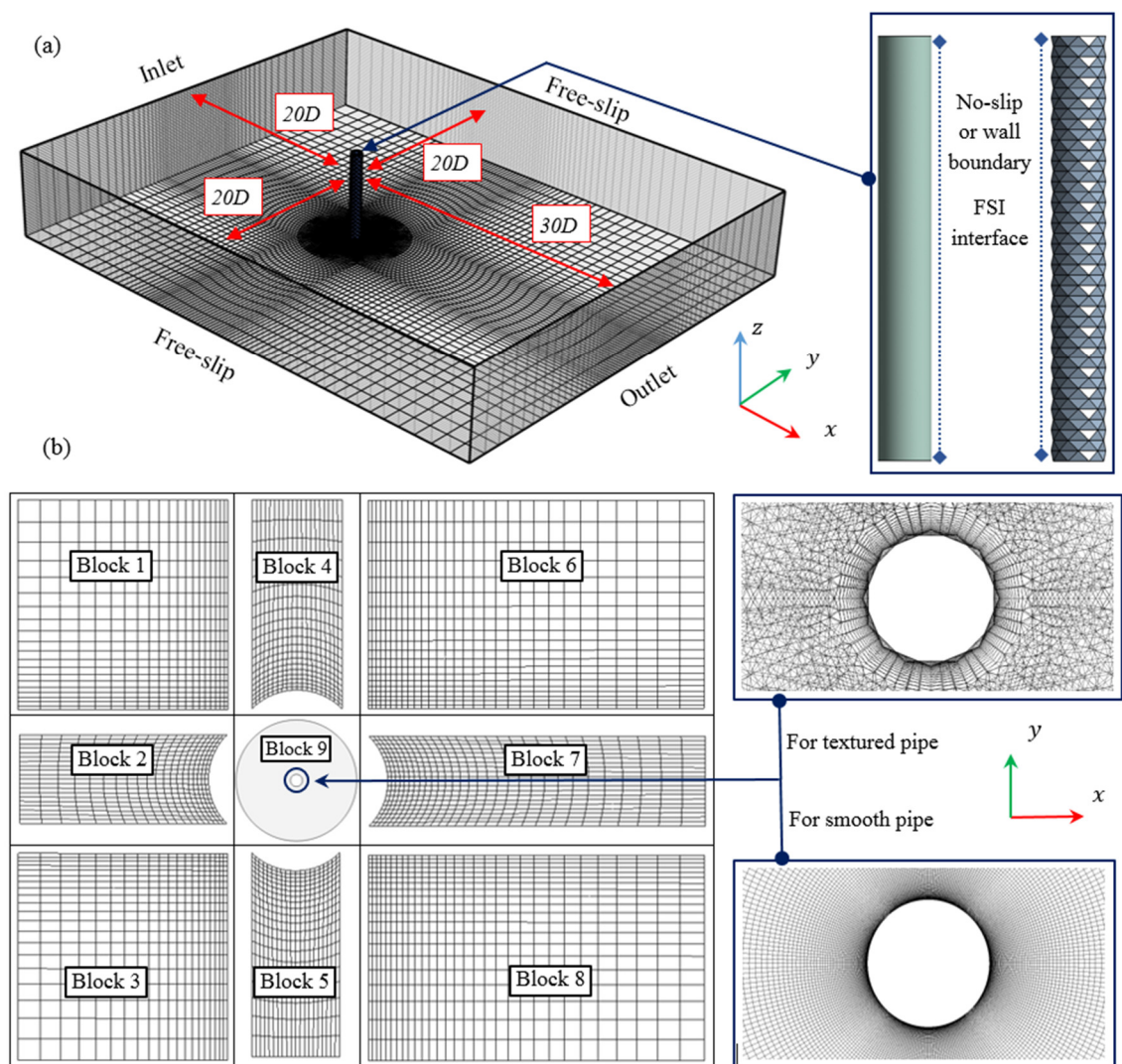


**Figure 4-3:** (a) An overview of the mesh grids and the utilized boundary conditions, (b)  $xy$ -plane of the domain and the associated block number.

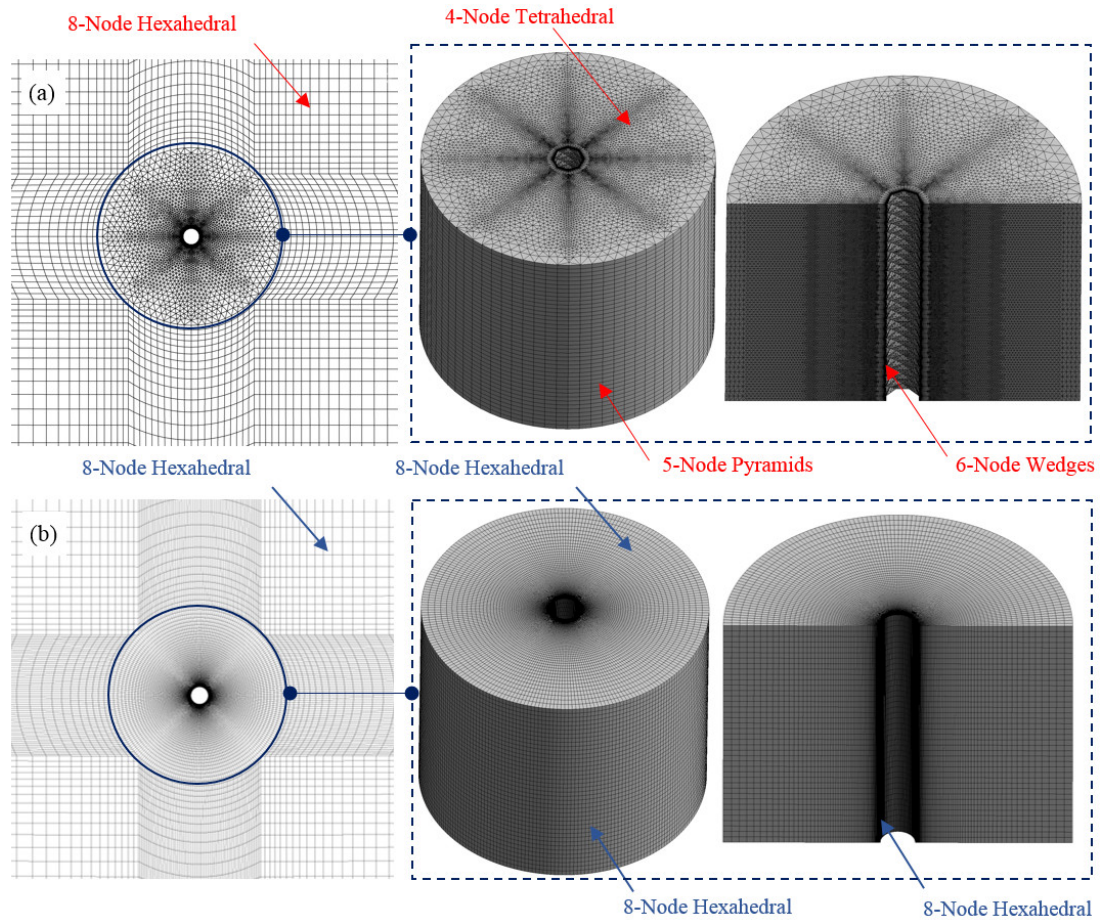


**Figure 4-4:** Details of different mesh grids adopted for the different sub-domains in (a) textured cylinder and (b) smooth cylinder.

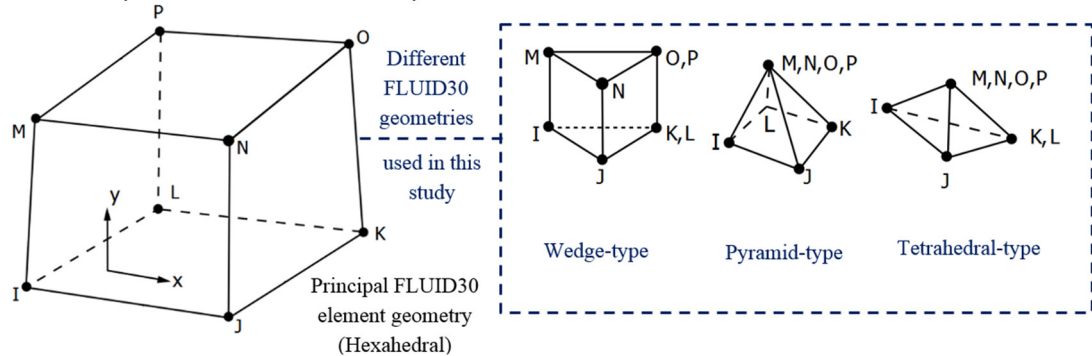


**Figure 4-5:** FLUID30 element with different shape functions used for modelling the fluid medium.

#### 4.3.2.3 Mesh deformation

In this study, the diffusion-based smoothing dynamic mesh motion is utilized to update the volume mesh in the moving zones and deforming boundaries ([Zhao and Cheng, 2011](#)). In this approach, the interior nodes of the meshes move, whereas the number of nodes and their connectivity remain constant throughout the transient analysis. For diffusion-based smoothing, the mesh motion is governed by the following diffusion equation:

$$\nabla \cdot (\gamma \nabla \vec{u}) = 0 \quad (4-7)$$

where  $\nabla$  is the differential operator,  $\vec{u}$  denotes the mesh displacement velocity, and  $\gamma$  is the diffusion coefficient, which describes how the boundary motion diffuses into the interior of the deforming mesh. With a constant  $\gamma$ , boundary motion diffuses uniformly throughout the fluid domain, while with a non-uniform value, nodes with high diffusivity tend to move with less relative motion. In the present study, a cell-volume-based diffusion coefficient is adopted, and it is defined as a function of the normalized cell volume size  $V$  as follows:

$$\gamma = \frac{1}{V^\beta} \quad (4-8)$$

in which  $\beta$  is the diffusion parameter and it is set to 1.5 in the present study. With this value, the grids in the immediate vicinity of the cylinders' wall moves almost rigidly with the cylinder, i.e., the uniformity of the near wall mesh resolution is preserved and the outermost grids are kept fixed. It may be worth mentioning that in the region with the tetrahedral mesh grids as used in the textured cylinder, the boundary displacement might become significantly large compared to the local cell sizes, which may cause an undesired deterioration in the cells' quality (or violation of the cells' skewness) and eventually result in the negative cell volumes. This will consequently lead to the convergence problem to the model when the solution is intended to be updated to the next computational time step. To circumvent this problem, the local facet and cell re-meshing method is applied in the present study. If any cell or facet cannot satisfy the skewness criterion, the grids are locally restructured with the new cells. Moreover, implicit mesh update scheme is also adopted in the numerical model, based on which mesh grids in the domain are updated not only in each time step but also in each computational sub-iteration. All these techniques guarantee the convergence and high quality of the numerical results.

### 4.3.3 Mechanical part

To estimate the vibration of the cylinders caused by the fluctuating fluid forces, both the smooth and textured pipes are submitted to the ANSYS mechanical solver. As shown in Figure 4-2(b)&(c), each cylinder is elastically suspended by four body-ground type springs (with stiffness  $\bar{k}$ ) with assigned remote displacement constraints, which allow them to vibrate in the transverse direction ( $y$ -direction) only.

The transverse equation of motion of an elastically-mounted rigid cylinder under VIV can be expressed as follows:

$$m \frac{\partial^2 y}{\partial t^2} + C \frac{\partial y}{\partial t} + \bar{k}y = F_L \quad (4-9)$$

where  $m$ ,  $C$  and  $\bar{k}$  are the oscillating mass, damping coefficient and spring constant, respectively;  $y$  is the transverse oscillation,  $F_L$  is the total lift force vector in the crossflow direction of the vibrating cylinder. Following the suggestions of many previous studies (e.g. [Lucor et al. \(2005\)](#), [Singh and Mittal \(2005\)](#), [Zhao et al. \(2014\)](#), [Gsell et al. \(2019\)](#)), the damping coefficient is assumed as zero in the present study though certain damping unavoidably exists in the test, and it may influence the vibration amplitudes of the cylinder. For example, in the two experimental studies used to validate the numerical model in Section 4.4, the damping ratios for the two tests were 0.0054 ([Khalak and Williamson, 1999](#)) and 0.0069 ([Assi et al., 2010](#)), respectively. On the other hand, it should be noted that when the damping is small, many previous studies indicated that the results with and without damping are almost the same. For example, [Shiels et al. \(2001\)](#) indicated that a damping ratio smaller than 0.01 has little effect on the cylinder motion with low mass ratio. [Pan et al. \(2007\)](#) used the standard RANS method to simulate the VIV response of an elastically-mounted rigid cylinder. In their numerical simulations, two cases were compared: In the first case, they adopted exactly the same parameters in [Khalak and Williamson \(1999\)](#), i.e.,  $m^* = 2.4$  and  $\zeta = 0.0054$  ( $m^*\zeta$  is thus 0.013). In the second case, they set  $\zeta$  to be zero ( $m^*\zeta$  is thus also zero). The numerical simulations showed that the two cases resulted in almost exactly the same results ([Pan et al., 2007](#)). Accordingly, in this study the structural damping  $\zeta$  is set to be zero.

To achieve a fully-mapped load transfer and mesh displacements between the two solvers, the solid parts (i.e., cylinders) are also discretized by the same finite element (FE) meshes on the FSI interface. Conservative interpolation method ([ANSYS®, 2016](#)) is adopted at the FSI interface, which makes the overall load transfer conservative, regardless of the mesh shape, size, grid topology, and face distribution across the interface.

#### 4.3.4 General numerical set-up

The time resolution is crucial for the success of the VIV simulation. The Courant-Friedrichs-Levy ( $CFL$ ) number as defined below is an appropriate indicator for setting the optimal time step in the transient flow simulation ([Holland et al., 2017](#)):

$$CFL = \frac{U\Delta t}{\Delta x} \quad (4-10)$$

where  $U$  is the local flow speed,  $\Delta t$  is the time step and  $\Delta x$  is the mesh cells size. Courant number should be less than or equal to 1 for most part of the computational domain ([Nishino et al., 2008](#)). To this end, as proposed by [Nishino et al. \(2008\)](#), the time step size of the transient calculations is determined by  $\Delta t = 0.02D/U_\infty$  in order to achieve an acceptable level of accuracy within a reasonable computational time frame. It should be mentioned that a transient two-way FSI simulation consists of two levels of iteration to reach a converged result: (i) the normal inner iteration used within each solver, and (ii) the coupling loop iteration in which the loads/displacements are sequentially updated between the Mechanical solver and CFD solver. In this study, the number of inner and coupling iterations are set to 10 and 30 respectively to provide the fully-converged results.

Another important indicator is the dimensionless wall distance  $y^+ = \Delta y u_t / \nu$ , in which  $\Delta y$  is the distance of the mesh grids adjacent to the cylinder's wall,  $u_t = \sqrt{\tau_w / \rho}$  is friction or wall shear velocity,  $\tau_w$  is viscous shear stress,  $\nu$  is fluid kinematic viscosity and  $\rho$  is the fluid density. It can be used to show whether the numerical model is able to resolve the boundary layer and reflect the flow separation pattern ([Wen and Qiu, 2017](#), [Tu et al., 2018](#)). It is normally suggested that  $y^+$  should be smaller than unity ( $y^+ < 1$ ) in order to resolve the mean velocity and turbulent quantities within the sub-layer ([Abrahamsen Prsic et al., 2014](#), [Argyropoulos and Markatos, 2015](#), [Tu et al., 2018](#)). In this study, very fine grid meshes are generated in the areas adjacent to the cylinder's wall, and this condition (i.e.,  $y^+ < 1$ ) is well maintained at all the wall-adjacent integration points.

Semi-Implicit Method for Pressure-Linked (SIMPLE) scheme, which is a pressure-based segregated algorithm, is used to achieve the pressure-velocity coupling on the mesh grids ([Tu et al., 2018](#)). This approach can give a converged solution quickly. A second-order upwind interpolation scheme is used for the convection term (left hand

side of Equation (4-5)), and the hybrid initialization method is utilized to initialize the flow field domain.

#### 4.4 Two-way FSI model verification

In this study, the experimental studies on the conventional smooth cylinders conducted by [Khalak and Williamson \(1999\)](#) and [Assi et al. \(2010\)](#) are used as benchmark tests to verify the numerical models. Dimensionless parameters governing the VIV responses are set to match with those in the test setup by [Khalak and Williamson \(1999\)](#). Accordingly, the mass ratio ( $m^*$ ), defined as the ratio of the cylinder mass ( $m$ ) to the displaced mass of the fluid, is set as 2.4 and the Reynolds number ( $Re$ ) varies from 2000 to 12000 in the numerical simulations.

##### 4.4.1 Mesh independency test

For both the smooth and textured cylinders, mesh independence tests are conducted in order to ensure that the numerical results are independent of the adopted mesh sizes. The tests are carried out for the normalized velocity  $U^* = 5$  (defined as  $U^* = U_\infty / f_n D$ , where  $U_\infty$  stands for the freestream fluid velocity and  $f_n$  is the natural frequency of the cylinder in the air). It should be noted although the cylinders are located in the water in the present study, the natural frequency of the cylinder in the air is used. This is because the experimental studies used to validate the numerical model presented the results with respect to  $f_n$ . For direct comparisons, the results in the present study are thus also presented with respect to  $f_n$ . To convert the natural frequency in the water ( $f_w$ ) into that in the air, the following empirical relationship is used, i.e.,  $f_w / f_n = \sqrt{m^* / (C_a + m^*)}$ , in which  $m^*$  is the mass ratio and  $C_a$  is the added mass coefficient, which can be assumed as 1 ([Zhao et al., 2014](#)). Four different mesh grid sizes are investigated to reach a converged result. The calculated maximum normalized amplitude response ( $A^*$ ), lift coefficient  $C_L^{max}$  and drag coefficient  $C_D^{max}$  are tabulated in Table 4-1.

**Table 4-1:** Mesh convergence test results.

	Conventional smooth cylinder				Textured cylinder			
	No. Element	$A^*$	$C_L^{max}$	$C_D^{max}$	No. Element	$A^*$	$C_L^{max}$	$C_D^{max}$
Coarse	268,800	0.63	1.17	3.81	684,128	0.53	0.57	2.16
Medium	900,000	0.72	1.35	3.88	1,151,443	0.56	0.62	2.31
Optimum	1,162,000	0.80	1.38	4.02	1,598,604	0.59	0.66	2.40
Dense	1,548,000	0.81	1.36	4.09	1,857,480	0.59	0.60	2.40

Data in Table 4-1 shows that the models with the element numbers of 1,162,000 for the smooth pipe and 1,598,604 for the textured pipe (i.e., the optimum cases in Table 4-1) lead to different results with those from the coarse and medium meshes but quite similar results from the dense mesh sizes, which indicate the numerical results are converged based on these mesh sizes. On the other hand, compared to the dense mesh case, the computational effort for the optimum case is significantly reduced. The models meshed by the optimum sizes are therefore used to calculate the VIV responses in the present study.

#### 4.4.2 Validation

In this section, the numerical model developed for the smooth cylinder is verified with the previous experimental tests. Figure 4-6 compares the maximum normalized oscillations  $A^*$  Figure 4-6(a) and the dominant peak frequencies of the normalized power spectrum density (PSD) of the cylinder oscillation (Figure 4-6(b)) obtained from the present study and the experimental studies.

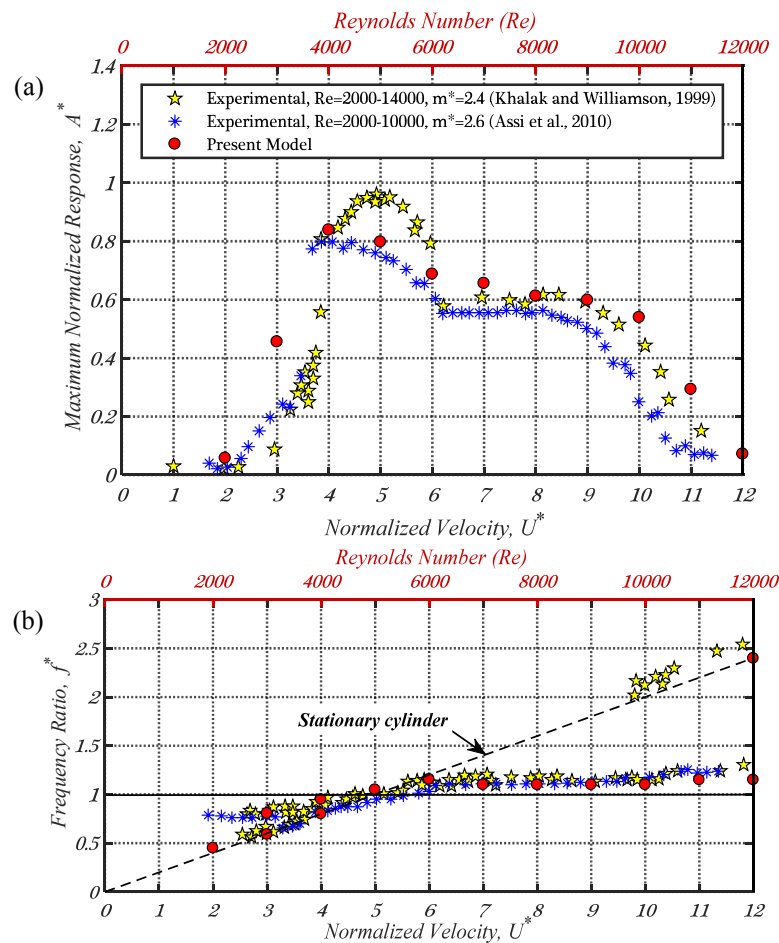


**Figure 4-6:** Comparisons between the present FSI model and the previous experimental studies on the smooth cylinders: (a) normalized maximum amplitude response ( $A^*$ ) and (b) dominant peaks in the spectrum of the cylinder oscillation.



As shown in Figure 4-6(a), the coupled FSI framework developed in the present study generally well captures the VIV phenomenon of smooth cylinder. As shown, the three typical VIV response regimes occurring in the conventional smooth cylinder known as the initial branch (when  $U^* \approx 2 - 3$ ), upper branch (when  $U^* \approx 4 - 6$ ) and lower branch (when  $U^* \approx 7 - 10$ ) are clearly shown in the numerical results. In addition, it can be seen that the normalized maximum amplitude  $A^*$  obtained in the present study is 0.84 when  $U^* = 4$ , which is slightly smaller than that in the experiment (0.97) (Khalak and Williamson, 1997, 1999). However, this value matches well with other comparable VIV tests conducted by Assi et al. (2010), in which the maximum value is about 0.8. Figure 4-6(b) shows that the numerical results can also well capture the dominant peaks in the spectrum of the cylinder oscillation. It can be seen that once the cylinder is vibrating in the initial branch, the dominant frequency of oscillation is close to the Strouhal frequency ( $f_s$ ) of the stationary cylinder, i.e., the dashed line in the figure. When the normalized velocity is increased to  $U^* = 3$  and  $U^* = 4$ , the cylinder starts to oscillate with two dominant peaks corresponding to  $f_s$  and the natural frequency of the cylinder in the water ( $f_w$ ) respectively. As the normalized velocity increases further and the vibrating system enters the upper and lower excitation regimes, cylinder oscillation follows neither  $f_n$  nor  $f_s$ , and it vibrates with a ‘locked’ or ‘synchronized’ frequency in between. These results are in well agreement with the test results as reported by Khalak and Williamson (1999) and Assi et al. (2010).

However, it also should be noted that there are some discrepancies between the numerical results and experimental data. Generally speaking, the numerical results match better with those obtained by Assi et al. (2010) in the upper range, and are closer to those by Khalak and Williamson (1999) in the lower branch as shown in Figure 4-6. The following three reasons may result in the discrepancies between the numerical results and experimental studies: (i) The RANS code equipped with *SST*  $K - \omega$  is adopted to simulate VIV. This model, inheritably, is unable to provide very accurate results for the VIV simulations because it reduces the fluctuations of velocity related to the turbulence of the flow and the mean value of the fluctuation is considered as equal to zero (Guilmineau and Queutey, 2004, Pan et al., 2007, Khan et al., 2018), (ii) Possible differences in the test set-up, measurement accuracy and/or the procedure of different tests can influence the responses of the cylinders. For the two tests adopted in the present study, Khalak and Williamson (1999) placed a larger cylinder with the

diameter of  $1.25D$  (where  $D$  was the diameter of the testing cylinder) coaxially to the main testing cylinder at the bottom end, and the top was rounded to match the test cylinder smoothly, while in the test by [Assi et al. \(2010\)](#), the model was designed as close as possible to the glass floor of the test section, (iii) The key parameters, namely the mass ratio  $m^*$  and damping ratio  $\zeta$  in the two tests were also slightly different. In particular,  $m^* = 2.4$  and  $\zeta = 0.0054$  in the Khalak and Williamson's test, and the corresponding values were 2.6 and 0.0069, respectively in [Assi et al. \(2010\)](#). As pointed out by [Riches and Morton \(2018\)](#), lower  $m^*$  generally gives a higher amplitude response in the upper branch, and a lower  $\zeta$  corresponds to a wider lock-in region.

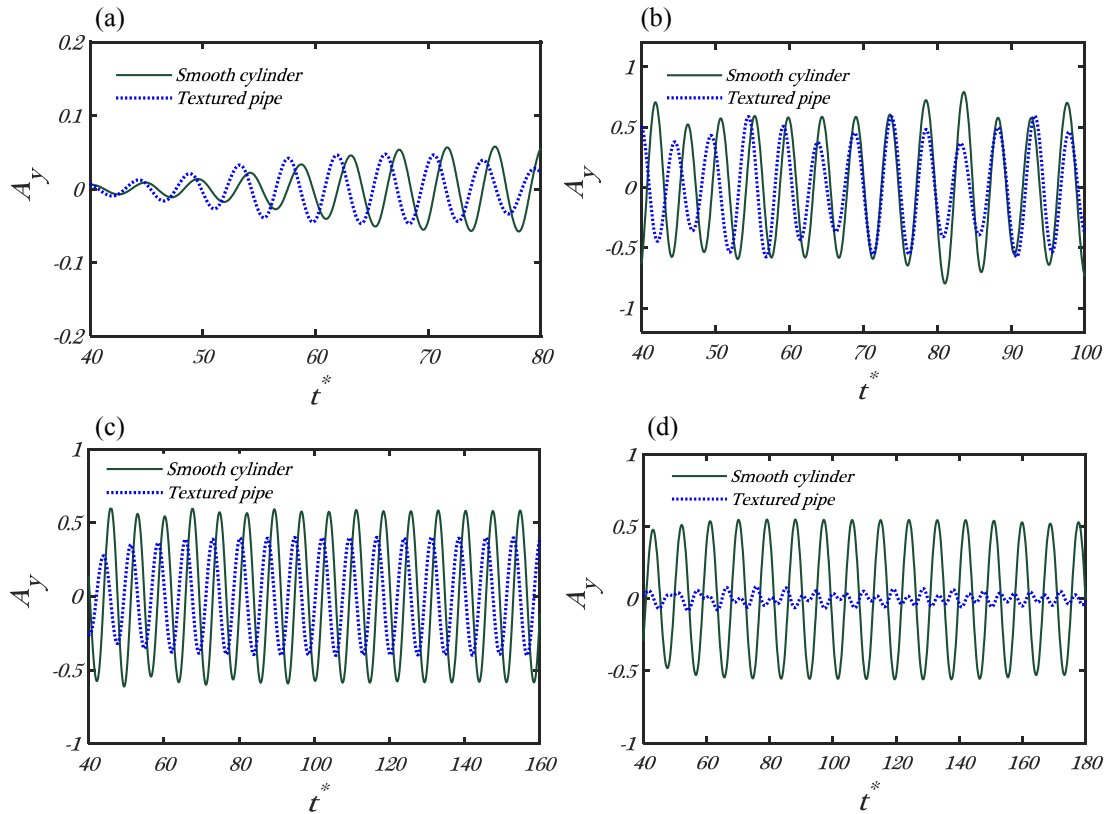
For the textured pipe, no experimental study has been carried out up to now, the direct verification is therefore not possible. However, once the FSI model for the smooth pipe is validated, it can be applied to the textured pipe because all the contributing factors such as systems' mass, spring stiffness, turbulence model and fluid domain size are the same. This verification approach have been widely adopted by many researchers. For example, [Zheng and Wang \(2017\)](#) adopted this approach in a numerical study of galloping oscillation of a cylinder with fairing and [Gao et al. \(2018b\)](#), [Gao et al. \(2018a\)](#) followed the same approach in the numerical VIV simulation of a circular cylinder with different surface roughness.

## 4.5 Results and discussion

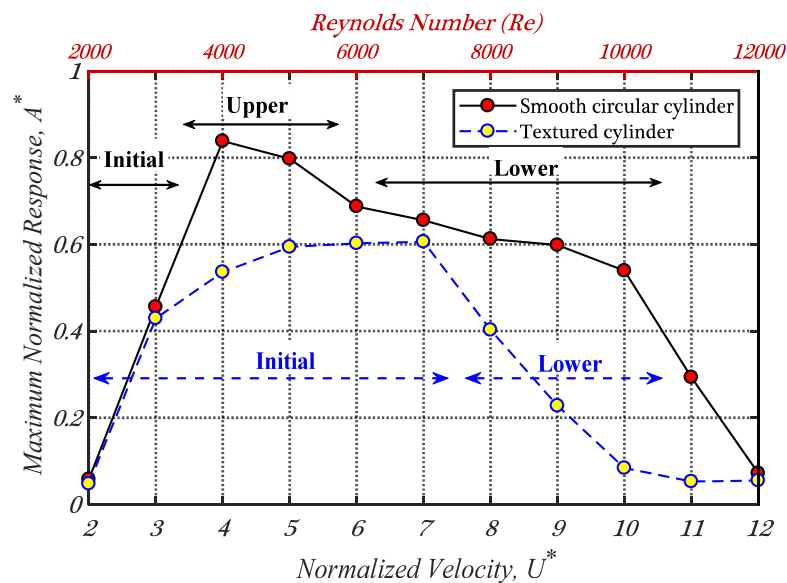
### 4.5.1 Oscillations and hydrodynamic forces

Figure 4-7 presents the non-dimensional oscillations ( $A_y = y/D$ ) of the two types of cylinders under four typical normalized velocities and the maximum amplitude of the non-dimensional oscillations under the different normalized velocities are shown in Figure 4-8. Comparing the results shown in these two figures, two general observations can be obtained: (i) The textured cylinder is effective in mitigating the VIV throughout the whole flow velocities, and the control effectiveness is more evident when the cylinder is vibrating under the relatively higher normalized velocities ( $\approx U^* > 7$ ). This is because under the larger flow velocities, as will be discussed in section 4.5.2, the textured cylinder oscillates in the non-lock-in region where the flow damps the structural vibration ([Bourguet et al., 2011](#)), and then a larger reduction could be achieved. Similar behaviours have been reported in the tests carried out by [Kiu et al. \(2011\)](#), [Park et al. \(2012\)](#), in which different roughness elements were produced on the

outer surface of the smooth cylinder, and more evident control effectiveness was obtained when the normalized velocities were relatively large. In addition, under small normalized velocities, as will be shown in section 4.5.3, the wake flow structure surrounding the cylinder is not disorganized strongly and the vortices shed in both the smooth and textured cylinders are relatively comparable.



**Figure 4-7:** Normalized time histories of the cylinder oscillations under four typical normalized velocities: (a)  $U^* = 2$ , (b)  $U^* = 5$ , (c)  $U^* = 8$  and (d)  $U^* = 10$ .



**Figure 4-8:** Comparisons of the normalized maximum amplitude responses ( $A^*$ ) between the smooth and textured cylinders.

(ii) For the conventional smooth cylinder, there are clearly three response branches with an obvious jump in the amplitude response from  $A^* = 0.46$  to  $A^* = 0.84$  when the normalized velocity is increased from  $U^* = 3$  to  $U^* = 4$ , whereas only a slight increase from  $A^* = 0.43$  to  $A^* = 0.54$  is obtained in the textured pipe. The appearance of a noticeable jump in the amplitude response of the smooth cylinder is associated with the response transition from the initial branch to the upper branch ([Khalak and Williamson, 1999](#)). Therefore, the lack of an obvious jump in the vibration response of the textured pipe shows that this transition does not occur in the textured pipe. It might be then reasonable to define only two response branches, namely the initial branch and the lower branch for the textured pipe, as suggested by [Khalak and Williamson \(1999\)](#) for the classical VIV response of a cylinder with high mass-damping ratio. The initial branch can be defined starting from almost the rest condition to the normalized velocity resulting in the highest VIV amplitude (i.e., from  $U^* \approx 2$  to  $U^* \approx 7$ ), while the rest belong to the lower branch. It should be mentioned that the interval of the normalized velocity adopted in the present study is 1, a smaller interval is needed in order to precisely define the boundaries of different VIV response regimes. This is, however, out of the scope of the present study.

The different VIV response regimes can also be characterized by plotting the phase angle ( $\phi$ ) between the lift force  $C_L(t)$  and the cylinder oscillations  $A_y(t)$ . To calculate the instantaneous phase angle  $\phi(t)$  of the cylinder, Hilbert transform ([Bracewell, 2000](#)) is adopted in the present study as suggested by [Khalak and Williamson \(1999\)](#). This procedure basically includes two steps: (i) under each reduced velocity, the displacement and lift force time histories of the cylinder can be calculated, Hilbert Transform is then applied to obtain the instantaneous values of  $\phi(t)$  based on these two time histories, (ii) After obtaining  $\phi(t)$ , the probability density function (PDF) of phase angles is calculated to identify the dominant phase angle, i.e., the phase angle that most frequently appears in the analysed reduced velocity. These dominant phase angles are plotted in Figure 4-9. It is commonly known that for the smooth cylinder the phase angle is  $\phi \approx 0^\circ$  in the initial and upper response branches, and  $\phi \approx 180^\circ$  for the lower branch ([Khalak and Williamson, 1999](#)). As shown, the commonly expected phase angles are well captured for the smooth cylinder. It is almost  $0^\circ$  over the initial ( $U^* \approx 2 - 3$ ) and upper regimes ( $U^* \approx 4 - 5$ ), and virtually  $180^\circ$  in the lower branch ( $U^* \approx 6 - 11$ ). The characteristic of transition from the upper branch to the lower one

is also captured as shown in the figure; when the smooth pipe is vibrating under  $U^* = 5$ , two dominant phase angles are obtained, indicating the transition from the upper to the lower excitation regime as noted by [Khalak and Williamson \(1999\)](#). For the textured pipe, no such sudden phase change is obtained. As shown, the phase angle gradually increases from almost  $0^\circ$  to about  $180^\circ$  when the normalized velocities change from 2 to 8, and then maintain at about  $180^\circ$ , indicating the textured cylinder is vibrating in the lower branch under these normalized velocities. These results again support the classification of two response branches for the textured cylinder as defined above. In other words, the upper branch, in which the vibration amplitude is remarkably large, can be eliminated by the textured pipe.

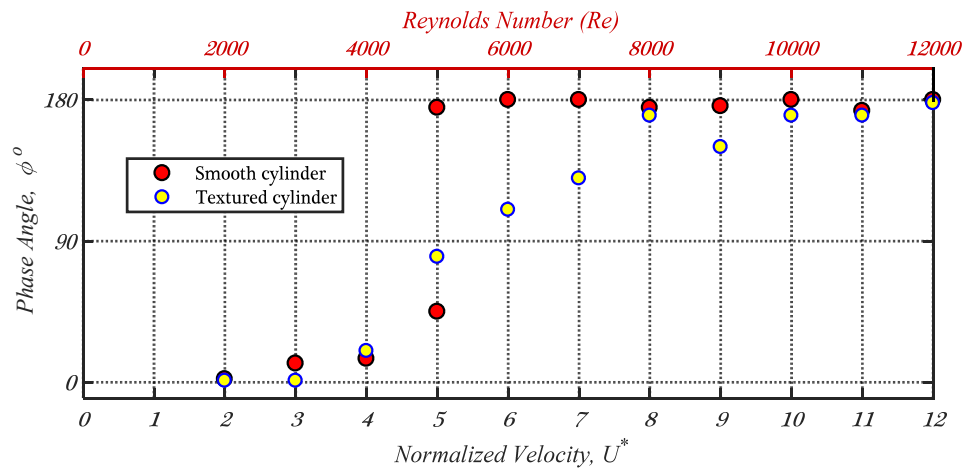


**Figure 4-9:** Comparisons of the phase angle ( $\phi$ ) between the smooth and textured cylinders. Besides the amplitude of oscillation, it is also desired to mitigate the drag force acting on the cylinder ([Dhanak and Xiros, 2016](#)). Figure 4-10 presents the non-dimensional time histories of the lift coefficient ( $C_L$ ) and drag coefficient ( $C_D$ ) obtained from both the smooth and textured cylinders under three typical normalized velocities, and Figure 4-11 compares the corresponding maximum values (i. e.,  $C_L^{max}$  and  $C_D^{max}$ ). It can be seen that the textured cylinder can significantly diminish the hydrodynamic forces. The reduction in the drag force can be explained by the mean wake streamlines patterns as depicted in Figure 4-12 for both the smooth and textured cylinders at the beginning of the separation flow. It is apparent that except for  $U^* = 2$ , the recirculation length behind the textured cylinder is much longer than that in the smooth cylinder. As indicated by [Breuer \(1998\)](#), the longer wake recirculation corresponds to the lower drag force and back-pressure behind the cylinder. The drop in the lift force is believed to be caused by the delayed separation point, which causes narrow wakes behind the textured cylinder. In fact, the textured cylinder, which has distorted surfaces in both

the cross-sectional and longitudinal directions, can cause local randomness in the flow separation points, and this eventually results in the lower lift forces and thus lower response amplitudes. It is also supported by comparing the iso-surfaces of the wake vortex structures as shown in Figure 4-13 and Figure 4-14 for two different normalized velocities. For the smooth cylinder, the commonly well-formed wake loops are clearly organized. Whereas in the case of textured cylinder, the shear layers are highly disorganized and the wake vortices are rolling up in a highly irregular manner. The poor roll up of shear layers and alternative generation of vortices from the top and bottom of the textured cylinder contribute to a lower VIV amplitude and lift force in this type of cylinder. In addition, as is shown in Figure 4-14, due to the local facets of the textured pipe, the stable spanwise correlation of vortex shedding disappears in this pipe, which also contributes to the significant reduction of the amplitude response as indicated by [Park et al. \(2012\)](#).

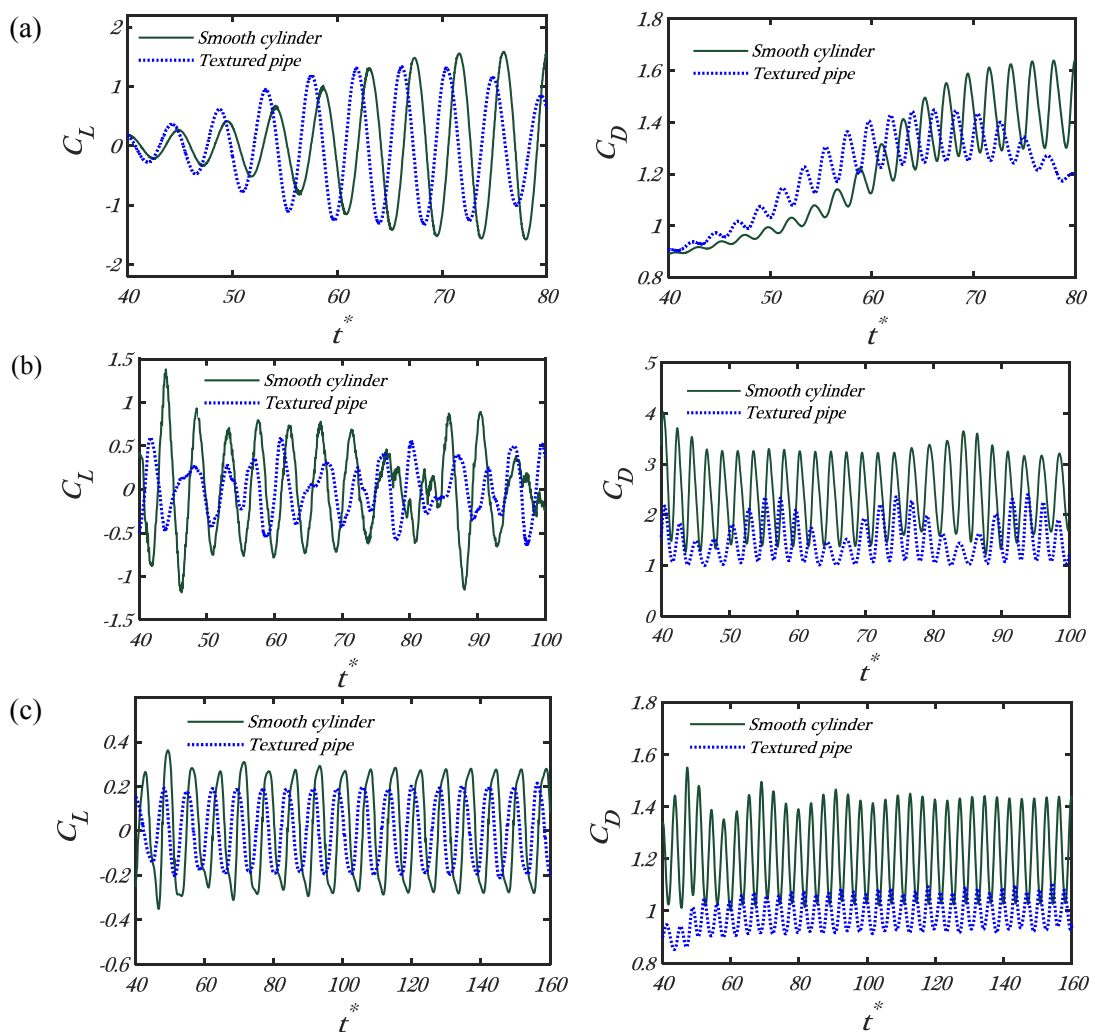


**Figure 4-10:** Normalized hydrodynamic force coefficient time histories of the smooth and textured cylinders under three typical normalized velocities: (a)  $U^* = 2$ , (b)  $U^* = 5$  and (c)  $U^* = 8$ .

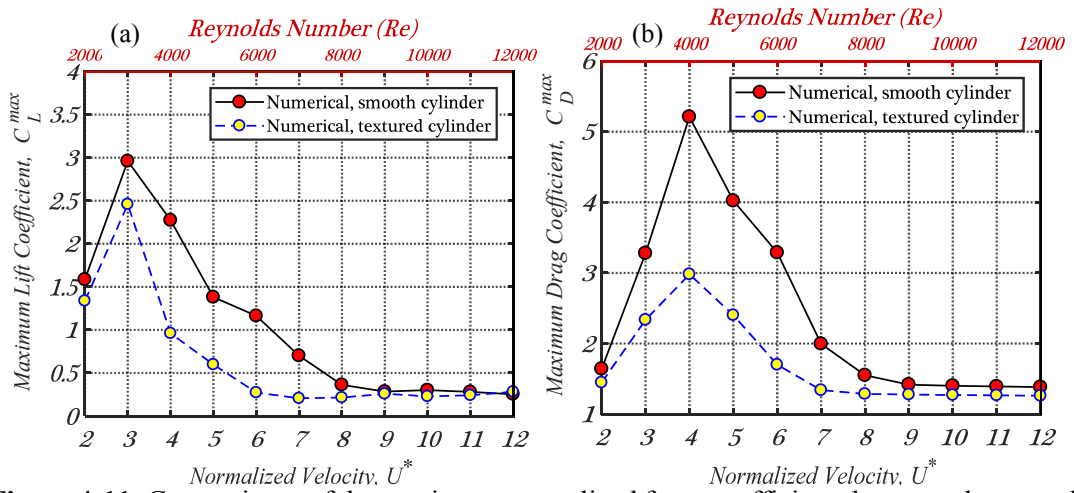


**Figure 4-11:** Comparisons of the maximum normalized force coefficients between the smooth and textured cylinders under different normalized velocities  $U^*$ .

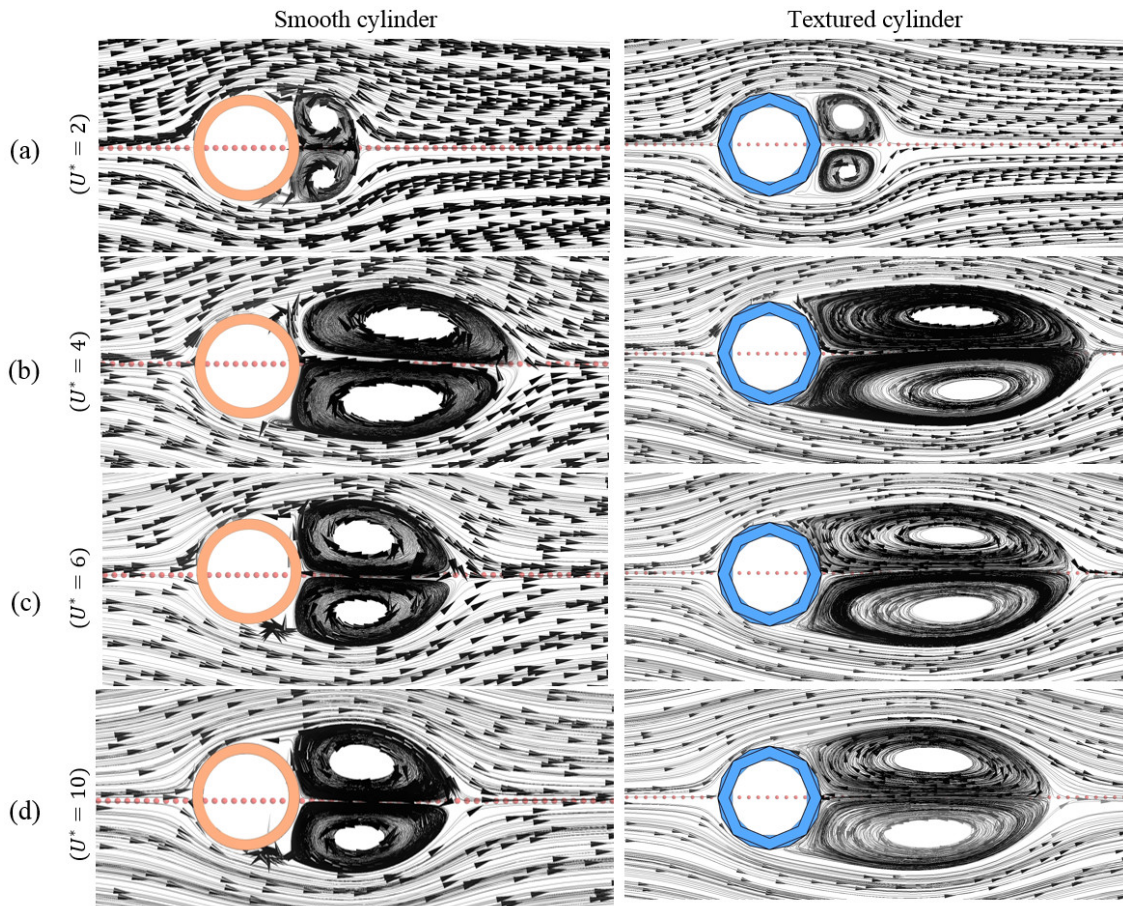


**Figure 4-12:** Comparisons of the mean streamlines between the smooth and textured cylinders under different normalized velocities: (a)  $U^* = 2$  (b)  $U^* = 4$ , (c)  $U^* = 6$  and (d)  $U^* = 10$ .

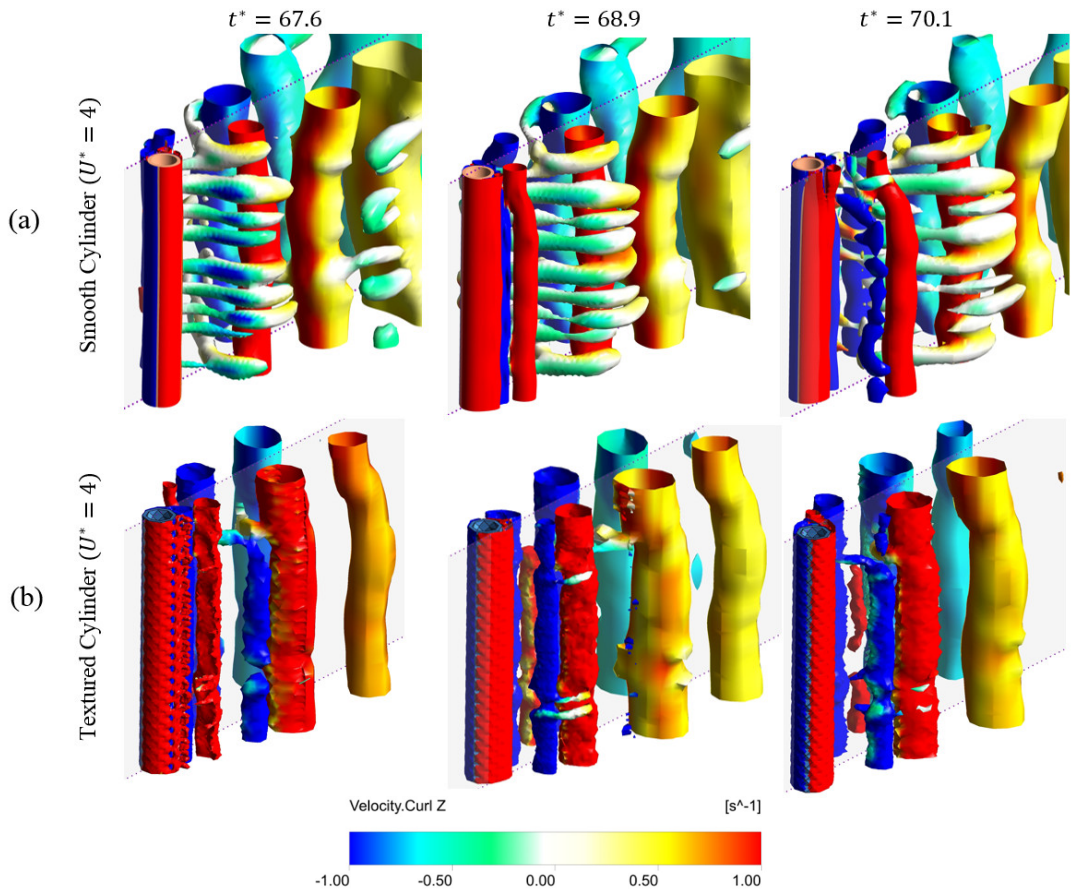


**Figure 4-13:** Comparisons of the  $Q$  Iso-surfaces of the vortex streets between the (a) smooth cylinder and (b) textured cylinder vibrating under  $U^* = 4$ .

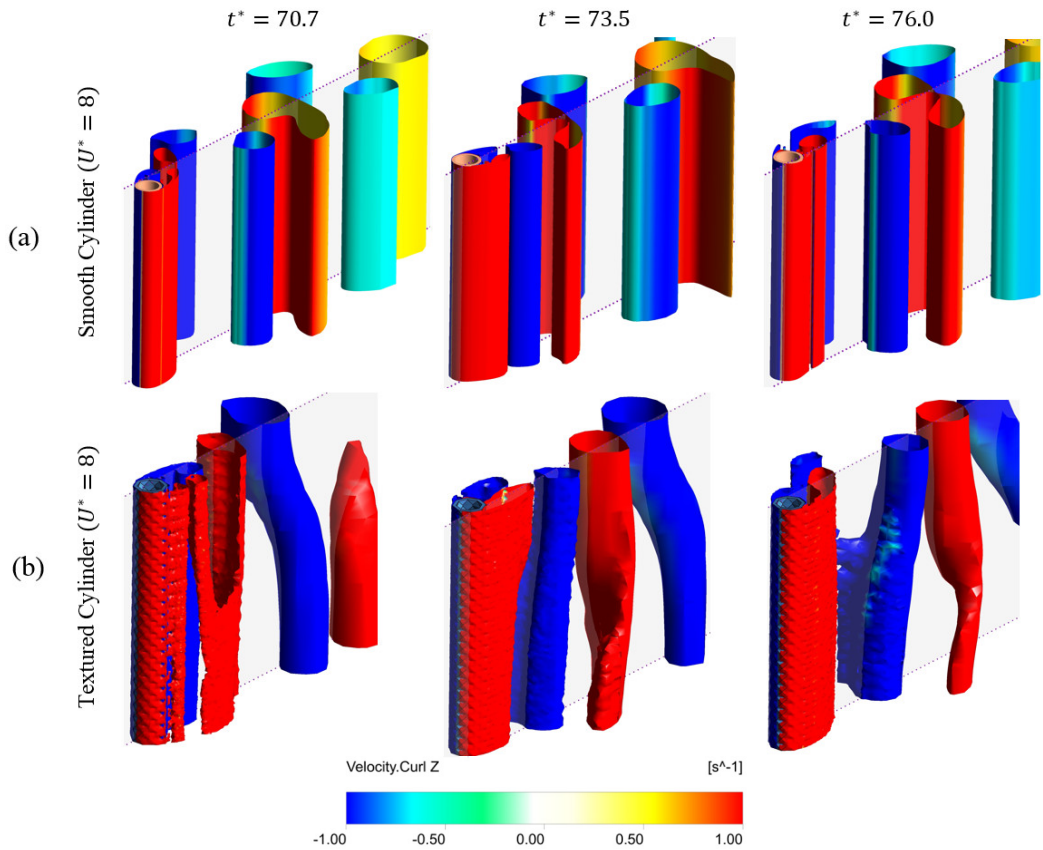


**Figure 4-14:** Comparisons of the  $Q$  Iso-surfaces of the vortex streets between the (a) smooth cylinder and (b) textured cylinder vibrating under  $U^* = 8$ .



### 4.5.2 Response frequencies

The normalized PSDs of the cylinder oscillations under different normalized velocities are plotted in Figure 4-15, and Figure 4-16 shows the dominant peaks of the frequency ratio ( $f^*$ ) under each normalized velocity. As shown in these figures, when the normalized velocity is very small ( $U^* = 2$ ), only one obvious peak, which is close to the vortex shedding of the static cylinder or the Strouhal frequency ( $f_s$ ) (the dashed line in Figure 4-16), appears in both the smooth and textured cylinders. When the normalized velocity increases to  $U^* = 3$  and 4, two dominant peaks are observed. In the smooth cylinder, these frequencies correspond to  $f_s$  and the natural frequency of the cylinder in the water ( $f_w$ ) respectively ([Matin Nikoo et al., 2018b](#)). For the textured pipe, the peaks are however slightly larger than  $f_s$ . [Khalak and Williamson \(1999\)](#) attributed this disparity to the influence of “effective added mass ( $C_{EA}$ )” that includes an apparent effect due to the total transverse fluid force in-phase with the body acceleration. When the smooth cylinder is subjected to the relatively high normalized velocities (e.g.  $U^* = 6 - 11$ ), the frequency ratio  $f^*$  is pulled away from the unity (horizontal line in Figure 4-16). This phenomenon was also captured in the test by [Khalak and Williamson \(1999\)](#), and it was called “non-classical” synchronization behaviour of  $f^*$ . Textured cylinder, on the other hand, shows a different trend. It yields the “classical” synchronization behaviour under the normalized velocity of  $U^* = 6$  and 7, whereas the “non-classical” behaviour is observed for  $U^* = 8 - 10$ .

This peculiarity raises the possibility of identifying the lock-in or synchronization regime in the textured pipe under VIV. To this end, the precise definition of lock-in regime as specified by [Khalak and Williamson \(1999\)](#) is adopted in this study: the lock-in regime is defined as the matching of the transverse force frequency ( $f_{lift}$ ) with the body oscillation frequency ( $f_o$ ). It should be noted that the latter frequency is approximately equal to the system natural frequency throughout the lock-in regime, i.e.,  $f_o \approx f_n$ . Moreover, for the VIV of a rigid cylinder with one-degree-of-freedom in the steady current, the vortex-shedding frequency is identical to the lift-force frequency ([Gao et al., 2015](#), [Gao et al., 2018a](#)). Therefore, Figure 4-17, which shows the dominant peaks of the normalized frequency of the transverse force ( $f_{lift}^* = f_{lift}/f_n$ ) over different normalized velocities, can be used to detect the lock-in or synchronization regime for both the smooth and textured cylinders. Based on which, the smooth cylinder is synchronized under the normalized velocities from  $U^* \approx 4$  to

$U^* \approx 10$ , whereas for the textured cylinder, this range can be defined as  $U^* \approx 4$  to  $U^* \approx 8$ . Although the interval (unity) of the normalized velocities in the current study is relatively big to precisely define the boundaries of different regimes as discussed above, the results in Figure 4-17 show that the textured cylinder can make the lock-in regime shorter compared to the smooth pipe, which again demonstrates the advantage of textured cylinder for VIV suppression.

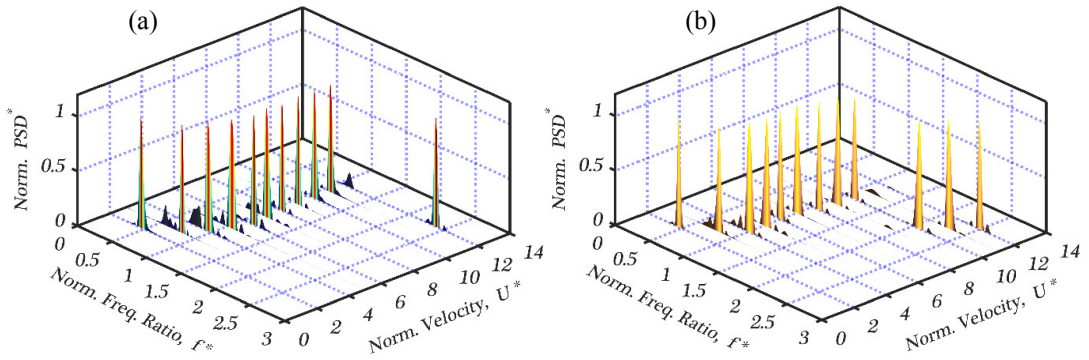


**Figure 4-15:** Normalized PSDs of the cylinder vibrations: (a) smooth cylinder and (b) textured cylinder.

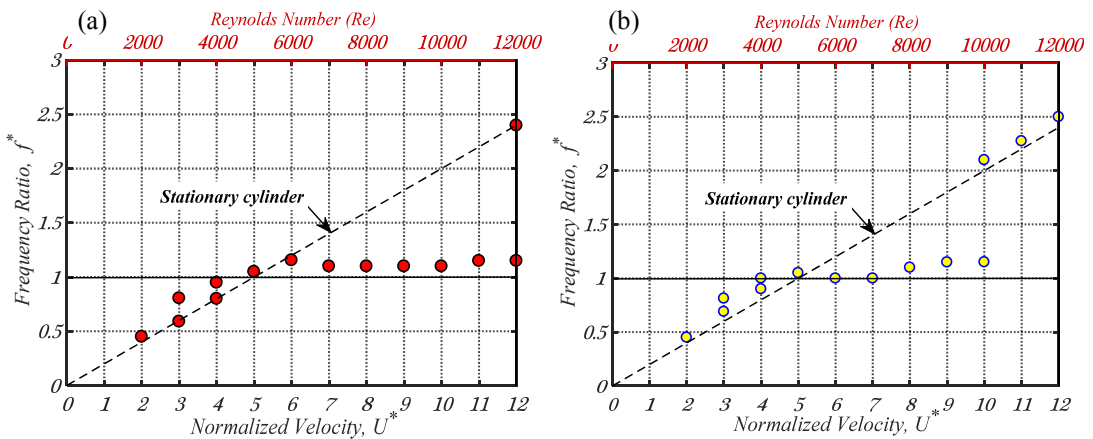


**Figure 4-16:** Dominant peaks in the spectrum of the normalized cylinder oscillations: (a) smooth cylinder and (b) textured cylinder.

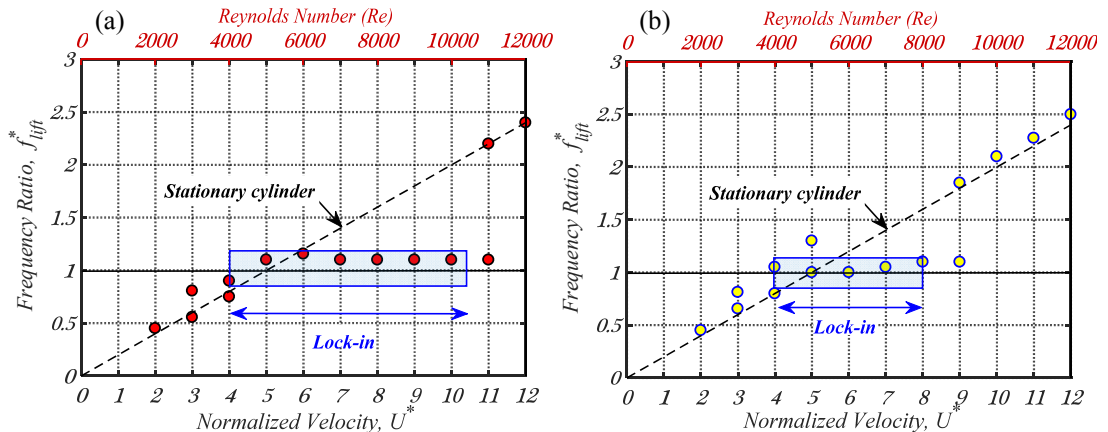


**Figure 4-17:** Dominant peaks in the spectrum of the normalized transverse force frequency: (a) smooth cylinder and (b) textured cylinder.

### 4.5.3 Wake vortex modes

The wake vortex patterns from different cylinders are discussed in this section. Figure 4-18 compares the 3-D vortex streets captured for the smooth and textured cylinders under different normalized velocities, and the 2-D vortex wake modes at the middle section of the cylinders ( $Z/D = 4$ ) are shown in Figure 4-19. It is well-known that for the conventional smooth cylinder, different wake modes are associated with the different excitation branches ([Khalak and Williamson, 1999](#)). As shown in Figure 4-18(a) and Figure 4-19(a), the classical 2S vortex formation mode with two dominant single vortices shedding alternately per cycle is observed for the smooth cylinder at the initial branch with the normalized velocity  $U^* = 2$ . This mode is also obtained in the textured cylinder vibrating in the initial branch. Figure 4-18(b) and Figure 4-19(b) show that when the smooth cylinder vibrates in the upper regime, the wake mode switches to the 2P vortex pattern consisting of two pairs of vortices shedding from two sides of the cylinder per cycle. For the textured cylinder, although the wake vortex pattern also switches to the 2P mode, two features should be noted: (i) The secondary vortex in the 2P mode is remarkably stronger as compared to that in the smooth cylinder, and (ii) the width of the wake vortices is smaller than the smooth case (refer to Figure 4-19(b)). As the normalized velocity continues to increase, the VIV responses of the both cylinders transit into the lower branch (Figure 4-18(c) and Figure 4-19(c&d)). Consistent with the experimental study, 2P wake mode is captured for the smooth cylinder in this regime, whereas the wake mode is back to the 2S mode again in the case of textured cylinder, and the width of the wake vortices is narrower than the smooth cylinder. This is because of the low amplitude vibration of the textured cylinder in this regime.

As highlighted in Figure 4-19, the textured cylinder can obviously reduce the width of the wake region, which is associated with the phenomenon of boundary layer transition from a laminar to turbulent state ([Kiu et al., 2011](#), [Behara and Mittal, 2011](#), [Deshpande et al., 2017](#)). These results (i.e., the well capture of the boundary layer transition), in turn, reflect the accuracy and validity of the developed numerical model in predicting the VIV of textured pipe.

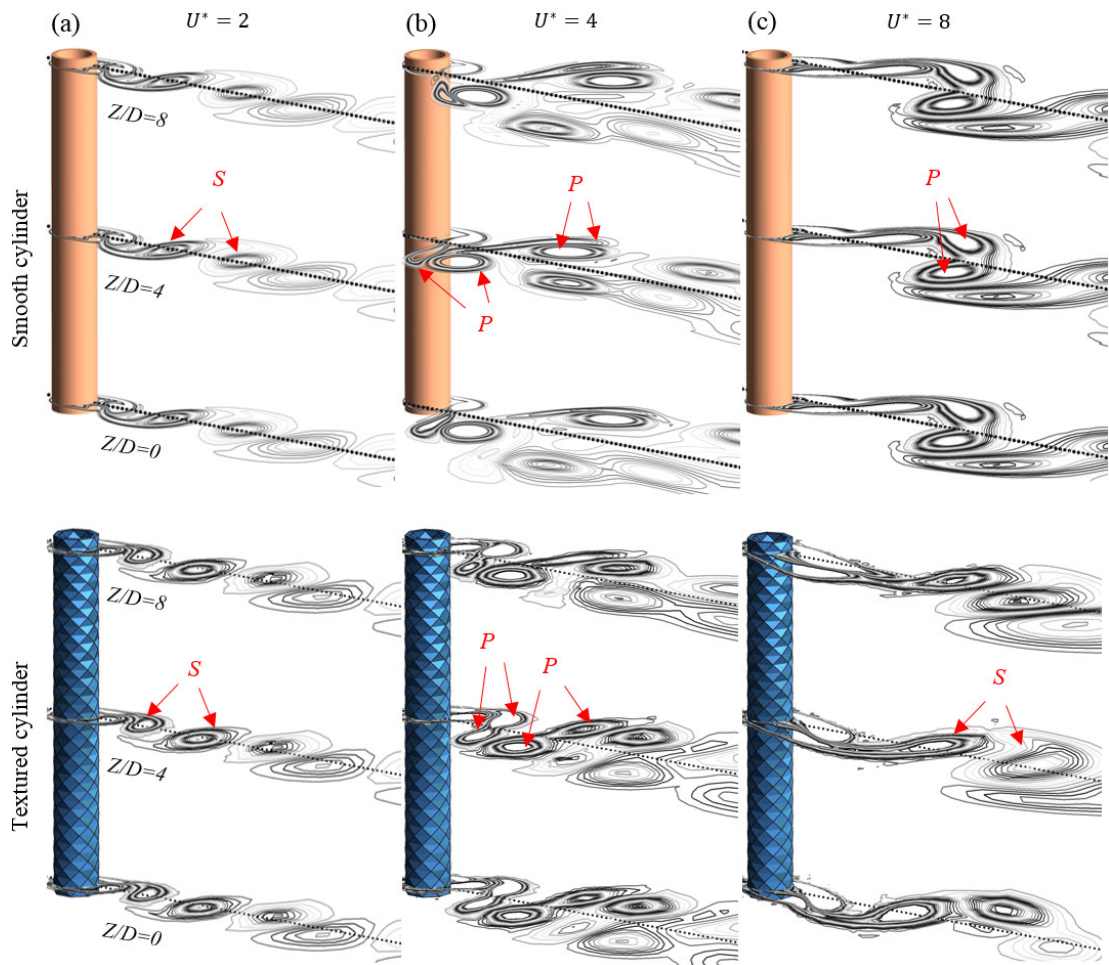


**Figure 4-18:** Contours of wake vortex streets along the smooth and textured cylinders at three cross sections ( $Z/D = 0, 4$  and  $8$ ) under different normalized velocities: (a)  $U^* = 2$  (b)  $U^* = 4$  and (c)  $U^* = 8$ .

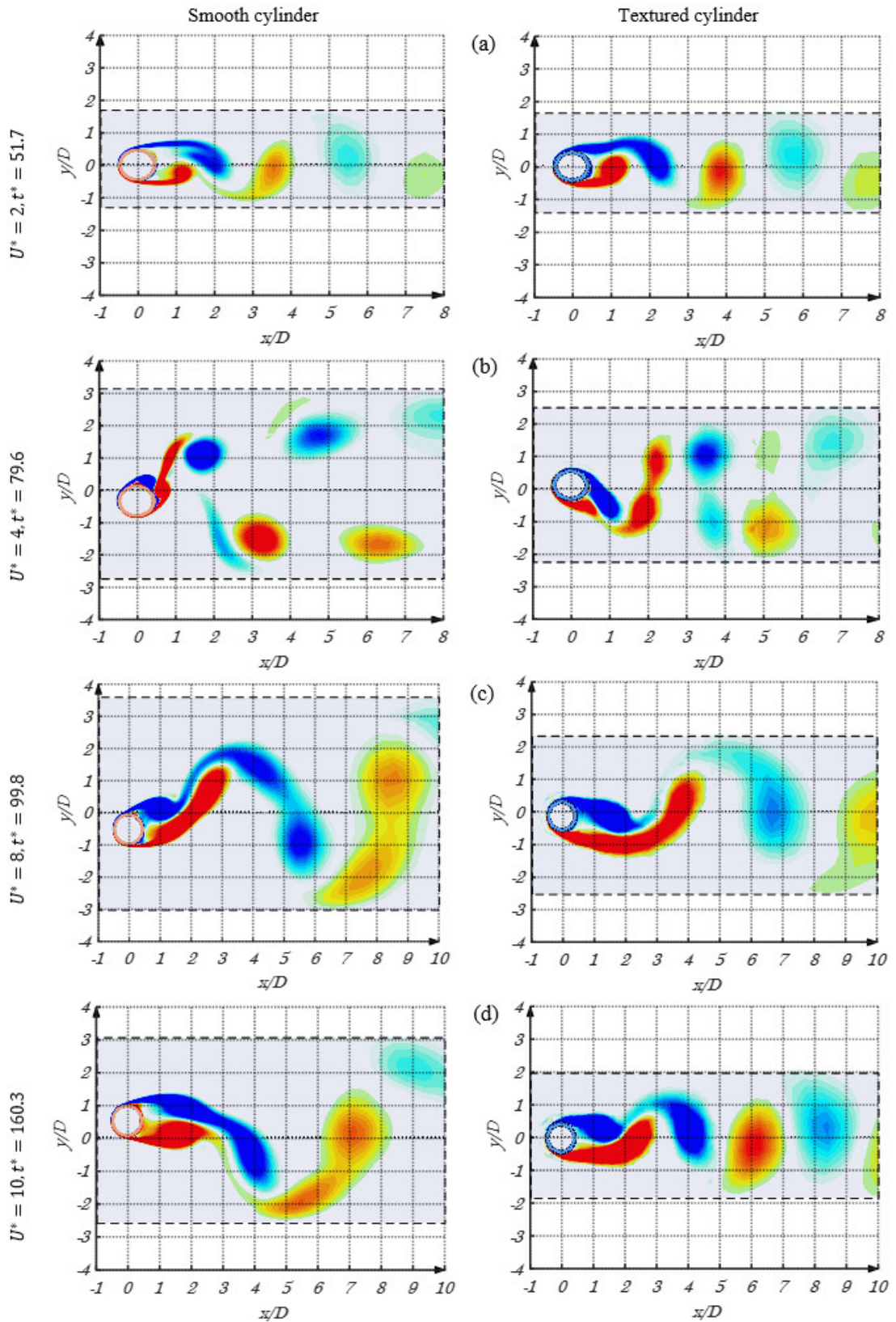


**Figure 4-19:** The instantaneous vortex wake modes obtained for the smooth and textured cylinders at different normalized velocities: (a)  $U^* = 2$  (b)  $U^* = 4$  (c)  $U^* = 8$  and (d)  $U^* = 10$ .

Overall, the results obtained in this study indicate that using the textured cylinder can obviously mitigate VIV. Together with its advantage on the enhanced propagation

buckling capacity, this pipe is believed has great application potentials for the offshore industry. It should be noted that all the above results are obtained based on the full-diamond shape as shown in Figure 4-1. This shape, on the other hand, does not necessarily result in the most evident VIV suppression. Obtaining the optimal shape of the textured pipe for VIV control is an interesting topic. It is, however, out of the scope of the present study.

#### **4.6 Conclusion**

Textured pipe has the improved propagating buckling capacity compared to the smooth pipe. Due to its special geometry, this pipe is believed to be able to obviously reduce the vortex-induced vibration (VIV). This paper carries out 3-D numerical simulations on the effectiveness of using a typical full-diamond (octagonal) textured cylinder for VIV control. A two-way coupled fluid-structure interaction (FSI) framework is developed by coupling the ANSYS mechanical and FLUENT solvers together. For comparison, an equivalent smooth pipe is also numerically investigated. Numerical results showed that:

- i) The textured cylinder can more evidently suppress VIV especially when the cylinder is vibrating under a relatively large normalized velocity.
- ii) The upper oscillation regime which commonly exists in the conventional smooth cylinder is eliminated by the textured cylinder.
- iii) The textured pipe can evidently reduce the hydrodynamic forces associated with the VIV phenomenon.
- iv) The textured cylinder is capable of shortening the range of lock-in or synchronization regime.

#### **4.7 References**

- Abrahamsen Prsic, M., Ong, M.C., Pettersen, B., Myrhaug, D. (2014). Large eddy simulations of flow around a smooth circular cylinder in a uniform current in the subcritical flow regime. *Ocean Engineering*, 77, 61-73.
- Achenbach, E. (1971). Influence of surface roughness on the cross-flow around a circular cylinder. *Journal of Fluid Mechanics*, 46 (2), 321-335.
- ANSYS®. (2016). Academic research, release 17.2, Theory guide.
- Apelt, C.J., West, G.S., Szewczyk, A.A. (1973). The effects of wake splitter plates on the flow past a circular cylinder in the range  $10^4 < Re < 5 \times 10^4$ . *Journal of Fluid Mechanics*, 61 (1), 187-198.

- Argyropoulos, C.D., Markatos, N.C. (2015). Recent advances on the numerical modelling of turbulent flows. *Applied Mathematical Modelling*, 39 (2), 693-732.
- Assi, G.R.S., Bearman, P.W., Meneghini, J.R. (2010). On the wake-induced vibration of tandem circular cylinders: the vortex interaction excitation mechanism. *Journal of Fluid Mechanics*, 661, 365-401.
- Assi, G.R.S., Bearman, P.W., Tognarelli, M.A. (2014). On the stability of a free-to-rotate short-tail fairing and a splitter plate as suppressors of vortex-induced vibration. *Ocean Engineering*, 92, 234-244.
- Bearman, P., Branković, M. (2004). Experimental studies of passive control of vortex-induced vibration. *European Journal of Mechanics - B/Fluids*, 23 (1), 9-15.
- Bearman, P., Harvey, J. (1993). Control of circular cylinder flow by the use of dimples. *AIAA Journal*, 31 (10), 1753-1756.
- Behara, S., Mittal, S. (2011). Transition of the boundary layer on a circular cylinder in the presence of a trip. *Journal of Fluids and Structures*, 27 (5), 702-715.
- Bourguet, R., Karniadakis, G.E., Triantafyllou, M.S. (2011). Lock-in of the vortex-induced vibrations of a long tensioned beam in shear flow. *Journal of Fluids and Structures*, 27 (5), 838-847.
- Bracewell, R.N. (2000). The Fourier transform and its applications, Third ed. *McGraw-Hill New York*.
- Breuer, M. (1998). Numerical and modeling influences on large eddy simulations for the flow past a circular cylinder. *International Journal of Heat and Fluid Flow*, 19 (5), 512-521.
- Callens, S.J.P., Zadpoor, A.A. (2018). From flat sheets to curved geometries: Origami and kirigami approaches. *Materials Today*, 21 (3), 241-264.
- Cebeci, T. (2004). Analysis of turbulent flows. *Elsevier*, Oxford.
- Cheng, W., Pullin, D.I., Samtaney, R. (2017). Large-eddy simulation of flow over a grooved cylinder up to transcritical Reynolds numbers. *Journal of Fluid Mechanics*, 835, 327-362.
- Choi, H., Jeon, W.-P., Kim, J. (2008). Control of flow over a bluff body. *Annu. Rev. Fluid Mech.*, 40, 113-139.
- Cicolin, M.M., Assi, G.R.S. (2017). Experiments with flexible shrouds to reduce the vortex-induced vibration of a cylinder with low mass and damping. *Applied Ocean Research*, 65, 290-301.
- Deshpande, R., Desai, A., Kanti, V., Mittal, S. (2017). Experimental investigation of boundary layer transition in flow past a bluff body. *Journal of Physics: Conference Series*, 822, 012003.
- Dhanak, M.R., Xiros, N.I. (2016). Springer handbook of ocean engineering. *Springer*, United States.
- Dong, S., Triantafyllou, G., Karniadakis, G. (2008). Elimination of vortex streets in bluff-body flows. *Physical Review Letters*, 100 (20), 204501.
- El-Gammal, M., Hangan, H., King, P. (2007). Control of vortex shedding-induced effects in a sectional bridge model by spanwise perturbation method. *Journal of Wind Engineering and Industrial Aerodynamics*, 95 (8), 663-678.
- Gao, Y., Fu, S., Ren, T., Xiong, Y., Song, L. (2015). VIV response of a long flexible riser fitted with strakes in uniform and linearly sheared currents. *Applied Ocean Research*, 52, 102-114.
- Gao, Y., Zong, Z., Zou, L., Jiang, Z. (2018a). Effect of surface roughness on vortex-induced vibration response of a circular cylinder. *Ships and Offshore Structures*, 13 (1), 28-42.
- Gao, Y., Zong, Z., Zou, L., Takagi, S., Jiang, Z. (2018b). Numerical simulation of vortex-induced vibration of a circular cylinder with different surface roughnesses. *Marine Structures*, 57, 165-179.

- Glezer, A., Amitay, M. (2002). Synthetic jets. *Annual review of fluid mechanics*, 34 (1), 503-529.
- Grant, R., Patterson, D. (1977). Riser fairing for reduced drag and vortex suppression. Offshore Technology Conference, Houston, Texas.
- Gsell, S., Bourguet, R., Braza, M. (2019). One versus two-degree-of-freedom vortex-induced vibrations of a circular cylinder at  $Re=3900$ . *Journal of Fluids and Structures*, 85, 165-180.
- Guilmineau, E., Queutey, P. (2004). Numerical simulation of vortex-induced vibration of a circular cylinder with low mass-damping in a turbulent flow. *Journal of Fluids and Structures*, 19 (4), 449-466.
- Holland, V., Tezdogan, T., Oguz, E. (2017). Full-scale CFD investigations of helical strakes as a means of reducing the vortex induced forces on a semi-submersible. *Ocean Engineering*, 137, 338-351.
- Jung, J.H., Yoon, H.S. (2014). Large eddy simulation of flow over a twisted cylinder at a subcritical Reynolds number. *Journal of Fluid Mechanics*, 759, 579-611.
- Karampour, H., Albermani, F. (2016). Buckle interaction in textured deep subsea pipelines. *Ships and Offshore Structures*, 11 (6), 625-635.
- Karampour, H., Alrsai, M., Albermani, F., Guan, H., Jeng, D.S. (2017). Propagation buckling in subsea pipe-in-pipe systems. *Journal of Engineering Mechanics*, 143 (9), 1-10.
- Khalak, A., Williamson, C.H.K. (1997). Fluid forces and dynamics of a hydroelastic structure with very low mass and damping. *Journal of Fluids and Structures*, 11 (8), 973-982.
- Khalak, A., Williamson, C.H.K. (1999). Motions, forces and mode transitions in vortex-induced vibrations at low mass-damping. *Journal of Fluids and Structures*, 13 (7-8), 813-851.
- Khalilpasha, H., Albermani, F. (2013). Textured deep subsea pipelines. *International Journal of Mechanical Sciences*, 68, 224-235.
- Khan, N.B., Ibrahim, Z., Khan, M.I., Hayat, T., Javed, M.F. (2018). VIV study of an elastically mounted cylinder having low mass-damping ratio using RANS model. *International Journal of Heat and Mass Transfer*, 121, 309-314.
- Kiu, K.Y., Stappenbelt, B., Thiagarajan, K.P. (2011). Effects of uniform surface roughness on vortex-induced vibration of towed vertical cylinders. *Journal of Sound and Vibration*, 330 (20), 4753-4763.
- Ko, N., Leung, Y., Chen, J. (1987). Flow past v-groove circular cylinders. *AIAA Journal*, 25 (6), 806-811.
- Law, Y.Z., Jaiman, R.K. (2017). Wake stabilization mechanism of low-drag suppression devices for vortex-induced vibration. *Journal of Fluids and Structures*, 70, 428-449.
- Lucor, D., Foo, J., Karniadakis, G.E. (2005). Vortex mode selection of a rigid cylinder subject to VIV at low mass-damping. *Journal of Fluids and Structures*, 20 (4), 483-503.
- Matin Nikoo, H., Bi, K., Hao, H. (2017). Passive vibration control of cylindrical offshore components using pipe-in-pipe (PIP) concept: An analytical study. *Ocean Engineering*, 142, 39-50.
- Matin Nikoo, H., Bi, K., Hao, H. (2018a). Effectiveness of using pipe-in-pipe (PIP) concept to reduce vortex-induced vibrations (VIV): Three-dimensional two-way FSI analysis. *Ocean Engineering*, 148 (Supplement C), 263-276.
- Matin Nikoo, H., Bi, K., Hao, H. (2018b). Three-dimensional vortex-induced vibration of a circular cylinder at subcritical Reynolds numbers with low-Re correction. *Marine Structures*, Under Review.
- McClure, J., Yarusevych, S. (2016). Vortex shedding and structural loading characteristics of finned cylinders. *Journal of Fluids and Structures*, 65, 138-154.



- Menter, F.R. (1994). Two-equation eddy-viscosity turbulence models for engineering applications. *AIAA Journal*, 32 (8), 1598-1605.
- Nishino, T., Roberts, G.T., Zhang, X. (2008). Unsteady RANS and detached-eddy simulations of flow around a circular cylinder in ground effect. *Journal of Fluids and Structures*, 24 (1), 18-33.
- Owen, J.C., Bearman, P.W., Szewczyk, A.A. (2001). Passive control of VIV with drag reduction. *Journal of Fluids and Structures*, 15 (3), 597-605.
- Pan, Z.Y., Cui, W.C., Miao, Q.M. (2007). Numerical simulation of vortex-induced vibration of a circular cylinder at low mass-damping using RANS code. *Journal of Fluids and Structures*, 23 (1), 23-37.
- Park, H., Bernitsas, M.M., Kumar, R.A. (2012). Selective roughness in the boundary layer to suppress flow-induced motions of circular cylinder at  $30,000 < Re < 120,000$ . *Journal of Offshore Mechanics and Arctic Engineering*, 134 (4), 041801.
- Prasanth, T., Mittal, S. (2008). Vortex-induced vibrations of a circular cylinder at low Reynolds numbers. *Journal of Fluid Mechanics*, 594, 463-491.
- Rashidi, S., Hayatdavoodi, M., Esfahani, J.A. (2016). Vortex shedding suppression and wake control: A review. *Ocean Engineering*, 126, 57-80.
- Riches, G., Morton, C. (2018). One degree-of-freedom vortex-induced vibrations at constant Reynolds number and mass-damping. *Experiments in Fluids*, 59 (10), 157.
- Roshko, A. (1961). Experiments on the flow past a circular cylinder at very high Reynolds number. *Journal of Fluid Mechanics*, 10 (3), 345-356.
- Senga, H., Larsen, C.M. (2017). Forced motion experiments using cylinders with helical strakes. *Journal of Fluids and Structures*, 68, 279-294.
- Shiels, D., Leonard, A., Roshko, A. (2001). Flow-induced vibration of a circular cylinder at limiting structural parameters. *Journal of Fluids and Structures*, 15 (1), 3-21.
- Singh, S.P., Mittal, S. (2005). Vortex-induced oscillations at low Reynolds numbers: Hysteresis and vortex-shedding modes. *Journal of Fluids and Structures*, 20 (8), 1085-1104.
- Song, Z., Duan, M., Gu, J. (2017). Numerical investigation on the suppression of VIV for a circular cylinder by three small control rods. *Applied Ocean Research*, 64, 169-183.
- Soumya, S., Prakash, K.A. (2017). Effect of splitter plate on passive control and drag reduction for fluid flow past an elliptic cylinder. *Ocean Engineering*, 141, 351-374.
- Strykowski, P.J., Sreenivasan, K.R. (1990). On the formation and suppression of vortex 'shedding' at low Reynolds numbers. *Journal of Fluid Mechanics*, 218, 71-107.
- Sui, J., Wang, J., Liang, S., Tian, Q. (2016). VIV suppression for a large mass-damping cylinder attached with helical strakes. *Journal of Fluids and Structures*, 62, 125-146.
- Tu, J., Yeoh, G.H., Liu, C. (2018). Computational fluid dynamics: a practical approach. *Butterworth-Heinemann*.
- Wang, C., Tang, H., Yu, S.C.M., Duan, F. (2016). Active control of vortex-induced vibrations of a circular cylinder using windward-suction- leeward-blowing actuation. *Physics of Fluids*, 28 (5), 053601.
- Wang, C., Tang, H., Yu, S.C.M., Duan, F. (2017). Control of vortex-induced vibration using a pair of synthetic jets: Influence of active lock-on. *Physics of Fluids*, 29 (8), 083602.

- Wang, E., Xiao, Q. (2016). Numerical simulation of vortex-induced vibration of a vertical riser in uniform and linearly sheared currents. *Ocean Engineering*, 121, 492-515.
- Wang, K., Ji, C., Chi, Q., Wu, H. (2018). Hydrodynamic force investigation of a rigid cylinder under the coupling CF and IL motion. *Journal of Fluids and Structures*, 81, 598-616.
- Wen, P., Qiu, W. (2017). Investigation of drag crisis phenomenon using CFD methods. *Applied Ocean Research*, 67, 306-321.
- Wilcox, D.C. (2006). Turbulence modeling for CFD, Third ed. *DCW industries La Canada, CA*.
- Yang, K., Xu, S., Shen, J., Zhou, S., Xie, Y.M. (2016). Energy absorption of thin-walled tubes with pre-folded origami patterns: Numerical simulation and experimental verification. *Thin-Walled Structures*, 103, 33-44.
- Yang, K., Xu, S., Zhou, S., Shen, J., Xie, Y.M. (2017). Design of dimpled tubular structures for energy absorption. *Thin-Walled Structures*, 112, 31-40.
- Yu, Y., Xie, F., Yan, H., Constantinides, Y., Oakley, O., Karniadakis, G.E. (2015). Suppression of vortex-induced vibrations by fairings: A numerical study. *Journal of Fluids and Structures*, 54, 679-700.
- Zdravkovich, M.M. (1981). Review and classification of various aerodynamic and hydrodynamic means for suppressing vortex shedding. *Journal of Wind Engineering and Industrial Aerodynamics*, 7 (2), 145-189.
- Zhang, K., Katsuchi, H., Zhou, D., Yamada, H., Han, Z. (2016). Numerical study on the effect of shape modification to the flow around circular cylinders. *Journal of Wind Engineering and Industrial Aerodynamics*, 152, 23-40.
- Zhang, K., Katsuchi, H., Zhou, D., Yamada, H., Zhang, T., Han, Z. (2017). Numerical simulation of vortex induced vibrations of a flexibly mounted wavy cylinder at subcritical Reynolds number. *Ocean Engineering*, 133, 170-181.
- Zhao, M., Cheng, L. (2011). Numerical simulation of two-degree-of-freedom vortex-induced vibration of a circular cylinder close to a plane boundary. *Journal of Fluids and Structures*, 27 (7), 1097-1110.
- Zhao, M., Cheng, L., An, H., Lu, L. (2014). Three-dimensional numerical simulation of vortex-induced vibration of an elastically mounted rigid circular cylinder in steady current. *Journal of Fluids and Structures*, 50, 292-311.
- Zheng, H., Wang, J. (2017). Numerical study of galloping oscillation of a two-dimensional circular cylinder attached with fixed fairing device. *Ocean Engineering*, 130, 274-283.
- Zhou, B., Wang, X., Guo, W., Gho, W.M., Tan, S.K. (2015). Control of flow past a dimpled circular cylinder. *Experimental Thermal and Fluid Science*, 69, 19-26.
- Zhu, H., Zhao, H., Yao, J., Tang, Y. (2016). Numerical study on vortex-induced vibration responses of a circular cylinder attached by a free-to-rotate dartlike overlay. *Ocean Engineering*, 112, 195-210.

# Chapter 5 Textured pipe-in-pipe system: a compound passive technique for vortex-induced vibration control

Under review

---

## ABSTRACT

A compound passive vortex-induced vibration (VIV) control technique, namely the textured pipe-in-pipe (Textured-PIP) system, is introduced in the present study for VIV suppression. This novel system, which is modified from the conventional PIP, includes a smooth inner pipe to transport the natural resources and a textured outer pipe to protect the inner pipe, and the inner and outer pipes are connected together by the optimized springs and dashpots. With such a design, the VIV responses are mitigated by appreciating the suppression mechanisms of tuned mass damper (TMD) and surface roughness. Three-dimensional (3-D) computational fluid dynamics (CFD) analyses are carried out to examine the effectiveness of the proposed method. For comparison and demonstration of the vibration mitigation effectiveness, the responses of a smooth pipe and a textured pipe of the same mechanical properties and mass, are also investigated. The results show that the textured-PIP technique can more evidently suppress the VIV compared to the textured pipe.

## 5.1 Introduction

When a slender cylindrical structure is subjected to the external flow, vortex-induced vibration (VIV) may occur due to the fluctuating forces induced by wake vortex shedding from the structure. It is well documented that VIV is a major cause of structural damages in many engineering applications such as offshore structures, suspension bridges, mooring systems and subsea pipelines ([Dhanak and Xiros, 2016](#), [Drumond et al., 2018](#)). In particular, when the periodic forces induced by vortex shedding approach a frequency close to the natural frequency of the structure, synchronization or “lock-in” phenomenon occurs, which in turn may result in the undesired large amplitude vibrations. Extensive research attempts have been devoted to reduce the destructive impact of VIV ([Raghavan et al., 2008](#), [Choi et al., 2008](#), [Rashidi et al., 2016](#), [Oruç, 2017](#), [Hong and Shah, 2018](#)).

Currently existing techniques for VIV control can be broadly classified into two subgroups based on whether energy input is required, namely the active and passive suppression methods. Active control strategies, which require external energy resources to operate, can effectively control the vibrations, they are however often challenging to be implemented in real engineering practices especially for the structures located in the marine environment. Passive devices, which do not need external power to operate, are in general more practical and economical compared to the active methods ([Rashidi et al., 2016](#)). Several passive control strategies have been developed to mitigate the adverse effect of VIV such as helical strakes ([Holland et al., 2017](#), [Senga and Larsen, 2017](#)), fairings ([Assi et al., 2014](#), [Yu et al., 2015](#)), splitter plates and C-shaped foil ([Assi et al., 2014](#), [Assi and Bearman, 2015](#), [Law and Jaiman, 2017](#)), perforated cylinders ([Pinar et al., 2015](#)), grooves ([Lee and Jang, 2005](#)), bumps ([Owen et al., 2001](#)), controlling rods ([Wu et al., 2012](#), [Song et al., 2017](#)), screen shrouds ([Azmi et al., 2015](#), [Cicolin and Assi, 2017](#)), surface roughness ([Kiu et al., 2011a](#), [Gao et al., 2018](#)), wavy cylinder ([Zhang et al., 2018b](#), [Assi and Bearman, 2018](#)) and twisted body ([Wu et al., 2018](#)). However, certain drawbacks are associated with these methods. For example, helical strakes, ropes and bumps may impose an additional undesired drag force to the objective structure. Splitter plates, fairings and shrouds are expensive to manufacture and the control effectiveness highly depends on the orientation and condition of the flow ([Huang, 2011](#), [Dhanak and Xiros, 2016](#)). They are also susceptible to the marine growth, extreme storm damages, and may even cause galloping in the structure ([Huang, 2011](#)). Further research attempts are thus necessary to develop more feasible yet effective devices for VIV suppression.

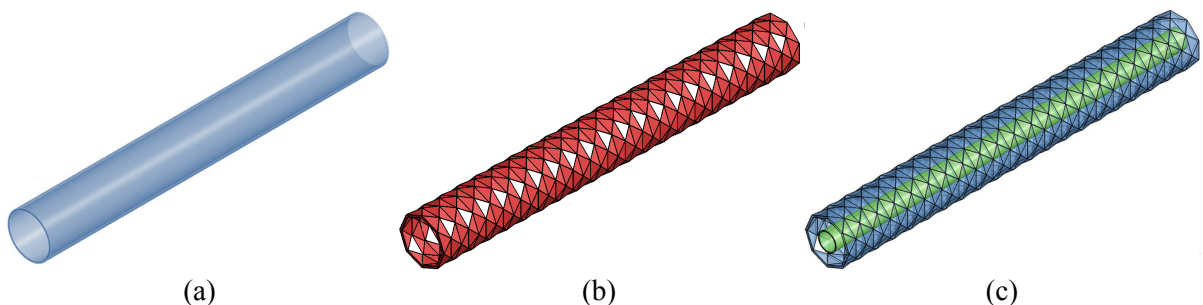


**Figure 5-1:** Schematic views of different pipe systems: (a) smooth pipe (b) textured pipe and (c) textured-PIP.

Recently, textured pipe (Figure 5-1(b)) was proposed to reduce the buckling propagation of subsea pipelines ([Khalilpasha and Albermani, 2013](#)). Compared to the smooth pipe (Figure 5-1(a)), a textured pipe has an origami shape with local facets in

both the longitudinal and cross-sectional directions (Figure 5-1(b)). With such a design, [Khalilpasha and Albermani \(2013\)](#) demonstrated that this cylinder can substantially increase the propagation buckling capacity compared to the equivalent smooth pipe. This pipe was also found to be able to considerably increase the energy absorption capacity when it is under axial loading and improve the crushing performance ([Yang et al., 2016](#)). Due to its special geometry, textured pipe was also found to have the ability for VIV suppression by altering the wake vortex street formation ([Matin Nikoo et al. \(2019b\)](#)). Three-dimensional (3-D) computational fluid dynamics (CFD) analyses revealed that this pipe could remove the upper VIV excitation regime and cause a reduction in the lock-in width ([Matin Nikoo et al., 2019b](#)). Since this pipe can increase the propagating buckling capacity and effectively control VIV without attaching any additional device, it may have wide application potentials especially in the ocean practices.

On the other hand, pipe-in-pipe (PIP) systems are being commonly used in the deep and ultra-deep waters ([Karampour et al., 2017](#), [Alrsai et al., 2018](#)). A conventional PIP system includes two smooth concentric pipes, i.e., the inner and outer pipes. The inner pipe is used to transport the natural resources (oil, gas, etc.) and the outer pipe protects the inner pipe from damage resulting from the high external hydrostatic pressure. Rigid centralizers are usually installed along the conventional PIP system to centralize the inner pipe with the outer pipe. This system was recently modified by [Bi and Hao \(2016\)](#) to mitigate earthquake induced vibration of subsea pipeline with suspended spans. In the revised system, the hard centralizers were replaced by the optimized springs and dashpots to connect the inner and outer pipes. In this case, the PIP forms a structure-tuned mass damper (TMD) system, with the outer pipe acting as the main structure and the inner pipe as the TMD. Numerical results showed that the modified PIP system can effectively reduce the seismic induced vibrations of the system ([Bi and Hao, 2016](#)). Moreover, different from the conventional TMD system in which the vibration of the TMD system is normally severe in order to dissipate energy, the vibrations of both the inner and outer pipes were significantly reduced in the revised PIP system due to the large mass ratio between the two pipes ([Bi and Hao, 2016](#)). This property makes this system very robust and the connecting devices (namely the springs and dashpots) can be easily designed. Inspired by this property, this system was used to mitigate VIV very recently, analytical ([Matin Nikoo et al., 2017](#)) and numerical

([Matin Nikoo et al., 2018](#)) studies were performed to examine the effectiveness of the proposed method. Both studies showed that the PIP system can noticeably control the VIV of marine cylindrical components, and the reduction is most evident when the cylinder is under more severe vibration.

This paper is an extension of the authors' previous studies ([Matin Nikoo et al., 2017, 2018, 2019b](#)), and a textured-PIP system is proposed to further improve the efficiency for passive VIV control. Figure 5-1(c) shows the proposed textured-PIP system. As shown, this system is similar to the PIP system investigated by [Matin Nikoo et al. \(2017, 2018\)](#), the only difference is that the outer pipe is not a smooth cylinder but a textured pipe ([Matin Nikoo et al., 2019b](#)). This new system is therefore a combination of the textured pipe and revised PIP system. According to the previous studies, the proposed textured-PIP system has the potential to more efficiently control VIV due to two passive suppression mechanisms: (i) through the TMD system provided by the PIP system, and (ii) by disturbing the wake vortex formation by the textured surface of the outer pipe. To investigate the effectiveness of the proposed system, 3-D CFD analyses are carried out within a coupled Fluid-Structure Interaction (FSI) framework. The VIV responses of the textured-PIP system are then estimated and compared with that of a smooth pipe and a textured pipe. This paper is organized as follows: Section 5.2 presents the overall methodology adopted to simulate the fluid flow and the corresponding body vibrations; verifications are carried out in Section 5.3 to validate the numerical framework; the effectiveness of using the textured-PIP design for VIV suppression is evaluated in Section 5.4; and finally some conclusions are drawn in Section 5.5.

## 5.2 Methodology

VIV is a multi-physics problem in which the fluid flow (section 5.2.1) and body oscillations (section 5.2.2) interact strongly with each other. A coupled FSI framework is therefore necessary to investigate the VIV phenomenon ([Jaiman et al., 2009](#)). In this study, ANSYS Mechanical finite element solver and FLUENT finite volume solver are used to model the solid and fluid parts respectively ([ANSYS®, 2016](#)), and the FSI coupling process is fulfilled through the ANSYS multi-field solver. In the adopted FSI scheme, the hydrodynamic forces on the cylinders wall are calculated by solving the flow equations (section 5.2.1.1) at the beginning of each computational time step, and the forces are then put into the equation of motion of the cylinder (section 5.2.2) to

estimate the cylinder's oscillations within the same time step. These procedures move forward until the end of the transient analysis. The FSI framework used in the present study was successfully employed to study the flow over a smooth cylinder ([Matin Nikoo et al., 2019a](#)), a textured pipe ([Matin Nikoo et al., 2019b](#)) and a smooth PIP system ([Matin Nikoo et al., 2018](#)).

## 5.2.1 Fluid part

### 5.2.1.1 Computational method

Different computational methods have been used to simulate the flow over the bluff bodies such as the direct numerical simulation (DNS), large-eddy simulation (LES) and Reynolds-Averaged Navier-Stokes (RANS). In the DNS technique, Navier-Stokes equations are directly solved with the entire range of energy scales without any approximation. In the LES method, large scale turbulence motions containing most of the momentum and kinetic energy are solved explicitly, whereas the effect of small scales is modelled by using a sub-grid model ([Yang, 2015](#)). DNS and LES solutions are computationally very expensive, and are thus difficult to be implemented for complex turbulent flows. RANS-based codes, on the other hand, can provide a reasonable balance between the computational effort and accuracy ([Argyropoulos and Markatos, 2015](#)), and is commonly used to simulate VIV and the associated wake modes (e.g. [Gao et al. \(2018\)](#), [Wang et al. \(2018\)](#)). RANS model is therefore used in the present study to investigate the effectiveness of using textured-PIP for VIV control. In this method, the mean continuity and momentum equations can be written as follows ([Cebeci, 2004](#)):

$$\frac{\partial \bar{u}_j}{\partial x_j} = 0 \quad (5-1)$$

$$\rho \frac{\partial \bar{u}_i}{\partial t} + \rho \frac{\partial}{\partial x_j} (\bar{u}_i \bar{u}_j) = -\frac{\partial \bar{p}}{\partial x_i} + \frac{\partial}{\partial x_j} (\bar{\tau}_{ij} - \rho \overline{u_i'' u_j''}) \quad (5-2)$$

where  $\rho$  is the fluid density,  $t$  is time,  $x_i$  and  $x_j$  are the components of the position vectors of the fluid unit ( $i, j \in [1,2,3]$ ),  $\bar{u}$ ,  $\bar{p}$  represent the time averages of velocity and pressure respectively.  $\overline{u_i'' u_j''}$  is the Reynolds-stress tensor which represents the small-scale fluctuation of fluid velocity.  $\bar{\tau}_{ij}$  is the viscous stress tensor which can be expressed as belows:

$$\bar{\tau}_{ij} = \mu \left( \frac{\partial \bar{u}_i}{\partial x_j} + \frac{\partial \bar{u}_j}{\partial x_i} \right) \quad (5-3)$$

in which  $\mu$  is the fluid dynamic viscosity.

In the present study, shear stress transport (*SST*)  $K - \omega$  turbulence model ([Menter, 1994](#)) is used to model the Reynolds-stress tensor by providing two additional transport equations for the turbulent kinetic energy  $K$  and its dissipation rate  $\omega$ . This model has two primary advantages for VIV simulations: (i) the flow separation under the strong adverse pressure gradients can be accurately estimated, and (ii) low- $R_e$  effect can be incorporated into the turbulence modelling. [Matin Nikoo et al. \(2019a\)](#) demonstrated that the inclusion of low- $R_e$  correction into the VIV simulation can improve the accuracy of the results compared to the conventional RANS *SST*  $K - \omega$  method. It is therefore incorporated in the present study.

#### 5.2.1.2 Computational mesh grids

Fluid motion is simulated in a 3-D computational domain in the FLUENT. As shown in Figure 5-2(a), it consists of a rectangular shape with the size of  $50D \times 40D \times 8D$  in the streamwise, crossflow and spanwise directions, respectively. The center of the cylinder is located at  $20D$  and  $30D$  from the inlet and outlet boundaries, respectively. Uniform velocity inlet boundary condition with a freestream velocity of  $U_\infty$  is set for the left side of the flow domain (i.e.,  $x = -20D$ ) and zero-gradient condition for velocity is applied at the outlet boundary (i.e.,  $x = 30D$ ), where the reference pressure is zero. Symmetry or free-slip boundary condition is adopted for the left, right, top and bottom sides, i.e.,  $y = \pm 20D$  and  $z = 0, 8D$  respectively. Non-slip wall boundary condition is applied on the outer pipes' wall, i.e., the fluid velocity on this surface is the same as the cylinder's vibration velocity estimated in the mechanical part.

As shown in Figure 5-2(b), the adopted computational domain is divided into different volumetric sub-blocks in order to generate optimal mesh grids in each block. Finer grids are generated for the areas close to the main circular block surrounding the pipe, while coarser meshes are used when they are far away from this block. For the cylinder with smooth wall, mesh grids with 8-node hexahedral shape are used for all the sub-blocks. For the textured pipe with sharp edges (Figure 5-2(b) and (c)), the main circular block is discretized by different grid functions in order to solve the rapid variation of flow variables that occur within the boundary layer region ([Matin Nikoo et al., 2019b](#)). Accordingly, very fine mesh grids with 6-node wedge shape are generated for the



regions very close to the textured edges, 4-node grids with tetrahedral shape are utilized for the zone located in the middle part of main block, and then 5-node pyramid elements are generated for the outermost part of the main block ([Matin Nikoo et al., 2019b](#)).

Diffusion-based dynamic mesh motion ([Zhao and Cheng, 2011](#)) is utilized to calculate the displacements of the mesh grids. It should be noted that negative mesh volume and numerical instability may occur in the region with the tetrahedral mesh grids in the textured pipe ([Matin Nikoo et al., 2019b](#)). Local re-meshing method is utilized in the present study to avoid this problem. With this technique, if any mesh cell or facet violates the minimum skewness criterion, the associated mesh grids are locally refined with the new sizes.

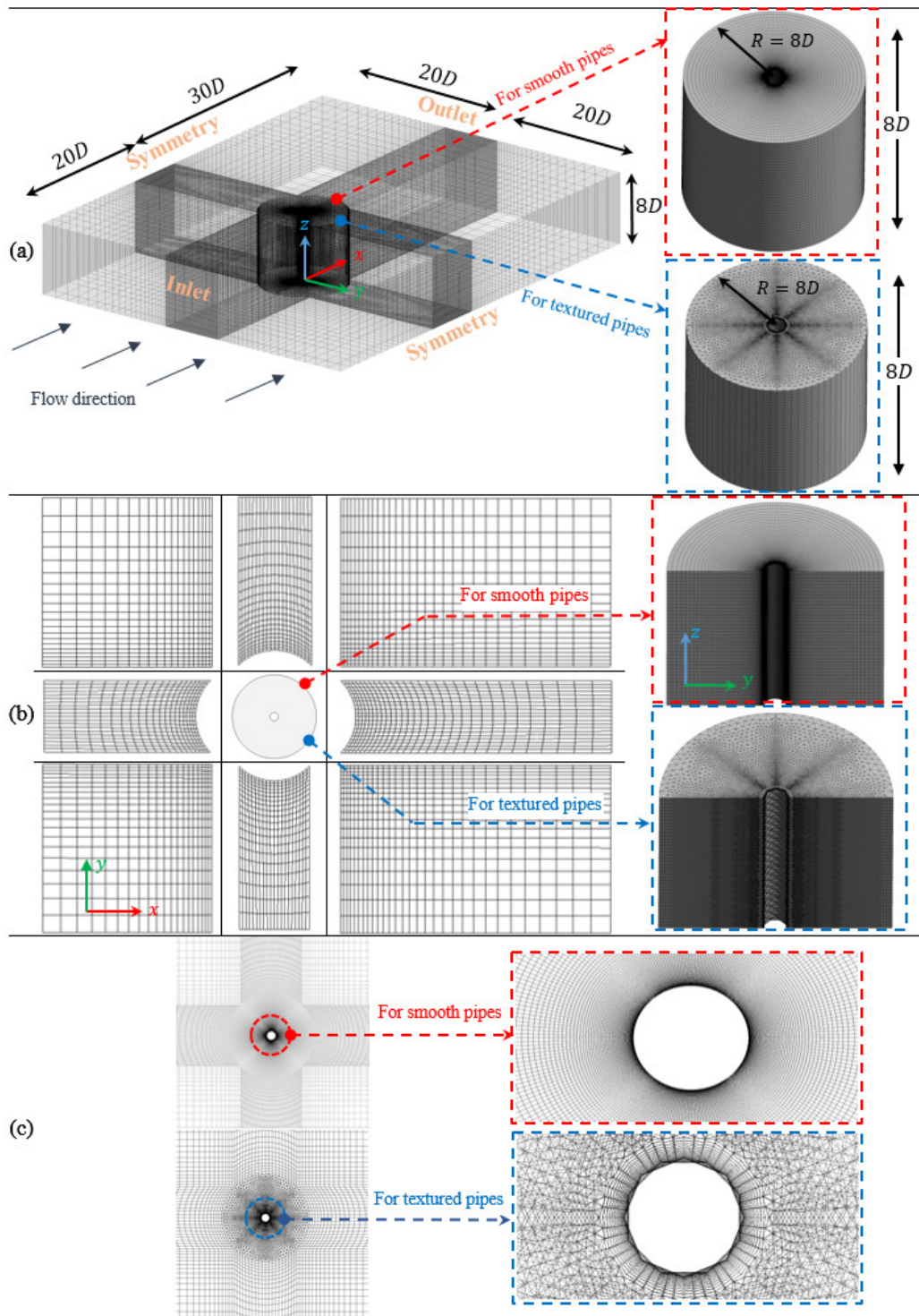


**Figure 5-2:** Computational fluid domain adopted in the Fluent solver for different pipe types (a) 3-D view and boundary conditions (b)  $xy$ -plan view and the corresponding mesh grids and (c) the mesh grids in the main circular subdomain.

### 5.2.2 Structural part

Three different cylindrical pipes, namely a smooth pipe, a textured pipe and a textured-PIP system, are investigated in the present study. For fair comparisons, the dimensions and total masses of the three systems are kept the same. Figure 5-3 shows the

modelling details. Each pipe is elastically suspended by four identical linear body-ground type springs with stiffness  $\bar{k}/4$ . All the simulations are initialized from a static condition. When the flow comes from  $x$  direction, these pipes oscillate in the crossflow direction (i.e., the  $y$  direction) due to vortex shedding.

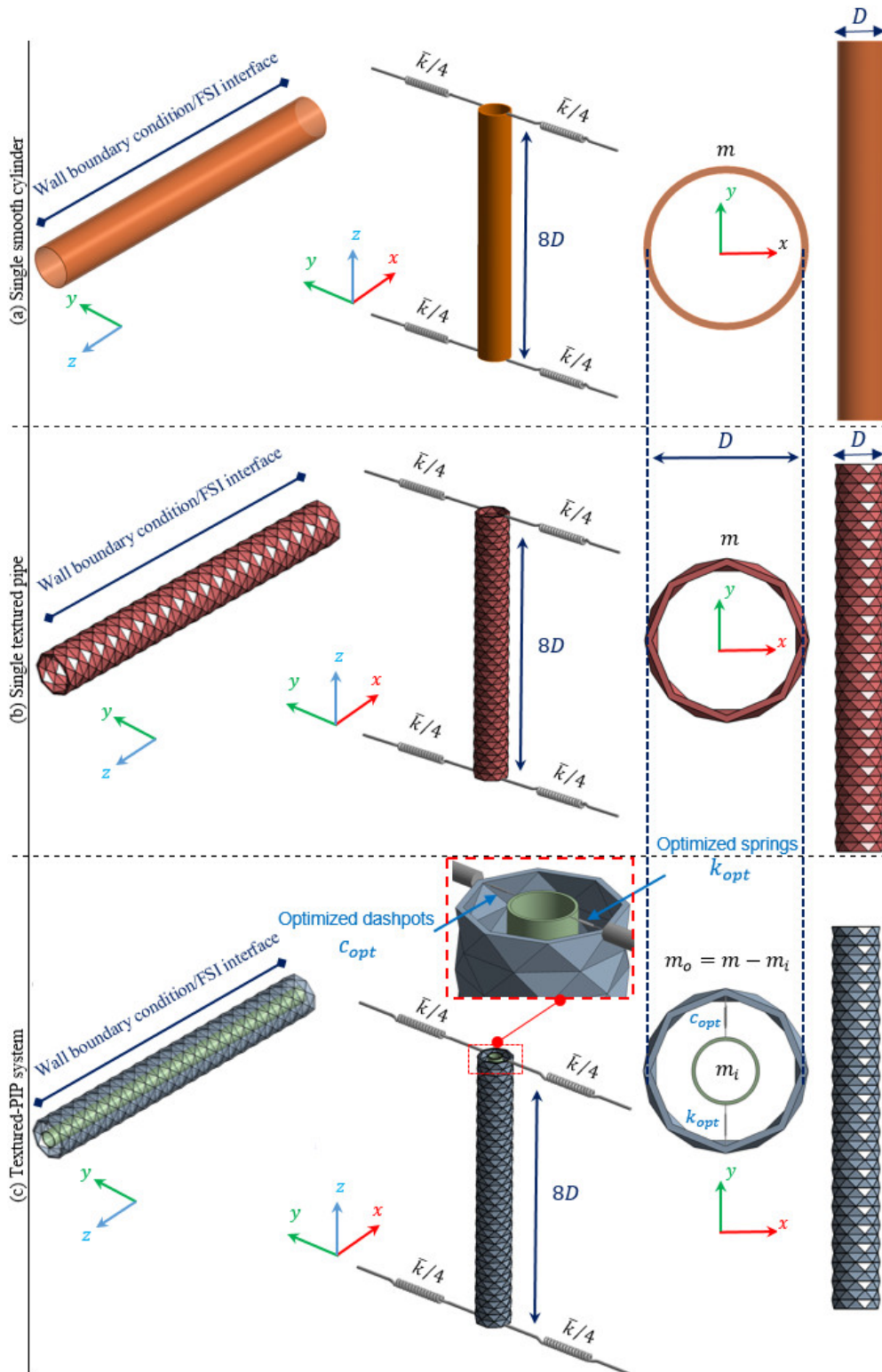


**Figure 5-3:** Different pipe systems in the ANSYS Mechanical solver: (a) a smooth cylinder, (b) a textured pipe and (c) a textured-PIP system.

As mentioned above, the inner and outer pipes are connected by the springs and dashpots in the textured-PIP system, and this connecting device should be optimized in order to make the system perform as a structure-TMD system and effective for vibration control. If the masses of the inner and outer pipes are  $m_i$  and  $m_o$ , [Matin Nikoo et al. \(2017\)](#) derived the optimal spring and dashpot parameters, and they can be estimated as follows:

$$f^{opt} = 1.10 - 0.48\sqrt{\mu} - 0.06\sqrt{\zeta} \quad (5-4)$$

$$\zeta^{opt} = 0.10 \ln(\mu) + 0.37 \quad (5-5)$$

in which  $\zeta$  is the damping ratio of the pipe system,  $\mu = m_i/m_o$  is the mass ratio between the inner and outer pipes, and it is assumed as 0.6 in this study.  $f^{opt}$  and  $\zeta^{opt}$  are the optimal frequency and damping ratios of the connecting device respectively.

The optimal stiffness ( $k_{opt}$ ) and damping coefficient ( $C_{opt}$ ) are thus:

$$k_{opt} = f^{opt^2} \mu \bar{k} \quad (5-6)$$

$$C_{opt} = 2\zeta^{opt} \sqrt{k_{opt} m_i} \quad (5-7)$$

For the above three systems, the equation of motion for each system can be expressed as follows:

$$[M]\{\ddot{y}\} + [C]\{\dot{y}\} + [\bar{k}]\{y\} = F_L(t) \quad (5-8)$$

where  $[M]$ ,  $[C]$  and  $[\bar{k}]$  are the mass, damping and stiffness matrix respectively;  $\{y\}$  is the transverse oscillation vector and the over dot denotes differentiation with respect to time  $t$ ;  $F_L$  represents the total lift force vector in the crossflow direction. In order to make a fully-mapped load/motion transfer between the two solvers, the cylinders are discretized by the same finite element grids on the FSI interface. Conservative interpolation method is adopted at the FSI interface, which makes the overall load transfer conservative, regardless of the mesh shape and size over the interface area ([ANSYS®, 2016](#)).

Combin14 element, which is a uniaxial tension-compression element with up to three degrees of freedom (DOF) at each node, is used to model the springs and dashpots that connect the inner and outer pipes in the textured-PIP system ([ANSYS®, 2016](#)). The optimized connection is achieved by setting proper spring and damping coefficients (calculated from Equations (5-6) and (5-7)) for this element. No mass, bending or

torsion is considered and only the movement in the crossflow direction ( $y$ ) is allowed in the simulations. To take into account the possible contact between the inner and outer pipes in the numerical simulations, a 3-D pair-based contact element namely CONTA174 is defined between the outer surface of the inner pipe and the inner surface of the outer pipe. Each CONTA174 element is associated with a target element named TARGE170, and contact occurs when the contact element penetrates the associated target surface.

### 5.2.3 FSI setup

The mesh grids in the boundary layer and time resolution of the numerical model are of great importance for the success of the VIV simulation ([Nishino et al., 2008](#), [Holland et al., 2017](#)). To address these effects, two parameters namely the Courant-Friedrichs-Levy (*CFL*) number and dimensionless wall distance  $y^+$  should be carefully selected. The Courant number should be less than or equal to 1 for most part of the computational domain. To reach this, the time step size of the transient calculations can be determined by  $\Delta t = 0.02D/U_\infty$  ([Nishino et al., 2008](#)).  $y^+$  should be normally smaller than unity ( $y^+ < 1$ ) to make sure that the numerical model is able to solve the boundary layer and reflect the flow separation pattern ([Argyropoulos and Markatos, 2015](#), [Tu et al., 2018](#)). In this study, very fine grid meshes are generated in the areas adjacent to the cylinder's wall, and this condition (i.e.,  $y^+ < 1$ ) is well maintained at all the wall-adjacent integration points.

A fully-mapped load/grid motion transfer between the fluid and structural parts is achieved by discretizing the same element meshes on the FSI interface, which makes the overall load transfer conservative, regardless of the mesh shape, size, grid topology, and face distribution across the interface.

Some other key setups in the FSI simulations include: a pressure-based segregated algorithm known as the Semi-Implicit Method for Pressure-Linked Equations (SIMPLE) is used for the mass conservation in order to obtain a converged solution quickly ([Tu et al., 2018](#)), a second-order upwind interpolation scheme is used for the convection discretization, the hybrid initialization method is utilized to initialize the flow field domain.

### 5.3 Verification study

To validate the developed FSI framework discussed in Section 5.2, the VIV responses of a benchmark smooth cylinder tested by [Khalak and Williamson \(1999\)](#) are investigated. It should be noted that no experimental study has been performed on the textured pipe to the best knowledge of the authors, the validation is thus only applied to the smooth pipe. However, this is a reasonable practice because the overall methodology and the model setups in the numerical simulations are exactly the same in both the smooth and textured pipes. Many researchers (e.g. [Zheng and Wang \(2017\)](#), [Gao et al. \(2018\)](#)) adopted the same practice for the VIV simulations.

In the test carried out by [Khalak and Williamson \(1999\)](#), the ratio  $m^*$ , which is defined as the ratio of the total cylinder mass to the displaced mass of the fluid, was set as 2.4, and the Reynolds number varied from 2000 to 12000. To be the same with the experimental study, these parameters are also utilized in the numerical simulations. For the damping, though it unavoidably exists in every experiment, it is assumed as zero in the numerical simulations in order to simplify the motion equation of the oscillating system. This is a reasonable assumption because when the value of the mass-damping parameter ( $m^*\zeta$ ) is very small, the variation of  $\zeta$  leads to no significant change in the maximum vibration amplitudes especially in the upper response branch. Damping coefficient  $\zeta$  thus can be omitted in order to simplify the motion equation of the oscillating system ([Pan et al., 2007](#), [Soti et al., 2018](#), [Riches and Morton, 2018](#), [Gsell et al., 2019](#)).

#### 5.3.1 Mesh independency test

Mesh convergence studies are conducted for the smooth and textured pipes in order to ensure that the obtained results are independent of the adopted mesh sizes. The tests are carried out for the normalized velocity  $U^* = 5$  ( $U^* = U_\infty/f_n D$ , where  $U_\infty$  stands for the freestream fluid velocity and  $f_n$  is the natural frequency of the cylinder in the air). Four different mesh grid scenarios namely coarse-a, coarse-b, medium and dense are considered, and the corresponding element numbers are listed in Table 5-1. The calculated maximum normalized amplitude responses ( $A^*$ ), lift coefficients  $C_L^{max}$  and drag coefficients  $C_D^{max}$  are also tabulated in the table. Table 5-1 shows that the medium models with the element number of 1,162,000 for the smooth pipe and 1,598,604 for the textured pipe lead to different results with those from the coarse-a and coarse-b scenarios but almost identical results from the dense case. On the other hand, the

computational effort for the medium scenarios are significantly reduced compared to the dense meshes. The models discretized by the medium grids are therefore employed to calculate the VIV responses of the pipes in the present study.

**Table 5-1:** Mesh convergence tests.

	smooth cylinder				textured pipe			
	No. Element	$A^*$	$C_L^{max}$	$C_D^{max}$	No. Element	$A^*$	$C_L^{max}$	$C_D^{max}$
Coarse-a	268,800	0.63	1.17	3.81	684,128	0.53	0.57	2.16
Coarse-b	900,000	0.72	1.35	3.88	1,151,443	0.56	0.62	2.31
Medium	1,162,000	0.80	1.38	4.02	1,598,604	0.59	0.66	2.40
Dense	1,548,000	0.81	1.36	4.09	1,857,480	0.59	0.60	2.40

### 5.3.2 Validation of the FSI model

To validate the numerical model, the key features obtained from the numerical simulations including the normalized maximum vibration amplitudes  $A^*$  (Figure 5-4), the corresponding dominant peak oscillation frequencies (Figure 5-5) and the wake vortex streets (Figure 5-6), are compared with the experimental results. As shown in Figure 5-4, the FSI framework developed in the present study can accurately capture the three typical VIV response regimes occurring in the conventional smooth cylinder known as the initial branch (when  $U^* \approx 2 - 3$ ), the upper branch (when  $U^* \approx 4 - 6$ ) and the lower branch (when  $U^* \approx 7 - 10$ ). The present model delivers a maximum amplitude  $A^*$  of 0.84 in the upper branch when  $U^* = 4$ , which is slightly smaller than the result reported in the test (0.97) (Khalak and Williamson, 1999). This discrepancy is primarily because of the inherent deficiency of the RANS model adopted in the numerical simulations. As reported by many researchers (e.g. Zhao et al. (2014), Zhang et al. (2018a)) the RANS model is unable to capture the maximum response of a cylinder occurring in the upper regime because this model inherently ignores the fluctuating part of the flow quantities. Figure 5-5 shows the dominant peaks in the spectra of the cylinder oscillations. It can be seen that the results coincide well with the experimental data: When the reduced velocity is small ( $U^* = 2$ ), the dominant frequency of the cylinder's oscillation is close to the Strouhal frequency ( $f_s$ ) of the stationary cylinder (the dashed line in the figure); As the normalized velocity increases to  $U^* = 3$  and  $U^* = 4$ , the cylinder starts to oscillate with two dominant peaks corresponding to  $f_s$  and the natural frequency of the cylinder in the water ( $f_w$ ) respectively; When the normalized velocity is further increased and the system enters the lower excitation regimes, the cylinder vibrates with a locked-in or synchronized frequency.

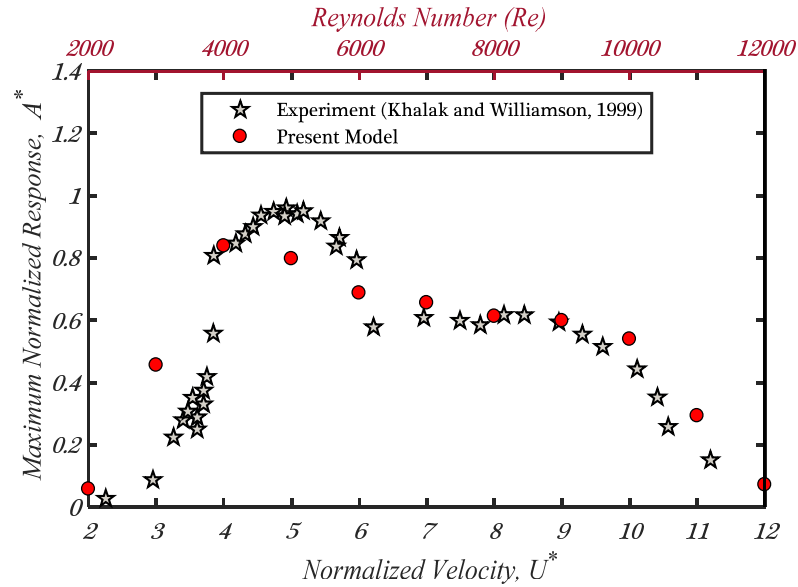


**Figure 5-4:** Normalized maximum amplitude response ( $A^*$ ) obtained from the experimental and numerical studies.

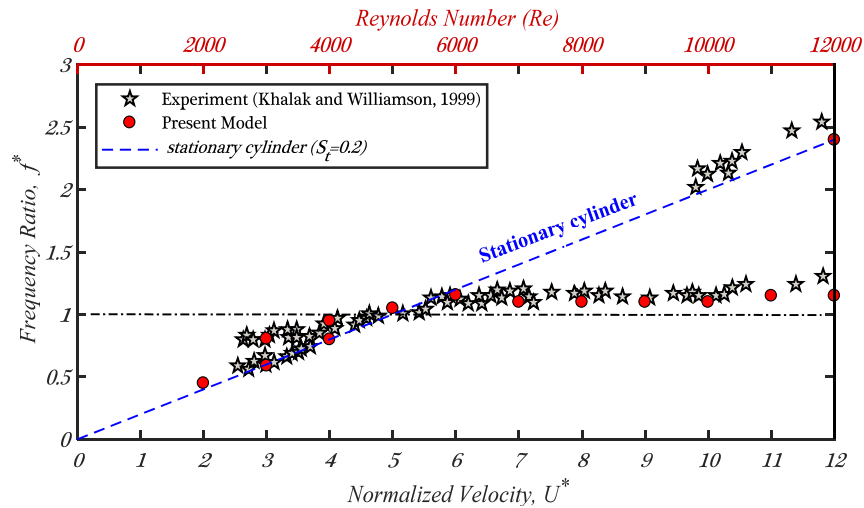


**Figure 5-5:** Dominant peaks in the spectra of the cylinder oscillations obtained from the experimental and numerical studies.

Figure 5-6 shows the typical wake vortex streets when the cylinder vibrates within different branches. As shown in Figure 5-6(a), two dominant single vortices, known as the 2S wake mode, are shown in the initial branch when the normalized velocity  $U^* = 3$ . Figure 5-6(b) and Figure 5-6(c) show that when the cylinder shifts to the upper and lower branches with the reduced velocity of  $U^* = 5$  and  $U^* = 9$  respectively, two pairs of vortices shed from two sides of the cylinder, and this is known as the 2P wake mode. These wake street modes match well with the experimental measurements (Khalak and Williamson, 1999) as shown.

All the above results show that the FSI framework developed in the present study can well capture the experimental data. It is therefore valid to adopt the framework for predicting the VIV responses of different pipes.



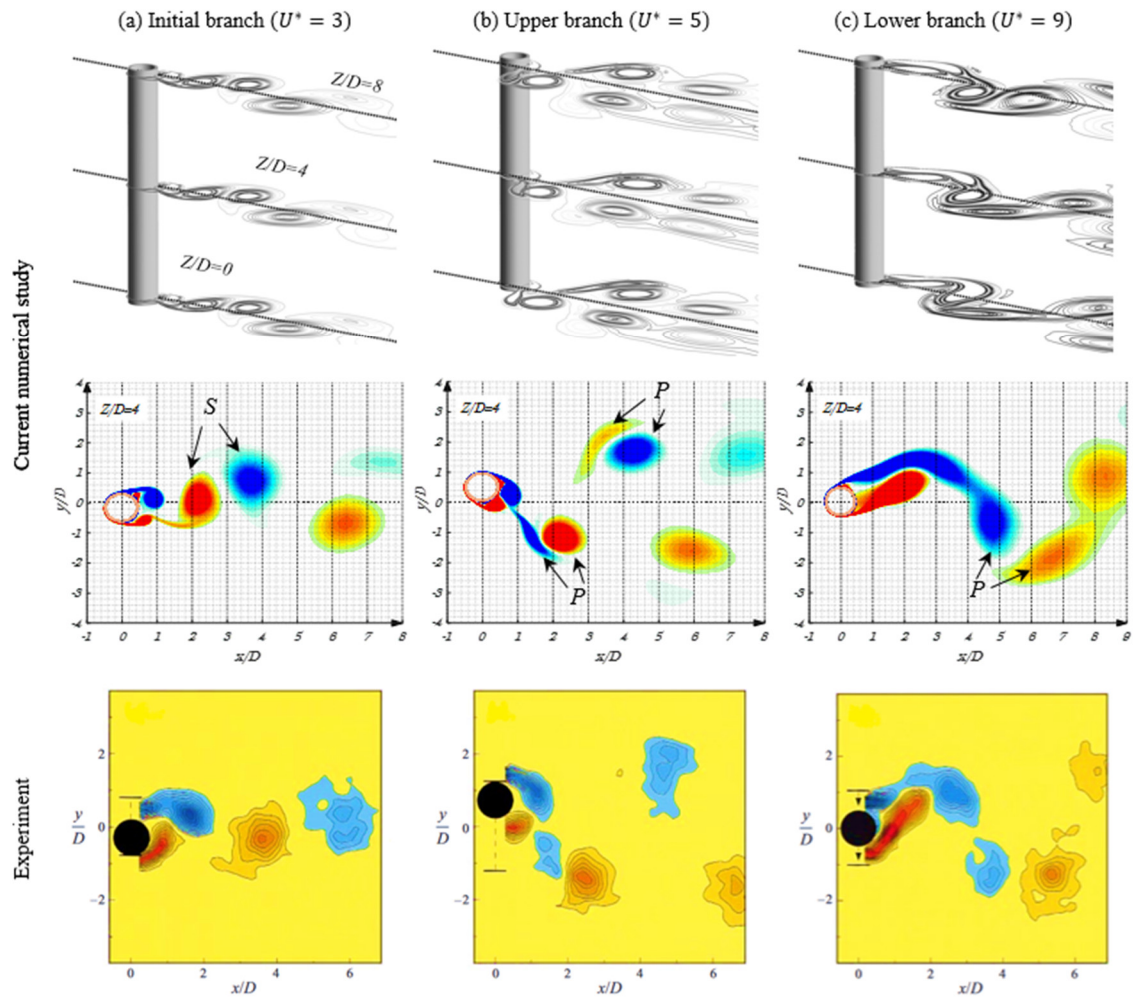


**Figure 5-6:** Typical wake vortex modes in different branches (a) initial branch ( $U^* = 3$ ) (b) upper branch ( $U^* = 5$ ) and (c) lower branch ( $U^* = 9$ ).

## 5.4 Results and discussion

### 5.4.1 Cylinder oscillations

Normalized vibration time histories ( $A_y = y/D$ ) of the single cylinders (smooth and textured) and the textured-PIP system under typical reduced velocities are shown in Figure 5-7, and Figure 5-8 presents the maximum amplitude of the normalized vibrations ( $A^*$ ) under all the examined reduced velocities. It can be seen that both the textured pipe and textured-PIP can obviously reduce the VIV responses and the textured-PIP generally results in more evident control effectiveness. To be more specific, under the very small reduced velocity  $U^* = 2$  (Figure 5-7(a) and Figure 5-8), almost the same vibration amplitudes are obtained for the three pipes. Two reasons lead to the results: Firstly, as demonstrated in many previous experimental studies (e.g. [Kiu et al. \(2011b\)](#), [Park et al. \(2012\)](#)), the effectiveness of surface roughness on VIV

suppression is more evident when the cylinder is vibrating under relatively large reduced velocities ( $\sim U^* > 7$ ). When the reduced velocity is small, the effect of surface roughness is not evident. Secondly, the amount of energy dissipated in the TMD system mainly depends on the relative displacement between the main structure and TMD, and larger structural response generally results in larger relative displacement between the TMD and main structure, and thus more evident control effectiveness ([Bi and Hao, 2016](#)). When the body is subjected to very small reduced velocities, the vibration amplitude of the structure is negligible, and therefore the TMD function in the textured-PIP system cannot be activated. When the reduced velocity increases to  $U^* = 3$ , cylinders/system start to vibrate with a larger amplitude, and the TMD function in the textured-PIP is thus activated, which results in the obvious amplitude suppression (about 40%) in the textured-PIP (see Figure 5-8). For the single textured pipe, the reduction is however not obvious due to the fact that the reduced velocity is still not significantly large. In the moderate range of reduced velocities ( $U^* = 4 - 7$ ), as shown in Figure 5-7 and Figure 5-8, the control efficiency of the textured-PIP system varies from 47% to 76%, while the reduction ratio for the single textured pipe is smaller, which varies from 8% to 36%. The reason is that the TMD function of the textured-PIP is well activated within this reduced velocity range since the vibration is severe as shown. When the reduced velocities become even higher ( $U^* > 7$ ), both the single textured pipe and textured-PIP can substantially mitigate VIV. VIV reductions for the textured pipe are 34%, 62%, 84% and 82% respectively when the reduced velocities are 8, 9, 10 and 11, and the corresponding values for the textured-PIP reach 80%, 91%, 93% and 85% respectively. In these cases, the surface modification contributes most to the response reduction. When  $U^* = 12$  (Figure 5-7(f) and Figure 5-8), the responses of the three pipes become similar again. This is because when the normalized velocity is very large, the dominant vortex shedding and cylinder vibration frequencies are significantly different, and therefore the cylinders behave almost like a static cylinder.

As discussed above, the VIV response of a smooth cylinder with low mass-damping ratio generally consists of three different response regimes, and the remarkable increase in the smooth cylinder from  $U^* = 3$  to  $U^* = 4$  (refer to Figure 5-8) is associated with the response transition from the initial to the upper branch ([Khalak and Williamson, 1999](#)). For the textured pipe and textured-PIP system, no sudden obvious

jump occurs, it might be reasonable to deduce that only two response branches, namely the initial and lower branches exist in these two pipes. To verify this hypothesis, the different VIV response regimes are investigated by calculating the phase angle ( $\phi$ ) between the lift force  $C_L(t)$  and the cylinder oscillations  $A_y(t)$ . To calculate the phase angle ( $t$ ), Hilbert transform ([Bracewell, 2000](#)) is adopted in the present study as suggested by [Khalak and Williamson \(1999\)](#). Figure 5-9 shows the dominant phase angles calculated from different cylinders. As shown, the expected phase angles are well estimated for the smooth cylinder, i.e., almost  $0^\circ$  over the initial ( $U^* \approx 2 - 3$ ) and upper regimes ( $U^* \approx 4 - 5$ ), and approximately  $180^\circ$  in the lower branch ( $U^* \approx 6 - 11$ ) ([Khalak and Williamson, 1999](#)). For the smooth pipe, the characteristic of transition from the upper branch to the lower branch is also captured: when the smooth pipe is vibrating at  $U^* = 5$ , two dominant phase angles with a clear jump are observed, indicating the transition from the upper to the lower regime as noted by [Khalak and Williamson \(1999\)](#). For the textured pipe and textured-PIP, no such a sharp jump is obtained, the phase angle increases gradually from almost  $0^\circ$  to about  $180^\circ$  when the normalized velocity changes from 2 to 8, and then maintains at about  $180^\circ$  as shown in Figure 5-9, which indicates the textured pipe and textured-PIP are vibrating in the lower branch under these normalized velocities. These results thus support the hypothesis that the upper branch is eliminated by both the textured pipe and textured-PIP system. The textured pipe and textured-PIP thus will significantly improve the safety of the structure (e.g. the fatigue life).

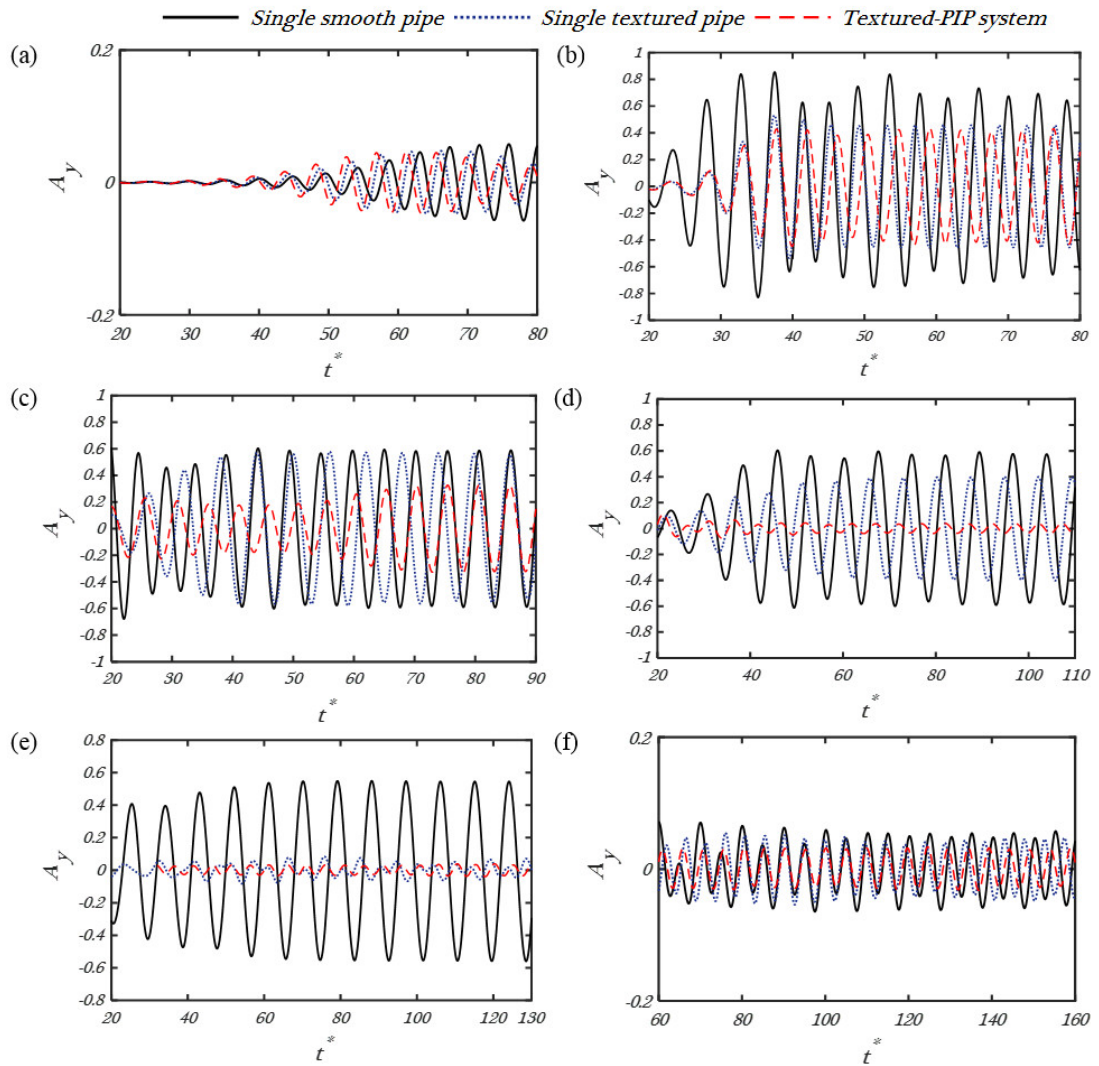


**Figure 5-7:** Normalized time histories of the cylinder oscillations under typical reduced velocities: (a)  $U^* = 2$ , (b)  $U^* = 4$ , (c)  $U^* = 6$ , (d)  $U^* = 8$ , (e)  $U^* = 10$  and (f)  $U^* = 12$ .

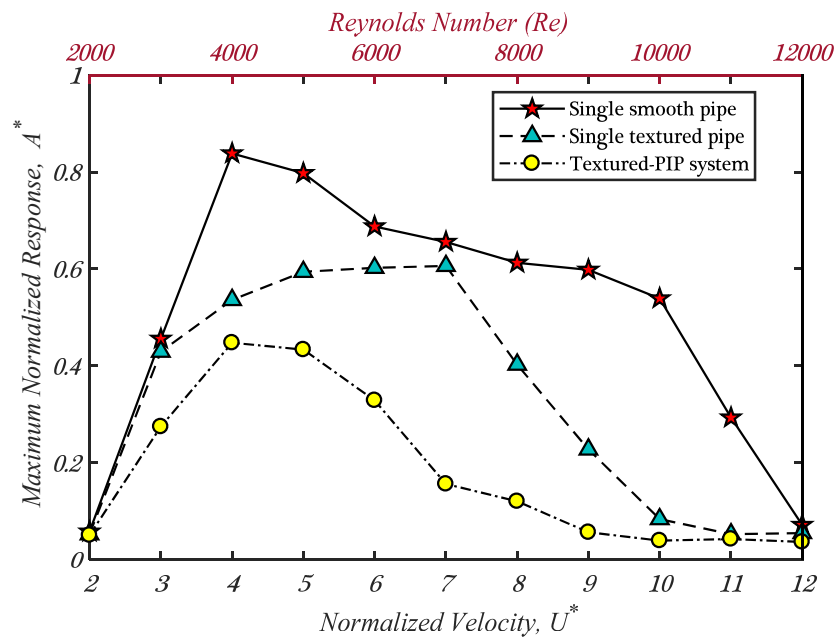


**Figure 5-8:** Normalized maximum amplitude responses ( $A^*$ ) between different pipes.

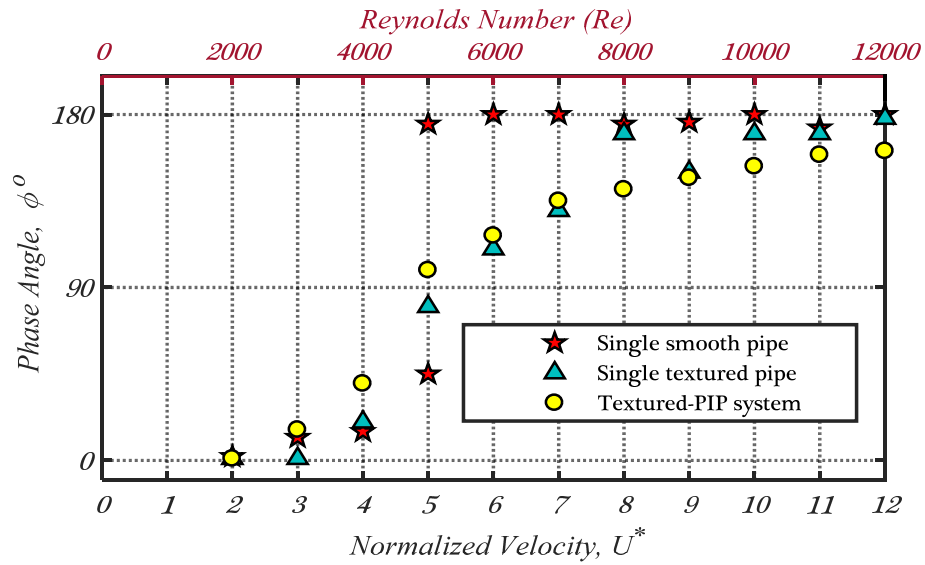


**Figure 5-9:** Comparisons of the phase angle ( $\phi$ ) between the deferent pipes/systems.

#### 5.4.2 Wake vortex modes

Different response branches are associated with different wake street modes ([Khalak and Williamson, 1999](#)). Figure 5-10 shows the wake vortex streets captured from different cylinders at three cross sections ( $Z/D = 0, 4$  and  $8$ ) under three typical normalized velocities. As shown, classical 2S vortex mode is formed for all the three systems when the reduced velocity is very small ( $U^* = 2$ ). When the reduced velocity becomes  $U^* = 4$ , the wake mode of the smooth pipe switches to the 2P mode, and this is consistent with the experimental results ([Khalak and Williamson, 1999](#)). For the textured pipes, the same switches are observed. By further increasing the normalized velocity (see Figure 5-10(c)), the VIV responses of the three cylinders transit into the lower branch. Consistent with the experimental study, 2P wake mode is captured for the smooth cylinder in this regime, whereas the wake mode changes back to the 2S mode again in the cases of textured pipe and textured-PIP, and the width of the wake vortices becomes narrower (comparing the last column in Figure 5-10), implying obvious VIV suppression appears within this regime for the textured pipe and textured-PIP ([Law and Jaiman, 2017](#)).

#### 5.4.3 Synchronization or lock-in phenomenon

VIV is associated with an unwanted phenomenon known as lock-in defined as the self-tuning of wake vortices to the natural frequency of the structure, which in turn causes system resonance. Therefore, it is desired to prevent this phenomenon. In theory, the

lock-in regime can be defined as the coalescence of the vortex shedding frequency ( $f_v$ ), the oscillation frequency ( $f_o$ ) and system natural frequency ( $f_n$ ), i.e.,  $f_v \approx f_o \approx f_n$ . Therefore, Figure 5-11, which shows the normalized vortex shedding frequency ( $f_v^* = f_v/f_n$ ) can be used to illustrate the lock-in regime for the cylinders. As shown, the lock-in range is shortened from  $U^* = 4 - 10$  in the smooth cylinder (Figure 5-11(a)) to  $U^* = 4 - 8$  in the textured pipe (Figure 5-11(b)). For the texture-PIP, the lock-in phenomenon totally disappears. As shown in Figure 11(c), the vortex shedding frequency is tuned to the Strouhal frequency or shedding frequency of a static cylinder for the whole considered reduced velocities. It again demonstrates the benefit of using textured-PIP system for VIV suppression.

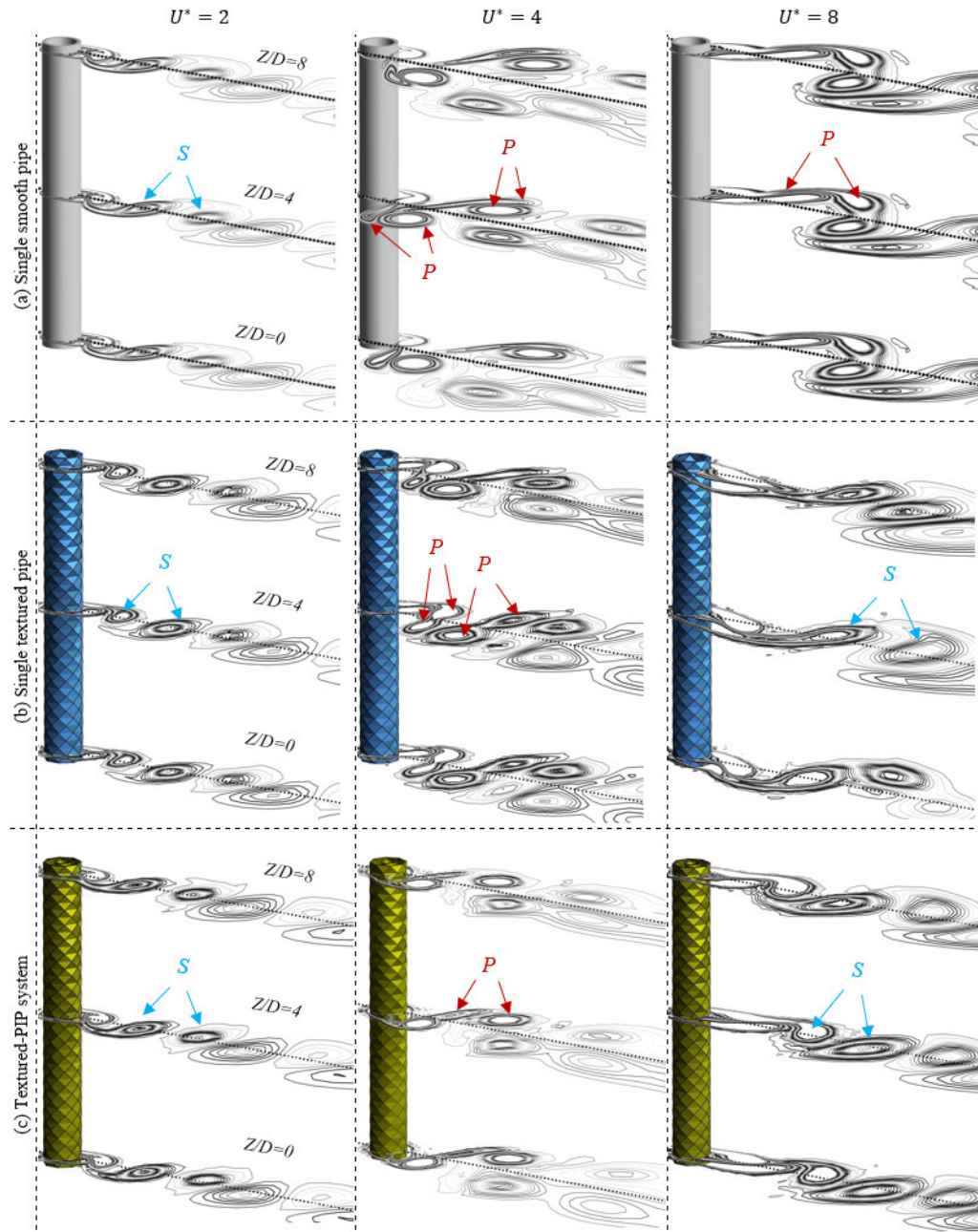


**Figure 5-10:** Contours of wake vortex streets along different cylinders at three cross sections ( $Z/D = 0, 4$  and  $8$ ) under different normalized velocities: (a)  $U^* = 2$  (b)  $U^* = 4$  and (c)  $U^* = 8$ .

#### 5.4.4 Drag force

As mentioned earlier, some VIV suppression devices such as helical strakes may cause undesired drag force onto the vibrating structure. Drag force should be also mitigated by a decent mitigation device ([Dhanak and Xiros, 2016](#)). Figure 5-12 compares the maximum normalized drag forces applied onto the cylinders ( $C_D^{max}$ ). It can be seen that the textured pipe and textured-PIP system can significantly diminish the drag force. Two mechanisms are behind these results: (i) the textured pipe with local distorted surface can cause local randomness in the flow separation points and

disorganize the correlation of vortex shedding, and (ii) the TMD system in the textured-PIP contributes to the disturbing of the time-dependent wake pressure fields and shear stress distributions ([Matin Nikoo et al., 2018](#)).

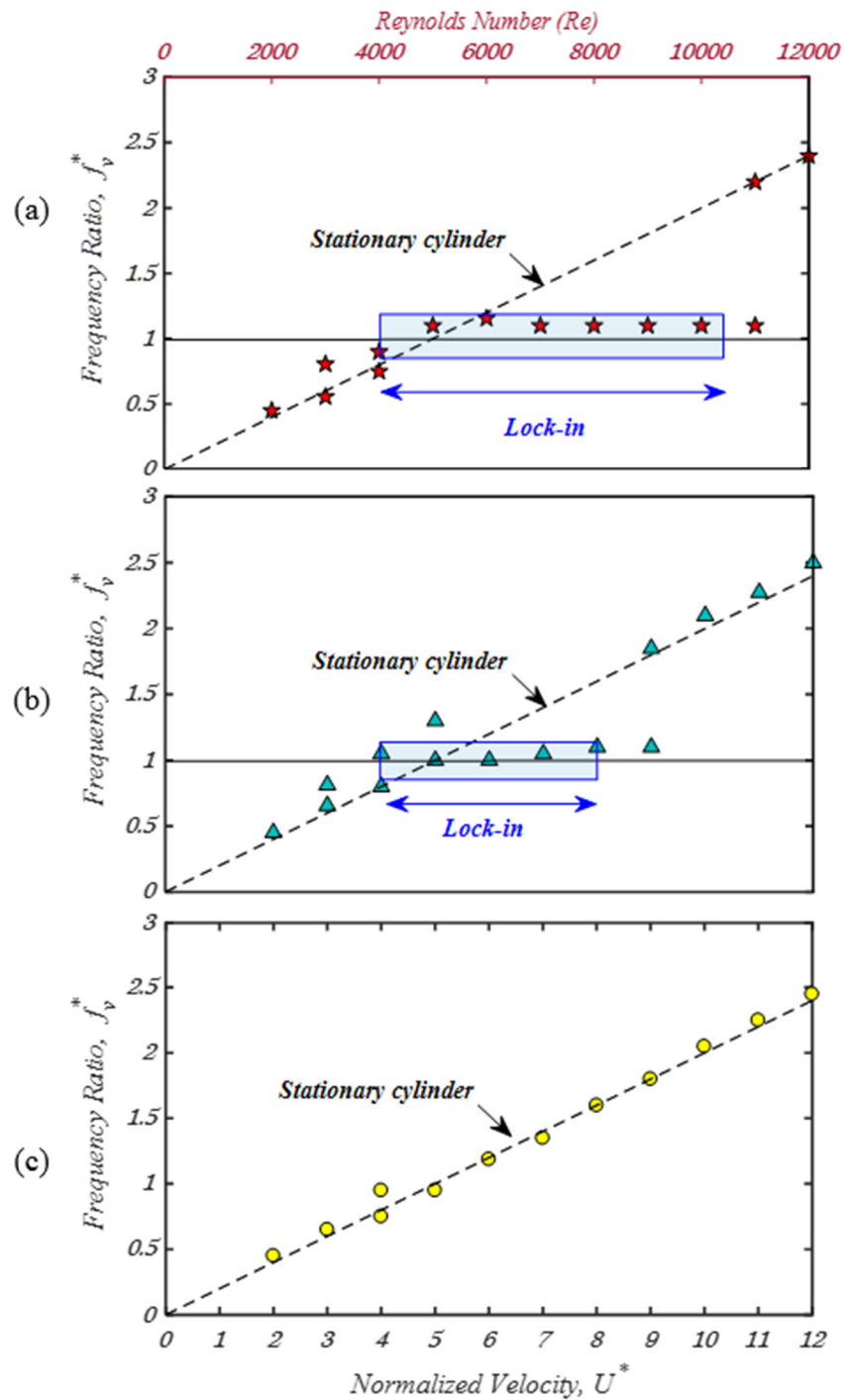


**Figure 5-11:** Lock-in or synchronization regimes obtained from different cylinders: (a) smooth cylinder ([Matin Nikoo et al., 2019a](#)) (b) textured pipe ([Matin Nikoo et al., 2019b](#)) and (c) textured-PIP system.



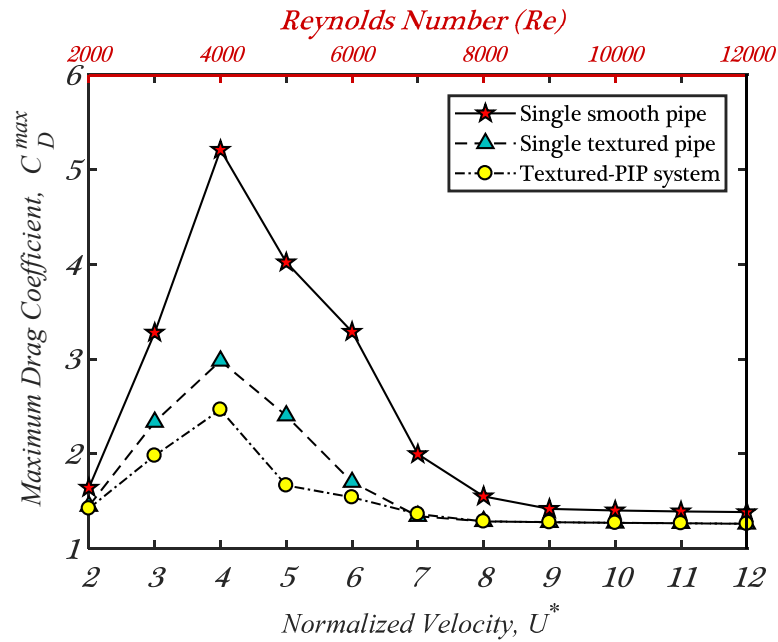


**Figure 5-12:** Comparisons of the drag forces obtained from different pipe systems.

As illustrated by [Dhanak and Xiros \(2016\)](#), a decent VIV suppression device should have three main characteristics: (i) reduce the body vibration, (ii) have a low drag coefficient, and (iii) be capable of handling the changing direction of the flow. The first two characteristics are obviously captured by the proposed textured-PIP system based on the results above. For the third characteristic, since the surface of the textured outer pipe is symmetrical in the cross-sectional direction, the same control effectiveness will be obtained under all the flow directions. Therefore, besides appreciating the benefits of the conventional PIP system, the textured-PIP is very effective for the VIV suppression.

## 5.5 Conclusion

A novel passive VIV control method, namely the textured-PIP, is proposed for VIV suppression in the present study. 3-D CFD analyses are carried out to examine the effectiveness of the proposed method. For comparison, the VIV responses of an equivalent smooth cylinder and a textured pipe are also investigated. Numerical results show that the textured-PIP can significantly suppress the undesired VIV responses. In particular, the control effectiveness is more evident compared to the textured pipe, the wake vortex streets are obviously changed, the lock-in regime is totally eliminated and the drag force is significantly reduced.

## 5.6 References

Alrsai, M., Karampour, H., Albermani, F. (2018). On collapse of the inner pipe of a pipe-in-pipe system under external pressure. *Engineering Structures*, 172, 614-628.

- ANSYS®. (2016). Academic research, release 17.2, Theory guide.
- Argyropoulos, C.D., Markatos, N.C. (2015). Recent advances on the numerical modelling of turbulent flows. *Applied Mathematical Modelling*, 39 (2), 693-732.
- Assi, G.R.S., Bearman, P.W. (2015). Transverse galloping of circular cylinders fitted with solid and slotted splitter plates. *Journal of Fluids and Structures*, 54, 263-280.
- Assi, G.R.S., Bearman, P.W. (2018). Vortex-induced vibration of a wavy elliptic cylinder. *Journal of Fluids and Structures*, 80, 1-21.
- Assi, G.R.S., Bearman, P.W., Tognarelli, M.A. (2014). On the stability of a free-to-rotate short-tail fairing and a splitter plate as suppressors of vortex-induced vibration. *Ocean Engineering*, 92, 234-244.
- Azmi, A.M., Zhou, T., Zhou, Y., Chen, J., Cheng, L. (2015). The effect of a screen shroud on vortex-induced vibration of a circular cylinder and its wake characteristics. The 25th International Offshore and Polar Engineering Conference, Hawaii, USA, 1086-1092.
- Bi, K., Hao, H. (2016). Using pipe-in-pipe systems for subsea pipeline vibration control. *Engineering Structures*, 109, 75-84.
- Bracewell, R.N. (2000). The Fourier transform and its applications, Third ed. *McGraw-Hill New York*.
- Cebeci, T. (2004). Analysis of turbulent flows. *Elsevier*, Oxford.
- Choi, H., Jeon, W.-P., Kim, J. (2008). Control of flow over a bluff body. *Annu. Rev. Fluid Mech.*, 40, 113-139.
- Cicolin, M.M., Assi, G.R.S. (2017). Experiments with flexible shrouds to reduce the vortex-induced vibration of a cylinder with low mass and damping. *Applied Ocean Research*, 65, 290-301.
- Dhanak, M.R., Xiros, N.I. (2016). Springer handbook of ocean engineering. *Springer*, United States.
- Drumond, G.P., Pasqualino, I.P., Pinheiro, B.C., Estefen, S.F. (2018). Pipelines, risers and umbilicals failures: A literature review. *Ocean Engineering*, 148, 412-425.
- Gao, Y., Zong, Z., Zou, L., Takagi, S., Jiang, Z. (2018). Numerical simulation of vortex-induced vibration of a circular cylinder with different surface roughnesses. *Marine Structures*, 57, 165-179.
- Gsell, S., Bourguet, R., Braza, M. (2019). One versus two-degree-of-freedom vortex-induced vibrations of a circular cylinder at  $Re=3900$ . *Journal of Fluids and Structures*, 85, 165-180.
- Holland, V., Tezdogan, T., Oguz, E. (2017). Full-scale CFD investigations of helical strakes as a means of reducing the vortex induced forces on a semi-submersible. *Ocean Engineering*, 137, 338-351.
- Hong, K.S., Shah, U.H. (2018). Vortex-induced vibrations and control of marine risers: A review. *Ocean Engineering*, 152, 300-315.
- Huang, S. (2011). VIV suppression of a two-degree-of-freedom circular cylinder and drag reduction of a fixed circular cylinder by the use of helical grooves. *Journal of Fluids and Structures*, 27 (7), 1124-1133.
- Jaiman, R.K., Shakib, F., Oakley, O.H., Constantinides, Y. (2009). Fully coupled fluid-structure interaction for offshore applications. ASME 2009 28th International Conference on Ocean, Offshore and Arctic Engineering, 757-765.
- Karampour, H., Alrsai, M., Albermani, F., Guan, H., Jeng, D.-S. (2017). Propagation Buckling in Subsea Pipe-in-Pipe Systems. *Journal of Engineering Mechanics*, 143 (9), 04017113.

- Khalak, A., Williamson, C.H.K. (1999). Motions, forces and mode transitions in vortex-induced vibrations at low mass-damping. *Journal of Fluids and Structures*, 13 (7-8), 813-851.
- Khalilpasha, H., Albermani, F. (2013). Textured deep subsea pipelines. *International Journal of Mechanical Sciences*, 68, 224-235.
- Kiu, K., Stappenbelt, B., Thiagarajan, K. (2011a). Effects of uniform surface roughness on vortex-induced vibration of towed vertical cylinders. *Journal of Sound and Vibration*, 330 (20), 4753-4763.
- Kiu, K.Y., Stappenbelt, B., Thiagarajan, K.P. (2011b). Effects of uniform surface roughness on vortex-induced vibration of towed vertical cylinders. *Journal of Sound and Vibration*, 330 (20), 4753-4763.
- Law, Y.Z., Jaiman, R.K. (2017). Wake stabilization mechanism of low-drag suppression devices for vortex-induced vibration. *Journal of Fluids and Structures*, 70, 428-449.
- Lee, S.J., Jang, Y.G. (2005). Control of flow around a NACA 0012 airfoil with a micro-riblet film. *Journal of Fluids and Structures*, 20 (5), 659-672.
- Matin Nikoo, H., Bi, K., Hao, H. (2017). Passive vibration control of cylindrical offshore components using pipe-in-pipe (PIP) concept: An analytical study. *Ocean Engineering*, 142, 39-50.
- Matin Nikoo, H., Bi, K., Hao, H. (2018). Effectiveness of using pipe-in-pipe (PIP) concept to reduce vortex-induced vibrations (VIV): Three-dimensional two-way FSI analysis. *Ocean Engineering*, 148, 263-276.
- Matin Nikoo, H., Bi, K., Hao, H. (2019a). Three-dimensional vortex-induced vibration of a circular cylinder at subcritical Reynolds numbers with low-Re correction. *Marine Structures*, 66, 288-306.
- Matin Nikoo, H., Bi, K., Hao, H. (2019b). Vortex-induced vibration of a full-diamond textured cylinder at subcritical Reynolds numbers. Under Review.
- Menter, F.R. (1994). Two-equation eddy-viscosity turbulence models for engineering applications. *AIAA Journal*, 32 (8), 1598-1605.
- Nishino, T., Roberts, G.T., Zhang, X. (2008). Unsteady RANS and detached-eddy simulations of flow around a circular cylinder in ground effect. *Journal of Fluids and Structures*, 24 (1), 18-33.
- Oruç, V. (2017). Strategies for the applications of flow control downstream of a bluff body. *Flow Measurement and Instrumentation*, 53 (Part B), 204-2014.
- Owen, J.C., Bearman, P.W., Szewczyk, A.A. (2001). Passive control of VIV with drag reduction. *Journal of Fluids and Structures*, 15 (3-4), 597-605.
- Pan, Z.Y., Cui, W.C., Miao, Q.M. (2007). Numerical simulation of vortex-induced vibration of a circular cylinder at low mass-damping using RANS code. *Journal of Fluids and Structures*, 23 (1), 23-37.
- Park, H., Bernitsas, M.M., Kumar, R.A. (2012). Selective roughness in the boundary layer to suppress flow-induced motions of circular cylinder at  $30,000 < Re < 120,000$ . *Journal of Offshore Mechanics and Arctic Engineering*, 134 (4), 041801.
- Pinar, E., Ozkan, G.M., Durhasan, T., Aksoy, M.M., Akilli, H., Sahin, B. (2015). Flow structure around perforated cylinders in shallow water. *Journal of Fluids and Structures*, 55, 52-63.
- Raghavan, A.K., Chan-Hyun, S., Bangalore, H.L.G. (2008). Passive control of vortex-induced vibrations: an Overview. *Recent Patents on Mechanical Engineering*, 1 (1), 1-11.
- Rashidi, S., Hayatdavoodi, M., Esfahani, J.A. (2016). Vortex shedding suppression and wake control: A review. *Ocean Engineering*, 126, 57-80.

- Riches, G., Morton, C. (2018). One degree-of-freedom vortex-induced vibrations at constant Reynolds number and mass-damping. *Experiments in Fluids*, 59 (10), 157.
- Senga, H., Larsen, C.M. (2017). Forced motion experiments using cylinders with helical strakes. *Journal of Fluids and Structures*, 68, 279-294.
- Song, Z., Duan, M., Gu, J. (2017). Numerical investigation on the suppression of VIV for a circular cylinder by three small control rods. *Applied Ocean Research*, 64, 169-183.
- Soti, A.K., Zhao, J., Thompson, M.C., Sheridan, J., Bhardwaj, R. (2018). Damping effects on vortex-induced vibration of a circular cylinder and implications for power extraction. *Journal of Fluids and Structures*, 81, 289-308.
- Tu, J., Yeoh, G.H., Liu, C. (2018). Computational fluid dynamics: a practical approach. *Butterworth-Heinemann*.
- Wang, K., Ji, C., Chi, Q., Wu, H. (2018). Hydrodynamic force investigation of a rigid cylinder under the coupling CF and IL motion. *Journal of Fluids and Structures*, 81, 598-616.
- Wu, C.H., Jaiman, R.K., Lim, T.B.A., Kang, C.W., Ma, S. (2018). A new passive control technique for the suppression of vortex-induced motion in deep-draft semisubmersibles. *Applied Ocean Research*, 80, 79-100.
- Wu, H., Sun, D.P., Lu, L., Teng, B., Tang, G.Q., Song, J.N. (2012). Experimental investigation on the suppression of vortex-induced vibration of long flexible riser by multiple control rods. *Journal of Fluids and Structures*, 30, 115-132.
- Yang, K., Xu, S., Shen, J., Zhou, S., Xie, Y.M. (2016). Energy absorption of thin-walled tubes with pre-folded origami patterns: Numerical simulation and experimental verification. *Thin-Walled Structures*, 103, 33-44.
- Yang, Z. (2015). Large-eddy simulation: Past, present and the future. *Chinese Journal of Aeronautics*, 28 (1), 11-24.
- Yu, Y., Xie, F., Yan, H., Constantinides, Y., Oakley, O., Karniadakis, G.E. (2015). Suppression of vortex-induced vibrations by fairings: A numerical study. *Journal of Fluids and Structures*, 54, 679-700.
- Zhang, B., Mao, Z., Song, B., Tian, W., Ding, W. (2018a). Numerical investigation on VIV energy harvesting of four cylinders in close staggered formation. *Ocean Engineering*, 165, 55-68.
- Zhang, K., Katsuchi, H., Zhou, D., Yamada, H., Bao, Y., Han, Z., Zhu, H. (2018b). Numerical study of flow past a transversely oscillating wavy cylinder at  $Re=5000$ . *Ocean Engineering*, 169, 539-550.
- Zhao, M., Cheng, L. (2011). Numerical simulation of two-degree-of-freedom vortex-induced vibration of a circular cylinder close to a plane boundary. *Journal of Fluids and Structures*, 27 (7), 1097-1110.
- Zhao, M., Cheng, L., An, H., Lu, L. (2014). Three-dimensional numerical simulation of vortex-induced vibration of an elastically mounted rigid circular cylinder in steady current. *Journal of Fluids and Structures*, 50, 292-311.
- Zheng, H., Wang, J. (2017). Numerical study of galloping oscillation of a two-dimensional circular cylinder attached with fixed fairing device. *Ocean Engineering*, 130, 274-283.

# Chapter 6 Three-dimensional vortex-induced vibration of a circular cylinder at subcritical Reynolds numbers with Low- $R_e$ correction

Journal of Marine Structures. Vol. 66, Pages 288-306, [10.1016/j.marstruc.2019.05.004](https://doi.org/10.1016/j.marstruc.2019.05.004).

---

## ABSTRACT

Reynolds-Averaged Navier-Stokes (RANS) method equipped with the shear stress transport (*SST*)  $K - \omega$  model is widely used to simulate the vortex induced vibration (VIV) of elastically-mounted rigid cylinders subjected to fluid flow. Previous studies show that this method is very difficult to capture the maximum response of the cylinder occurring in the upper regime. Moreover, previous numerical studies by using this method mainly focus on the two-dimensional (2-D) simulations. In reality, VIV is a three-dimensional (3-D) phenomenon, the 3-D effect must then be incorporated in the numerical simulations. To improve the accuracy of the RANS method with *SST*  $K - \omega$ , the low-Reynolds numbers ( $R_e$ ) correction technique is applied to the numerical model in the present study and the 3-D VIV responses of an elastically-mounted cylinder subjected to the subcritical flow fluid regime are numerically investigated. The two-way coupled Fluid-Structure Interaction (FSI) framework is developed and computational fluid dynamics (CFD) analyses are performed for a range of Reynolds numbers  $R_e = 2000 - 12000$ . Numerical results show that the present method can lead to more accurate VIV response estimations compared to the previous numerical studies. Moreover, the formation of the wake vortex shedding modes and its transition are well captured by this method.

## 6.1 Introduction

When fluid flow past a bluff body it may result in a complicated phenomenon known as the vortex-induced vibration (VIV). VIV of cylindrical structural components is an important issue for many engineering structures such as marine risers, subsea pipelines, buoys, wind turbines, bridges and high-rise buildings. When the frequency of vortex shedding is close to the natural frequency of the structure/structural component, responses with remarkably large amplitude are expected, which in turn may result in the fatigue damage to the structural components or even catastrophic failure to the whole structure. It is therefore important to understand the mechanism of

VIV. Extensive research works have been carried out in this area. These works can be generally divided into three groups: experiments, analytical models and numerical (CFD) simulations. For the experimental studies, Williamson and his research group ([Khalak and Williamson, 1996](#), [1997a](#), [1999](#), [Williamson and Govardhan, 2008](#), [Mackowski and Williamson, 2013](#)) have made remarkable contributions in developing the fundamental perspective on understanding the response of an elastically-mounted cylinder subjected to VIV. It is generally recognized that for a cylinder with low mass-damping coefficient  $m^* \zeta$  (in which  $m^*$  is the mass of the oscillating body divided by the mass of the displaced fluid, and  $\zeta$  is the damping coefficient), three oscillation regimes termed as initial, upper and lower branches exist when the fluid flow velocity increases. With the high mass-damping coefficient, the upper branch, however, disappears. It is also recognized that the transition from the initial oscillations to the upper regime is hysteric, while the transition from the upper to the lower branch involves an intermittent switching with a jump in the phase angle between the lift force and cylinder oscillation by about  $180^\circ$ . Quite a few review papers (e.g. [Gabbai and Benaroya \(2005\)](#), [Williamson and Govardhan \(2008\)](#)) have summarized the previous experimental studies.

A variety of analytical VIV models have been developed to model both the structure and fluid ([Postnikov et al., 2017](#)). For example, in the wake oscillator models, the wake dynamics are assumed to follow a van der Pol equation and the cylinder is modeled by another oscillator excited by the wake variable ([Facchinetti et al., 2004](#), [Farshidianfar and Zanganeh, 2010](#)). A Comprehensive review of the analytical models and wake oscillator models can be found in [Williamson and Govardhan \(2004\)](#) and [Kurushina et al. \(2018\)](#).

Extensive attempts have also been made on the numerical simulations on the VIV responses of elastically-mounted rigid cylinders. Four computational approaches including Direct Numerical Simulation (DNS), Large Eddy Simulation (LES), Detached Eddy Simulation (DES) and Reynolds Averaged Navier-Stokes (RANS) Simulation are normally adopted to model the turbulent flow around the cylinder. [Argyropoulos and Markatos \(2015\)](#) has reviewed the different turbulence modelling approaches and summarized the advantages and disadvantages of each method. In general, DNS, LES and DES methods can provide more accurate results compared to the RANS simulations. RANS-based codes, on the other hand, provides the best

balance between the accuracy and the computational costs. It is therefore more practical for the fluid flow simulations and a considerable amount of literature have used the RANS codes for VIV simulation (e.g. [Guilmineau and Queutey \(2004\)](#), [Pan et al. \(2007\)](#), [Ong et al. \(2009\)](#), [Zhao et al. \(2014\)](#), [Rahmanian et al. \(2014\)](#), [Gao et al. \(2018b\)](#), [Khan et al. \(2018\)](#), [Wang et al. \(2018\)](#)).

In the RANS codes, the entire spectrum of turbulence is modelled by a set of transport equations arising from decomposing the turbulence into a mean and a fluctuating component, which results in an additional term dubbed the Reynolds Stress tensor in the fluid flow equations ([Cebeci, 2004](#)). Additional modelling scheme, such as the shear stress transport (*SST*)  $K - \omega$  ([Menter, 1994](#)), is then required to close the RANS equations. The *SST*  $K - \omega$  method improves the prediction of flows with strong adverse pressure gradients and separation ([Cebeci, 2004](#), [Pan et al., 2007](#)). However, certain shortcomings exist for this method especially when the subcritical flow regime is of interest ([Tutar and Holdø, 2001](#), [Cebeci, 2004](#), [Ong et al., 2009](#)). Firstly, within this regime, though the wake vortex field is turbulent, the separation points on the cylinder surface remain laminar and there are strong gradients in the flow variable ([Blevins, 1990](#)). The standard *SST*  $K - \omega$  model thus cannot accurately predict the development of laminar-turbulent transition processes because it inherently assumes the flow is fully turbulent ([McNaughton et al., 2014](#)). Secondly, in this model, turbulence damping is related to the wall distance and the low-Reynolds number ( $Re$ ) effect is ignored ([McNaughton et al., 2014](#)). Without considering this effect, this model cannot accurately predict the sharp peak in the turbulence kinetic energy close to the non-slip wall and it is unable to resolve the rapid variation of flow variables that occurs within the viscous and boundary layers ([Cebeci, 2004](#)). Due to these two limitations, the standard RANS *SST*  $K - \omega$  model is normally very difficult to capture the maximum response of the cylinder occurring in the upper regime as indicated in many previous studies. For example, [Guilmineau and Queutey \(2004\)](#) used the two-dimensional (2-D) *SST*  $K - \omega$  scheme to simulate the VIV of the experiment conducted by [Khalak and Williamson \(1997a, 1999\)](#). Their numerical model reasonably predicted the response amplitude and wake vortices modes in the lower branch. However, the model failed to capture the high amplitude oscillation occurring in the upper regime. [Pan et al. \(2007\)](#) used the same turbulence model and carried out a detailed numerical simulation on the influence of Reynolds-averaging procedure on

the VIV behaviour. Their results confirmed the incapability of the *SST*  $K - \omega$  method to capture the maximum response when the cylinder is vibrating in the upper branch. They referred this discrepancy between the numerical results and the experimental data to the irregular behaviour of the VIV response, hydrodynamic forces, and the wake vortex formation. Very recently, ([Khan et al., 2018](#)) simulated the VIV responses of a low mass-damping rigid cylinder oscillating freely in the crossflow direction by adopting the 2-D *SST*  $K - \omega$  method. They obtained a higher value of the maximum VIV amplitude in the upper branch compared to the previous studies. However, a noticeable discrepancy with the experiments was obtained in terms of the transition from the upper branch to the lower branch.

It should be noted that most previous numerical studies by using the *SST*  $K - \omega$  model ([Guilmineau and Queutey, 2004](#), [Pan et al., 2007](#), [Kang et al., 2017](#), [Khan et al., 2018](#), [Gao et al., 2018b](#)) mainly focused on the 2-D simulations. In reality, flow in the wake of a circular cylinder is three-dimensional (3-D) when the Reynolds number is greater than 170-200 ([Miller and Williamson, 1994](#), [Zhao et al., 2014](#)), these 2-D models therefore are not able to address the 3-D effect of the flow. To fully understand the characteristics of the fluid flow, some researchers performed 3-D numerical simulations on VIV. For example, [Zhao et al. \(2014\)](#) studied the variation of the vortex shedding flow in the axial direction of an elastically-mounted rigid cylinder and the transition of the flow from 2-D to 3-D. They reported that the strongest 3-D effect of the wake flow occurs in the upper branch. [Wang and Xiao \(2016\)](#), [Wang et al. \(2017\)](#) performed 3-D VIV simulations of a flexible riser and a rigid cylinder. It was confirmed that the wake flow is entirely 3-D along the axis of the riser and cylinder. [Matin Nikoo et al. \(2018\)](#) carried out 3-D two-way fluid-structure interaction (FSI) analysis of a pipe-in-pipe system, and the same conclusion was obtained. Another aim of the present study is to extend the 2-D simulation of VIV to 3-D by using the *SST*  $K - \omega$  model.

The aim of the present study is to improve the accuracy of standard RANS *SST*  $K - \omega$  method in predicting the VIV response of cylindrical structural components. To this end, the low- $R_e$  modification technique as proposed by [Wilcox \(2006\)](#) is incorporated into the standard RANS *SST*  $K - \omega$  method. By doing so, the effect of laminar-turbulent transition can be considered. To the best knowledge of the authors, this is the first study that adopts this technique for VIV prediction. To demonstrate the



effectiveness of the proposed method, a two-way FSI algorithm is developed by coupling the ANSYS Mechanical and FLUENT finite volume solvers, and computational fluid dynamics (CFD) analyses are performed to obtain the 3-D VIV responses of an elastically-mounted rigid cylinder subjected to the fluid flow with the Reynolds numbers falling within the subcritical regime ( $Re = 2000 - 12000$ ). The paper is organized as follows: The two-way FSI method and the governing equations of the fluid and structure are presented in section 6.2; the mesh dependency study is discussed in section 3.3; the obtained results in terms of the oscillation amplitude, hydrodynamic forces, response frequencies and wake vortices are discussed and compared with previous studies in detail in section 6.5; and finally some conclusions are drawn in Section 6.6.

## **6.2 Method of Solution, Computational Approach and Governing Equations**

### **6.2.1 Two-way FSI**

VIV phenomenon is a multi-physics problem where the responses of the structure and flow field are mutually dependent and interact strongly with each other. The varying pressure distributions initiated by the periodic vortex shedding act on the surface of the structure and cause a motion to the structure. This motion, in turn, disturbs the surrounding flow, imparts or removes energy to or from the flow. VIV is therefore a typical problem which needs to be investigated through a two-way FSI approach.

In this study, a two-way FSI algorithm is developed by coupling the ANSYS Mechanical and FLUENT finite volume solvers ([ANSYS®, 2016](#)) together. Figure 6-1 shows an overall view of the adopted model. In the FLUENT part, as shown in Figure 6-1(a), a 3-D multi-block rectangular fluid domain is utilized to simulate the fluid flow over the cylinder. The cylinder, as shown in Figure 6-1(b), is suspended by four springs at the two spanwise boundary surfaces, the stiffness of each spring is  $\bar{k}/4$ , where  $\bar{k}$  is the spring constant. Remote displacement constraints are assigned to these two boundaries which allow cylinder to vibrate only in the crossflow direction ( $y$ ). The outer surface of the cylinder is set to be the FSI interface where hydrodynamic quantities and displacements continuously transfer throughout the transient analysis.

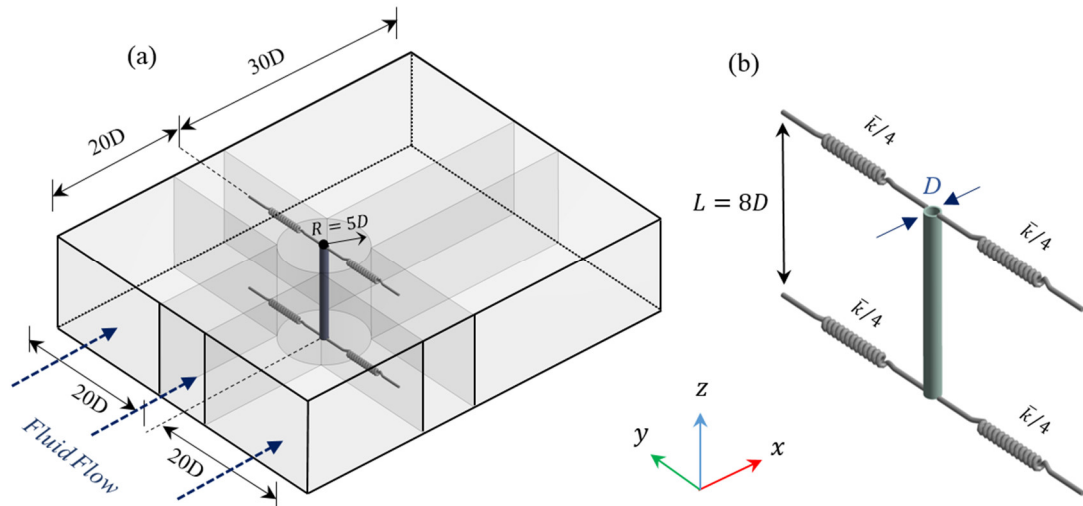


**Figure 6-1:** (a) 3-D fluid domain adopted in the FLUENT solver and (b) suspended solid cylinder modelled in the ANSYS Mechanical solver.

Computational fluid domain dimensions play critical role in the accuracy of generating the wake vortices, especially for an oscillating cylinder. In this study, the crossflow and spanwise lengths of the fluid domain are adopted to be  $40D$  and  $8D$  respectively, in which  $D$  is the cylinder diameter. The upstream and downstream boundaries are also located at  $20D$  and  $30D$  from the center of the cylinder respectively. These values have been proved to be able to take into account the three-dimensionality and blockage effects accurately ([Prasanth and Mittal, 2008](#), [Zhao et al., 2014](#), [Law and Jaiman, 2017](#), [Matin Nikoo et al., 2018](#)).

Figure 6-2 illustrates the FSI procedure to reach a converged result. In each time step, the fluid equations (section 6.2.2.1) are solved numerically and the corresponding hydrodynamic loads are transferred to the mechanical part as inputs exerted on the cylinder. Within the same time step, the structural dynamics equation (section 4.3.3) is then solved and the obtained cylinder oscillations are returned back to the surrounding fluid, which in turn, cause a deformation in the mesh grids of the fluid part (section 4.3.2.3). This procedure continues up to reach an almost steady state response of the system.

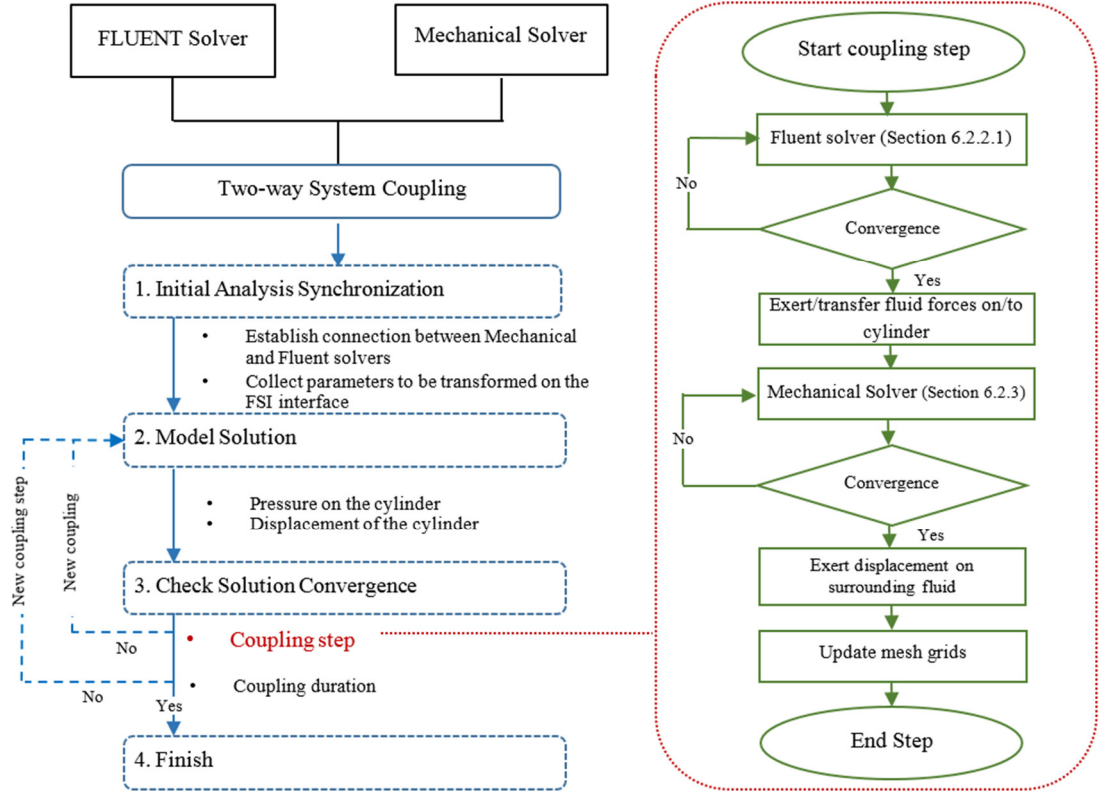


**Figure 6-2:** Two-way FSI procedure.

## 6.2.2 Computational fluid model

### 6.2.2.1 Fluid flow and turbulence model

In this paper, RANS codes are used to simulate the uniform incompressible flow past the cylinder. In this method, the mean continuity and momentum equations can be written as below (Cebeci, 2004):

$$\frac{\partial \bar{u}_j}{\partial x_j} = 0 \quad (6-1)$$

$$\rho \frac{\partial \bar{u}_i}{\partial t} + \rho \frac{\partial}{\partial x_j} (\bar{u}_i \bar{u}_j) = -\frac{\partial \bar{p}}{\partial x_i} + \frac{\partial}{\partial x_j} (\bar{\tau}_{ij} - \rho \overline{u_i'' u_j''}) \quad (6-2)$$

where  $\rho$  is the fluid density,  $t$  is time,  $x_i$  and  $x_j$  are the components of the position vectors of the fluid unit ( $i, j \in [1,2,3]$ ),  $\bar{u}$ ,  $\bar{p}$  represent the time averages of the velocity and pressure respectively, and  $\bar{\tau}_{ij}$  is the viscous stress tensor. The small-scale fluctuation of fluid velocity related to the turbulence, known as the Reynolds-stress tensor, is represented by the term  $\overline{u_i'' u_j''}$ . As Equations (6-1) and (6-2) are undetermined, they require additional equations to model the Reynolds stress term (Cebeci, 2004).

In the present study, the two-equation eddy viscosity *SST*  $K - \omega$  model ([Menter, 1994](#)) is used to provide two additional transport equations for the turbulent kinetic energy  $K$  and the dissipation rate  $\omega$ . This model, which adopts the baseline  $K - \omega$  model in the inner part of the boundary layer and  $K - \varepsilon$  model ( $\varepsilon$  is isotropic dissipation of the turbulence energy) in the free shear layer, has two advantages in the VIV simulation: (i) it can give accurate predictions on the flow separation under adverse pressure gradients by the inclusion of transport effects and (ii) can be used as a low- $R_e$  turbulence model without any extra damping wall function. However, as discussed in the introduction, this method cannot accurately predict the development of laminar-turbulent transition processes, and the turbulent damping is not accurately considered by this model. To improve the accuracy of VIV response estimations by adopting RANS *SST*  $K - \omega$  model, the low- $R_e$  correction technique proposed by [Wilcox \(2006\)](#) is adopted into the standard *SST*  $K - \omega$  model.

In the low- $R_e$  correction method, the modelling of transition is realized by damping the turbulent viscosity parameter ( $\mu_t = \rho K / \omega$ ) with a correction coefficient ( $\alpha^*$ ) ([Wilcox, 2006](#)):

$$\alpha^* = \frac{0.024 + R_{e_t}/R_k}{1 + R_{e_t}/R_k} \quad (6-3)$$

Another two coefficients also need to be defined:

$$\alpha = \frac{13}{25} \frac{\alpha_o + R_{e_T}/R_\omega}{1 + R_{e_T}/R_\omega} (\alpha^*)^{-1} \quad (6-4)$$

$$\beta^* = \frac{9}{100} \frac{100\beta_o/27 + (R_{e_T}/R_\beta)^4}{1 + (R_{e_T}/R_\beta)^4} \quad (6-5)$$

where  $R_{e_t} = \rho k / \mu \omega$  is the turbulence Reynolds number and  $\beta_o = 0.0708$ ,  $\alpha_o = 1/9$ ,  $\alpha_o^* = 1/3 \beta_o$ ,  $R_\beta = 8$ ,  $R_k = 6$  and  $R_\omega = 2.61$  as suggested by [Wilcox \(2006\)](#). It should be noted that the main aim of this low- $R_e$  correction technique is to develop a simplified but universal modification factor that is independent of the flow geometry ([Wilcox, 2006](#)). This model with the parameter given above has been applied in the many problems with the pressure gradient boundary layer, incompressible flat plate, channel flow and pipe flow ([Wilcox, 1994](#)), it also has been adopted in many other studies, for example, to investigate the flow around oscillating airfoils ([Wang et al., 2010](#)) and flow effect around the vertical axis turbine ([McNaughton et al., 2014](#)). Since

the aim of the present study is to demonstrate the effectiveness of adopting this technique to improve the accuracy for VIV simulation based on the RANS *SST*  $K - \omega$  method, the coefficients as suggested by [Wilcox \(2006\)](#) are therefore directly adopted for the VIV simulation in the present study. The parameters that may further influence the numerical results are briefly discussed in the conclusions.

Semi-Implicit Method for Pressure-Linked algorithm (SIMPLE) is used to achieve the pressure-velocity coupling on the mesh grids ([Tu et al., 2018](#)). A second-order upwind interpolation scheme is used for the convection term (left hand side of Equations (6-2)), and the hybrid initialization method is used to initialize the flow field domain.

#### **6.2.2.2 Fluid mesh grids and associated boundary conditions**

To solve the governing equations presented in Section 6.2.2.1, a 3-D multi-block domain consisting of 9 blocks (BCKs) is adopted in the present study. Figure 6-3 shows the schematic details of the fluid domain and the corresponding mesh grids. As shown in Figure 6-3, the high spatial grid resolution surrounding the cylinder is achieved by generating a very fine mesh in the annular sub-domain (BCK.5) close to the cylinder, while larger meshes are generated when they are far from the cylinder. The circular domain surrounding the cylinder is discretized with uniformly spaced grids in the azimuthal coordinate and exponentially stretched in the radial direction. The remaining rectangular blocks are meshed with hexahedral elements where various intensities are considered for the meshes.

A steady uniform flow with a freestream velocity of  $U_\infty$  is specified at the inlet boundary ( $x = -20D$ ). Transverse and spanwise velocity components are set as zero at this boundary ( $v = w = 0$ ). For the top, bottom and two lateral boundaries of the domain ( $z = \pm 4D, y = \pm 20D$ ), symmetry (free-slip) plane conditions are applied, i.e., the velocity component perpendicular to the boundary is zero. The zero-gradient condition for velocity is applied at the outlet boundary ( $x = 30D$ ), where the reference pressure is assigned to be zero. On the cylinder's smooth surface, non-slip wall condition is specified, i.e., the fluid velocity on this surface is the same with the cylinder's displacement speed.

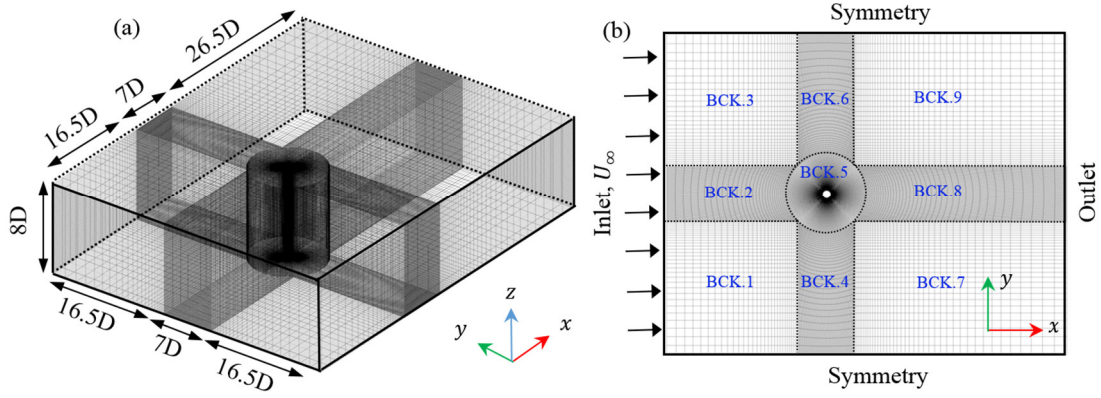


**Figure 6-3:** (a) 3-D multi-block computational domains and the corresponding mesh grids, (b) mesh in the  $xy$ -plane, the corresponding boundary conditions and the associated block number.

### 6.2.2.3 Mesh deformation

To estimate the deformation of the mesh grids, the smoothing dynamic mesh motion is utilized based on the diffusion equation ([Zhao and Cheng, 2011](#)):

$$\nabla \cdot (\gamma \nabla \vec{u}) = 0 \quad (6-6)$$

where  $\nabla$  is the differential operator,  $\vec{u}$  denotes the mesh displacement velocity, and  $\gamma$  is the diffusion coefficient, which describes how the boundary motion diffuses into the interior of the deforming mesh. With a constant  $\gamma$ , boundary motion diffuses uniformly throughout the fluid domain, while with a non-uniform value, nodes with high diffusivity tend to move together. In the present study, a non-uniform diffusion coefficient is adopted as a function of the normalized cell volume size  $V$  as follows:

$$\gamma = \frac{1}{V^\alpha} \quad (6-7)$$

in which  $\alpha$  is the diffusion parameter and it is set as 1.5 in the present study. With this value, the grids in the immediate vicinity of the cylinder wall moves almost rigidly with the cylinder, i.e., the uniformity of the near wall mesh resolution is preserved and the outermost grids are kept fixed. Mesh deformation takes place in the region in between. This area is given sufficient space so that fair mesh quality can be ensured even in the case with intensive VIV amplitude. Implicit mesh update scheme is also adopted based on which mesh motion will be updated in each computational iteration. This scheme is beneficial for the applications where the mesh motion is strongly coupled with the fluid flow.

### 6.2.3 Structural dynamics model and the associated hydrodynamics loads

In the developed FSI model, the cylinder is suspended by four body-ground type springs at the two spanwise boundary surfaces as shown in Figure 6-1(b), which allows cylinder to vibrate only in the transverse direction ( $y$ ). The crossflow equation of motion of an elastically-mounted rigid cylinder under VIV can be expressed as follows:

$$m \frac{\partial^2 y}{\partial t^2} + C \frac{\partial y}{\partial t} + \bar{k} y = F_L \quad (6-8)$$

where  $m$ ,  $C$  and  $\bar{k}$  are the oscillating mass, structural damping and spring constant, respectively,  $y$  is the crossflow displacement,  $F_L$  is the total lift force vector in the crossflow direction of the cylinder and the value per unit length can be expressed as follows:

$$F_L = \int_0^{2\pi} -p \sin \theta dA + \int \tau_w \cos \theta dA \quad (6-9)$$

where  $dA = D/2 d\theta$ ,  $D$  is the cylinder diameter,  $\theta$  is the angle position of a point on the cylinder measured from the horizontal axis, and  $p$  denotes the pressure of a given point and  $\tau_w$  is the shear stress on the cylinder's wall. The dimensionless lift coefficient  $C_L$  then can be calculated as:

$$C_L = \frac{F_L}{1/2 \rho U_\infty^2 D} \quad (6-10)$$

Similarly, the drag force  $F_D$  and the corresponding drag coefficient  $C_D$  can be calculated as follows:

$$F_D = \int_0^{2\pi} p \cos \theta dA + \int \tau_w \sin \theta dA \quad (6-11)$$

$$C_D = \frac{F_D}{1/2 \rho U_\infty^2 D} \quad (6-12)$$

In the present study, the structural damping coefficient is assumed as zero ([Zhao et al., 2014](#), [Zhang et al., 2017a](#)).

### 6.3 Mesh dependency study

In the present study, the cylinder experimentally investigated by [Khalak and Williamson \(1997a, 1999\)](#) is used as the main benchmark to compare with the numerical model. The Reynolds numbers and other dimensionless parameters are

therefore set to match with those in the experimental setup as much as possible. Accordingly, the mass ratio ( $m^*$ ) is set as 2.4 and the Reynolds number varies from 2000 to 12000 in the present study by changing the inlet flow velocity  $U_\infty$ . Table 6-1 tabulates the detailed information of the cylinder and surrounding fluid.

**Table 6-1:** Properties of the cylinder and surrounding fluid.

Parameter	Symbol	Value
Cylinder diameter	$D$	0.05(m)
Cylinder length	$L$	$8 \times D$ (m)
Cylinder mass	$m$	1.88(kg)
Fluid density	$\rho$	1000(kg/m <sup>3</sup> )
Fluid dynamic viscosity at 20°	$\mu$	$1.003 \times 10^{-3}$ (Pa.s)
Spring stiffness	$\bar{k}$	11.9(N/m)
Damping ratio	$\zeta$	zero

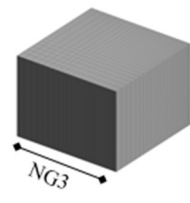
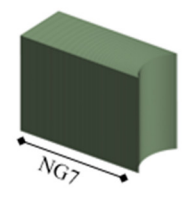
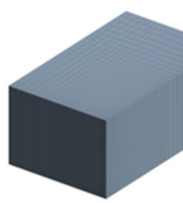
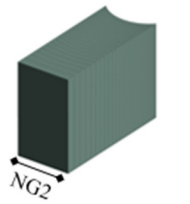
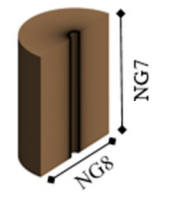
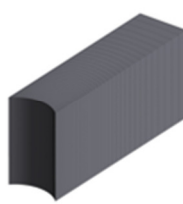
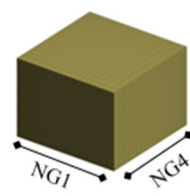
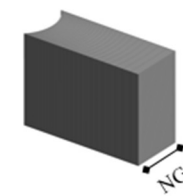
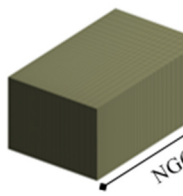
In order to ensure that the numerical results are independent of the adopted mesh size, mesh convergence study is carried out in this section. To this end, each block (BCK) as shown in Figure 6-3, is discretized by four different mesh size scenarios as illustrated in Table 6-2 and Table 6-3. Table 6-3 provides the total number of elements generated in each block in different cases. In both tables, NG stands for the number of grids seeding on each edge of the block. The calculated Strouhal number ( $S_t$ ), the root mean square of lift coefficient ( $C_L^{rms}$ ) and normalized amplitude response ( $A_y^{rms}$ ) are tabulated in Table 6-2.

**Table 6-2:** Mesh convergence testing results.

	NG1	NG2	NG3	NG4	NG5	NG6	NG7	NG8	N <sub>element</sub>	$S_t$	$C_L^{rms}$	$A_y^{rms}$
Case-1	15	24	15	15	24	25	40	40	268,800	0.21	0.38	0.31
Case-2	20	50	20	20	50	30	40	80	900,000	0.22	0.39	0.32
Case-3	20	60	20	20	60	30	40	80	1,162,000	0.22	0.43	0.39
Case-4	25	70	2540	25	70	35	40	100	1,548,000	0.22	0.43	0.40



**Table 6-3:** Number of elements generated in each BCK in different case scenarios.

	<p><b>BCK.3</b></p> <ul style="list-style-type: none"> <li>• Case1: 9,000</li> <li>• Case2: 16,000</li> <li>• Case3: 16,000</li> <li>• Case4: 25,000</li> </ul>		<p><b>BCK.6</b></p> <ul style="list-style-type: none"> <li>• Case1: 14,400</li> <li>• Case2: 40,000</li> <li>• Case3: 48,000</li> <li>• Case4: 70,000</li> </ul>		<p><b>BCK.9</b></p> <ul style="list-style-type: none"> <li>• Case1: 15,000</li> <li>• Case2: 24,000</li> <li>• Case3: 24,000</li> <li>• Case4: 35,000</li> </ul>
	<p><b>BCK.2</b></p> <ul style="list-style-type: none"> <li>• Case1: 14,400</li> <li>• Case2: 40,000</li> <li>• Case3: 48,000</li> <li>• Case4: 70,000</li> </ul>		<p><b>BCK.5</b></p> <ul style="list-style-type: none"> <li>• Case1: 153,600</li> <li>• Case2: 640,000</li> <li>• Case3: 864,000</li> <li>• Case4: 1,120,000</li> </ul>		<p><b>BCK.8</b></p> <ul style="list-style-type: none"> <li>• Case1: 24,000</li> <li>• Case2: 60,000</li> <li>• Case3: 72,000</li> <li>• Case4: 98,000</li> </ul>
	<p><b>BCK.1</b></p> <ul style="list-style-type: none"> <li>• Case1: 9,000</li> <li>• Case2: 16,000</li> <li>• Case3: 16,000</li> <li>• Case4: 25,000</li> </ul>		<p><b>BCK.4</b></p> <ul style="list-style-type: none"> <li>• Case1: 14,400</li> <li>• Case2: 40,000</li> <li>• Case3: 48,000</li> <li>• Case4: 70,000</li> </ul>		<p><b>BCK.7</b></p> <ul style="list-style-type: none"> <li>• Case1: 15,000</li> <li>• Case2: 24,000</li> <li>• Case3: 24,000</li> <li>• Case4: 35,000</li> </ul>

It can be seen that case-4 leads to similar results as those in case-3, while the total number of elements in case-3 is much less than that in case-4, i.e., much less computational effort is required for case-3. The numerical model developed in case-3 therefore can be regarded as converged and the mesh sizes in case-3 are thus adopted in the numerical simulations. It is worth mentioning that while the same mesh sizes in BCKs 1, 3, 7 and 9 are adopted in case-2 and case-3, the higher oscillations of the cylinder are obtained in case-3. This is because of the finer meshes in the vicinity of the vibrating cylinder (BCK.5) in case-3, revealing that the VIV response of the cylinder is significantly dependent on the grid quality directly surrounding the cylinder. It also should be noted that, according to the previous experimental results as shown in Figure 6-5, the reduced velocity that resulted in the peak response amplitude might occur at a normalized velocity between 4 and 5. In the present study, the convergence test is conducted at the normalized velocity of  $U^* = 5$ . The accuracy of the numerical results might be further improved if the convergence test is performed at the reduced velocity that resulted in the peak response amplitude as well as at the highest normalized velocity corresponding the highest Reynolds numbers.

#### 6.4 Results and discussion

As mentioned above, the cylinder experimentally investigated by [Khalak and Williamson \(1997a, 1999\)](#) is used as the main benchmark for the numerical model in

the present study. To further demonstrate the accuracy of the present method, some other relevant studies are also adopted. Table 6-4 summarizes the adopted studies and the corresponding governing parameters. The maximum amplitude responses in the upper regime are also tabulated in the table. As discussed above, the Reynolds number considered in the present study is within the range of 2000 and 12000, which corresponds to the normalized velocity varying from 2 to 12, and an interval of 1 is adopted in the present study. It should be noted that the damping coefficient  $\zeta$  is assumed as zero in the present numerical simulations as mentioned above, while certain damping unavoidably exist in the experimental studies as shown in the table. This is because, as supported by many experimental and numerical studies ([Khalak and Williamson, 1997b](#), [Govardhan and Williamson, 2006](#), [Pan et al., 2007](#), [Riches and Morton, 2018](#)), when the value of the mass-damping parameter ( $m^*\zeta$ ) is very small, the maximum VIV amplitude response predominantly depends on the product of  $m^*\zeta$ , but not on the specific value of mass ratio  $m^*$  or structural damping coefficient  $\zeta$ . With the very small  $m^*\zeta$  (around zero), the variation of  $\zeta$  leads to almost no change in the amplitude response ([Govardhan and Williamson, 2006](#), [Pan et al., 2007](#)). Because of this fact, many numerical studies (e.g. [Lucor et al. \(2005\)](#), [Singh and Mittal \(2005\)](#), [Zhao et al. \(2014\)](#)) used the terminology of “low mass-damping ratio” though the damping coefficient  $\zeta$  was set to zero in the numerical simulations.

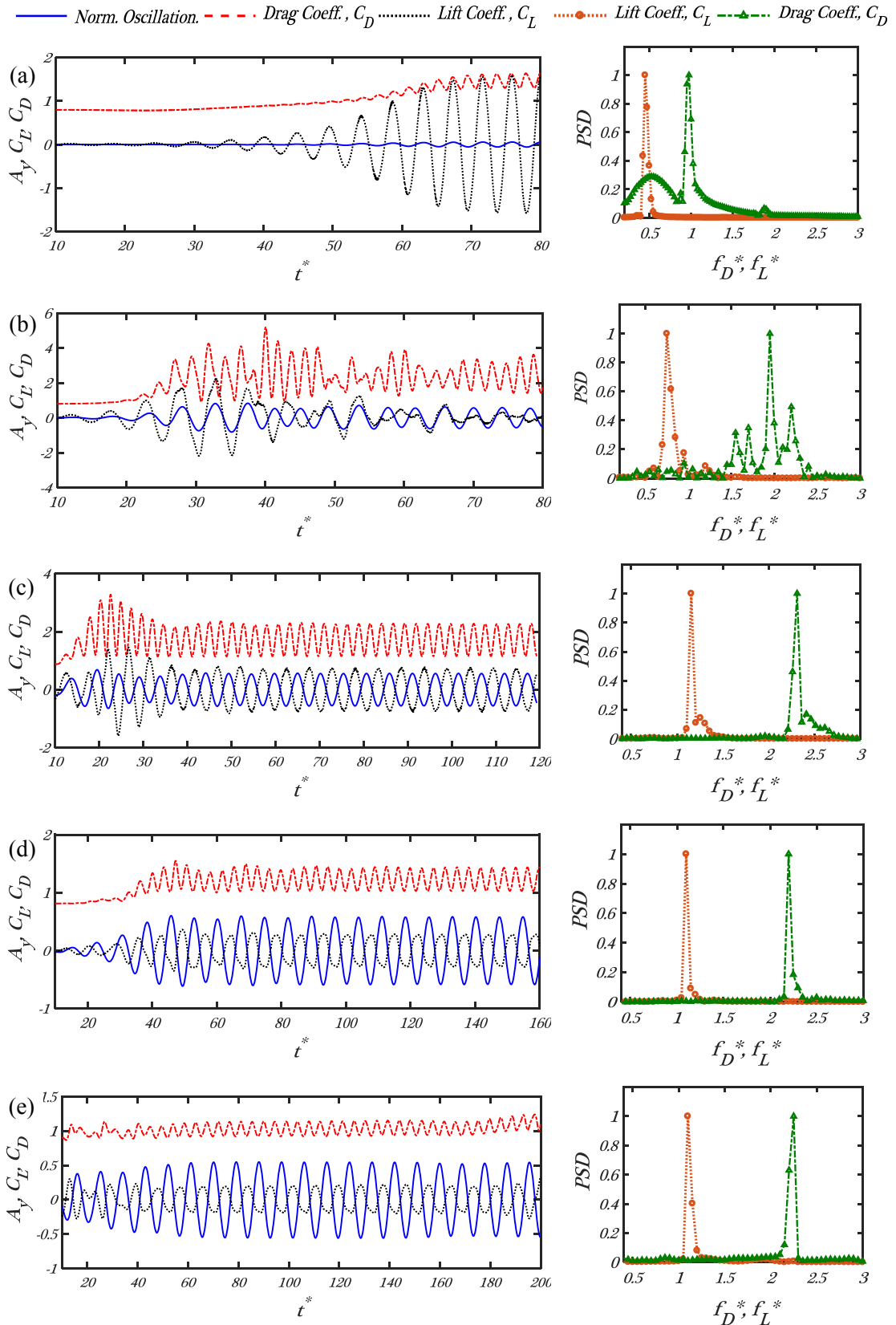
**Table 6-4:** Adopted previous studies and governing parameters.

	Method of Study	$R_e$	$m^*$	$A_{max}^*$ (in upper branch)
<a href="#">Khalak and Williamson (1997a, 1999)</a>	Experimental	2000-12000	2.4	0.97
<a href="#">Assi et al. (2010)</a>	Experimental	2000-10000	2.6	0.80
<a href="#">Cicolin and Assi (2017)</a>	Experimental	5000-25000	2.9	0.90
<a href="#">Pan et al. (2007)</a>	Numerical (2D standard SSTK – $\omega$ )	2500-13000	2.4	0.70
<a href="#">Khan et al. (2018)</a>	Numerical (2D standard SSTK – $\omega$ )	2000-14000	2.4	0.86*
Present study	Numerical (3D SSTK – $\omega$ with low- $R_e$ correction)	2000-12000	2.4	0.84

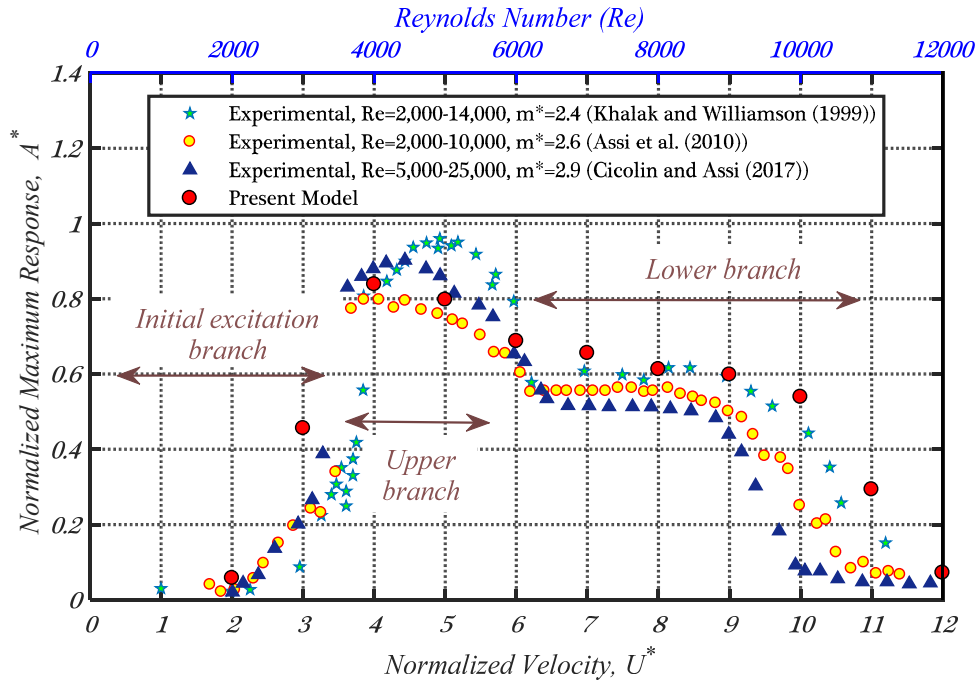
#### 6.4.1 Oscillation amplitudes and hydrodynamic forces

Figure 6-4 presents the time histories of the non-dimensional oscillation response ( $A_y$ ) and the corresponding instantaneous normalized hydrodynamic force coefficients ( $C_D, C_L$ ) for the typical normalized velocities. The power spectrum density (PSD) functions of the forces are also shown in the figure. It is well recognized that for an elastically-mounted cylinder with low mass-damping coefficient, the VIV response of

the cylinder includes three regimes, i.e., the initial, upper and lower branches. In the initial branch, two single vortices will shed per cycle (and it is dubbed 2S vortex shedding mode), and the lift force ( $F_L$ ) and cylinder oscillation ( $y$ ) are mainly in-phase. In the upper branch, the lift force and the cylinder oscillation are still in-phase, but two pairs of vortices will shed per cycle, i.e., 2P vortex shedding mode occurs. In the lower branch, 2P vortex shedding mode still dominates but the force and oscillation become out-of-phase. The numerical results shown in Figure 6-4 match well with the general observations. As shown in Figure 6-4(a) and (b), the normalized displacement and the lift coefficient are mostly in phase when  $U^* = 2$  (within the lower branch) and  $U^* = 4$  (within the upper branch). When  $U^* = 6, 8$  and  $10$  (within the lower branch, Figure 6-4(c), (d) and (e)), the two responses become out-of-phase. The corresponding vortex shedding modes will be discussed in Section 6.4.3. It will be seen that the 2S and 2P vortex shedding modes are well captured in different branches. The results also show that when  $U^* = 4$  (Figure 6-4(b)), the cylinder shows certain extent of irregular oscillations (with multi-frequency responses), i.e., the beating phenomenon occurs at this normalized velocity, which is consistent with both the physical test ([Khalak and Williamson, 1999](#)) and numerical simulations ([Pan et al., 2007](#)). This is because at this normalized velocity, the cylinder is vibrating at two or more frequencies due to the continuous complex interaction between the vibrating cylinder and the surrounding fluid. For the dominant frequencies, it can be seen from Figure 6-4 that the dominant frequency of the drag force is approximately twice that of the lift force, which again is consistent with previous studies (e.g. [Blevins \(1990\)](#)).



**Figure 6-4:** Time histories of the normalized oscillation ( $A_y$ ), the force coefficients ( $C_L, C_D$ ) and the corresponding normalized PSDs with different normalized velocities (a)  $U^* = 2$ , (b)  $U^* = 4$ , (c)  $U^* = 6$ , (d)  $U^* = 8$  and (e)  $U^* = 10$ .



**Figure 6-5:** Comparison of the normalized maximum amplitude response ( $A^*$ ) between the present model and the previous experimental studies.

Figure 6-5 compares the normalized maximum oscillations at different normalized velocities obtained in the present study and those from the previous experimental studies. It should be noted that [Khalak and Williamson \(1997a, 1999\)](#) and [Assi et al. \(2010\)](#) carried out the experimental studies in the water, for fair comparisons, some efforts are made to convert the normalized velocities based on the natural frequency in the water ( $f_w$ ) to those based on the structural natural frequency in the air ( $f_n$ ) as adopted by [Zhao et al. \(2014\)](#). As shown in Figure 6-5, the numerical model developed in the present study well captures the three typical branches. The normalized maximum vibration amplitude ( $A_{max}^*$ ) obtained in the present study is 0.84, which matches well with those reported by [Assi et al. \(2010\)](#) and [Cicolin and Assi \(2017\)](#), in which the maximum values are 0.8 and 0.9 respectively. The results also show that this value (0.84) is slightly smaller than that reported by [Khalak and Williamson \(1997a, 1999\)](#) (0.97). However, as will be shown in Figure 6-9, in general, this method yields better results compared to the other numerical models by using the  $SST K - \omega$  method, which demonstrates the effectiveness of the proposed method.

To more clearly show the accuracy of the numerical model, Figure 6-6 compares the Lissajou figure (phase plots of  $C_L(t)$  versus  $A_y(t)$ ) for three excitation regimes obtained from this study and that reported by [Khalak and Williamson \(1997a, 1999\)](#). Again good matches are obtained. These figures also clearly show the very periodic

nature of the oscillations in the lower branch (Figures 6-4(a), (b)), and the less steady dynamics in the upper branch. As shown in Figure 6-4(c), (d) and (e), the responses and forces almost vary periodically when  $U^* = 6, 8$  and  $10$ .

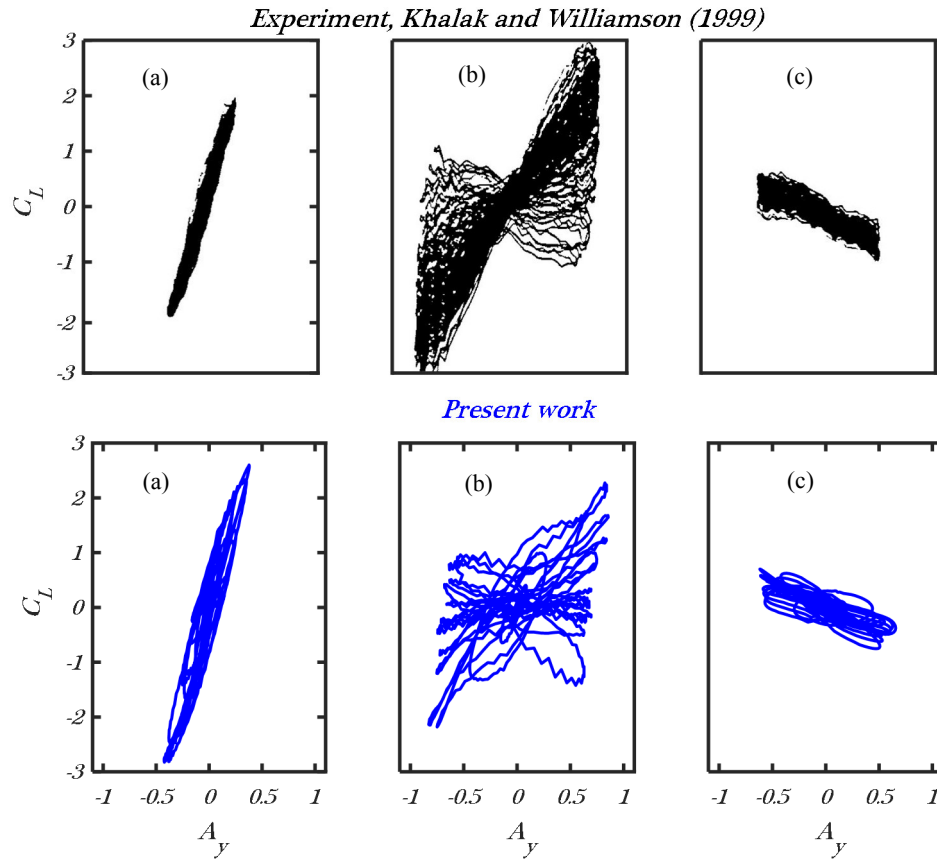


**Figure 6-6:** Phase plane portraits of  $C_L(t)$  versus  $A_y(t)$  obtained from the testing results ([Khalak and Williamson, 1999](#)) and the present model for the (a) initial (b) upper and (c) lower excitation regimes.

The different branches of VIV amplitude response can also be characterized by plotting the phase angle ( $\phi$ ) between the lift force ( $C_L$ ) and cylinder oscillation ( $y$ ). In the present study, as adopted by [Khalak and Williamson \(1997a, 1999\)](#), the Hilbert Transform ([Bracewell, 2000](#)) is utilized to detect the synchronization between the lift force and the crossflow vibration of the cylinder. The probability density function (PDF) of the phase shift ( $\phi$ ) obtained from the Hilbert Transform for different normalized velocities are shown in Figure 6-7, and an overall comparison between the dominant phase angles obtained in this study and those from the previous experimental studies is depicted in Figure 6-8. As shown in Figure 6-7(a) and (b), the lift force and the crossflow displacement demonstrate a very narrow phase shift histogram at almost  $0^\circ$  in the initial excitation regime, which indicates the force and oscillation are dominantly coherent and this regime is associated with the quasi-periodic (QP) and periodic (P) regimes as denoted by [Khalak and Williamson \(1997a, 1999\)](#). When the

dynamic system shifts from  $U^* = 3$  (initial branch, Figure 6-7(b)) to  $U^* = 4$  (the upper branch, Figure 6-7(c)), although the phase angle histogram distribution becomes broader, the dominant phase angle remains constant at approximately  $0^\circ$ . However, when  $U^* = 5$ , the vibrating system shows obvious unsteady responses, and the phase histogram becomes more wider with two dominant phase angles as shown in Figure 6-7(d), which is well consistent with the observations as reported in [Khalak and Williamson \(1999\)](#). As the normalized velocity increases further, the system moves to the lower regime, and the phase angle is switched and locked mainly to one mode with  $\phi \simeq 180^\circ$  as shown in Figure 6-7(d) and (e), representing a fully periodic response again.

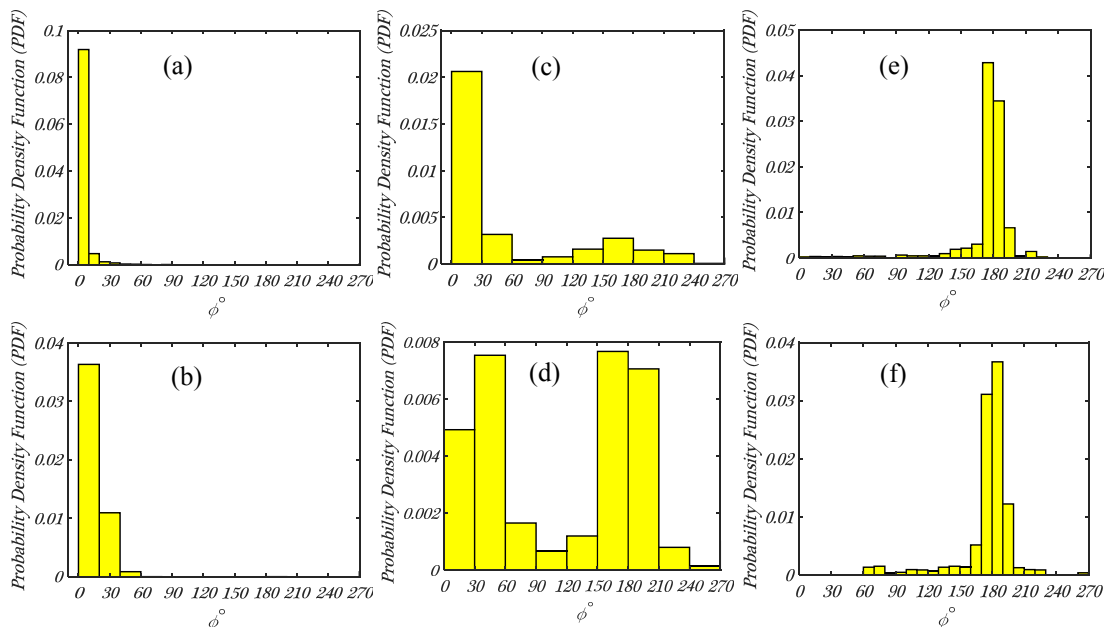


**Figure 6-7:** PDF of the phase angle ( $\phi$ ) between the lift force and cylinder crossflow displacement in different branches: (a&b) initial branch  $U^* = 2$ & $3$ ; (c&d) upper branch  $U^* = 4$ & $5$ ; and (e&f) lower branch  $U^* = 9$ & $10$ .

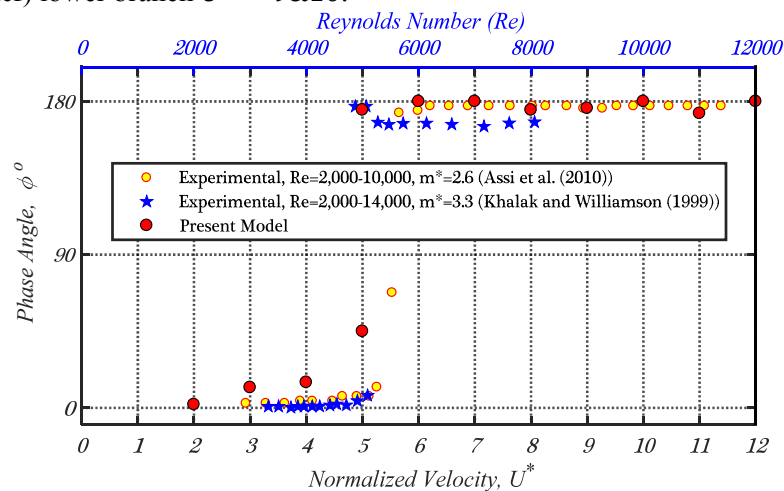
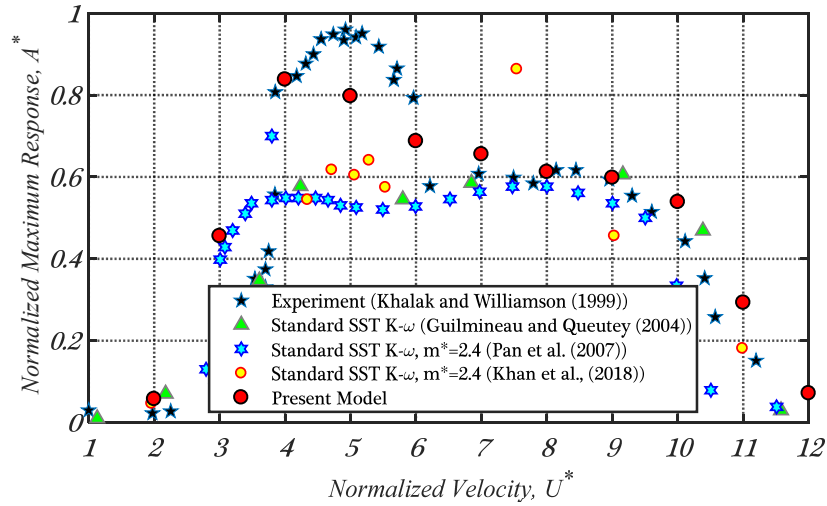


**Figure 6-8:** Comparison of the phase angle ( $\phi$ ) between the present model and previous experimental studies.

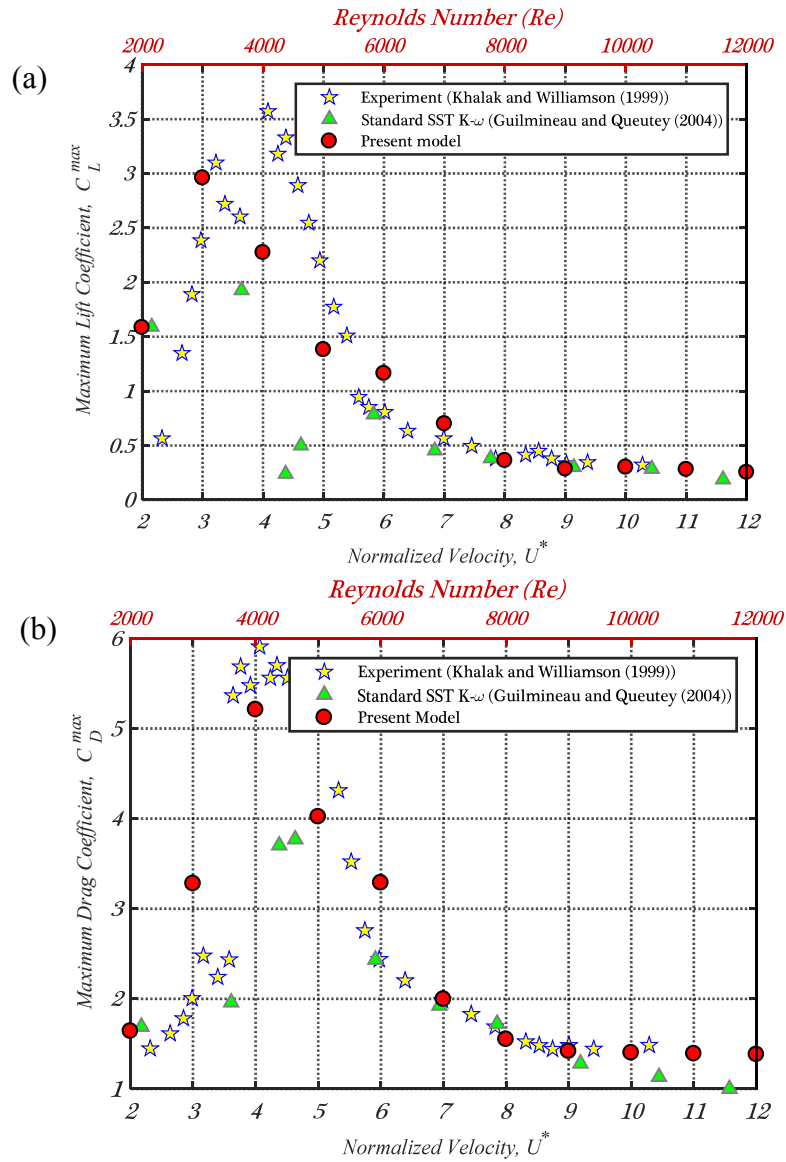
In the open literature, there are extensive numerical studies that investigated the VIV responses of a rigid cylinder based on the RANS solver. Among these studies, the ones carried out by [Guilmineau and Queutey \(2004\)](#), [Pan et al. \(2007\)](#) and [Khan et al. \(2018\)](#) are highly comparable with the current work. In these studies, same as the current work, all the simulations have been conducted for the transverse response of an elastically-mounted cylinder and the parameters have been set to be the same as those in [Khalak and Williamson \(1997a, 1999\)](#). However, it should be noted that the standard  $SST K - \omega$  method was adopted in [Guilmineau and Queutey \(2004\)](#), [Pan et al. \(2007\)](#), [Khan et al. \(2018\)](#), the low- $R_e$  correction technique is however incorporated in the current study. Furthermore, only 2-D VIV simulations were performed in [Guilmineau and Queutey \(2004\)](#), [Pan et al. \(2007\)](#), [Khan et al. \(2018\)](#), 3-D simulations are carried out in the present study. Figure 6-9 compares the normalized maximum responses obtained in the present study and [Pan et al. \(2007\)](#) and [Khan et al. \(2018\)](#). It is obvious that the current model gives the most accurate results especially in the upper branch, where it is quite challenging to reach a reasonably good results as discussed above. For the numerical model developed by [Pan et al. \(2007\)](#), although it delivered accurate results in the lower branch, there is a noticeable difference in the upper excitation regime. As shown in Figure 6-9, in the experiment ([Khalak and Williamson, 1997a, 1999](#)), larger vibrations occur within the range of  $U^* = 4 - 6$  with the normalized maximum response  $A^*$  about 0.97. The normalized maximum response reported in [Pan et al. \(2007\)](#) was however only 0.7, which is 27.8% lower than the experimental result. For the very recent study by [Khan et al. \(2018\)](#), a larger normalized maximum response was obtained and the maximum value reached 0.86 (with a difference of 11.3%). However, it should be noted that there is a significant delay in the transition from the upper branch to the lower branch. As shown in Figure 6-9, the maximum responses occurred at  $U^* = 7.5$ . In other words, this model ([Khan et al., 2018](#)) did not accurately predict the branches of the VIV responses. The numerical model developed in the present study not only well predicts the maximum response in the upper regime, but also significantly improves the accuracy in terms of the transition of oscillation regimes compared to [Khan et al. \(2018\)](#). As shown in Figure 6-9, the normalized maximum response reaches 0.84 in the present study and the difference is 13.4% compared to the experimental result. For the results in the lower branch, the present numerical model also gives very good estimations.



Figure 6-10 shows the comparisons of the normalized force coefficients obtained from the present study and previous experimental study and numerical results obtained based on the standard  $SST K - \omega$  method. Again, these results clearly show that the 3-D numerical model with the implementation of the low- $R_e$  correction technique can yield better results compared to the standard  $SST K - \omega$  method. However, it is also worth mentioning that though the present numerical simulations generally result in more accurate results compared to the previous numerical studies, some obvious discrepancies still exist compared to the experimental data. For example, as shown in Figure 6-5, when  $U^* = 3$ , the current numerical simulation yields a much larger vibration amplitude. Moreover, in the lower branch, the differences are also quite obvious especially compared to the results from [Assi et al. \(2010\)](#) and [Cicolin and Assi \(2017\)](#). The following three reasons may result in these discrepancies: (i) In this study, the RANS code equipped with  $SST K - \omega$  is adopted to simulate VIV. This model, inheritably, is unable to provide very accurate results for the VIV simulations because it reduces the fluctuations of velocity related to the turbulence of the flow and the mean value of the fluctuation is considered as equal to zero ([Cebeci, 2004](#)). (ii) The experimental results are not necessarily very accurate. For example, the three tests presented in Figure 6-5 were fairly comparable, but the obtained testing results were different due to the possible differences in the test set-up, measurement accuracy and/or the procedure of different tests, which can change the responses of the cylinders ([Khalak and Williamson, 1999](#), [Assi et al., 2010](#)). Accordingly, as shown in Figure 6-5, the numerical results are closer to [Cicolin and Assi \(2017\)](#) testing results in the upper branch, while they match [Khalak and Williamson \(1997a, 1999\)](#) results more in the lower branch. (iii) In this study, the interval of the normalized velocity ( $U^*$ ) is one, some more detailed results then might be missed at the unexamined reduced velocities in between. Responses with higher precisions are expected if smaller intervals are adopted.



**Figure 6-9:** Comparison of the normalized maximum amplitude response ( $A^*$ ) between the present model and other numerical investigations adopting  $SSTK - \omega$  method.



**Figure 6-10:** Comparisons of the maximum normalized force coefficients between the current model and previous experimental and numerical results: (a) maximum lift coefficient  $C_L^{max}$  and (b) maximum drag coefficient  $C_D^{max}$ .

## 6.4.2 Response frequencies

The normalized PSDs of the cylinder oscillations under different normalized velocities are shown in Figure 6-11. In this figure, under a particular normalized velocity, the corresponding PSD values are divided by its maximum value, i.e., for each  $U^*$ , the PSD curve varies between 0 and 1. Figure 6-12 provides the dominant peak frequencies under each normalized velocity together with the previous experimental results. As shown in Figure 6-11, when the normalized velocity is very small ( $U^* = 2$ ), one obvious peak occurs in the PSD function, and the dominant frequency is close to the Strouhal frequency ( $f_s$ ) of the static cylinder (the dashed blue line in Figure 6-12). When the normalized velocity reaches  $U^* = 3$  and  $U^* = 4$ , the spectra of oscillation show two peaks, and they correspond to  $f_s$  and the natural frequency of the cylinder in the water ( $f_w$ ) respectively. Taking  $U^* = 3$  for example,  $f_s \approx 0.58$  and  $f_w \approx 0.81$  respectively, and two obvious peaks, marked by the arrows, occur at these two frequencies as shown in Figure 6-12. As the normalized velocity increases further and the system shifts to the upper regime (e.g.  $U^* = 5$ ), the oscillation frequency ( $f_o$ ), natural frequency of the cylinder ( $f_n$ ) and the Strouhal frequency  $f_s$  become almost the same, which gives  $f^* \approx 1$ . When the system enters the lower excitation regime,  $f_o$  follows neither  $f_n$  nor  $f_s$ , and the cylinder vibrates periodically with a ‘locked’ or ‘synchronized’ frequency in between. These results coincide well with the test results as reported by [Khalak and Williamson \(1997a, 1999\)](#). In addition, when the normalized velocity is very large (e.g.  $U^* = 12$ ), two dominant frequencies are observed again. At this normalized velocity, the system falls into a new excitation region known as the ‘lock-out’ or ‘unsynchronized’ region, where the dominant vortex shedding and cylinder vibration frequencies are significantly different. The characteristics of this region are shown in Figure 6-13. The vibrating response of the cylinder is predominately governed by the high frequency of wake vortices and is clearly unsynchronized from its natural frequency. The cylinder therefore behaves almost like a fixed cylinder again and then the dominant oscillation frequency matches the Strouhal frequency of the static cylinder (dashed blue line) as shown in Figure 6-12. Similar results were obtained in [Khalak and Williamson \(1997a\)](#) and [Khalak and Williamson \(1999\)](#). It should be noted that for the VIV of a cylinder in the steady current, the vortex-shedding frequency is identical to the lift-force frequency ([Gao et al., 2015](#), [Gao et al., 2018a](#)). The vortex shedding frequency in the wake region

in the figure is therefore determined as the dominant frequency of the lift force by performing a fast Fourier transform (FFT) to the time series of the lift force. On the other hand, it also should be noted that this effect began to occur at a relatively smaller normalized velocity in the test. As shown in Figure 6-12, two peaks began to appear when  $U^*$  is larger than 10.

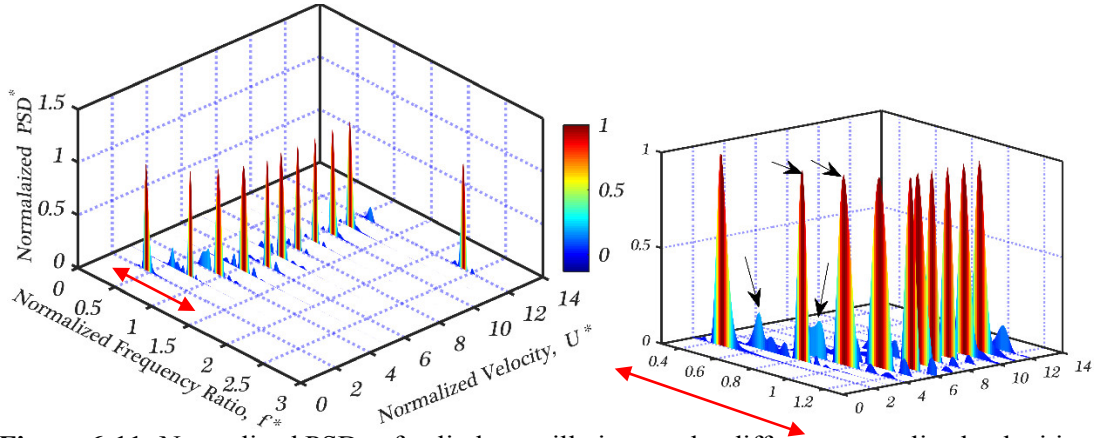


**Figure 6-11:** Normalized PSDs of cylinder oscillations under different normalized velocities.

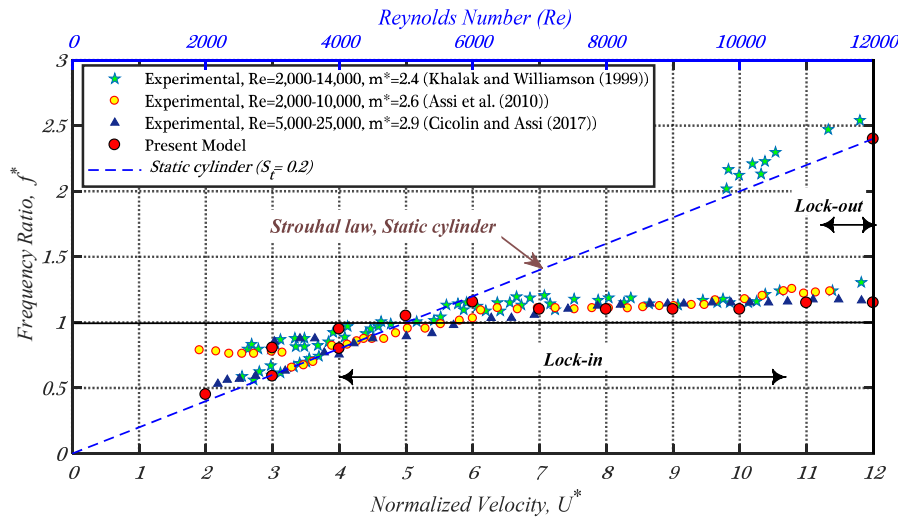


**Figure 6-12:** Dominant peaks in the spectrum of oscillation obtained in the present study (Matin Nikoo et al., 2019) and from previous experimental data.

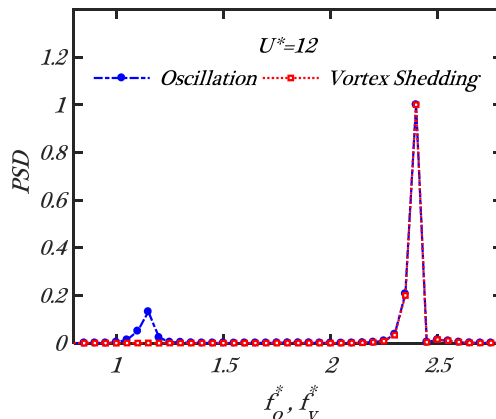


**Figure 6-13:** Normalized PSDs when  $U^* = 12$ .

### 6.4.3 Wake vortex streets

Figure 6-14 shows the 3-D vortex streets in different branches obtained in the present study. For comparison, the particle image velocimetry (PIV) as reported by [Govardhan and Williamson \(2000\)](#) are also shown in the figure. It should be noted that only the 2-D plan views of the wake vortices were given in [Govardhan and Williamson \(2000\)](#). For more straightforward comparison, the 2-D wake vortices obtained in this study at the middle of the cylinder ( $Z/D = 4$ ) are also plotted in the figure.

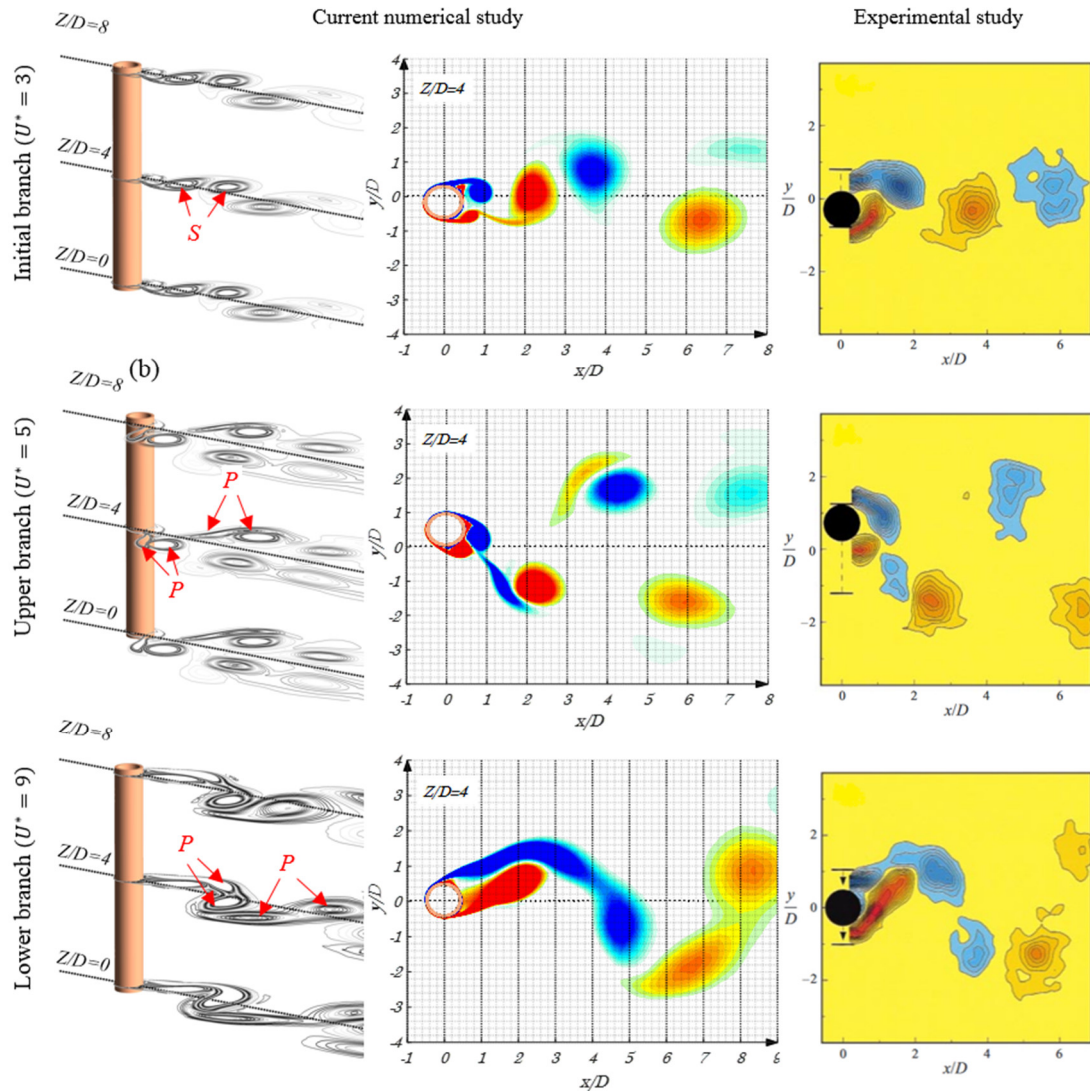


**Figure 6-14:** Comparisons between the wake vortex streets obtained in the present study ([Matin Nikoo et al., 2019](#)) and previous experimental study ([Govardhan and Williamson, 2000](#)), (a)  $U^* = 3$  (initial branch), (b)  $U^* = 5$  (upper branch) and (c)  $U^* = 9$  (lower branch).

As shown in Figure 6-14(a), at the initial branch with velocity  $U^* = 3$ , the classical 2S vortex formation mode with two dominant single vortices shedding alternately per cycle is observed. When the system arrives at the upper excitation regime (Figure 6-14(b)), the 2S mode switches to the 2P vortex pattern consisting of two pairs

of vortices shedding from two sides of the cylinder per cycle. As the normalized velocity continues to increase, the VIV responses of the cylinder transits into the lower branch with the wake mode remaining at 2P (Figure 6-14(c)). However, as described in [Govardhan and Williamson \(2000\)](#), the secondary vortex in the 2P lower branch is significantly stronger as compared to that in the upper regime. The comparisons between the current results and experimental data show very good consistence, which again demonstrates the accuracy of the 3-D FSI analyses carried out in the present study. If 2-D simulations were adopted, such good agreement may not be obtained ([Williamson and Govardhan, 2004](#)).

To more clearly show the 3-D effect, Figure 6-15 shows the pressure distribution along the cylinder's span in the three excitation branches, Figure 6-16 depicts the wake vortex streets at three spanwise cross sections ( $Z/D = 0, 4$  and  $8$ ) and Figure 6-17 plots the 3-D vortex-identification around the cylinder based on the  $Q$ -criterion ([Zhang et al., 2017b](#)) for various normalized velocities. As shown in Figure 6-15(a) and (b), when the cylinder is vibrating in the lower regime (with  $U^* = 2$  and  $3$ ), the pressure is well organized and correlated, and exhibits closely matched pattern. Since the pressure along the cylinder shows obvious 2-D feature, the 2-D models might be good enough to predict the responses in this regime. However, when the cylinder falls within the upper and lower regimes as shown in Figure 6-15(c) to (f), the variation of the pressure along the cylinder starts to grow, which consequently results in the variation of the phase difference between the lift force and cylinder oscillation along the cylinder as shown in Figure 6-7 ([Lucor et al., 2005](#), [Wang et al., 2017](#)). The 2-D models are therefore difficult to give the accurate response predictions. Similar conclusions can be drawn based on the results from Figure 6-16 and Figure 6-17.

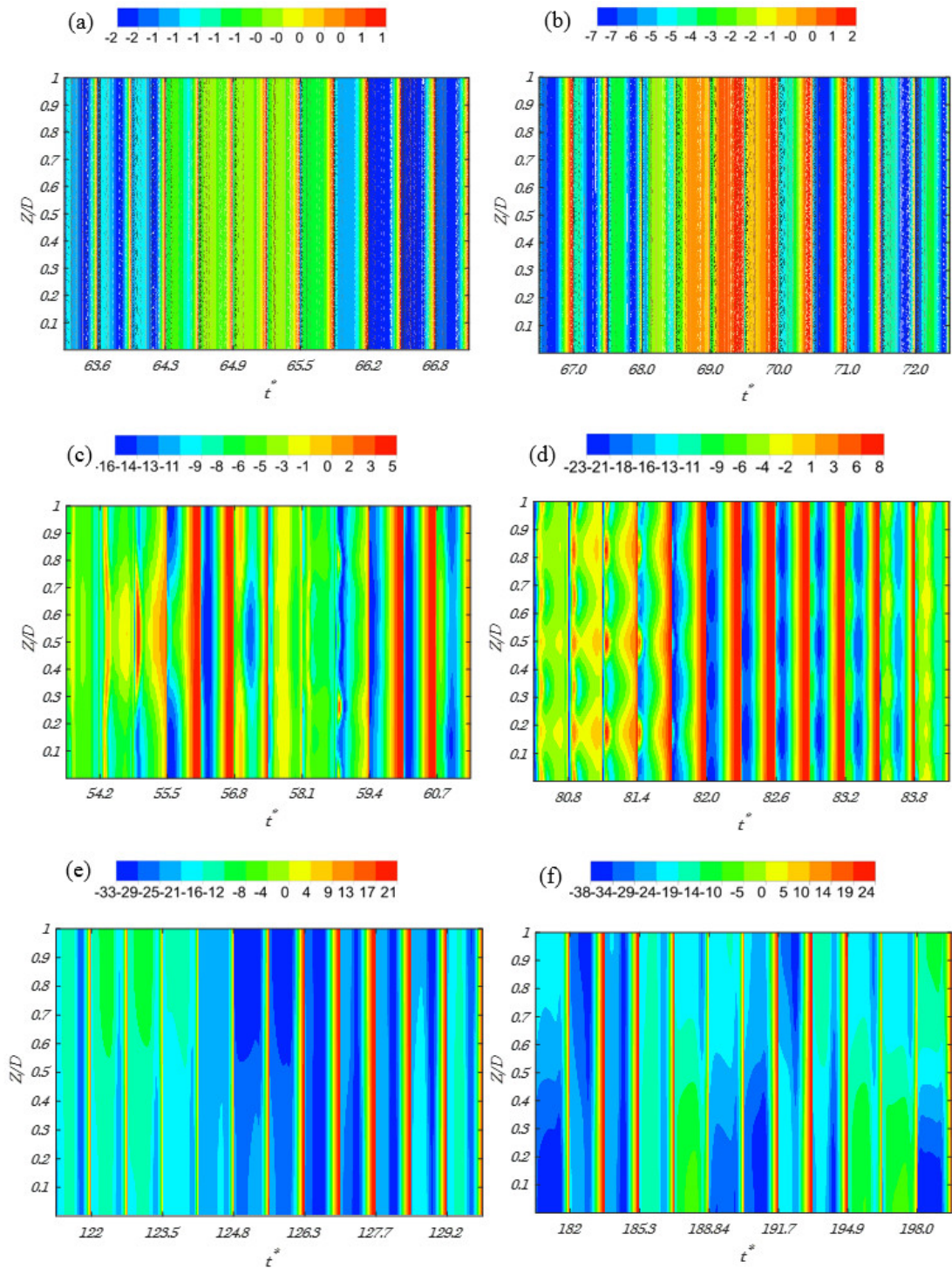


**Figure 6-15:** Contours of the pressure along the cylinder surface for (a)  $U^* = 2$  (b)  $U^* = 3$  (c)  $U^* = 4$  (d)  $U^* = 5$ , (e)  $U^* = 9$  and (f)  $U^* = 10$ .

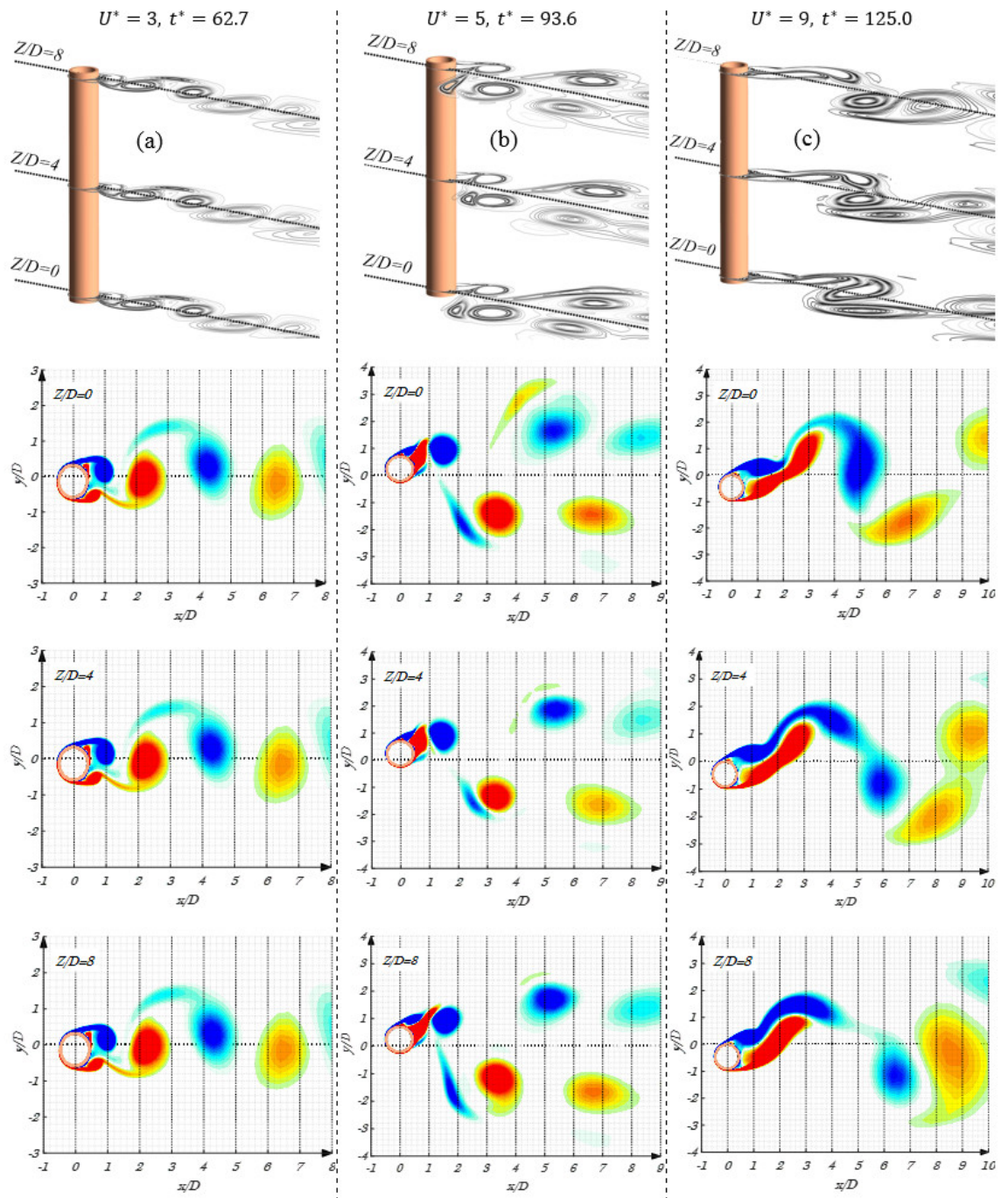


**Figure 6-16:** Contours of vortex streets along the cylinder at three cross sections ( $Z/D = 0, 4$  and  $8$ ) at (a) initial (b) upper and (c) lower branches.



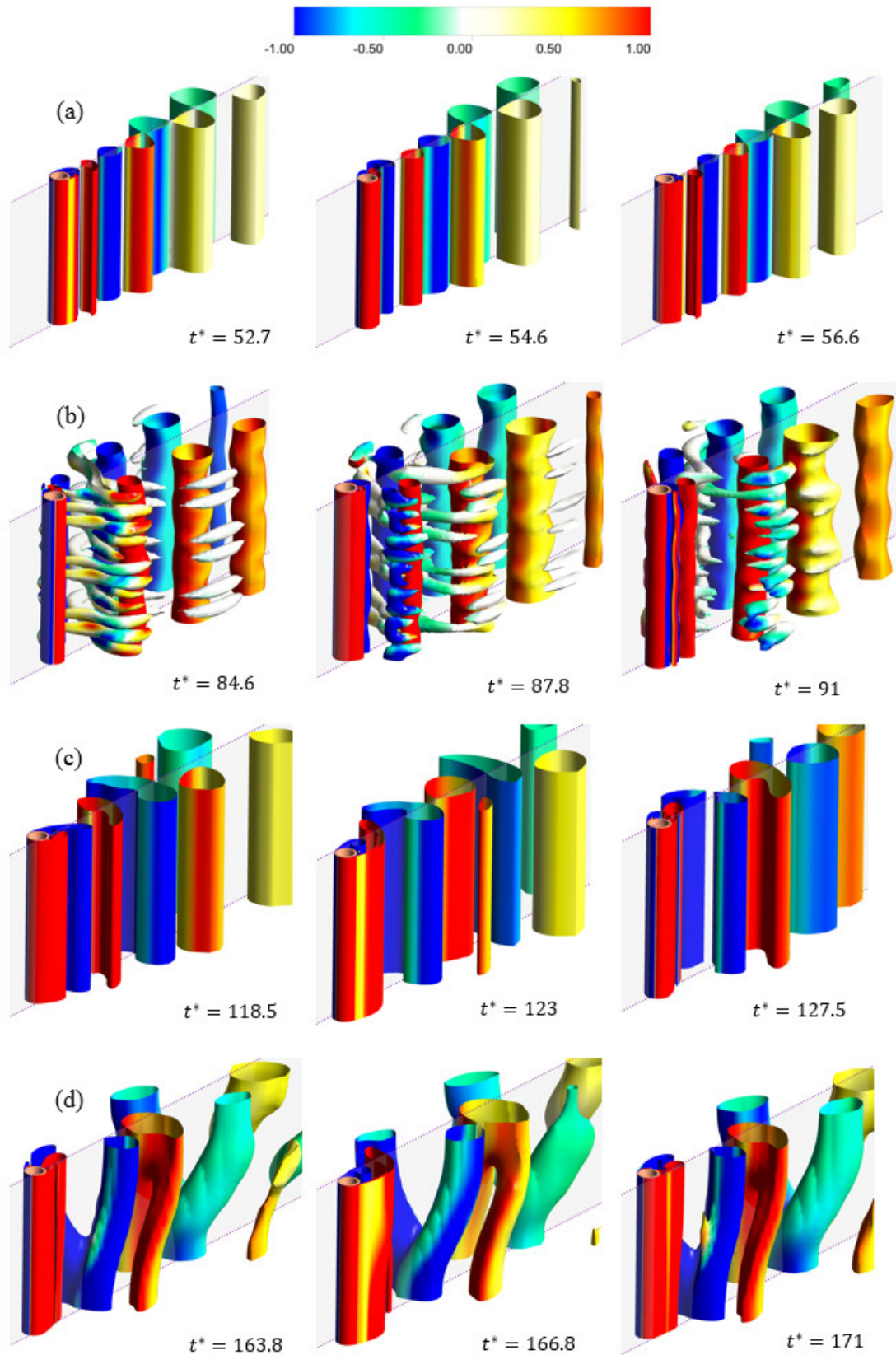


**Figure 6-17:** Q Iso-surfaces of the vortex streets around the cylinder at different normalized velocities (a)  $U^* = 3$  (b)  $U^* = 5$  (c)  $U^* = 7$  (d)  $U^* = 9$ .

## 6.5 Conclusion

This paper proposes using RANS  $SST K - \omega$  method with low- $R_e$  correction technique to calculate the 3-D VIV responses of an elastically-mounted rigid cylinder subjected to the fluid flow. A coupled CFD-FSI framework is developed by coupling the ANSYS Mechanical and FLUENT finite volume solvers together. The numerical results in terms of the oscillation amplitude, hydrodynamic forces, response frequencies and wake vortices are obtained and compared with previous studies in detail. Numerical results show that the proposed method can significantly improve the accuracy of the VIV response estimation of the cylinder especially in the upper branch. Moreover, the 3-D vortex streets around the cylinder can be well captured by using this method.

Though the effectiveness of the Wilcox's low- $R_e$  correction technique is demonstrated in the present study, following topics deserve further investigations:

(i) Only the subcritical flow regime is considered in the present study. In some cases, critical and supercritical flow regimes may be important. Notwithstanding the fact that CFD simulations of the flow past a cylinder at high Reynolds numbers are quite challenging and time-consuming, further investigations are needed to demonstrate the applicability of the Wilcox's method in these regimes.

(ii) In the present study, the coefficients suggested by [Wilcox \(2006\)](#) are directly adopted for the VIV simulations. The parameters in Equations (6-3)-(6-5) such as  $R_\beta$ ,  $R_k$  and  $R_\omega$  might obviously influence the numerical results. The proper selection of these parameters may further improve the accuracy of the numerical results, therefore deserves investigation in the future.

## 6.6 References

- ANSYS®. (2016). Academic research, release 17.2, Theory guide.
- Argyropoulos, C.D., Markatos, N.C. (2015). Recent advances on the numerical modelling of turbulent flows. *Applied Mathematical Modelling*, 39 (2), 693-732.
- Assi, G.R.S., Bearman, P.W., Meneghini, J.R. (2010). On the wake-induced vibration of tandem circular cylinders: the vortex interaction excitation mechanism. *Journal of Fluid Mechanics*, 661, 365-401.
- Blevins, R. (1990). Flow-Induced Vibration. *Van Nostrand Reinhold Company, New York*.
- Bracewell, R.N. (2000). The Fourier transform and its applications, Third ed. *McGraw-Hill New York*.
- Cebeci, T. (2004). Analysis of turbulent flows. *Elsevier, Oxford*.

- Cicolin, M.M., Assi, G.R.S. (2017). Experiments with flexible shrouds to reduce the vortex-induced vibration of a cylinder with low mass and damping. *Applied Ocean Research*, 65, 290-301.
- Facchinetti, M.L., De Langre, E., Biolley, F. (2004). Coupling of structure and wake oscillators in vortex-induced vibrations. *Journal of Fluids and Structures*, 19 (2), 123-140.
- Farshidianfar, A., Zanganeh, H. (2010). A modified wake oscillator model for vortex-induced vibration of circular cylinders for a wide range of mass-damping ratio. *Journal of Fluids and Structures*, 26 (3), 430-441.
- Gabbai, R., Benaroya, H. (2005). An overview of modeling and experiments of vortex-induced vibration of circular cylinders. *Journal of Sound and Vibration*, 282 (3), 575-616.
- Gao, Y., Fu, S., Ren, T., Xiong, Y., Song, L. (2015). VIV response of a long flexible riser fitted with strakes in uniform and linearly sheared currents. *Applied Ocean Research*, 52, 102-114.
- Gao, Y., Zong, Z., Zou, L., Jiang, Z. (2018a). Effect of surface roughness on vortex-induced vibration response of a circular cylinder. *Ships and Offshore Structures*, 13 (1), 28-42.
- Gao, Y., Zong, Z., Zou, L., Takagi, S., Jiang, Z. (2018b). Numerical simulation of vortex-induced vibration of a circular cylinder with different surface roughnesses. *Marine Structures*, 57, 165-179.
- Govardhan, R.N., Williamson, C.H.K. (2000). Modes of vortex formation and frequency response of a freely vibrating cylinder. *Journal of Fluid Mechanics*, 420, 85-130.
- Govardhan, R.N., Williamson, C.H.K. (2006). Defining the 'modified Griffin plot' in vortex-induced vibration: revealing the effect of Reynolds number using controlled damping. *Journal of Fluid Mechanics*, 561, 147-180.
- Guilmineau, E., Queutey, P. (2004). Numerical simulation of vortex-induced vibration of a circular cylinder with low mass-damping in a turbulent flow. *Journal of Fluids and Structures*, 19 (4), 449-466.
- Kang, Z., Ni, W., Sun, L. (2017). A numerical investigation on capturing the maximum transverse amplitude in vortex induced vibration for low mass ratio. *Marine Structures*, 52, 94-107.
- Khalak, A., Williamson, C.H.K. (1996). Dynamics of a hydroelastic cylinder with very low mass and damping. *Journal of Fluids and Structures*, 10 (5), 455-472.
- Khalak, A., Williamson, C.H.K. (1997a). Fluid forces and dynamics of a hydroelastic structure with very low mass and damping. *Journal of Fluids and Structures*, 11 (8), 973-982.
- Khalak, A., Williamson, C.H.K. (1997b). Investigation of relative effects of mass and damping in vortex-induced vibration of a circular cylinder. *Journal of Wind Engineering and Industrial Aerodynamics*, 69-71, 341-350.
- Khalak, A., Williamson, C.H.K. (1999). Motions, forces and mode transitions in vortex-induced vibrations at low mass-damping. *Journal of Fluids and Structures*, 13 (7-8), 813-851.
- Khan, N.B., Ibrahim, Z., Khan, M.I., Hayat, T., Javed, M.F. (2018). VIV study of an elastically mounted cylinder having low mass-damping ratio using RANS model. *International Journal of Heat and Mass Transfer*, 121, 309-314.
- Kurushina, V., Pavlovskaja, E., Postnikov, A., Wiercigroch, M. (2018). Calibration and comparison of VIV wake oscillator models for low mass ratio structures. *International Journal of Mechanical Sciences*, 142-143, 547-560.
- Law, Y.Z., Jaiman, R.K. (2017). Wake stabilization mechanism of low-drag suppression devices for vortex-induced vibration. *Journal of Fluids and Structures*, 70, 428-449.

- Lucor, D., Foo, J., Karniadakis, G.E. (2005). Vortex mode selection of a rigid cylinder subject to VIV at low mass-damping. *Journal of Fluids and Structures*, 20 (4), 483-503.
- Mackowski, A., Williamson, C. (2013). An experimental investigation of vortex-induced vibration with nonlinear restoring forces. *Physics of Fluids*, 25 (8), 087101.
- Matin Nikoo, H., Bi, K., Hao, H. (2018). Effectiveness of using pipe-in-pipe (PIP) concept to reduce vortex-induced vibrations (VIV): Three-dimensional two-way FSI analysis. *Ocean Engineering*, 148 (Supplement C), 263-276.
- Matin Nikoo, H., Bi, K., Hao, H. (2019). Three-dimensional vortex-induced vibration of a circular cylinder at subcritical Reynolds numbers with low-Re correction. *Marine Structures*, 66, 288-306.
- McNaughton, J., Billard, F., Revell, A. (2014). Turbulence modelling of low Reynolds number flow effects around a vertical axis turbine at a range of tip-speed ratios. *Journal of Fluids and Structures*, 47, 124-138.
- Menter, F.R. (1994). Two-equation eddy-viscosity turbulence models for engineering applications. *AIAA Journal*, 32 (8), 1598-1605.
- Miller, G.D., Williamson, C.H.K. (1994). Control of three-dimensional phase dynamics in a cylinder wake. *Experiments in Fluids*, 18 (1), 26-35.
- Ong, M.C., Utnes, T., Holmedal, L.E., Myrhaug, D., Pettersen, B. (2009). Numerical simulation of flow around a smooth circular cylinder at very high Reynolds numbers. *Marine Structures*, 22 (2), 142-153.
- Pan, Z.Y., Cui, W.C., Miao, Q.M. (2007). Numerical simulation of vortex-induced vibration of a circular cylinder at low mass-damping using RANS code. *Journal of Fluids and Structures*, 23 (1), 23-37.
- Postnikov, A., Pavlovskaja, E., Wiercigroch, M. (2017). 2DOF CFD calibrated wake oscillator model to investigate vortex-induced vibrations. *International Journal of Mechanical Sciences*, 127, 176-190.
- Prasanth, T., Mittal, S. (2008). Vortex-induced vibrations of a circular cylinder at low Reynolds numbers. *Journal of Fluid Mechanics*, 594, 463-491.
- Rahmanian, M., Cheng, L., Zhao, M., Zhou, T. (2014). Vortex induced vibration and vortex shedding characteristics of two side-by-side circular cylinders of different diameters in close proximity in steady flow. *Journal of Fluids and Structures*, 48, 260-279.
- Riches, G., Morton, C. (2018). One degree-of-freedom vortex-induced vibrations at constant Reynolds number and mass-damping. *Experiments in Fluids*, 59 (10), 157.
- Singh, S.P., Mittal, S. (2005). Vortex-induced oscillations at low Reynolds numbers: Hysteresis and vortex-shedding modes. *Journal of Fluids and Structures*, 20 (8), 1085-1104.
- Tu, J., Yeoh, G.H., Liu, C. (2018). Computational fluid dynamics: a practical approach. *Butterworth-Heinemann*.
- Tutar, M., Holdø, A. (2001). Computational modelling of flow around a circular cylinder in sub-critical flow regime with various turbulence models. *International journal for numerical methods in fluids*, 35 (7), 763-784.
- Wang, E., Xiao, Q. (2016). Numerical simulation of vortex-induced vibration of a vertical riser in uniform and linearly sheared currents. *Ocean Engineering*, 121, 492-515.
- Wang, E., Xiao, Q., Incecik, A. (2017). Three-dimensional numerical simulation of two-degree-of-freedom VIV of a circular cylinder with varying natural frequency ratios at Re=500. *Journal of Fluids and Structures*, 73, 162-182.

- Wang, K., Ji, C., Chi, Q., Wu, H. (2018). Hydrodynamic force investigation of a rigid cylinder under the coupling CF and IL motion. *Journal of Fluids and Structures*, 81, 598-616.
- Wang, S., Ingham, D.B., Ma, L., Pourkashanian, M., Tao, Z. (2010). Numerical investigations on dynamic stall of low Reynolds number flow around oscillating airfoils. *Computers & Fluids*, 39 (9), 1529-1541.
- Wilcox, D.A. (1994). Simulation of transition with a two-equation turbulence model. *AIAA Journal*, 32 (2), 247-255.
- Wilcox, D.C. (2006). Turbulence modeling for CFD, Third ed. *DCW industries La Canada, CA*.
- Williamson, C.H.K., Govardhan, R.N. (2004). Vortex-induced vibrations. *Annu. Rev. Fluid Mech.*, 36, 413-455.
- Williamson, C.H.K., Govardhan, R.N. (2008). A brief review of recent results in vortex-induced vibrations. *Journal of Wind Engineering and Industrial Aerodynamics*, 96 (6-7), 713-735.
- Zhang, K., Katsuchi, H., Zhou, D., Yamada, H., Zhang, T., Han, Z. (2017a). Numerical simulation of vortex induced vibrations of a flexibly mounted wavy cylinder at subcritical Reynolds number. *Ocean Engineering*, 133, 170-181.
- Zhang, Y., Liu, K., Xian, H., Du, X. (2017b). A review of methods for vortex identification in hydroturbines. *Renewable and Sustainable Energy Reviews*, 81 (1), 1269-1285.
- Zhao, M., Cheng, L. (2011). Numerical simulation of two-degree-of-freedom vortex-induced vibration of a circular cylinder close to a plane boundary. *Journal of Fluids and Structures*, 27 (7), 1097-1110.
- Zhao, M., Cheng, L., An, H., Lu, L. (2014). Three-dimensional numerical simulation of vortex-induced vibration of an elastically mounted rigid circular cylinder in steady current. *Journal of Fluids and Structures*, 50, 292-311.

# Chapter 7 Using stress-blended eddy simulation (SBES) method to simulate vortex-induced vibration of an elastically-mounted cylinder

Under review

---

## ABSTRACT

Vortex-induced vibration (VIV) has received extensive attentions due to its frequent occurrence in many engineering structures. Various turbulence models have been adopted to simulate VIV and the associated wake vortex streets. The most commonly used turbulence models, namely the Reynolds-Averaged Navier-Stokes (RANS)-based codes are inherently poor in simulating the flows with massive separation such as VIV. On the other hand, although scale-resolving simulations such as large eddy simulation (LES) can provide more accurate results, they are computationally unfeasible in most practical applications. As a solution in between, a hybrid RANS-LES model, which combines the advantages of both RANS and LES methods, can offer a good balance between accuracy and computational cost. In the present study, a hybrid RANS-LES turbulence model, namely the stress-blended eddy simulation (SBES) method, is used to simulate the VIV of an elastically-mounted rigid cylinder within a coupled fluid-structure interaction (FSI) framework. To illustrate the efficiency of the proposed method, the results obtained by using this method are compared with the experimental data and the RANS simulation results. Three-dimensional (3-D) numerical results show that the SBES model can accurately simulate the VIV and capture the wake vortex modes. In particular, the SBES model provides significant improvement in capturing the maximum amplitude response occurring in the upper branch where the widely used RANS models usually fail to capture.

## 7.1 Introduction

When a flow passes a bluff body such as a cylinder it may cause wake vortex shedding, which in turn leads to the transient fluctuating forces and vibrations to the body. This phenomenon is known as the vortex-induced vibration (VIV). On the one hand, when the periodic forces induced by vortex shedding occur at a frequency close to the natural frequency of the structure, synchronization or lock-in phenomenon occurs. This

phenomenon is associated with large amplitude oscillations of the body and may threaten the overall stability of the whole structure. VIV is thus recognized as a main cause of damage in many structures such as subsea pipelines and marine risers ([Pastrana et al., 2018](#)). On the other hand, VIV has been recently acknowledged as a renewable source of energy, and various methods with different mechanisms have been proposed to harvest the energy from VIV ([Ding et al., 2016](#), [Huynh et al., 2018](#), [Zhu et al., 2018](#), [Zhang et al., 2019](#)). To address this important problem, extensive experimental and numerical attempts have been devoted ([Gabbai and Benaroya, 2005](#), [Bearman, 2011](#), [Wu et al., 2012](#), [Rostami and Armandei, 2017](#), [Kurushina et al., 2018](#)).

On the experimental side, a few decades of research efforts have yielded an extensive literature on VIV. These experiments were performed primarily on the elastically-mounted rigid cylinder in the water channel with attentions mainly on the vibrations of the cylinder in the crossflow direction. According to these experimental studies, it was found that the main influencing parameters on the VIV include the product of mass and damping ratio  $m^*\zeta$  (in which,  $m^*$  is the mass of the oscillating body divided by the mass of the displaced fluid, and  $\zeta$  is the damping ratio), the governing Reynolds number ( $Re$ ), the turbulence level and the surface roughness. Among these parameters, mass-damping ratio  $m^*\zeta$  significantly influences the maximum oscillation amplitude of VIV. For a cylinder with low mass-damping ratio, there are generally three principal oscillation regimes, namely the ‘initial’, ‘upper’ and ‘lower’ branches ([Khalak and Williamson, 1999](#)). The ‘upper’ branch, however, disappears when the mass-damping ratio is high. [Williamson and Govardhan \(2004\)](#), [Gabbai and Benaroya \(2005\)](#) and [Williamson and Govardhan \(2008\)](#) broadly reviewed these experimental studies.

Extensive research efforts have been also made to accurately capture the VIV by using numerical simulation tools. Computations of unsteady wake vortices, turbulent flow features and separated flow fields associated with VIV phenomenon require a carefully selected turbulence model. In general, there are three methods for VIV simulation, namely the Direct Numerical Simulation (DNS), the Large Eddy Simulation (LES), and the Reynolds-Averaged Navier-Stokes Simulation (RANS). In the DNS method, all the spatial and temporal scales of turbulence need to be solved, it is therefore extremely time consuming, even for the case with simple geometry and low Reynolds number ([Chaouat, 2017](#)). In the LES method, large scale turbulence motions of the flow are explicitly solved, whereas the effect of the small scales is modelled by using

a sub-grid model ([Yang, 2015](#)). Although LES method has received much attention recently in the turbulent flow simulations ([Prsic et al., 2016](#)), it is still computationally too expensive due to the need of extremely fine mesh grids near the wall boundary especially under large Reynolds numbers ([Chaouat, 2017](#)). To save computing resources, turbulent fluctuations of the flow are averaged in the RANS approach. This method thus only yields results for the mean quantities of the flow, while the entire turbulence spectrum is modelled with a number of empirical constants. The RANS models perform well in the boundary-layer region but show significant weaknesses in the separated regions where the unsteady scales play an important role ([Fröhlich and Von Terzi, 2008](#), [Yeon et al., 2016](#), [Kornev et al., 2019](#)). It also should be noted that the RANS models are incapable of capturing many crucial turbulent features of the flow such as irregularity and diffusivity ([Yadav et al., 2019](#)).

Table 7-1 summarizes the featured experimental studies on VIV, and Table 7-2 tabulates the typical numerical investigations. The overall VIV responses obtained from these numerical studies with different turbulence models are shown in Figure 7-1. It can be seen that most of the numerical models failed to capture the maximum amplitude of the cylinder, which is however of significant importance for designers in engineering practices. A very few attempts have been made recently to address this challenge ([Kang et al., 2017](#), [Zheng and Wang, 2017](#)). To the best knowledge of the authors, only three attempts made by [Zheng and Wang \(2017\)](#), [Zhang et al. \(2017\)](#) and [Saltara et al. \(2011\)](#) captured the maximum VIV amplitude of elastically-mounted rigid cylinder vibrating in the crossflow direction. However, some clarifications should be made regarding these models: (i) [Zheng and Wang \(2017\)](#) adopted a two-dimensional (2-D) model to predict the VIV responses. On the other hand, as illustrated by many researchers (e.g. [Mittal and Balachandar \(1995\)](#) and [Singh and Mittal \(2005a\)](#)), for the flow regime with  $Re > 180$  the flow undergoes obvious three-dimensional (3-D) transitional instabilities. The 2-D model as adopted by [Zheng and Wang \(2017\)](#) thus may not be able to accurately predict the 3-D characteristics of the flow. Moreover, capability of the proposed model to capture other important features of the VIV problem such as vortex shedding frequencies and wake modes are not discussed in the study. Furthermore, the inherent hypothesis of the RANS model as adopted by [Zheng and Wang \(2017\)](#) is the separation of mean and turbulent scales, which is however not strictly observed at the subcritical Reynolds numbers ([Rosetti](#)



[and Vaz, 2017](#)). (ii) It is well known that Reynolds number can strongly influence the VIV response of the cylinder ([Govardhan and Williamson, 2006](#)). A constant Reynolds number ( $R_e = 5000$ ) was adopted in the LES simulations by [Zhang et al. \(2017\)](#), which ignored the significant effect of this factor. In addition, as discussed above, LES is a very computation-intensive model and is not easy to be implemented in many applications. (iii) The maximum VIV amplitude obtained in [Saltara et al. \(2011\)](#) by using the Detached Eddy Simulation (DES, which will be discussed in the next paragraph) is noticeably higher than the testing results, and more importantly this model failed to accurately capture the VIV response branches as shown in Figure 7-1(d).

**Table 7-1:** Summary of VIV experiments.

	$\sim R_e$	$m^*$	$\zeta$	$\sim A^*$
<a href="#">Khalak and Williamson (1999)</a>	2,000-12,000	2.40	0.0054	0.97
<a href="#">Govardhan and Williamson (2000)</a>	1,000-10,000	1.19	0.0050	1.02
<a href="#">Assi et al. (2006)</a>	3,000-13,000	1.92	0.0070	0.90
<a href="#">Kiu et al. (2011)</a>	17,000-83,000	2.36	0.0060	0.98
<a href="#">Wang et al. (2017)</a>	3,000-13,000	1.00	0.0173	0.97
<a href="#">Soti et al. (2018)</a>	3,805-11,416	3.00	0.0025	0.92
<a href="#">Modir and Goudarzi (2019)</a>	15,000-60,000	2.26	0.0500	0.98

**Table 7-2:** Summary of numerical VIV simulations.

	Domain	Flow simulation	$\sim R_e$	$m^*$	$\zeta$	$\sim A^*$
<a href="#">Guilmineau and Queutey (2004)</a>	2D	RANS SST $K - \omega$	900-15,000	2.4	0.0054	0.61
<a href="#">Zheng and Wang (2017)</a>	2D	RANS SST $K - \omega$ with TVD <sup>^</sup> scheme	Not available	2.4	0.0054	0.97
<a href="#">Pan et al. (2007)</a>	2D	RANS SST $K - \omega$	2,500-13,000	2.4	zero and 0.0054	0.70
<a href="#">Khan et al. (2018)</a>	2D	RANS SST $K - \omega$	1,700-14,000	2.4	0.0004	0.86
<a href="#">Zhang et al. (2018)</a>	2D	RANS SST $K - \omega$	1,850-13,500	2.4	0.0045	0.84
<a href="#">Zhao et al. (2014)</a>	2D	RANS	1,000	2.0	zero	0.57
<a href="#">Matin Nikoo et al. (2019)</a>	3D	RANS SST $K - \omega$ with low- $R_e$ correction	2000-12000	2.4	zero	0.87
<a href="#">Li et al. (2014)</a>	2D	RANS with RNG <sup>^^</sup> $K - \varepsilon$ scheme	1,700-11,600	2.4	0.0054	0.73
<a href="#">Gsell et al. (2019)</a>	3D	DNS	3,900	2.0	zero	0.80
<a href="#">Lucor and Triantafyllou (2008)</a>	2D	DNS	Not available	2.0	zero	0.60
<a href="#">Navrose and Mittal (2013)</a>	3D	DNS	1,000	10	zero	0.70
<a href="#">Zhao et al. (2014)</a>	3D	DNS	1,000	2.0	zero	0.72
<a href="#">Lucor et al. (2005)</a>	3D	DNS	1,000-3,000	2.0	zero	0.83
<a href="#">Zhao and Cheng (2014)</a>	3D	DNS	300	2.0	zero	0.74
<a href="#">Zhang et al. (2017)</a>	3D	LES	5,000	2.5	zero	0.98
<a href="#">Matin Nikoo et al. (2018)</a>	3D	LES	1,000	2.0	zero	0.79
<a href="#">Al-Jamal and Dalton (2004)</a>	2D	LES	8,000	1.67	0.0200	0.87
<a href="#">Saltara et al. (2011)</a>	3D	DES	10,000	3.3	0.0026	1.05

<sup>^</sup>Total Variation Diminishing <sup>^^</sup>Re-Normalization Group

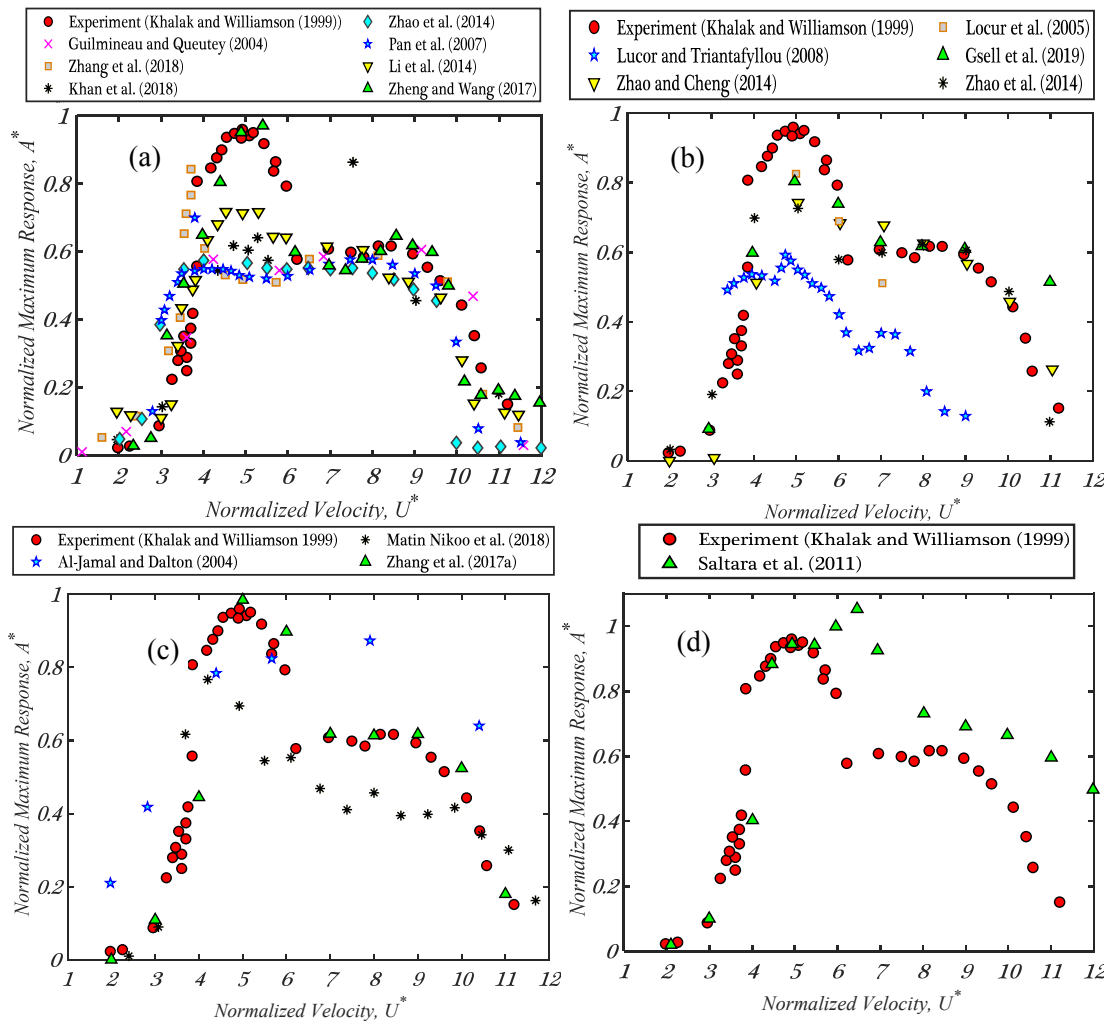


**Figure 7-1:** Obtained normalized maximum responses in the VIV numerical simulations by using different turbulence models: (a) RANS (b) DNS (c) LES and (d) DES.

Critical literature review reveals that most previous numerical models failed to capture the maximum VIV amplitude, and for those models captured the maximum amplitude, certain limitations exist. It is thus imperative to develop more reliable models for VIV simulation with improved accuracy and affordable computational cost. Hybrid RANS-LES turbulence strategy has been proposed as a viable approach to simulate turbulence flow to preserve both the advantages of LES and RANS methods ([Fröhlich and Von Terzi, 2008](#)), and quite a few hybrid RANS-LES models have been proposed such as the DES ([Spalart, 1997](#)), Wall-Modelled Large-Eddy Simulation (WMLES) ([Mukha et al., 2019](#)), Very Large Eddy Simulation (VLES) ([Liu and Shih, 2006](#)) and Partially Resolved Numerical Simulation (PRNS) ([Shih and Liu, 2004](#)). Numerical results showed that these hybrid models generally lead to more accurate results compared to RANS while more computational friendly compared to LES ([Alam et al., 2014](#)). It is predicted that the hybrid models will become the norm for engineering designs by 2030 ([Slotnick et al., 2014](#)). Very recently, a new hybrid RANS-LES approach, the

Stress-Blended Eddy Simulation (SBES), is proposed by [Menter \(2018\)](#). This method consists of a direct combination of RANS and LES models using a built-in blending function, and allows for more flexible combination of RANS and LES methods than DES. The accuracy of SBES model has been recently shown in the simulations of vane pressure side film cooling ([Ravelli and Barigozzi, 2018](#)), segmental orifice plates ([Straka et al., 2018](#)) and bluff-body stabilized flames ([Yadav et al., 2019](#)). Generally speaking, four principal advantages can be provided by the SBES technique ([Spalart and Venkatakrishnan, 2016](#), [Ravelli and Barigozzi, 2018](#)): (i) it provides a rapid transition from RANS to LES in separating shear layers, which leads to more accurate solutions with higher internal consistency, (ii) it allows RANS-LES transition on much coarser grids than other classical turbulence models, (iii) it improves asymptotic shielding of RANS boundary layer, and (iv) it is useful for separated flows which requires detailed unsteady information such as the flow over vibrating bodies. Due to these advantages, it is believed ideal for the VIV simulation. However, to the best knowledge of the authors, the efficiency of using this model to simulate VIV of a cylinder with low mass-damping ratio has not been reported in the open literature yet.

In the present study, the SBES turbulence model is adopted to simulate the responses of an elastically-mounted rigid cylinder subjected to VIV. 3-D computational fluid dynamics (CFD) simulations are carried out by developing a coupled Fluid-Structure Interaction (FSI) framework. Numerical results are compared with the widely used RANS *SST*  $K - \omega$  model and experimental data. This paper is organized as follows: Section 7.2 describes the general numerical framework used to model the fluid flow and the corresponding cylinder oscillations; the mesh dependency study is carried out in Section 7.3; the numerical results including the cylinder's vibration amplitude, response frequencies and wake vortex modes are comprehensively presented and discussed in Section 7.4; and finally some conclusions are drawn in Section 7.5.

## 7.2 FSI numerical framework

Due to the strong interactions between the motion of the cylinder and the surrounding fluid, VIV is normally investigated through a coupled FSI framework. In this study, a two-way FSI algorithm is developed, in which the flow over the cylinder is solved with finite volume method (FVM) by using the commercial Fluent solver, while the dynamic responses of the structure are calculated by finite element method (FEM) via ANSYS Mechanical solver ([ANSYS®, 2016](#)). The coupling FSI process is fulfilled

through the ANSYS Multi-field framework. This approach has been successfully used to study VIV in many previous studies ([Wang and Xiao, 2016](#)).

## 7.2.1 Fluid module

### 7.2.1.1 Computational domain and boundary conditions

As shown in Figure 7-2(a), the flow is discretized within a 3-D rectangular domain with the dimension of  $50D \times 40D \times 8D$  in the streamwise, transverse and spanwise directions respectively, in which  $D$  is the diameter of the cylinder. The center of the cylinder is located at  $(x, y) = (0, 0)$ , i.e.,  $20D$  and  $30D$  from the inlet ( $x = -20D$ ) and outlet ( $x = 30D$ ) respectively. A blockage factor (which is defined as the ratio of the cylinder diameter ( $D$ ) to the crossflow dimension ( $y$ ) of the fluid domain) of 2.5% is adopted for the crossflow direction. Previous studies illustrated that the adopted domain can reliably take into account the three-dimensionality and blockage effects on the VIV responses of the cylinder ([Zhao et al., 2014](#), [Law and Jaiman, 2017](#)).

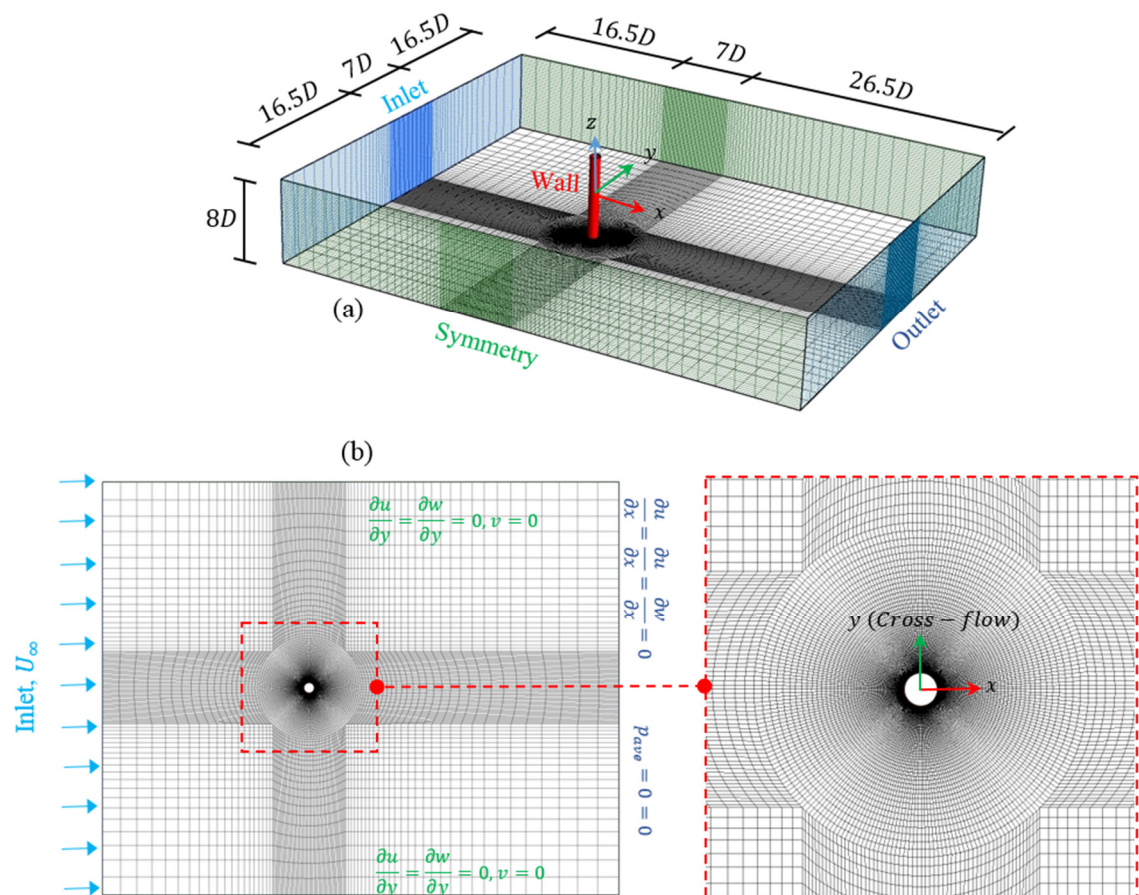


**Figure 7-2:** (a) An overview of the mesh grids and the corresponding boundary conditions, (b)  $xy$ -plane view of the domain.

Figure 7-2(b) shows the schematic plane view of the generated mesh grids and the corresponding boundary conditions. As shown, the high spatial grid resolution

required around the cylinder is achieved by adopting very fine grids in the central circular sub-domain, while coarser meshes are generated for the regions far away from the body. The central annular sub-domain is discretized with uniformly spaced grids in the azimuthal coordinate and exponentially stretched meshes in the radial direction. Hexahedral meshes with different intensities are generated for the remaining rectangular blocks. At the inlet boundary ( $x = -20D$ ), a uniform freestream velocity of  $u = U_\infty$  is set, while at the outlet boundary ( $x = 30D$ ), the zero-gradient condition for velocity is applied. Symmetry (non-slip) boundary condition is applied to the laterals, top and bottom sides, i.e.,  $y = \pm 20D$  and  $z = \pm 4D$  respectively. Non-slip wall condition is utilized on the outer surface of the cylinder, i.e., the fluid velocity on this surface is the same as the cylinder's displacement speed estimated in the mechanical part.

### 7.2.1.2 Flow turbulence model

The SBES turbulence method ([Menter, 2018](#)) is used to simulate the flow over the oscillating cylinder in the present study. As discussed in the introduction, SBES is a hybrid RANS-LES turbulence model which allows different RANS and LES models to be combined by using a blending function to automatically switch between them. In this method, the continuity and momentum equations can be written as follows ([Straka et al., 2018](#), [Menter, 2018](#)):

$$\frac{\partial \bar{u}_i}{\partial x_i} = 0 \quad (7-1)$$

$$\frac{\partial \bar{u}_i}{\partial t} + \bar{u}_j \frac{\partial \bar{u}_i}{\partial x_j} = -\frac{1}{\rho} \frac{\partial \bar{p}}{\partial x_i} + \frac{\partial}{\partial x_j} \left[ (v + v_t) \frac{\partial \bar{u}_i}{\partial x_j} \right] \quad (7-2)$$

where  $\rho$  is the fluid density,  $t$  is time,  $v$  is kinematic viscosity,  $x_i$  and  $x_j$  are the components of the position vectors of the fluid unit ( $i, j \in [1,2,3]$ ),  $\bar{u}_i = (\bar{u}, \bar{v}, \bar{w})$  and  $\bar{p}$  represent the RANS averaged or spatially filtered LES velocity and pressure respectively. In Equations (7-2)  $v_t$  is the turbulent eddy viscosity, which approximates the RANS or LES viscous stress tensor ( $\tau_{ij}$ ) in order to represent the effect of non-resolved turbulent momentum. By adopting the SBES turbulence model,  $v_t$  can be calculated with the help of shielding function  $f_{SBES}$ , which blends the turbulent eddy viscosity between RANS ( $v_t^{RANS}$ ) and LES ( $v_t^{LES}$ ) by the following equation:

$$v_t^{SBES} = f_{SBES} v_t^{RANS} + (1 - f_{SBES}) v_t^{LES}, 0 \leq f_{SBES} \leq 1 \quad (7-3)$$

In the RANS domain, *SST*  $K - \omega$  scheme ([Menter, 1994](#)) is adopted to estimate  $\nu_t^{RANS}$ , and it can be calculated as  $\nu_t^{RANS} = \rho K / \omega$ , in which  $K$  represents turbulent kinetic energy,  $\omega$  is the dissipation rate. This model improves the prediction of flows with strong adverse pressure gradients and separation ([Cebeci, 2004](#), [Pan et al., 2007](#)). However, the standard *SST*  $K - \omega$  model is unable to accurately yield the laminar-turbulent transition process ([McNaughton et al., 2014](#)), and resolve the rapid variation of flow variables occurring within the viscous and boundary layers ([Cebeci, 2004](#)). To alleviate these weaknesses, low- $R_e$  modification technique is incorporated into the standard *SST*  $K - \omega$  in this study, which can considerably improve the accuracy of the VIV simulations ([Matin Nikoo et al., 2019](#)). In the LES domain, the Smagorinsky-Lilly model ([Smagorinsky, 1963](#)) is applied to calculate  $\nu_t^{LES} = (C_s \bar{\Delta})^2 |\bar{S}|$ , in which  $\bar{\Delta} = \sqrt[3]{\Delta_i \Delta_j \Delta_k}$  denotes the grid filter width,  $|\bar{S}|$  is the norm of the strain rate tensor and  $C_s$  is the Smagorinsky constant.  $C_s$  is not a universal constant and its value may affect the accuracy of the results ([Sagaut, 2006](#)). To avoid this problem, time-dependent Smagorinsky-Lilly method is adopted in this study, in which  $C_s$  is a dynamic variable determined locally based on the energy content of the smallest resolved turbulence scale.

The hybrid SBES model is set up by the commercial ANSYS Fluent solver ([ANSYS®, 2016](#)), in which RANS *SST*  $K - \omega$  turbulence model ([Menter, 1994](#)) with low- $R_e$  correction technique ([Wilcox, 2006](#)) is utilized in the immediate near-wall regions ( $f_{SBES} = 1$ ), while the dynamic Smagorinsky-Lilly LES model ([Smagorinsky, 1963](#)) is applied in the free shear flows ( $f_{SBES} = 0$ ). As recommended by [Menter \(2012\)](#), Semi-Implicit Method for Pressure-Linked (SIMPLE) scheme, which is a pressure-based segregated solver algorithm, is used to achieve the pressure-velocity coupling on the mesh grids. Time integration is initialized by using a bounded second-order implicit Euler scheme and hybrid initialization method is applied to initialize the flow field domain.

### 7.2.1.3 Mesh motion

In this study, the diffusion-based dynamic mesh motion is utilized to update the volume mesh motion in the moving zones and deforming boundaries ([Zhao and Cheng, 2011](#)). In this approach, the overall number of grids and their connectivity remain constant while the interior meshes are able to move by the following diffusion equation:

$$\nabla \cdot (\gamma \nabla \vec{u}) = 0 \quad (7-4)$$

where  $\nabla$  is the differential operator,  $\vec{u}$  denotes the mesh displacement velocity, and  $\gamma$  is the diffusion coefficient. In the present study, a cell-volume-based diffusion coefficient ( $\gamma$ ) is utilized:

$$\gamma = \frac{1}{V\beta} \quad (7-5)$$

in which  $V$  is the normalized cell volume size and  $\beta$  denotes the diffusion parameter, which is set to 1.5 in the present study (Matin Nikoo et al., 2018). With this value, the grids in the immediate vicinity of the cylinders' wall tend to move almost rigidly with the cylinder, and therefore the uniformity of the near wall mesh resolution can be preserved.

### 7.2.2 Mechanical module

To estimate the vibrations of the cylinder caused by the fluctuating fluid forces, the cylinder is submitted to the ANSYS Mechanical solver. The cylinder, as shown in Figure 7-3, is elastically mounted by four linear-body-ground springs at the top ( $z = 8D$ ) and bottom ( $z = 0$ ) boundaries where remote displacement constraints are assigned which allow cylinder to vibrate in the crossflow direction ( $y$ ) only. The stiffness of each spring is  $\bar{k}/4$ , where  $\bar{k}$  is the spring constant.

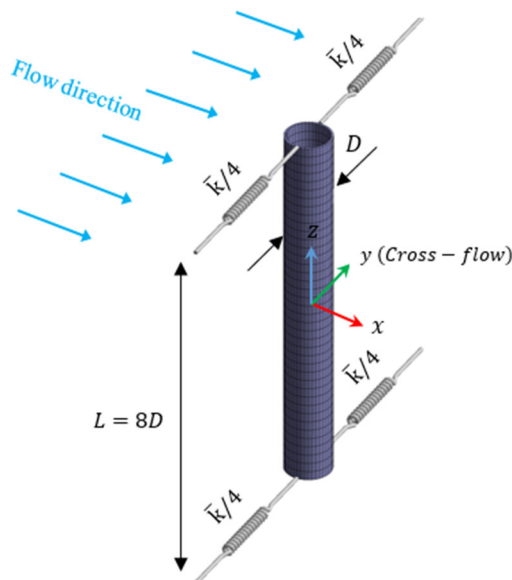


**Figure 7-3:** Elastically-mounted cylinder suspended by four linear springs modelled in the ANSYS Mechanical module.

The equation of crossflow motion of an elastically-mounted cylinder under VIV can be expressed as follows:

$$m \frac{\partial^2 y}{\partial t^2} + C \frac{\partial y}{\partial t} + \bar{k} y = F_L \quad (7-6)$$

where  $m$ ,  $C$  and  $\bar{k}$  are the oscillating mass, damping coefficient and spring constant, respectively,  $y$  is the transverse oscillation, and  $F_L$  is the total lift force vector in the crossflow direction, and the value per unit length can be expressed as follows:

$$F_L = \int_0^{2\pi} -p \sin \theta dA + \int \tau_w \cos \theta dA \quad (7-7)$$

where  $dA = D/2 d\theta$ , with  $\theta$  denoting the angle position of a point on the cylinder measured from the horizontal axis,  $p$  is the pressure and  $\tau_w$  denotes the shear stress. The dimensionless lift coefficient  $C_L$  then can be calculated as:

$$C_L = \frac{F_L}{1/2 \rho U_\infty^2 D} \quad (7-8)$$

Similarly, the drag force  $F_D$  and the corresponding drag coefficient  $C_D$  can be calculated as follows:

$$F_D = \int_0^{2\pi} p \cos \theta dA + \int \tau_w \sin \theta dA \quad (7-9)$$

$$C_D = \frac{F_D}{1/2 \rho U_\infty^2 D} \quad (7-10)$$

In this study, the damping coefficient  $\zeta$  is assumed as zero as suggested in many previous studies (refer to Table 7-2) though certain damping unavoidably exists in the real VIV tests. This is a reasonable assumption because when the value of the mass-damping parameter ( $m^*\zeta$ ) is very small, the variation of  $\zeta$  leads to no significant change in the maximum vibration amplitudes as indicated in many previous studies ([Shiels et al., 2001](#), [Govardhan and Williamson, 2006](#), [Pan et al., 2007](#), [Soti et al., 2018](#), [Riches and Morton, 2018](#)). Damping coefficient  $\zeta$  can thus be omitted in order to simplify the motion equation of the oscillating system. Because of this fact, many numerical studies (e.g. [Singh and Mittal \(2005b\)](#), [Zhao et al. \(2014\)](#), [Gsell et al. \(2019\)](#)) still used the terminology of “low mass-damping ratio” although the damping coefficient  $\zeta$  was set as zero in their numerical simulations.

To achieve a fully-mapped load transfer and mesh displacements between the two solvers, the solid part (i.e., the cylinder) is also discretized by the same finite element (FE) meshes on the FSI interface. Conservative interpolation method is adopted at the



FSI interface, which makes the overall load transfer conservative, regardless of the mesh shape, size, grid topology, and face distribution across the interface.

### 7.2.3 General numerical settings

The time step adopted in the transient numerical simulation is crucial for the success of the VIV simulation. The Courant-Friedrichs-Levy (*CFL*) number can be used as an indicator for setting the optimal time resolution in the flow simulations ([Holland et al., 2017](#)):

$$CFL = \frac{U\Delta t}{\Delta x} \quad (7-11)$$

where  $U$  is the local flow speed,  $\Delta t$  is the time step and  $\Delta x$  is the mesh size. The *CFL* number should be less than or equal to 1 over the computational domain ([Nishino et al., 2008](#)). To this end and to achieve an acceptable level of accuracy within a reasonable computational time, the time step of the transient analysis is determined by  $\Delta t = 0.02D/U_\infty$  in the present study ([Nishino et al., 2008](#)). It should be noted that the transient two-way FSI framework adopted in the present study consists of two levels of iteration: (i) the normal inner iteration used in the mechanical and fluid parts, and (ii) the coupling-loop iteration, in which the loads/displacements are sequentially updated between the Mechanical solver and CFD solver. In this study, the number of inner and coupling iterations are set to 10 and 30 respectively to guarantee the fully-converged results.

To ensure that the adopted numerical model is able to resolve the turbulent quantities within the boundary layer and reflect the flow separation pattern accurately, the dimensionless wall distance parameter defined as  $y^+ = \Delta y u_t / \nu$  (in which  $\Delta y$  is the distance of the mesh grids adjacent to the cylinder's wall, and  $u_t = \sqrt{\tau_w / \rho}$  is the friction or wall shear velocity) should be smaller than unity ( $y^+ < 1$ ) ([Argyropoulos and Markatos, 2015](#), [Tu et al., 2018](#)). In this study, very fine mesh grids are generated in the areas adjacent to the cylinder's wall, and this condition (i.e.  $y^+ < 1$ ) is well maintained at all the wall-adjacent integration points.

### 7.3 Mesh grid sensitivity study

Mesh convergence study is performed in this section. The governing dimensionless parameters are set to match with those in the experimental setup by [Khalak and Williamson \(1999\)](#), i.e., the mass ratio ( $m^*$ ) is set as 2.4 and the Reynolds number

varies from 2000 to 12000 by changing the inlet flow velocity  $U_\infty$ . The adopted computational domain is discretized by four different mesh size scenarios as illustrated in Table 7-3 and Figure 7-4. Table 7-3 also provides the number of grids seeding (GS) on each edge of the domain and the total number of elements generated in each scenario.

**Table 7-3:** Mesh convergence test results.

	GS1	GS2	GS3	GS4	GS5	GS6	GS7	GS8	$N_{\text{element}}$	$C_L^{\text{max}}$	$C_D^{\text{max}}$	$A^*$
Coarse	15	24	15	15	24	25	40	40	268,800	1.17	3.81	0.63
Medium	20	50	20	20	50	30	40	80	900,000	1.35	3.88	0.72
Optimum	20	60	20	20	60	30	40	80	1,162,000	1.38	4.02	0.80
Dense	25	70	2540	25	70	35	40	100	1,548,000	1.36	4.09	0.81

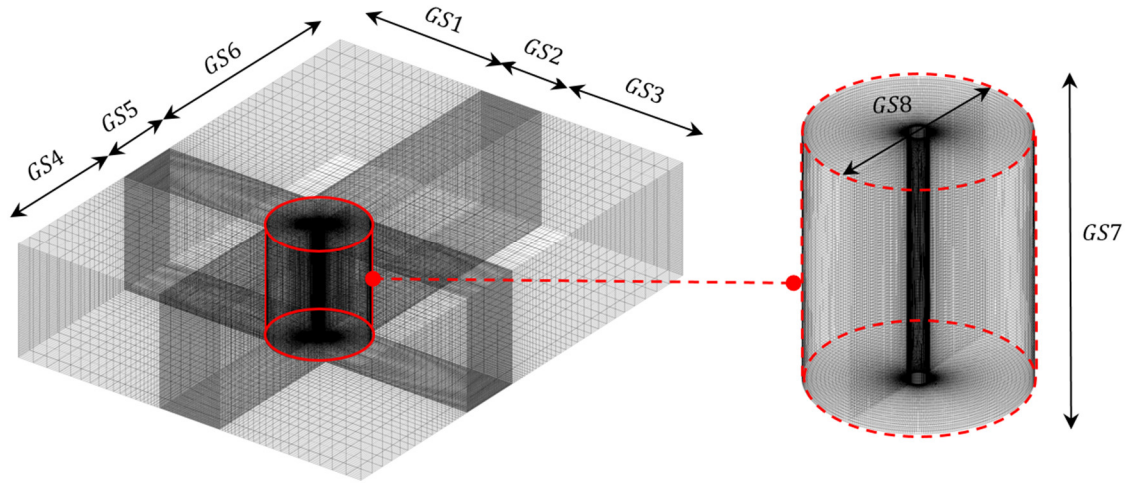


**Figure 7-4:** Schematic view of the fluid domain discretized with different grid densities.

The calculated Strouhal number ( $S_t$ ), normalized maximum hydrodynamic coefficients ( $C_L^{\text{max}}, C_D^{\text{max}}$ ) and amplitude response ( $A^*$ ) are tabulated in Table 7-3. Data in Table 7-3 shows that the optimum case with the element numbers of 1,162,000 leads to different results with those from the coarse and medium meshes but quite similar results with the dense mesh size. The numerical model developed in the optimum model therefore can be regarded as fully converged, and it is utilized in the following numerical simulations.

#### 7.4 Results and discussion

As mentioned in Section 7.3, the experimental work carried out by [Khalak and Williamson \(1999\)](#) is adopted as the benchmark to validate the numerical model in the present study. In the experimental study, the Reynolds number varied from 2000 to 12000, which corresponds to the normalized velocity varying from 2 to 12. In the numerical simulations, an interval of 1 is adopted for the normalized velocity. RANS model is the most widely used method to simulate VIV, the results obtained in the

present study are thus compared with those obtained from the RANS method ([Matin Nikoo et al., 2019](#)) in most of the following subsections. It should be noted that all the contributing factors such as cylinder mass, spring stiffness, domain dimensions and Reynolds numbers are the same for both studies.

#### 7.4.1 Vibration responses

Figure 7-5 shows the maximum normalized amplitude responses ( $A^* = y_{max}/D$ ) of the cylinder obtained by the SBES model together with the most accurate results obtained by other turbulence models (refer to Table 7-1). It can be seen that the figure has three distinguishing features: (i) The three response branches observed in the test by [Khalak and Williamson \(1999\)](#), namely the initial branch ( $U^* \approx 2 - 4$ ), the upper branch ( $U^* \approx 4 - 6$ ) and the lower branch ( $U^* \approx 6 - 10$ ), can be well captured by using the SBES, DNS and LES models. The DES model and RANS model, on the other hand, fail to correctly capture the upper branch. As shown, the maximum vibration amplitude occurred at around  $U^* \approx 5$  in the tests. For the RANS and DES models, the maximum amplitude however appears at  $U^* \approx 4$  and  $U^* \approx 6$  respectively. Moreover, it is worth reiterating again that the LES and DNS models are very time consuming compared to the SBES model. The SBES model can obtain the accurate results with much less computational effort. (ii) Not only the branches, the SBES model can also correctly capture the maximum amplitude. As shown in Figure 7-5, the normalized maximum amplitude obtained in the tests was 0.97 ([Khalak and Williamson, 1999](#)), and the corresponding value obtained by the SBES model is 0.99, which is in excellent agreement with the experimental result. For the RANS model, the maximum value was only 0.84 due to the inherent shortages of this method as discussed above. Moreover, this maximum response does not occur at the same reduced velocity in the tests as discussed. Similar trend is observed for the DES method though the maximum amplitude (1.05) is closer to the test. For the DNS model, it can be seen that the maximum amplitude response (0.8) is significantly underestimated due to the fact that only a constant Reynolds number ( $Re = 3,900$ ) was considered ([Gsell et al., 2019](#)). The maximum amplitude and the corresponding reduced velocity are well captured by the LES model ([Zhang et al., 2017](#)) as shown, but LES model is a very time consuming method and is unfeasible to adopt in many practical applications as mentioned. (iii) Under the very high reduced velocities ( $U^* \geq 11$ ), the amplitudes predicted by the SBES model are higher than the test results. This

is because of the influence of damping ratio. As discussed in Section 7.2.2, the damping ratio is set to zero in the current study by following the suggestions from many previous studies since it has negligible effect on the response amplitude over the synchronization region. On the other hand, as shown in some experimental (Gopalkrishnan, 1993) and numerical (Gsell et al., 2016) studies, damping ratio can affect the VIV responses of the cylinder when it is subjected to high reduced velocity range, which corresponds to the onset of the lock-out or desynchronized regime. Moreover, as shown in Figure 7-5, except the LES model, all other models show certain discrepancies when the reduced velocity is large, and the SBES model yields a result in between other models.

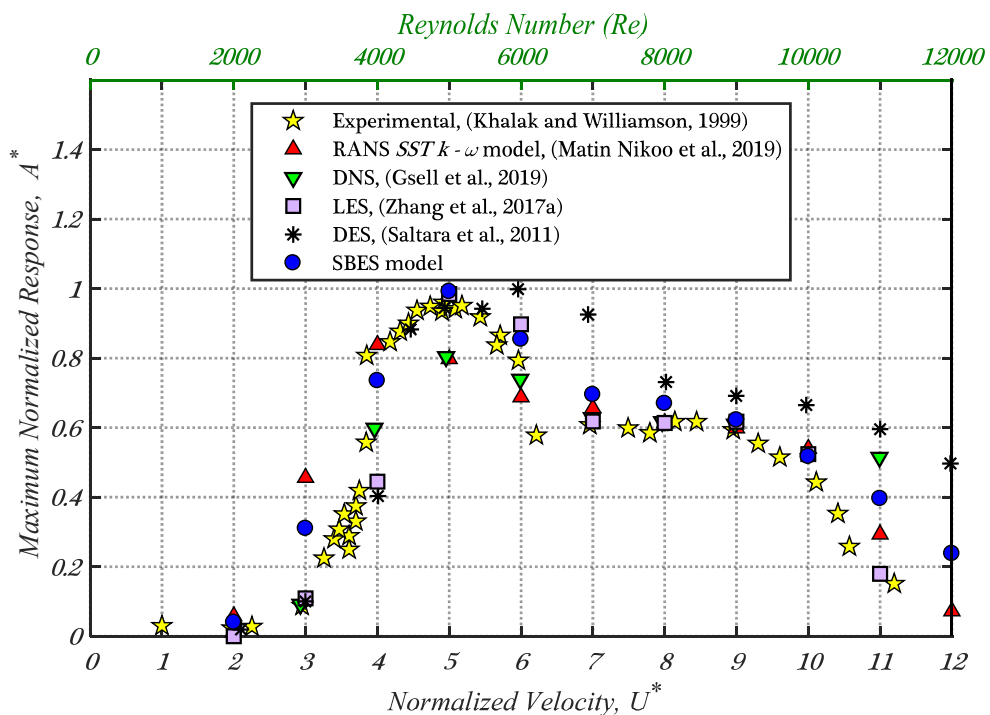


**Figure 7-5:** Comparisons of the normalized maximum amplitudes between the experimental data and the most accurate numerical results obtained based on different turbulence models.

The above results show that the suggested SBES model can yield better VIV response estimations compared to the DNS, DES and RANS models. Though the accuracy of SBES model is slightly less than the LES model, it is however much less time consuming. In other words, the SBES model can yield the most accurate results with the affordable computational effort. It therefore has great application potentials. The above results are actually expected since as shown in Equations (7-3), the contribution of the LES model is reserved in the SBES model, such that a broader spectrum of turbulent scales are solved in the SBES model compared to the widely used RANS code, which in turn yields more accurate results.

### 7.4.2 Phase angles

Instantaneous phase angles ( $\phi$ ) between the lift force  $C_L(t)$  and cylinder oscillation  $A_y(t)$  are estimated in order to discretise different VIV response regimes and the transition in between. To this end, Hilbert transform is performed ([Bracewell, 2000](#)). The probability density functions (PDFs) of the phase angle under some typical reduced velocities and the corresponding dominant values for the whole range are depicted in Figure 7-6 and Figure 7-7 respectively. The results obtained by the commonly used RANS model are also presented for comparison. As shown, the phase angles estimated by the SBES model are generally in very good agreement with the test, i.e., it is almost  $0^\circ$  over the initial (left column in Figure 7-6(a)) and upper (left column in Figure 7-6(b)) regimes, and virtually  $180^\circ$  in the lower branch (left column in Figure 7-6(d)). When the reduced velocity  $U^* = 6$  (Figure 7-6(c)), two dominant phase angles (i.e.,  $0^\circ$  and  $180^\circ$ ) appear, which indicate the transition from the upper to the lower excitation regime ([Khalak and Williamson, 1999](#)), and agrees well with the experimental results shown in Figure 7-5. When the RANS model is adopted, it can be seen from Figure 7-5 that the maximum vibration amplitude occurs at  $U^* = 4$ , and the transition from the upper branch to lower branch occurs at  $U^* = 5$  since two dominant phase angles appear at this reduced velocity (the right column in Figure 7-6(b)), which are not consistent with the experimental data. These results again show that the SBES model can more accurately simulate the VIV of the cylinder compared to the commonly used RANS model.

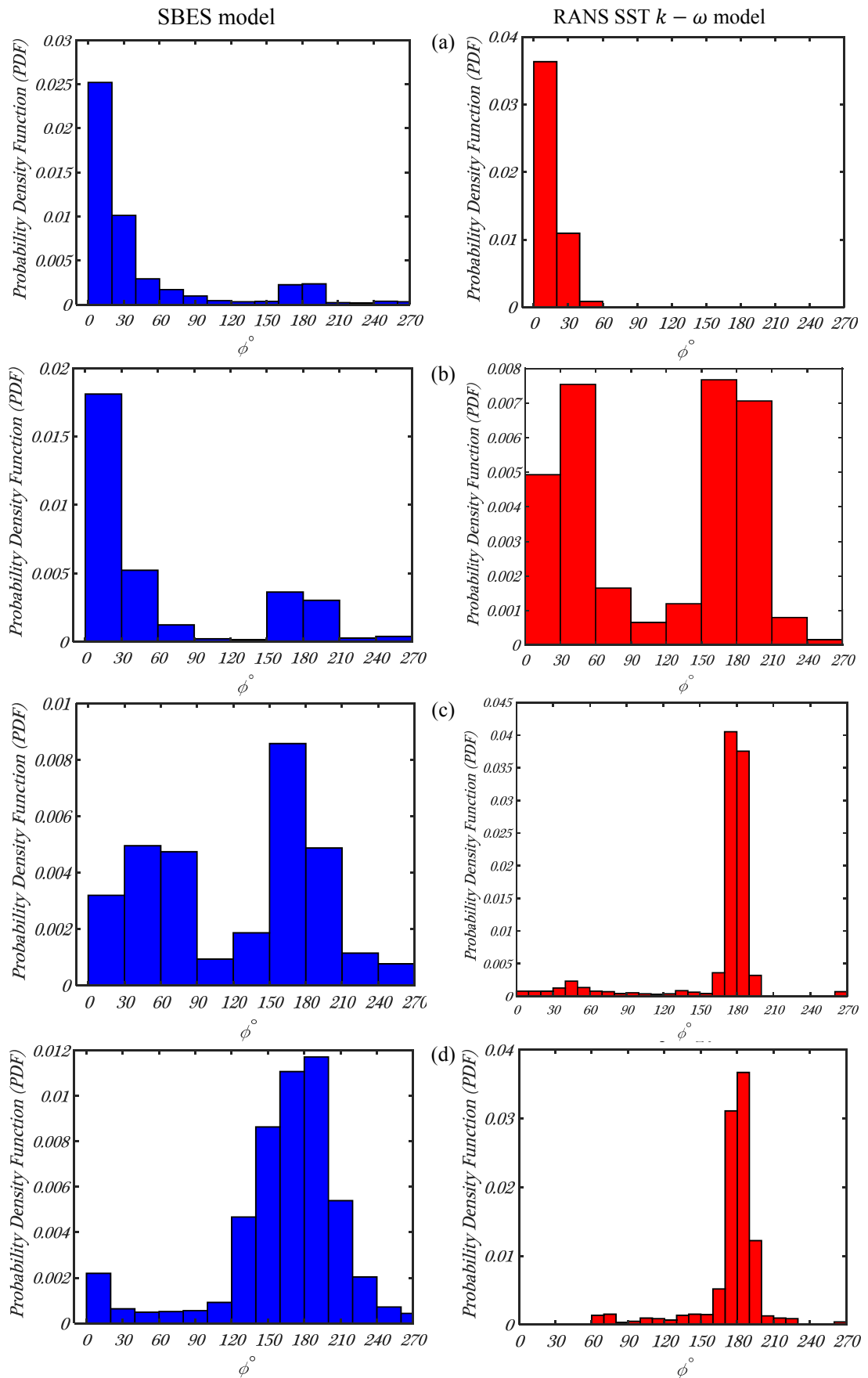


**Figure 7-6:** Comparisons of the PDFs of the phase angles ( $\phi$ ) obtained by the SBES and RANS models: (a)  $U^* = 3$ , (b)  $U^* = 5$ , (c)  $U^* = 6$  and (d)  $U^* = 10$ .

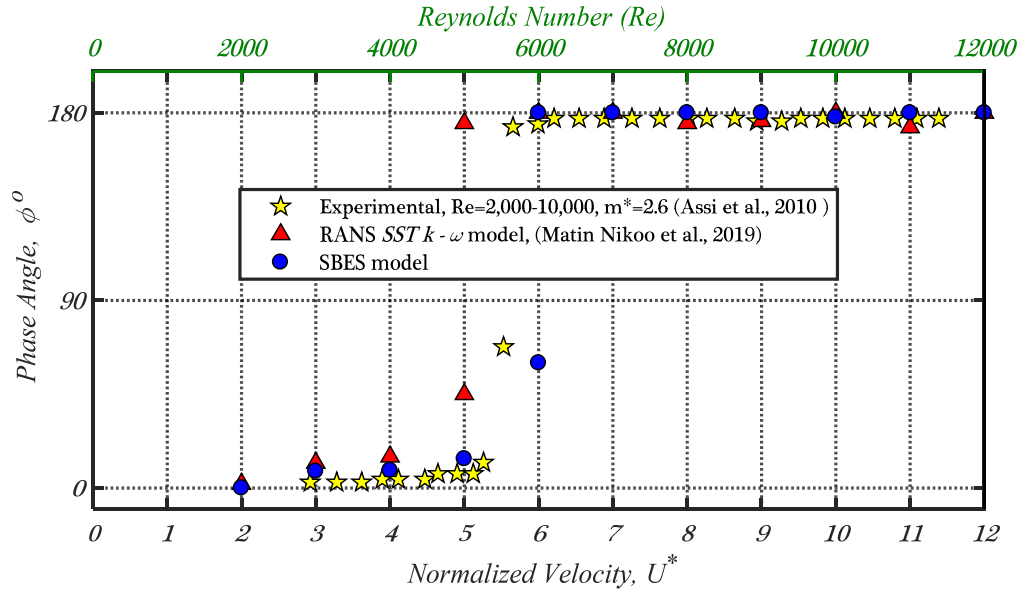


**Figure 7-7:** Comparisons of the dominant phase angles between the experimental and numerical simulations with SBES and RANS models.

### 7.4.3 Response frequencies

The power spectral densities (PSDs) of the cylinder oscillations under different normalized velocities can be easily calculated once the oscillation time histories of the cylinder are obtained. The dominant peaks in the PSDs therefore can be identified. Figure 7-8 shows the normalized dominant peaks of the frequency ratio ( $f^* = f_o/f_n$ ) under each normalized velocity obtained by using the SBES and RANS models. For comparison, the corresponding experimental results are also shown in the figure. As shown, the results obtained by the SBES and RANS models in general agree well with the experimental data. For the initial normalized velocity ( $U^* = 2$ ), the cylinder is vibrating with a single frequency close to the Strouhal frequency ( $f_s$ ) of the static cylinder, i.e., the dashed line in the figure. When the normalized velocity increases to  $U^* = 3$ , two dominant peaks are obtained in both the SBES and RANS models. These frequencies correspond to  $f_s \approx 0.58$  and the natural frequency of the cylinder in the water  $f_w \approx 0.8$  respectively ([Khalak and Williamson, 1999](#)). When the oscillating system shifts to the upper regime (e.g.  $U^* = 5$ ), the oscillation frequency ( $f_o$ ), Strouhal frequency  $f_s$  and the natural frequency of the cylinder ( $f_n$ ) become almost the same, which in turn results in  $f^* \approx 1$ . When the reduced velocity keeps increasing to the lower excitation regime ( $U^* \approx 6 - 11$ ), the oscillation frequency  $f_o$  follows neither  $f_n$  nor  $f_s$ , and the cylinder vibrates at a ‘locked’ or ‘synchronized’ frequency in between. Such deviation is attributed to the variability of the effective added mass ([Khalak and Williamson, 1999](#), [Gsell et al., 2016](#)). Finally, under very

large normalized velocity (e.g.  $U^* = 12$ ), the oscillating system falls into a new excitation region known as the ‘lock-out’ or ‘unsynchronized’ region, where the dominant responses of the cylinder obtained by the SBES and RANS models are unsynchronized from its natural frequency, and the dominant oscillation frequency almost matches again with the Strouhal frequency. The same results were reported in the tests ([Khalak and Williamson, 1999](#)). Figure 7-8 also shows that SBES model delivers slightly more accurate results within the lower branch compared to the RANS code, which demonstrates the superiority of the SBES model.

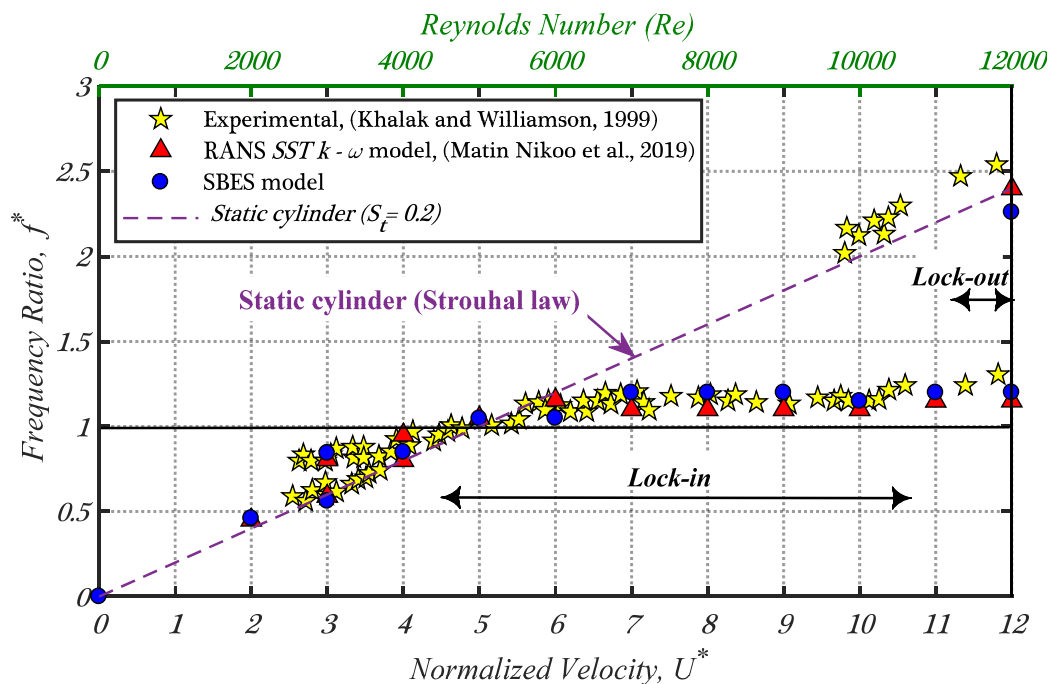


**Figure 7-8:** Dominant peaks in the spectrum of the cylinder oscillations obtained from the test results and numerical simulations with SBES and RANS models.

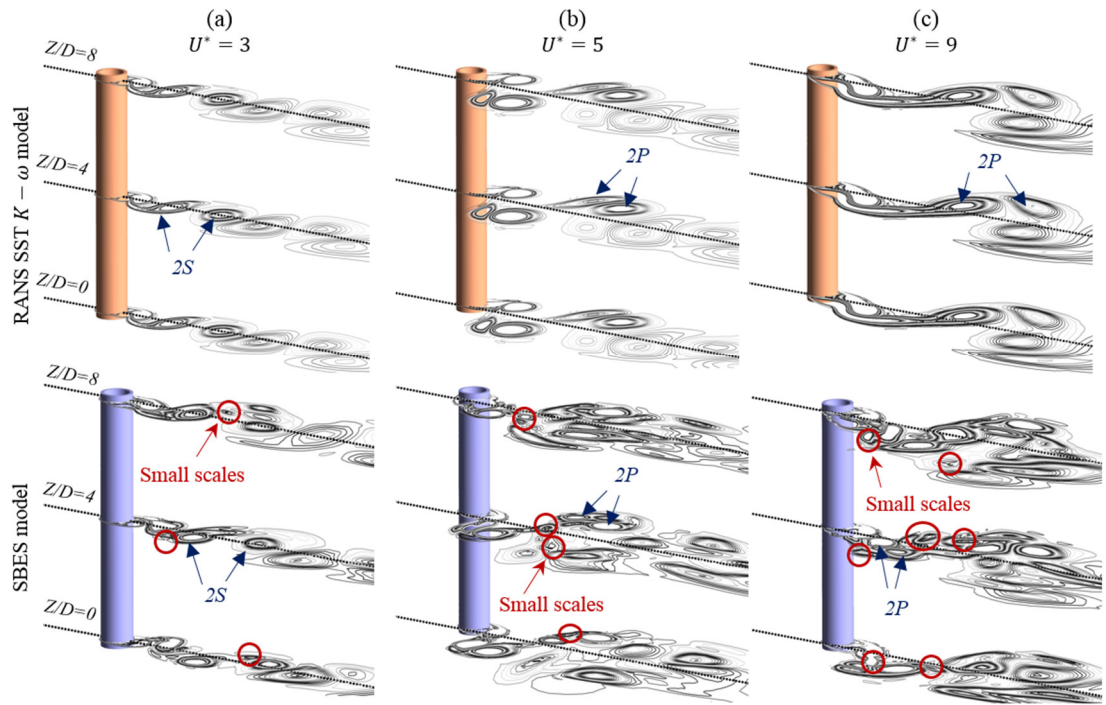
#### 7.4.4 Wake topology

There is an inherent interrelation between the cylinder’s oscillation and the wake vortex shedding characteristics. The wake vortex formations are primarily associated with two modes dubbed 2S and 2P modes. The former corresponds to two dominant single (S) vortices shed alternately per cycle, whereas the latter consisting of two pairs (P) of vortices shedding from two sides of the cylinder per oscillation cycle. For an elastically-mounted rigid cylinder, the initial branch is associated with the 2S mode, while the upper and lower branches correspond to the 2P mode ([Khalak and Williamson, 1999](#)). Figure 7-9 shows the wake vortex streets at three different cross-sections ( $Z/D = 0, 4$  and  $8$ ) along the cylinder captured by the SBES and RANS models under typical normalized velocities. To more clearly show the results,

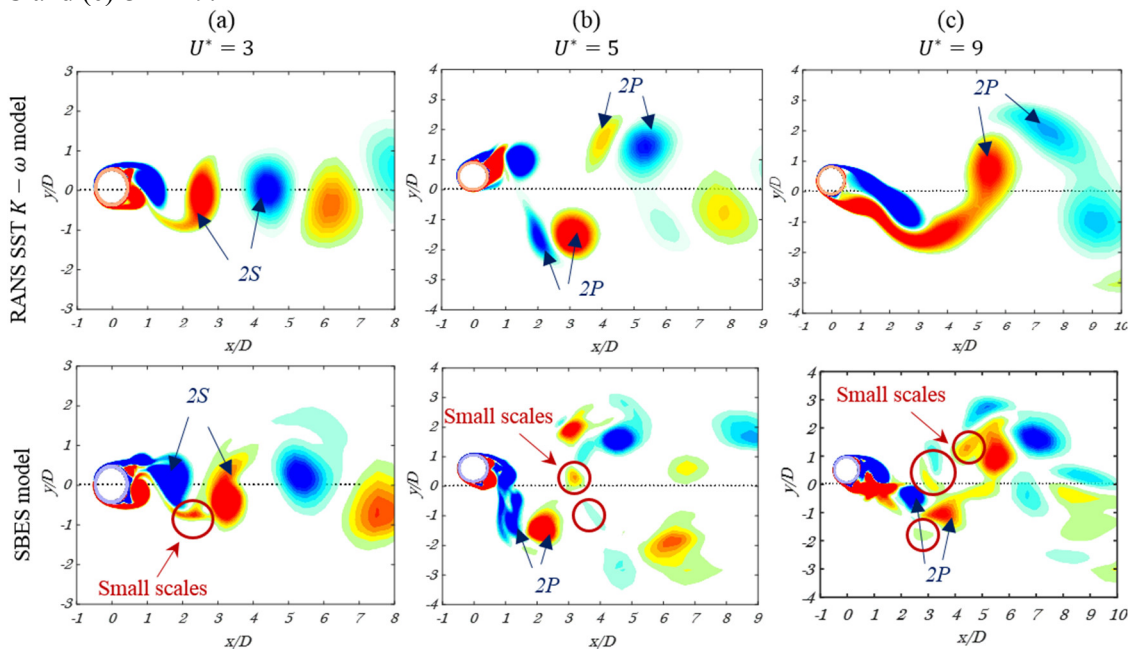


Figure 7-10 shows the 2-D vortex wake modes at the middle of the cylinder ( $Z/D = 4$ ), and the typical vortex street modes obtained by the dye-injection flow visualization method in the experimental study carried out by [Klamo \(2007\)](#) are shown in Figure 7-11. The experimental tests were carried out in a water tunnel (i.e., with low-mass ratio condition) under subcritical flow regime, which makes the results comparable with the current numerical study. As shown in Figure 7-9(a) and Figure 7-10(a), when the cylinder is vibrating in the initial branch with normalized velocity  $U^* = 3$ , the classical 2S vortex formation mode is captured by both the SBES and RANS models. However, it should be noted that the RANS method cannot capture the small scale vortices (marked by red circles in Figure 7-11(a)). SBES method, on the other hand, well captures the vorticity counters with small magnitudes, which are clearly shown in the test results (Figure 7-11(a)). When the system is vibrating under  $U^* = 5$  (upper branch) and  $U^* = 9$  (lower branch), the 2S mode switches to the 2P mode as shown in Figure 7-9(b&c) and Figure 7-10(b&c). Similarly, in addition to the main 2P vortices, a wider range of small flow scales are resolved by the SBES model compared to the RANS model where only two strong vortices are calculated. This observation is in agreement with the test data ([Klamo, 2007](#)) again as shown in Figure 7-11(b), where small vortex structures are clearly observed together with the main 2P modes. These results again show that the SBES model can deliver more accurate results in terms of the wake vortex shedding.

VIV in nature is a 3-D phenomenon ([Zhao and Cheng, 2014](#)). To more clearly illustrate the efficiency of each turbulence model to capture the 3-D effect, the spanwise wake structures are shown in Figure 7-12 under three typical reduced velocities, and Figure 7-13 shows the test results obtained by [Klamo \(2007\)](#). As shown, a very chaotic flow with swirling characteristic is predicted by the SBES model along the span of the vibrating cylinder, which is again in good agreement with the test observation as shown in Figure 7-13, while RANS model delivers almost 2-D results.



**Figure 7-9:** Comparisons of the wake vortex streets along the cylinder at three cross sections ( $Z/D = 0, 4$  and  $8$ ) of the cylinder under different normalized velocities: (a)  $U^* = 3$  (b)  $U^* = 5$  and (c)  $U^* = 9$ .



**Figure 7-10:** 2-D comparisons of the wake vortex streets at the middle cross section ( $z/D = 4$ ) of the cylinder under different normalized velocities: (a)  $U^* = 3$  (b)  $U^* = 5$  and (c)  $U^* = 9$ .

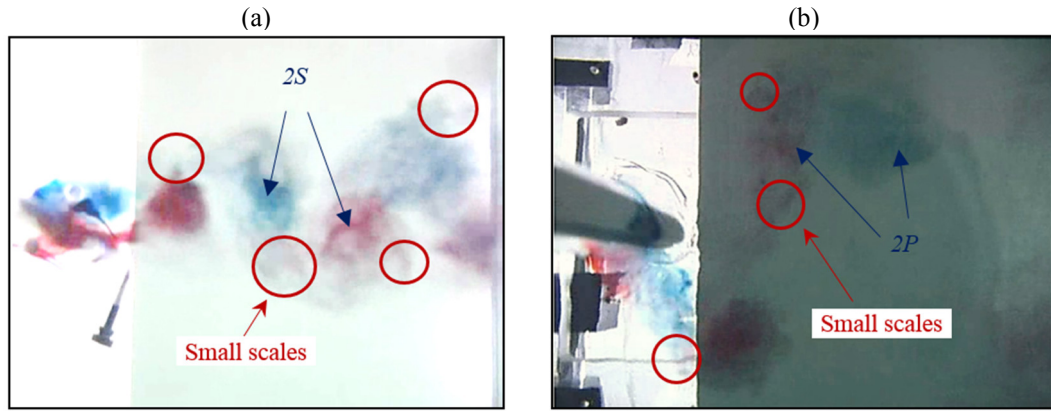


**Figure 7-11:** Typical (a) 2S and (b) 2P modes obtained in the water tunnel tests carried out by [Klamo \(2007\)](#) under subcritical Reynolds numbers.

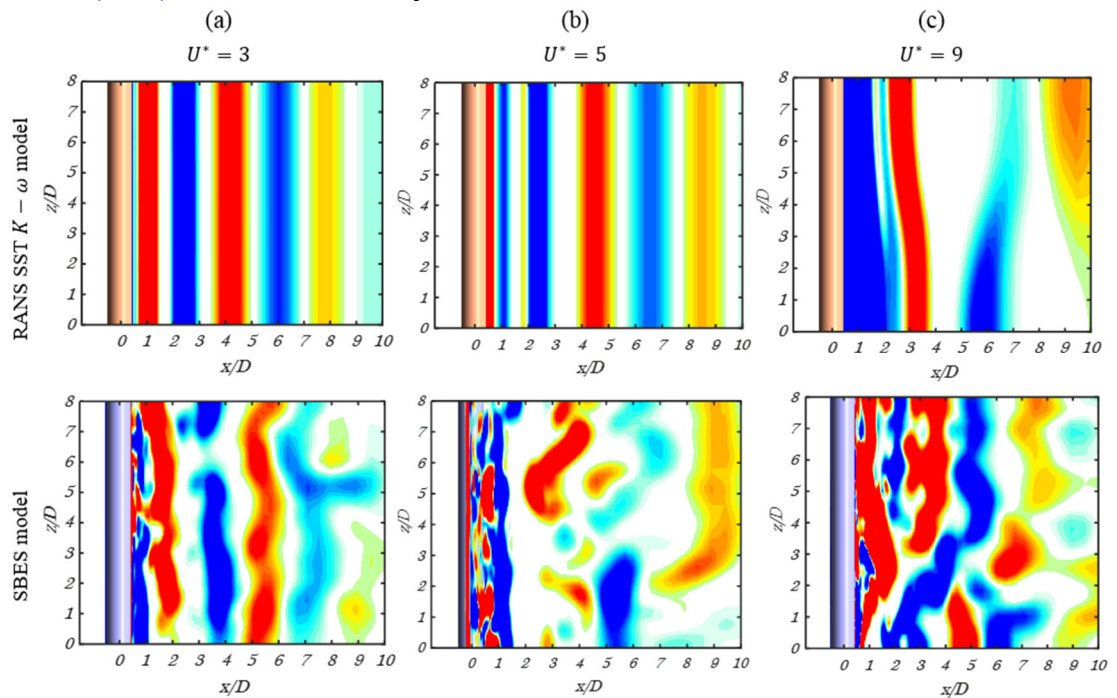


**Figure 7-12:** Spanwise flow view of instantaneous wake structures obtained from SBES and RANS turbulence models under different normalized velocities: (a)  $U^* = 3$  (b)  $U^* = 5$  and (c)  $U^* = 9$ .

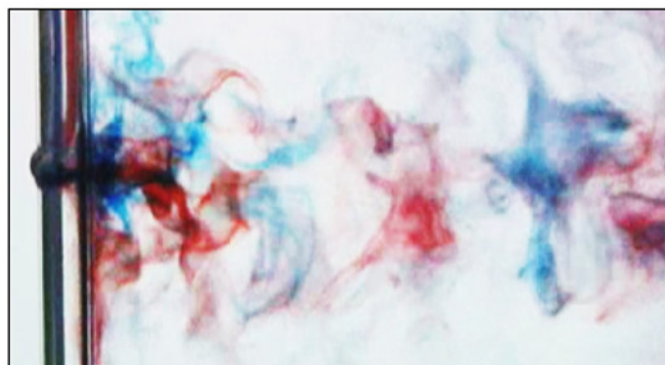


**Figure 7-13:** Typical spanwise flow visualization in the water tunnel tests carried out by [Klamo \(2007\)](#).

It is worth mentioning that, due to the unavailability of supercomputer, all the above simulations were computed on the Intel Core with specifications of CPU Xeon E5-

1620 v4 @3.5 GHz and 64GB RAM. The required computational time were highly depended to Reynolds number. On average, each simulation took about 10 days to finish for the RANS model, while 12 days were required for the SBES model. In other words, 20% more computational time was required for the SBES model compared to the RANS model. On the other hand, this increment is believed worthy when the accuracies of the results are of concern. It also should be noted that the simulations based on the DNS method were not performed in the present study, much more time is expected due to the existence of wider turbulence scales in this model.

## 7.5 Conclusion

A hybrid LES-RANS turbulence model namely the SBES method is adopted to simulate the flow over an elastically-mounted rigid cylinder in the present study. 3-D numerical simulations are carried out by developing a two-way coupled FSI framework. For comparison, the results obtained by the commonly used turbulence model, i.e., the RANS code equipped with  $SST k - \omega$  are also presented and discussed. The numerical results demonstrate the superiority of the SBES model over the other numerical models in terms of the level of accuracy and computational effort. In particular, very accurate VIV response amplitude is obtained in the upper branch where most of the current models fail to capture, three VIV response braches are well captured by the SBES model whereas the RANS code yields inaccurate transition from the upper branch to the lower regime, and a broader range of vortices scales are resolved by the SBES model which results in more realistic wake vortex patterns compared to the RANS model.

## 7.6 References

- Al-Jamal, H., Dalton, C. (2004). Vortex induced vibrations using Large Eddy Simulation at a moderate Reynolds number. *Journal of Fluids and Structures*, 19 (1), 73-92.
- Alam, M.F., Thompson, D.S., Walters, D.K. (2014). Hybrid Reynolds-Averaged Navier–Stokes/Large-Eddy Simulation Models for Flow Around an Iced Wing. *Journal of Aircraft*, 52 (1), 244-256.
- ANSYS®. (2016). Academic research, release 17.2, Theory guide.
- Argyropoulos, C.D., Markatos, N.C. (2015). Recent advances on the numerical modelling of turbulent flows. *Applied Mathematical Modelling*, 39 (2), 693-732.
- Assi, G.R.S., Meneghini, J.R., Aranha, J.A.P., Bearman, P.W., Casaprima, E. (2006). Experimental investigation of flow-induced vibration interference between two circular cylinders. *Journal of Fluids and Structures*, 22 (6), 819-827.
- Bearman, P.W. (2011). Circular cylinder wakes and vortex-induced vibrations. *Journal of Fluids and Structures*, 27 (5), 648-658.

- Bracewell, R.N. (2000). The Fourier transform and its applications, Third ed. *McGraw-Hill New York*.
- Cebeci, T. (2004). Analysis of turbulent flows. *Elsevier*, Oxford.
- Chaouat, B. (2017). The State of the Art of Hybrid RANS/LES Modeling for the Simulation of Turbulent Flows. *Flow, Turbulence and Combustion*, 99 (2), 279-327.
- Ding, L., Zhang, L., Bernitsas, M., Chang, C.C. (2016). Numerical simulation and experimental validation for energy harvesting of single-cylinder VIVACE converter with passive turbulence control. *Renewable Energy*, 85, 1246-1259.
- Fröhlich, J., Von Terzi, D. (2008). Hybrid LES/RANS methods for the simulation of turbulent flows. *Progress in Aerospace Sciences*, 44 (5), 349-377.
- Gabbai, R., Benaroya, H. (2005). An overview of modeling and experiments of vortex-induced vibration of circular cylinders. *Journal of Sound and Vibration*, 282 (3), 575-616.
- Gopalkrishnan, R. (1993). Vortex-induced forces on oscillating bluff cylinders. *Massachusetts Institute of Technology*, Department of Ocean Engineering, PhD Thesis.
- Govardhan, R.N., Williamson, C.H.K. (2000). Modes of vortex formation and frequency response of a freely vibrating cylinder. *Journal of Fluid Mechanics*, 420, 85-130.
- Govardhan, R.N., Williamson, C.H.K. (2006). Defining the 'modified Griffin plot' in vortex-induced vibration: revealing the effect of Reynolds number using controlled damping. *Journal of Fluid Mechanics*, 561, 147-180.
- Gsell, S., Bourguet, R., Braza, M. (2016). Two-degree-of-freedom vortex-induced vibrations of a circular cylinder at  $Re=3900$ . *Journal of Fluids and Structures*, 67, 156-172.
- Gsell, S., Bourguet, R., Braza, M. (2019). One versus two-degree-of-freedom vortex-induced vibrations of a circular cylinder at  $Re=3900$ . *Journal of Fluids and Structures*, 85, 165-180.
- Guilmineau, E., Queutey, P. (2004). Numerical simulation of vortex-induced vibration of a circular cylinder with low mass-damping in a turbulent flow. *Journal of Fluids and Structures*, 19 (4), 449-466.
- Holland, V., Tezdogan, T., Oguz, E. (2017). Full-scale CFD investigations of helical strakes as a means of reducing the vortex induced forces on a semi-submersible. *Ocean Engineering*, 137, 338-351.
- Huynh, B., Tjahjowidodo, T., Zhong, Z.-W., Wang, Y., Srikanth, N. (2018). Design and experiment of controlled bistable vortex induced vibration energy harvesting systems operating in chaotic regions. *Mechanical Systems and Signal Processing*, 98, 1097-1115.
- Kang, Z., Ni, W., Sun, L. (2017). A numerical investigation on capturing the maximum transverse amplitude in vortex induced vibration for low mass ratio. *Marine Structures*, 52, 94-107.
- Khalak, A., Williamson, C.H.K. (1999). Motions, forces and mode transitions in vortex-induced vibrations at low mass-damping. *Journal of Fluids and Structures*, 13 (7-8), 813-851.
- Khan, N.B., Ibrahim, Z., Khan, M.I., Hayat, T., Javed, M.F. (2018). VIV study of an elastically mounted cylinder having low mass-damping ratio using RANS model. *International Journal of Heat and Mass Transfer*, 121, 309-314.
- Kiu, K.Y., Stappenbelt, B., Thiagarajan, K.P. (2011). Effects of uniform surface roughness on vortex-induced vibration of towed vertical cylinders. *Journal of Sound and Vibration*, 330 (20), 4753-4763.
- Klamo, J.T. (2007). Effects of damping and Reynolds number on vortex-induced vibrations. *California institute of technology*, Department of Mechanical Engineering, PhD Thesis.

- Kornev, N., Shevchuk, I., Abbas, N., Anschau, P., Samarbakhsh, S. (2019). Potential and limitations of scale resolved simulations for ship hydrodynamics applications. *Ship Technology Research*, 1-14.
- Kurushina, V., Pavlovskaya, E., Postnikov, A., Wiercigroch, M. (2018). Calibration and comparison of VIV wake oscillator models for low mass ratio structures. *International Journal of Mechanical Sciences*, 142-143, 547-560.
- Law, Y.Z., Jaiman, R.K. (2017). Wake stabilization mechanism of low-drag suppression devices for vortex-induced vibration. *Journal of Fluids and Structures*, 70, 428-449.
- Li, W., Li, J., Liu, S. (2014). Numerical simulation of vortex-induced vibration of a circular cylinder at low mass and damping with different turbulent models. OCEANS 2014 - TAIPEI, 1-7.
- Liu, N.S., Shih, T.H. (2006). Turbulence modeling for very large-eddy simulation. *AIAA Journal*, 44 (4), 687-697.
- Lucor, D., Foo, J., Karniadakis, G.E. (2005). Vortex mode selection of a rigid cylinder subject to VIV at low mass-damping. *Journal of Fluids and Structures*, 20 (4), 483-503.
- Lucor, D., Triantafyllou, M.S. (2008). Parametric study of a two degree-of-freedom cylinder subject to vortex-induced vibrations. *Journal of Fluids and Structures*, 24 (8), 1284-1293.
- Matin Nikoo, H., Bi, K., Hao, H. (2018). Effectiveness of using pipe-in-pipe (PIP) concept to reduce vortex-induced vibrations (VIV): Three-dimensional two-way FSI analysis. *Ocean Engineering*, 148, 263-276.
- Matin Nikoo, H., Bi, K., Hao, H. (2019). Three-dimensional vortex-induced vibration of a circular cylinder at subcritical Reynolds numbers with low-Re correction. *Marine Structures*, 66, 288-306.
- McNaughton, J., Billard, F., Revell, A. (2014). Turbulence modelling of low Reynolds number flow effects around a vertical axis turbine at a range of tip-speed ratios. *Journal of Fluids and Structures*, 47, 124-138.
- Menter, F. (1994). Two-equation eddy-viscosity turbulence models for engineering applications. *AIAA Journal*, 32 (8), 1598-1605.
- Menter, F. (2012). Best practice: scale-resolving simulations in ANSYS CFD, ANSYS Germany GmbH, First ed.
- Menter, F. (2018). Stress-Blended Eddy Simulation (SBES)-A new paradigm in hybrid RANS-LES modeling. Proceedings of Progress in Hybrid RANS-LES Modelling, 27-37.
- Mittal, R., Balachandar, S. (1995). Effect of three-dimensionality on the lift and drag of nominally two-dimensional cylinders. *Physics of Fluids*, 7 (8), 1841-1865.
- Modir, A., Goudarzi, N. (2019). Experimental investigation of Reynolds number and spring stiffness effects on vortex induced vibrations of a rigid circular cylinder. *European Journal of Mechanics - B/Fluids*, 74, 34-40.
- Mukha, T., Rezaeiravesh, S., Liefvendahl, M. (2019). A library for wall-modelled large-eddy simulation based on OpenFOAM technology. *Computer Physics Communications*, 239, 204-224.
- Navrose, Mittal, S. (2013). Free vibrations of a cylinder: 3-D computations at Re=1000. *Journal of Fluids and Structures*, 41, 109-118.
- Nishino, T., Roberts, G.T., Zhang, X. (2008). Unsteady RANS and detached-eddy simulations of flow around a circular cylinder in ground effect. *Journal of Fluids and Structures*, 24 (1), 18-33.

- Pan, Z.Y., Cui, W.C., Miao, Q.M. (2007). Numerical simulation of vortex-induced vibration of a circular cylinder at low mass-damping using RANS code. *Journal of Fluids and Structures*, 23 (1), 23-37.
- Pastrana, D., Cajas, J.C., Lehmkuhl, O., Rodríguez, I., Houzeaux, G. (2018). Large-eddy simulations of the vortex-induced vibration of a low mass ratio two-degree-of-freedom circular cylinder at subcritical Reynolds numbers. *Computers & Fluids*, 173, 118-132.
- Prsic, M.A., Ong, M.C., Pettersen, B., Myrhaug, D. (2016). Large eddy simulations of flow around a circular cylinder close to a flat seabed. *Marine Structures*, 46, 127-148.
- Ravelli, S., Barigozzi, G. (2018). Stress-blended eddy simulation of coherent unsteadiness in pressure side film cooling applied to a first stage turbine vane. *Journal of Heat Transfer*, 140 (9), 092201-092214.
- Riches, G., Morton, C. (2018). One degree-of-freedom vortex-induced vibrations at constant Reynolds number and mass-damping. *Experiments in Fluids*, 59 (10), 157.
- Rosetti, G.F., Vaz, G. (2017). On the numerical simulations of captive, driven and freely moving cylinder. *Journal of Fluids and Structures*, 74, 492-519.
- Rostami, A.B., Armandei, M. (2017). Renewable energy harvesting by vortex-induced motions: Review and benchmarking of technologies. *Renewable and Sustainable Energy Reviews*, 70, 193-214.
- Sagaut, P. (2006). Large eddy simulation for incompressible flows: an introduction. *Springer Science & Business Media*.
- Saltara, F., Neto, A.D.A., Lopez, J.I.H. (2011). 3D CFD simulation of vortex-induced vibration of cylinder. *International Journal of Offshore and Polar Engineering*, 21 (03), 192-197.
- Shiels, D., Leonard, A., Roshko, A. (2001). Flow-induced vibration of a circular cylinder at limiting structural parameters. *Journal of Fluids and Structures*, 15 (1), 3-21.
- Shih, T.H., Liu, N.S. (2004). Partially resolved numerical simulation, from RANS towards LES for engine turbulent flows, 42nd AIAA Aerospace Sciences Meeting and Exhibit. *ARC*.
- Singh, S.P., Mittal, S. (2005a). Flow past a cylinder: shear layer instability and drag crisis. *International journal for numerical methods in fluids*, 47 (1), 75-98.
- Singh, S.P., Mittal, S. (2005b). Vortex-induced oscillations at low Reynolds numbers: Hysteresis and vortex-shedding modes. *Journal of Fluids and Structures*, 20 (8), 1085-1104.
- Slotnick, J., Khodadoust, A., Alonso, J., Darmofal, D., Gropp, W., Lurie, E., Mavriplis, D. (2014). CFD vision 2030 study: a path to revolutionary computational aerosciences report, 1-58.
- Smagorinsky, J. (1963). General circulation experiments with the primitive equations: I. The basic experiment. *Monthly weather review*, 91 (3), 99-164.
- Soti, A.K., Zhao, J., Thompson, M.C., Sheridan, J., Bhardwaj, R. (2018). Damping effects on vortex-induced vibration of a circular cylinder and implications for power extraction. *Journal of Fluids and Structures*, 81, 289-308.
- Spalart, P.R. (1997). Comments on the feasibility of LES for wings, and on a hybrid RANS/LES approach. Proceedings of first AFOSR international conference on DNS/LES.
- Spalart, P.R., Venkatakrishnan, V. (2016). On the role and challenges of CFD in the aerospace industry. *The Aeronautical Journal*, 120 (1223), 209-232.
- Straka, M., Fiebach, A., Eichler, T., Koglin, C. (2018). Hybrid simulation of a segmental orifice plate. *Flow Measurement and Instrumentation*, 60, 124-133.

- Tu, J., Yeoh, G.H., Liu, C. (2018). Computational fluid dynamics: a practical approach. *Butterworth-Heinemann*.
- Wang, E., Xiao, Q. (2016). Numerical simulation of vortex-induced vibration of a vertical riser in uniform and linearly sheared currents. *Ocean Engineering*, 121, 492-515.
- Wang, X.K., Wang, C., Li, Y.L., Tan, S.K. (2017). Flow patterns of a low mass-damping cylinder undergoing vortex-induced vibration: Transition from initial branch and upper branch. *Applied Ocean Research*, 62, 89-99.
- Wilcox, D.C. (2006). Turbulence modeling for CFD, Third ed. *DCW industries La Canada, CA*.
- Williamson, C.H.K., Govardhan, R.N. (2004). Vortex-induced vibrations. *Annu. Rev. Fluid Mech.*, 36, 413-455.
- Williamson, C.H.K., Govardhan, R.N. (2008). A brief review of recent results in vortex-induced vibrations. *Journal of Wind Engineering and Industrial Aerodynamics*, 96 (6), 713-735.
- Wu, X., Ge, F., Hong, Y. (2012). A review of recent studies on vortex-induced vibrations of long slender cylinders. *Journal of Fluids and Structures*, 28, 292-308.
- Yadav, R., Verma, I., Orsino, S., Sharkey, P., Nakod, P., Li, S. (2019). Bluff-body stabilized flame simulations using SBES in combination with the flamelet generated manifold combustion model, AIAA Scitech 2019 Forum. *American Institute of Aeronautics and Astronautics*.
- Yang, Z. (2015). Large-eddy simulation: Past, present and the future. *Chinese Journal of Aeronautics*, 28 (1), 11-24.
- Yeon, S.M., Yang, J., Stern, F. (2016). Large-eddy simulation of the flow past a circular cylinder at sub-to super-critical Reynolds numbers. *Applied Ocean Research*, 59, 663-675.
- Zhang, B., Mao, Z., Song, B., Tian, W., Ding, W. (2018). Numerical investigation on VIV energy harvesting of four cylinders in close staggered formation. *Ocean Engineering*, 165, 55-68.
- Zhang, K., Katsuchi, H., Zhou, D., Yamada, H., Zhang, T., Han, Z. (2017). Numerical simulation of vortex induced vibrations of a flexibly mounted wavy cylinder at subcritical Reynolds number. *Ocean Engineering*, 133, 170-181.
- Zhang, L.B., Dai, H.L., Abdelkefi, A., Wang, L. (2019). Experimental investigation of aerodynamic energy harvester with different interference cylinder cross-sections. *Energy*, 167, 970-981.
- Zhao, M., Cheng, L. (2011). Numerical simulation of two-degree-of-freedom vortex-induced vibration of a circular cylinder close to a plane boundary. *Journal of Fluids and Structures*, 27 (7), 1097-1110.
- Zhao, M., Cheng, L. (2014). Vortex-induced vibration of a circular cylinder of finite length. *Physics of Fluids*, 26 (1), 015111.
- Zhao, M., Cheng, L., An, H., Lu, L. (2014). Three-dimensional numerical simulation of vortex-induced vibration of an elastically mounted rigid circular cylinder in steady current. *Journal of Fluids and Structures*, 50, 292-311.
- Zheng, H., Wang, J. (2017). Numerical study of galloping oscillation of a two-dimensional circular cylinder attached with fixed fairing device. *Ocean Engineering*, 130, 274-283.
- Zhu, H., Zhao, Y., Zhou, T. (2018). CFD analysis of energy harvesting from flow induced vibration of a circular cylinder with an attached free-to-rotate pentagram impeller. *Applied Energy*, 212, 304-321.



## Chapter 8 Conclusions and recommendations

---

### 8.1 Thesis contributions and concluding remarks

Vortex-induced vibration (VIV) has been widely recognized as a major cause of damages in many offshore structures. Extensive research efforts have been made to mitigate this adverse effect. Currently widely used VIV suppression techniques have some limitations. It is desired to develop more economic yet effective methods to control VIV. In the present thesis, three novel techniques, i.e., the revised pipe-in-pipe (PIP) system, textured pipe and textured-PIP system, are proposed for VIV mitigation. Analytical and numerical studies are carried out to examine the effectiveness of the proposed techniques. Moreover, due to the inherent characteristics of VIV (namely the fluid and structure are strongly coupled with each other), the current numerical simulation methods are either too time consuming or resulting in inaccurate VIV response estimations. To more accurately and efficiently simulate VIV, two methods namely the Reynolds-Averaged Navier-Stokes (RANS) method with Wilcox's low- $R_e$  correction technique and stress-blended eddy simulation (SBES) method are investigated. The major findings in this thesis are summarized below:

#### 8.1.1 Novel techniques for VIV suppression

- Chapters 2 and 3 respectively carry out analytical and numerical studies on the effectiveness of using modified pipe-in-pipe (PIP) system for VIV suppression. The results reveal that PIP system can significantly suppress the VIV of offshore cylindrical components. The control efficiency is most evident in the upper branch where the vibration of the system is most violent. Comparing to the conventional PIP system, the modified PIP can obviously change the wake vortices formation and reduce the drag force on the cylinder. Moreover, the proposed suppression method is not sensitive to the frequency of excitation due to the large mass ratio of the system. Modified PIP can be a cost-effective passive solution to suppress VIV of offshore cylindrical components.
- Chapter 4 numerically investigates the effectiveness of using textured pipe for VIV mitigation. Numerical results reveal that this pipe can effectively suppress VIV by disturbing the formation of wake vortices. Vibration reduction is more obvious when the cylinder is vibrating under a relatively large normalized

velocity. The upper excitation regime occurring in the conventional smooth cylinder is eliminated by the textured cylinder and the width of the lock-in regime is remarkably shortened. Together with its advantage of higher propagation buckling capacity, this pipe may have application potentials for the offshore industry.

- As a combination of the PIP system and textured pipe, the effectiveness of using textured-PIP system for VIV mitigation is investigated in Chapter 5. Numerical results show that this novel strategy is able to simultaneously provide two suppression mechanisms, namely tuned mass damper (TMD) and surface modification. It thus can lead to the most evident control effectiveness among the three techniques investigated in this study. In particular, the wake vortex streets are significantly changed, the lock-in regime is totally eliminated and the drag force is remarkably reduced by this novel technique.

It should be noted that all these techniques are based on or modified from the existing practices. In other words, they can effectively suppress the VIV without change too much of the existing designs, they are believed having great application potentials.

### **8.1.2 Numerical models for VIV prediction**

- In Chapter 6, the Wilcox's low- $Re$  correction technique is incorporated into the commonly used RANS *SST*  $k - \omega$  model, and 3-D VIV responses of a cylinder obtained by using this method are compared with experimental studies. Numerical results show that this modification leads to more accurate VIV response estimations compared to the commonly used RANS *SST*  $k - \omega$  method especially within the upper branch.
- In Chapter 7, SBES hybrid turbulence model is used to further improve the accuracy of VIV simulation. Numerical results revealed that very accurate VIV response amplitudes can be obtained in the upper branch where most of the current models fail to capture. Three VIV response branches and the corresponding transitions can be well captured by the SBES model, and a broader range of vortices scales are resolved by the SBES model which results in more realistic wake vortex patterns compared to the RANS model.

## **8.2 Recommendations for future research works**

Following investigations could be further made in the future studies:

- Comprehensive numerical studies are carried out in the present thesis to show the effectiveness of the three new passive techniques for VIV control. Experimental studies are needed to further validate the obtained results.
- Only rigid cylinders and subcritical flow regime are considered in the present thesis. Offshore cylindrical components in real applications are mostly flexible, and they may face high Reynolds numbers during their service lives. Flexible structures subjected to critical and supercritical flow regimes may need to be investigated to further demonstrate the merits of the proposed methods in this thesis.
- Vibration control by using PIP concept can be extended to other structural arrangements such as triple bundle cylinders. Further study on this topic is worthy.
- Different facet shapes can be obtained for the textured pipe with different design parameters. In this thesis, only a full-diamond pattern with eight folded lobes is investigated. This shape does not necessarily result in the most evident VIV suppression. Further studies need to be carried out to find the optimal shape of the textured pipe for VIV control.
- In the present study, the predefined Wilcox coefficients are adopted for VIV simulations. Though the effectiveness of using Wilcox's correction technique is demonstrated in the present thesis, the correction coefficients might influence the numerical results. Further study can be performed to investigate how these parameters influence the numerical results.

## Bibliography Disclaimer

Every reasonable effort has been made to acknowledge the owners of copyright material. I would be pleased to hear from any copyright owner who has been omitted or incorrectly acknowledged.



Signature: ..... *Hamid Matin Nikoo*  
11-Nov-19

Date: 11-Nov-19

# Appendices

## Appendix A

### Copyright Declaration

I warrant that I have obtained, where necessary, permission from the copyright owners to use any third-party copyright material reproduced in the thesis, or to use any of my own published work in which the copyright is held by another party.



*Hamid Matin Nikoo*

Signature: ..... *11-Nov-19*

Date: 11-Nov-19



**RightsLink**<sup>®</sup>



**Title:** Passive vibration control of cylindrical offshore components using pipe-in-pipe (PIP) concept: An analytical study  
**Author:** Hamid Matin Nikoo, Kaiming Bi, Hong Hao  
**Publication:** Ocean Engineering  
**Publisher:** Elsevier  
**Date:** 15 September 2017  
© 2017 Elsevier Ltd. All rights reserved.

Please note that, as the author of this Elsevier article, you retain the right to include it in a thesis or dissertation, provided it is not published commercially. Permission is not required, but please ensure that you reference the journal as the original source. For more information on this and on your other retained rights, please visit: <https://www.elsevier.com/about/our-business/policies/copyright#Author-rights>



RightsLink®



**Title:** Effectiveness of using pipe-in-pipe (PIP) concept to reduce vortex-induced vibrations (VIV): Three-dimensional two-way FSI analysis

**Author:** Hamid Matin Nikoo, Kaiming Bi, Hong Hao

**Publication:** Ocean Engineering

**Publisher:** Elsevier

**Date:** 15 January 2018

© 2017 Elsevier Ltd. All rights reserved.

Please note that, as the author of this Elsevier article, you retain the right to include it in a thesis or dissertation, provided it is not published commercially. Permission is not required, but please ensure that you reference the journal as the original source. For more information on this and on your other retained rights, please visit: <https://www.elsevier.com/about/our-business/policies/copyright#Author-rights>



RightsLink®



**Title:** Three-dimensional vortex-induced vibration of a circular cylinder at subcritical Reynolds numbers with low- $R_e$  correction

**Author:** Hamid Matin Nikoo, Kaiming Bi, Hong Hao

**Publication:** Marine Structures

**Publisher:** Elsevier

**Date:** July 2019

© 2019 Elsevier Ltd. All rights reserved.

Please note that, as the author of this Elsevier article, you retain the right to include it in a thesis or dissertation, provided it is not published commercially. Permission is not required, but please ensure that you reference the journal as the original source. For more information on this and on your other retained rights, please visit: <https://www.elsevier.com/about/our-business/policies/copyright#Author-rights>

## Appendix B

### Statement of Co-authors

#### To whom it may concern

I, Hamid Matin Nikoo, carried out numerical simulations, analysis of the results and written the manuscript for the papers titled below. The manuscripts were revised and edited by other co-authors.

(Hamid Matin Nikoo)

  
(.....) *Hamid Matin Nikoo*  
11-Nov-19

1. Passive vibration control of cylindrical offshore components using pipe-in-pipe (PIP) concept: An analytical study, (Chapter 2).
2. Effectiveness of using pipe-in-pipe (PIP) concept to reduce vortex-induced vibrations (VIV): Three-dimensional two-way FSI analysis, (Chapter 3).
3. Vortex-induced vibration of a full-diamond textured cylinder at subcritical Reynolds numbers, (Chapter 4).
4. Textured pipe-in-pipe system: a compound passive technique for vortex-induced vibration control, (Chapter 5).
5. Three-dimensional vortex-induced vibration of a circular cylinder at subcritical Reynolds numbers with low-Re correction, (Chapter 6).
6. Using stress-blended eddy simulation (SBES) method to simulate vortex-induced vibration (VIV) of an elastically-mounted cylinder, (Chapter 7).

I, as a co-author, endorse that this level of contribution by the candidate is appropriate.

(Prof. Hong Hao)



(Dr. Kaiming Bi)

